A multiple cell tracking method dedicated to the analysis of memory formation in vivo

Felipe Delestro

PSL
UNIVERSITÉ PARIS

THÈSE DE DOCTORAT
DE L'UNIVERSITÉ PSL

Préparée à l'École Normale Supérieure

A multiple cell tracking method dedicated to the analysis of memory formation *in vivo*

Soutenue par
Felipe Delestro
Le 25 Octobre 2018

École doctorale n°
Ecole Doctorale Complexité du vivant ED515

Spécialité
Biologie cellulaire

ENS

Composition du jury :

M. Auguste GENOVESIO Ecole normale supérieure	*directeur de these*
Mme Florence CLOPPET Équipe SIP, Université Paris Descartes	*Président du jury, Rapporteur*
Mme Angela GIANGRANDE Institut de génétique et de biologie moléculaire et cellulaire, Université de Strasbourg	*Rapporteur*
M. David DI GREGORIO Dynamic Neuronal Imaging, Institut Pasteur	*Examinateur*
Mme Perrine PAUL-GILLOTEAUX Institut de Recherche en Santé, Université de Nantes	*Examinateur*
M. Thomas PRÉAT Gènes et Dynamique des Systèmes de Mémoire, ESPCI	*Examinateur*

Acknowledgements

For sure it was a huge adventure to go through this thesis, it was a process of great scientific and personal growth! And there's no way it could be done all alone.

I would like to thank all my family for the great the support, including the difficult task of having me moving to another continent. Also, adapting to the new life here in France would be way more difficult without my partner Juliana, that always was up to face all the challenges of living in new country.

Being here was much more than just scientific growth, and I thank all the great friendships that I made throughout the years! I'll be always ready whenever you all want to go out after work.

None of this would be possible without the thrust that Auguste placed in me since our first contact. With his great guidance during the whole thesis it was possible to make these years here at IBENS a period of great discoveries. Also, it was fundamental our collaboration with ESPCI, and all the great scientific discussions with Thomas.

Finally, I would like to thank Paris Sciences & Lettres and the Labex MemoLife for the financial support during this thesis, as well as the École Normale Supérieure for all the infrastructure necessary.

Abstract

Formation and consolidation of new memories is one of the fundamental characteristics of the brain, responsible for learning and high cognitive behavior. While important, the process isn't fully understood to the present day and is the subject of various studies, spanning from the activity analysis of individual synapses to the reconstruction of brain connectivity maps. In this work, we propose a bold approach, on which we aim to measure *in vivo* the activity of every single neuron from the whole Mushroom body (MB) of the *Drosophila melanogaster*, in a fully automated procedure. After a 3D image acquisition over time of the MB by means of confocal microscopy, an automated detection and tracking of the neurons is performed. The whole process takes place while the fly is awake and subjected to different odor stimulations, so that it is possible to associate the activity patterns at the single cell level to the stimulus that is being received. By comparing the response patterns from flies that were trained and flies that were not trained to associate an odor with an electric shock we identified changes in neuronal activity, providing information on how memory is formed. Beyond the methodological innovation that brought the possibility to track the activity of a large set of single neurons, this work contributed to the current understanding of long term memory formation.

Résumé

La formation et la consolidation de souvenirs est l'une des caractéristiques fondamentales du cerveau, responsable de l'apprentissage et de comportements cognitifs élevés. Malgré son importance, ce processus n'est pas entièrement compris à ce jour et fait l'objet de nombreux travaux de de recherche, allant de l'analyse de l'activité des synapses individuelles à la reconstruction de cartes de connectivité du cerveau. Dans ce travail, nous proposons une approche intégrée pour mesurer *in vivo* l'activité de chaque neurone du corps pédonculé (Mushroom body, MB) de la *Drosophila melanogaster* dans une procédure entièrement automatisée. Il s'agit d'imager en 3D et dans le temps le MB dans sa totalité par microscopie confocale et d'opérer un suivi temporel de la position de chaque neurone afin de relever leur niveau individuel d'activité. En utilisant cette approche, nous avons découvert que pendant la formation de la mémoire à long terme, de nouveaux neurones sont recrutés au sein du corps pédonculés, tandis que l'intensité de la réponse des neurones individuels reste inchangée. Au delà de l'apport méthodologique qui permet à présent de quantifier automatiquement l'activité d'un grand nombre de neurones, ce travail a contribué à une meilleure compréhension de la formation de la mémoire à long terme.

Summary

Chapter 1

Introduction

> *If the brain were so simple we could understand it, we would be so simple we couldn't.*
>
> **Lyall Watson**

1.1 Context

The brain is one of the most complex systems known to mankind. This, at least, according to the brain itself. It is common for us to separate our consciousness from it — and in fact this was the common reasoning for thousands of years — but all of our thoughts, passions, desires and beliefs are no much more than a group of cells firing in the right order.

But the result of these rather simple cells working together is something that is much bigger than the sum of its parts. The brain likes to label itself as "intelligent", even though this is a term that is extremely hard to be objectively defined. One of current interpretations, structured by Jeff Hawkins on his book "On Intelligence" [1], is the *Memory prediction framework*, which states that intelligence is nothing more than the ability to make predictions, based on previous experiences. Simply put, the brain is always trying to predict the next stage of the input signals it is receiving, using the previously stored memories as database in this highly nonlinear model. Thus, for Hawkins, memory is at the core of intelligent behavior.

In fact, during the past decades we just started to understand how neurons can work together to process information. This brought an enormous impact, not only because it allows us to better understand ourselves, but also because it was the seed that started the current technological revolution we are experiencing, the born and raise of Artificial Intelligence.

Computers are more and more able to behave in a way that can be considered intelligent, and it all started with the first *in silico* simulations of neurons, like perceptrons and simple neural networks [2]. Since then, the increased computational power allowed the development of more elaborated networks, capable of solving complex problems. This new approach, termed *deep learning* [3], is inspired by the way neurons connect in layers within the brain cortex, and is able of remarkable achievements, as the recognition of images with high precision [4] or the simulation of speak patterns in a way that is indistinguishable from a real human [5]. The core of this success is the fact that neural networks are capable of learning from presented data, thus having a memory stored in the weights that connect the artificial neurons. Something like what the real

neurons do inside our brains.

None of this would be achievable without an understanding of how neurons are capable of processing and storing information. However, we are still far from having a complete model of how they are able of such features, and a better comprehension of the mechanisms of memory could bring astonishing innovations.

The irony is that the brains we need to learn from are everywhere, waiting to be investigated. Evolution has shaped the nervous system for millions of years, into a superb machine for memorization and prediction. The problem is that this machine doesn't come with an instructions manual, and the only way to understand how it works is by exploring and asking the right questions. And this is the main objective of this thesis, to delve into the mechanisms of memory formation and bring new insights on how memory works.

1.2 Problematic

The biggest challenge to achieve this goal is methodological. To have a global view of the neuronal activity, while memories are being recalled, we need to be able to check the activity of individual neurons *in vivo*. Furthermore, because memories are stored in a sparse distribution within the brain [6], the whole structure needs to be scanned at once.

These constrains make two common approaches, neuronal electrophysiology [7] and functional magnetic resonance imaging (fMRI) [8], unqualified. Electrophysiology brings a high resolution, measuring directly the voltage changes in the membrane of neurons, but it is limited to a restricted number of simultaneous measurements, as a physical probe is used for the recordings. On the other side, fMRI is capable of measuring the activity over the whole brain (even for the huge mammal brain), but lacks the capability of single cell resolution. During a fMRI scan, the brain activity is measured by changes associated to the blood flow, which doesn't allow a single cell resolution. Consequently, the the recorded activity is assigned to a fixed volume in space, not necessarily a single cell.

1.2.1 Approach

Therefore, we approach the problem via fluorescent imaging. Further details will be given upon Chapter 3, but the basic idea is that by being able to measure the Ca^{2+} changes within neurons, and also having a nuclei marker to identify individual cells, we will be able to know the level of activity at the single cell level. The downside of this approach is that the desired field of view should be imaged, in 3D, fast enough to capture the responses from the neurons and with high enough resolution so that individual neurons could be detected. The current state of the art technologies in microscopy wouldn't allow the acquisition of a whole vertebrate brain within these standards.

Although the complexity of a mammal brain is indisputable, and much can be studied from it, the bases of the system are well found in other organisms. In our case, is particularly interesting the model of the fruit fly, *Drosophila melanogaster*. Vastly used in current research for its flexibility, it is one of the most important animal models nowadays, and will be further discussed during Chapter 2. Besides having a brain small enough to fit into a single 3D field

of view of a confocal microscope, the fruit fly is capable of conditioned learning, making it an ideal model for the study of associative memory.

The idea is simple: take a group of flies, make them learn something and record the brain activity while they remember the lesson. As control, also record the brain of another group of flies that didn't learned anything. The differences between these two groups should show what were the structural changes within the brain during the learning process. The details of the protocol will be explained within Chapters 2 and 3.

1.2.2 Queries

From this, few questions about the mechanisms of memory can emerge. Are new neurons recruited to represent the acquired information? Is the activity of the neurons that represent the stimulus increased, in comparison to the group that didn't learned? Even simple inquires like these were never fully answered in a precise and quantitative way.

Technically challenging, the answer to these questions rely on the development of new methodology. For the best of our knowledge, no research group was able to perform the extensive 3D recordings in vivo of a whole Mushroom body, automatically detect neurons and measure their activity. The computational techniques that were designed for these goals are explained in detail during Chapters 4, 5, 6 and 7.

Being in the intersection of state of the art technologies from both biology and computer sciences, the work developed on this Thesis is highly interdisciplinary. Aspects regarding the biological bases will be explained within this Chapter, in Section 1.4 and the computational aspects needed to better comprehend the methods during Section 1.5.

1.3 Work environment

This work was developed within the laboratory of Computational Bioimaging and Bioinformatics of the *Institut de Biologie de l'Ecole Normale Supérieure* (IBENS), under the supervision of Auguste Genovesio. The laboratory develops projects in different fields of computer sciences, ranging from image analysis to bioinformatics, in partnership with several other Parisian institutions.

The project would not have been possible without the partnership with the laboratory of *Gènes et Dynamique des Systèmes de Mémoire*, directed by Thomas Preat, at the *Ecole Superiéure de Physique et de Chimie Industrielles de la Ville de Paris* (ESPCI). Their laboratory is deeply involved in the research of the mechanisms of memory using the *Drosphila melanogaster* as a role model.

1.4 Biological aspects

During this Section we'll explore a few key points for the better understanding of the biological aspects of this Thesis.

1.4.1 Memory

For more than a century, one of the greatest challenges of neuroscience has been the understanding of the mechanisms of memory formation and restoration. The process of memorization breaks down into three stages: learning, storage/consolidation and recall.

Learning is defined as the acquisition of

information that can be manifested by a change in behavior based on experience. The persistence of this behavioral change over time is the revealer of the formation of a memory, including the consolidation phase and the recall phase.

In the human being, memory takes on different facets. Declarative and non-declarative memories are generally distinguished [9]. Semantic memory and episodic memory, which are two systems of long-term conscious representation, constitute the declarative memory.

Semantic memory is based on global knowledge and knowledge of oneself and the world [10], while episodic memory focuses on past moments and events [11]. Nevertheless, episodic memory events tend to amalgamate to form a semantic corpus. Among the non-declarative memories, we find the procedural memory allowing unconscious kinetic automatisms, to develop skills such as walking, playing a musical instrument, or even artistic abilities like drawing [12]. These learnings are unconscious. Fears learned or dislikes involving the amygdala are also forms of non-declarative memory [13]

Furthermore, it is possible to categorize memory according to its time course. Long-term memories can last for days, months or years, while short-term memories will fade away more quickly. In the extreme, working memory is a very short-term memory, which stores information for a few seconds or tens of seconds, and needs to be re-mobilized regularly to last a little longer [14, 15]. The subjectivity of this categorization, particularly related to human language, makes it difficult to extrapolate to other animal species.

In most animal species, the nervous system serves as a basis for supporting these memory processes. Although huge morphological differences exist between them, it is possible to compare some basic principles of functioning of the nervous system, differences and common points that can be found between different sorts of brains. This can allow us to be better equipped to compare the *Drosophila* to other species such as mammals.

Further aspects of memory, in specific to the *Drosophila* model, will be discussed upon Chapter 2.

1.4.2 Neuronal morphology & physiology

At the anatomical level, neurons are rather bipolar in the central nervous system of mammals, while invertebrates, and in *Drosophila* in particular, they are unipolar (as seen in Figure 1.1). These neurons are organized into ganglia in the nervous system of insects, while vertebrates are more complex. In the latter, the cerebral hemispheres of prosencephalic origin have a particular structure, the cerebral cortex which itself has a particular diversity across species. In reptiles like the alligator, the cortex consists of a single layer of neurons, while up to six layers can be distinguished in mammals such as rats or humans. Without seeking to be exhaustive, we must note that many other differences exist between animal species at different levels in the physiology of the nervous system. For example, the propagation of electrical signals is not in the form of action potentials in the nematode worm, and in insects, and in particular *Drosophila*, the axonal fibers are not myelinated.

At the neuronal scale, the electrical and synaptic properties are conserved globally. Both excitatory neurons and in-

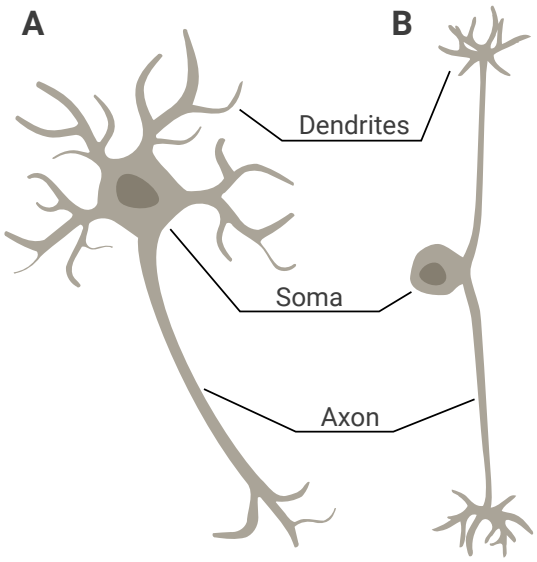

Figure 1.1: Different morphologies of neurons. (A) Bipolar neuron, where the dendritic compartment is upstream of the cell body and downstream is the axonal compartment. (B) Unipolar neuron, on which the dendrites and the axon are in continuity, deriving from the cell body.

hibitory neurons are found in different species. In a related fashion, most of the neurotransmitters used in the nervous system are shared: acetylcholine, glutamate, dopamine, serotonin, GABA, as well as different neuropeptides [16–18]. All these homologies result from the existence of orthologous genes between the different species. In this case, the conservation of neurotransmitters comes from a strong conservation in the biosynthetic enzymes of these neurotransmitters [19].

Synaptic plasticity, a fundamental mechanism for storing information, is also very well preserved. We can also note that synaptic retrograde messengers exist in most species: *Drosophila*, for example, exhibits NO-dependent retrograde communication [20]. In addition, there may also be non-synaptic connections between neurons, via communicating junctions, able to form electrical synapses, including in *Drosophila* [21]. Another very common feature of central nervous systems in many species, including the fruit fly, is the presence of glial cells, in greater or lesser proportion to neurons [22]. If glial cells, and in particular astrocytes, are predominant in mammals, glial cells (astrocytes, cortical glia and glean "sheathing") remain a minority in *Drosophila*. However, these glial cells appear to be able to perform functions equivalent to those of astrocytes in mammals, as they surround the cell bodies and proximal neurites, are coupled to the vascular network and are closely associated with synapses [23–25]. Finally, it can also be noted that many signal transduction pathways are conserved and that metabotropic receptors and ionotropic receptors are found in different species [26, 27].

At the organization level of the neural networks, one can still note some similarities. Because of the need to explore the environment and react, sensory neurons associate in an intermediate stage which itself contacts, downstream, the motor neurons. Such an organization is found both in the reflex arc of mammals and in the innate responses to aversive odors in *Drosophila*. Moreover, in different organisms, an innate response can be modulated by learning, involving a derivation of information to integrating centers [28, 29].

1.4.3 Classical conditioning

Most of the questions underlying the formation of memory relates to the nature, duration, location and mechanisms of changes in the nervous system, changes that are also called memory traces. One of the first neurobiologists to take an interest in these mechanisms was Ivan Pavlov (1849-1936). Noticing that dogs tended to salivate before actually making contact with food, he decided to investigate this "psychic

secretion" in more detail. Thus, he discovered the basic laws of acquisition and the loss of conditional reflexes (which would later become conditioned responses) that is, reflex responses, such as salivation, which do occur only conditionally to specific experimental conditions in the animal [30].

He developed the concept of classical conditioning, which focuses on the consequences of learning related to the association between environmental stimuli and the automatic reactions of the body. This notion of involuntary reaction is the main point that differentiates it from operant conditioning, where learning leads to a voluntary change in behavior.

The principle of classical conditioning has been adapted many times to study in more detail the mechanisms underlying the formation of these conditioned reflexes. Initial works, on the study of the defensive reflexes of *Aplysia* (a gastropod mollusc), in response to tactile stimuli has allowed major advances. The tactile stimulation of the gills and the siphon located on the back of this organism causes a reflex of withdrawal. Repeated application of this stimulus and its association with another stimulus causes habituation reactions (gradual decrease in the intensity or frequency of appearance of the conditioned reflex) and sensitization (gradual increase in intensity or the frequency of appearance of the conditioned reflex when associated with an unpleasant stimulus) [31–33].

The results obtained on Aplysia by E. Kandel (Nobel Prize in Physiology and Medicine, 2000) have determined that learning is based on functional changes in the effectiveness of existing excitatory connections [34, 35]. This work also revealed the importance of the cyclic 3'-5 'adenosine monophosphate (cAMP) pathway [36] and protein kinase A (PKA) in the formation of short-term memories (sensitization) [37] and CREB transcription factor (cAMP -response element binding protein) in long-term memory formation [38]. Thus, it has been proposed that the formation of short-term memory is based on changes in synaptic efficiency while long-term memory induces changes in the number of these synapses.

The study of learning and memory also benefited from the contribution of another neurobiologist, Seymour Benzer (1921-2007). He first became interested in molecular biology, including the structure and regulation of genes, and developed a recombination-based system for the systematic study of mutations [39, 40]. He then turned to neuroscience, and more particularly to the neurogenetic mechanisms of behavior in the fruit fly, *Drosophila melanogaster*. Based on its experience in molecular biology, Benzer has developed the bottom-up approach for the study of neurobiological mechanisms. This approach is based on the principle that a point mutation of a given gene has important consequences on the physiology and behavior of the animal. Thus, the study of a precise mutation makes it possible to understand molecular and then cellular mechanisms involved in a mechanism as complex as learning [41].

Benzer was one of the first to realize that understanding the genetic mechanisms of behavior in *Drosophila* would help understand the functioning of more complex brains. S. Benzer's laboratory has developed many paradigms for the study of Drosophila behavior [42]. These have identified a number of "behavioral genes" such as period [43], the first identified circadian rhythm mutant, or amnesiac (amn) [44] and dunce (dnc) [45], both involved in olfactory learning.

Nearly 40 years after the identification of the first mutants, the physiological role of the genes affected is still far from being fully elucidated, despite considerable progress.

1.4.4 The Fruit fly model

During this thesis, we use the *Drosophila melanogaster* as a model organism. Besides its small size, the fruit fly is the seat of complex neuronal processes, and it is proving to be a model of choice for several studies thanks in particular to the powerful tools of molecular genetics.

A *Drosophila* can form an aversive or appetitive associative olfactory memory, depending on whether an odor is associated with a punishment or reward. As an aversive, if the conditioning is repeated at least five times with intervals of rest, the memory is consolidated by involving protein synthesis *de novo* and can then last more than a week, being called Long Term Memory (LTM). In the context of the appetitive paradigm, there is also an LTM dependent on *de novo* protein synthesis, but its formation is engaged in the first cycle of learning.

The Mushroom body is the brain center where olfactory memory is encoded and it is composed of about 2000 neurons per hemisphere, called Kenyon Cells (KCs). They receive connections from by about 150 cholinergic projection neurons providing them with olfactory information, but also by about 130 afferent dopaminergic neurons and only 34 efferent neurons.

The use of *Drosophila* as a model organism derives in particular from major practical aspects. In the first place, its breeding is simple, taking place in bottles or tubes of nutrient medium placed in incubators with finely controlled conditions (temperature, humidity, day/night cycle). On the other hand, its reproductive cycle is particularly short: 10 days at 25°C. This gives the laboratory the opportunity to obtain a large number of individuals quickly and at relative low cost, when compared to other animal models. The fruit fly also offers the possibility of performing routine genetic manipulations (recombinations of two mutations for example) in relatively short times (a few weeks). Finally, the short reproductive cycle associated with behavioral devices that accommodate large *Drosophila* groups offers an exceptional statistical dimension to experiments.

Further aspects of memory conditioning, as well as more specific protocols for the drosophila model, will be explored during Chapter 2

1.5 Computational aspects

This section explores a few important topics linked to the computational aspects of the Thesis.

1.5.1 Image analysis

For us, humans, the vision is usually the first source of information when trying to understand a given phenomena. Digital images are capable of largely expanding the limits of our vision, by broadening the possible frequency spectrum to wavelengths that our eyes can normally see, or by revealing small details that would not usually be distinguishable. This makes straightforward the need to use computers to process digital images, with the ultimate goal of better extracting informations from them.

Digital images are composed of a grid

of units, called *pixels*. The pixel is the smallest unit of information storage within an image, that can usually be encoded in 8-bit (values ranging from 0 to 255) or 16-bit (from 0 to 65535). In microscopy, the amount of pixels within the image is defined by the camera sensor, which in our case records 512x512 pixels at 16-bit.

To extract the desired information from these images, innumerous algorithms and tools have been developed though the past decades. From spot detection [46–48] to image segmentation [49–51] or particle tracking [52–54], classical subjects have been explored for a long time, but no standard universal approach exists to solve every problem. Some software packages aim to solve the more common needs with well established algorithms, as ImageJ/Fiji [55], Icy [56] or CellProfiller [57]. However, usually state of the art research demand the development of new, custom, tools for specific problems.

When it comes to developing new software for image analysis, different programming languages can be used, each with their own strength and weakness. During the progress of this thesis, we opted for using Python as a programming language [58]. It is one of the biggest growing languages in the world [59], with a solid open-source communities for fields like image processing [60] ormMachine learning [61]. The language makes prototyping relatively easy, allowing a well needed exploratory phase during scientific research, while having a relatively high efficiency [62].

Especially challenging, the analysis of 3D images is of great importance. The majority of the available algorithms and software are suited only for 2D images, being some times not possible a direct extrapolation for a 3D space. In case the data is truly constituted of a three-dimensional structure, usual dimensionality reductions like axial projections can lead to wrong interpretations. For the cases when the data is 3D, but structures form a 2D-manifold that crosses the space, the extraction of this manifold directly from the 3D space is of great help for the further stages of processing [63].

1.5.2 Spot detection

Spot detection tools are extensively used to collect positions of biological objects and extract quantitative information from 3D microscopy images. The fluorescently labeled objects of interest can range from tiny biological objects as individual proteins, viral particles or endosoms to much larger objects such as cell nuclei or parasites, depending on the microscope resolution. This is an important point, as the methodology chosen to detect a certain kind of structure can completely change, just based on the scale of the acquisition.

An interesting example is the case of nuclei detection. Depending on the species or tissue, the nuclei size can vary greatly. Together with the variation of resolution of the acquisition, the diameter of an individual nuclei can vary from just a few pixels to hundreds, as seen in Figure 1.2.

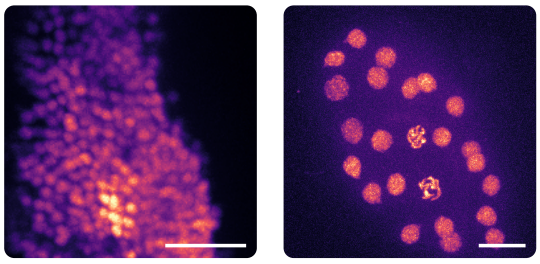

Figure 1.2: Comparison of nuclei sizes. On the left, the nuclei from the Mushroom body of the *Drosophila melanogaster*; on the right nuclei from the embryo of *Caenorhabditis elegans*. Both images are an axial max intensity projection, and scale bars are of 10 µm.

For the case of nuclei the size of the ones shown for the *C. elegans*, the process would be more properly addressed as "object" detection, as the structure is clearly above the resolution of the microscope. Regarding this case, specific methodologies have been developed [64, 65].

When analyzing the image of the *D. melanogaster* (thus, the data used for the development of this Thesis), the structures are barely above the diffraction limit of the light, resembling true spots. So, for this case, techniques that handle sub-resolution spots can be used.

Reliable 3D detection of diffraction-limited spots in fluorescence microscopy images is an important task in subcellular observation. In general, fluorescence microscopy images are strongly degraded by noise and non-specific background, which makes reliable detection difficult. Several methods have been developed for this task during the past years, and have been compared in recent reviews [66, 67].

1.5.3 Object tracking

Object tracking refers to the identification of spots through a sequence of images to determine their evolution [68] and it is of great importance for the quantitative analysis of intracellular dynamic processes from temporal microscopy image data. Since manual detection and tracking of a large number of individual particles is not feasible, the development of automated methods for this task is essential .

An "object" can be anything from a single molecule to a macromolecular complex, organelle, virus or microsphere [69]. Currently, dozens of software tools are available for particle tracking [70]. The image analysis methods on which they are based can generally be divided into two stages: Firstly, a particle detection (the spatial aspect), in which the spots that stand out from the background according to certain criteria are identified and their coordinates estimated at each image of the image sequence. Secondly, the data association (the temporal aspect), in which the detected particles are connected from one frame to another using another set of criteria to form tracks. For each of these steps, many methods have been developed over the years [71–76], that sometimes are also derived from other areas of data analysis [77, 78].

A recent review on tracking methods [79] indicates that, at present, there is no universal method of particle tracking, and users should be aware that a method reported to work for some experiments may not be the right choice for their application. It is advisable to use synthetic image data mimicking real data, both to find the best parameters of a given method and to evaluate its potential performance. Users should be especially cautious when the Signal to Noise Ratio (SNR) of their images is significantly less than 4, although in the case of more diffusive (rather than directed) particle motions, most methods yield accurate estimates of dynamics for lower SNR.

The same review also points the importance of parameter tuning and the optimal use of prior knowledge about the data. The authors defend that the comprehension of the basic aspects of the data is crucial for an successful tracking of the desired objects.

1.5.4 3D microscopy

If we want to be completely strict, 3D microscopy doesn't exist at all (or at least, not with current technology). Every microscope that uses a camera to capture photons (as a Charge-coupled device —CCD— for example) possess a 2D sensor, thus being capable only of acquiring 2D images. What is commonly called as a 3D image is in fact a stack of 2D acquisitions, at different focal planes.

This fact brings one of the main compromises of imaging in depth, the lower resolution on the axial direction regarding the acquisition plain (as seen in Figure 1.3. The distance between the focal planes can be as small as the pixel size of the camera sensor, but the resolving power of it will still be limited by the diffraction limit of the light.

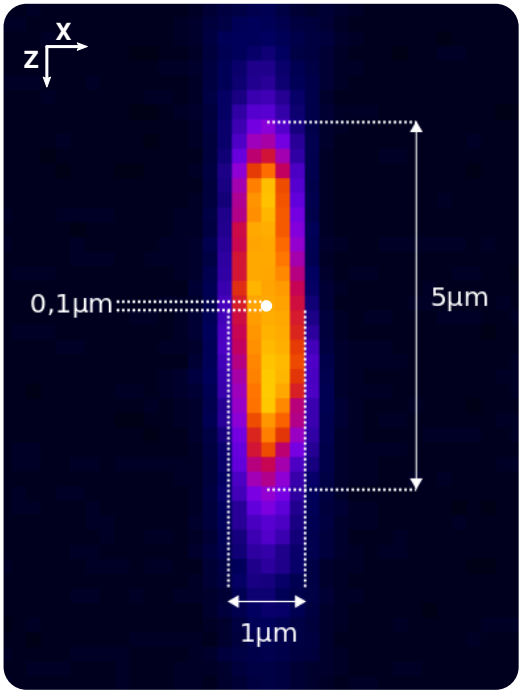

Figure 1.3: Point spread function obtained from a fluorescent bead of size 0.1 µm, schematized in white at the center of the image. Note how the axial distortion (vertical axis) is considerably higher than in the XY plane.

1.5.5 Super-resolution microscopy

Although not directly used for the data acquisition of the work presented here, the concept of super-resolution microscopy is of great importance, as it is a recent technological innovation that surpassed the diffraction limits of light for microscopy imaging. Besides, the tracking methodology exposed in the Chapter 5 is loosely inspired by this methodology.

The super-resolution microscopy, which development brought the 2014 Nobel Prize of Chemistry to E. Betzig, W. E. Moerner and S. Hell, aims to exceed the refraction limit of light by shaping the excitation beam [80] (STED for Stimulated Emission Depletion), or by sequentially activating the fluorophores present in the sample [81] (PALM for Photoactivated Localization Microscopy, or STORM for Stochastic Optical Reconstruction Microscopy).

Nanoscopy techniques represent one of the major evolutions for the years to come, but there are still few in vivo applications in neurobiology so far. These studies mainly concern the dendritic spines of neurons [82]. The main limitations of these techniques for their application to living imaging are their low signal-to-noise ratio, the difficulty of using them deeply in biological tissues, their weak temporal dynamics (for use in microscopy systems PALM or STORM), and the use of high laser powers (especially for STED microscopy).

The image of a point object is not punctual but consists of a diffraction pattern, called Airy figure for circular pupils, which is the case of the microscope objectives used. The obtained Airy figure is an interference figure that constitutes the impulse response of the microscope

otherwise known as point spread function (PSF). Thus, two objects very close to one another spatially, separated by a distance d, will effectively be perceived as two distinct objects, according to the Rayleigh criterion [83], only if d is greater than or equal to the radius r of the spot's Airy disk, which corresponds to the central ring of the diffraction pattern.

1.5.6 Two-photon microscopy

Two-photon microscopy is based on a nonlinear physical process of simultaneous absorption of two photons by the fluorophore. This process was theoretically planned in 1931 by Maria Göppert-Mayer but it was only applied to microscopy much later [84] thanks to the technological development of lasers. The absorbed photons have about half the energy required to transition from the ground level to the first excited state, but the fluorescence emitted by the fluorophore is the same as if it had been excited by a single-photon absorption process.

The conditions necessary for the two-photon absorption are a very high photon density from a spatial and temporal point of view to ensure a good efficiency of simultaneous absorption of two photons by the fluorophore. Thus, the excitation sources mainly used for the two-photon excitation are intense pulsed lasers emitting in the near infrared, pulse duration of the order of a few tens of femtoseconds: typically it is often a laser whose amplifier element is a sapphire crystal doped with titanium ions. The two-photon absorption quadratically depends on the intensity of the excitatory light. Thus, the excited volume will be limited where the laser beam is the most focused, spatially limiting the effects of photobleaching and phototoxicity.

Nevertheless, the use of pulsed lasers of high power can lead to a heating of the sample limiting the benefits in terms of phototoxicity of the confinement of the excitation. This confining characteristic of the excitation, however, makes biphotonic microscopy intrinsically confocal, without the need to use a filtering hole. Indeed, unlike confocal microscopy where the photons not coming from the focal plane are filtered, the two-photon excitation produces fluorescence only at the level of the focal volume, thus ensuring a direct optical sectioning.

Typically, to excite EGFP-type fluorophores, the optimal two-photon excitation wavelength is about 930 nm versus 490 nm for linear single-photon excitation [85]. This shift of the wavelengths towards the red will make it possible to image more deeply because the exciter light will be less diffused and absorbed by the out-of-focus sample planes [85]. In addition, the wavelength range for the two-photon excitation is less invasive for biological tissues because it corresponds to the "therapeutic window", a spectral region typically between 700 nm and 1 µm in which tissue absorption biological is minimal. Despite all the advantages of biphotonic microscopy presented above, this technique suffers from the same limitation as confocal microscopy because the only difference between these two types of microscopy is the fluorescence excitation process. A point-by-point scan of the sample is required to recreate two-dimensional optical sections, and then an axial scan to reconstruct a three-dimensional image of the sample. In order to overcome this scanning time, full-field microscopy techniques capable of optical sectioning, such as light-sheet microscopy or structured illumination microscopy, have been developed.

1.6 Plan

This thesis is divided in Chapters, explaining the main aspects of what was developed, as well as annexes of the resulting publications.

During the Chapter 2 — Flies, neurons & memory — in deep details of the biological model are explained.

Chapter 3 — Data acquisition — deals with the methodology and problems encountered when acquiring the data we used for the analysis.

The methodology we developed to detect the neurons from the Mushroom body is explained during Chapter 4 — Neuron detection.

Once having the detected neurons, their tracking through time is needed, a process detailed in Chapter 5 — Neuron tracking.

Chapter 6 — Measuring neuronal activity — deals with the measurement of the neuronal activity from the acquired tracks.

The quantification of this signal, as well as the identification of the responsive neurons, is detailed during Chapter 7 — Memory traces.

General conclusions are given in Chapter 8 — Conclusion — and some remarks on future works are presented in Chapter 9 — Perspectives.

Chapter 10 — Annexes contains the publications that were a direct result of the presented work.

1.7 Conclusion

The global processes that lead to the encoding of memories are still barely understood. Deciphering memory formation events remains technically challenging due to the interconnected nature of neurons and the sparsity of their response to a stimulus. To date, experiments are restricted to partial observations because researchers need to choose between monitoring activity of a few individual neurons at high resolution or monitoring activity of a larger subset of the brain at low resolution, without access to the individual neuron response. In any case, we know of no work where both the observations would be exhaustive enough to encompass every neuron involved in a given type of stimuli while being able to capture individual neuron signal.

However, this combination of dimensions is crucial to further our understanding of memory formation. We'll demonstrate during the next Chapters of this thesis how an comprehensive view of the Mushroom body is possible, and how it can lead to new insights on the long-term memory mechanisms.

Chapter 2

Flies, neurons & memory

> *[Tax] dollars go to projects that have little or nothing to do with the public good, things like fruit fly research in Paris, France. I kid you not.*
>
> **Sarah Palin**

It might not be so obvious for the eyes of someone that is not familiar with the subject, but the fruit fly, formally named as *Drosophila melanogaster*, is one of the fundamental tools for several research fields. From developmental biology to neuroscience, this small insect played the main role for six Nobel prizes, bringing groundbreaking advances to modern science. Along this Chapter we'll explore what makes the *D. melanogaster* such an important model, how its brain is organized and how memories can be stored and retrieved in such a simple organism.

2.1 *Drosophila melanogaster* as a model organism

The fruit fly (shown in Figure 2.1) has similarities with humans to an unexpected degree, being that we share up to 60% of the same DNA sequences. Furthermore, about $\frac{3}{4}$ of the human disease genes have an ortholog in the *D. melanogaster*[86], making it an interesting model for the current studies as, for example, the research on neurodegenerative diseases, especially on the better understanding of the Alzheimer's disease [87–89].

Nevertheless, the use of the fruit fly as a model organism is not new. It was first introduced by W. Castle in 1906 [90] and, since then the amount of publications involving the *D. melanogster* increased

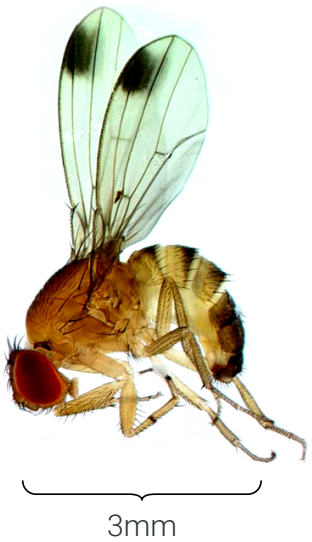

Figure 2.1: Picture of a *Drosophila Melanogaster*.

exponentially, as seen in Figure 2.2.

2.1.1 Shorter cycles, faster research

One of the main advantages of using the *D. melanogaster* as a model is its short life cycle and fast grow rate. The flies can be breded and raised in simple tubes containing a nutritive support medium, so that thousands of flies lineages can be kept in a rather inexpensive way. The development is fast, as one life cycle takes about 30 days at 29°C, being that the development from egg to adult can be achieved in one week (with a larval period of about 4 days) [91]. Just after 8 to 12 hours succeeding emergence, the female flies are already receptive to males, starting a new cycle [92].

This allows researchers to breed specific transgenic lines rather quickly, when compared to other species. One new lineage can be developed in about 2 months, in contrast to the six months needed for a new mice lineage.

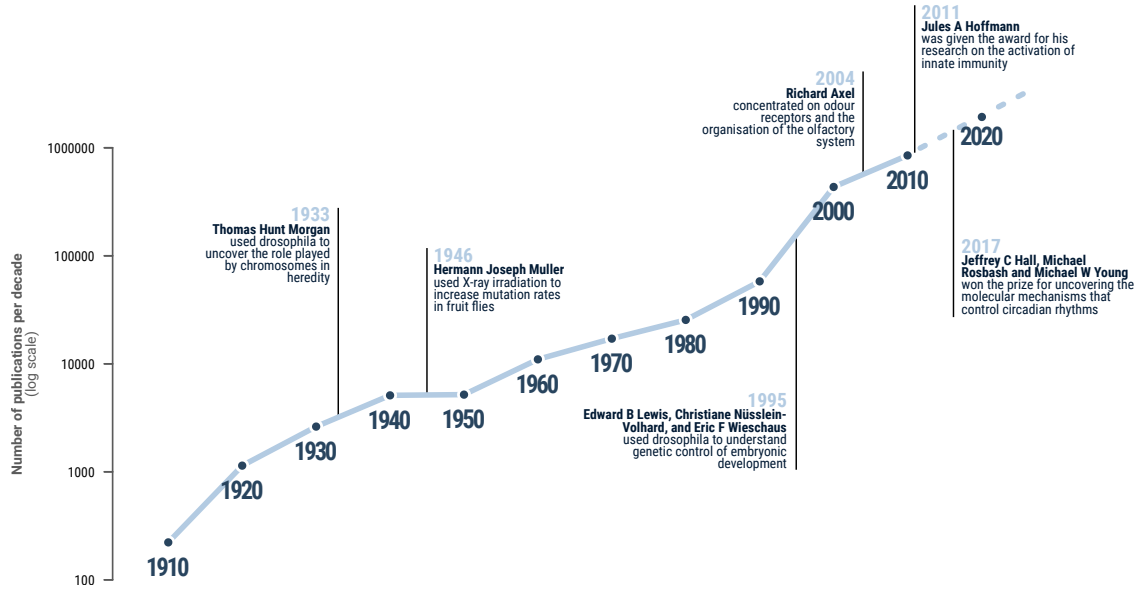

Figure 2.2: Amount of publications containing the term "Drosophila" per decade (source: Google Scholar). The plot shows how the number of publications increased exponentially (axis in log scale). Pointed are all the Nobel prizes that included the fruit fly as the model organism.

2.1.2 Unlocked genome

Genetic research using the *Drosophila melanogaster* has been progressing for decades, and is nowadays in highly developed stage. The fruit fly had its genome fully sequenced in the year 2000 [93], being composed of about 140 million base pairs and contains around 15 thousand genes (for comparison, the human genome has about 3400 million bases and may have around 22500 genes).

The fact that several genetic systems that guide basic developmental processes are conserved between different species, makes the *Drosophila* model even more interesting, as insights and discoveries can be directly applied to vertebrate systems. Several research projects that use the the *Drosophila* as a base for the comprehension of human diseases exist, as the identification of proteins targeted for degradation by the UBE3A ubiquitin E3 ligase, which is mutated in Angelman syndrome, or that antioxidant proteins (as TSA and PAG) can be candidates for causing Alzheimer-related diseases [94].

2.2 Savvy flies

The *Drosophila melanogaster* is a small and simple insect, but is capable of some relatively complex behaviors. Besides innate tasks, as navigation during flight and sexual court conduct, fruit flies are also capable of basic learning. For example, they can learn to associate new odors to a source of food or danger.

In total, the brain is made of about 10^5 neurons, that form a central nervous system. This is an advantage of the fruit fly as a model when compared to other simple organisms with a diffuse nervous system, as the *C. elegans*, as a more direct comparison with the ways that a vertebrate brain works is possible. An anatomical analogy can not, however, be directly made between the brains of vertebrates and fruit flies whose organization is radically different, but the basic elements constituting their nervous system are common: neurons and glial cells. Communication between neurons is by the same type of synapses, and many neurotransmit-

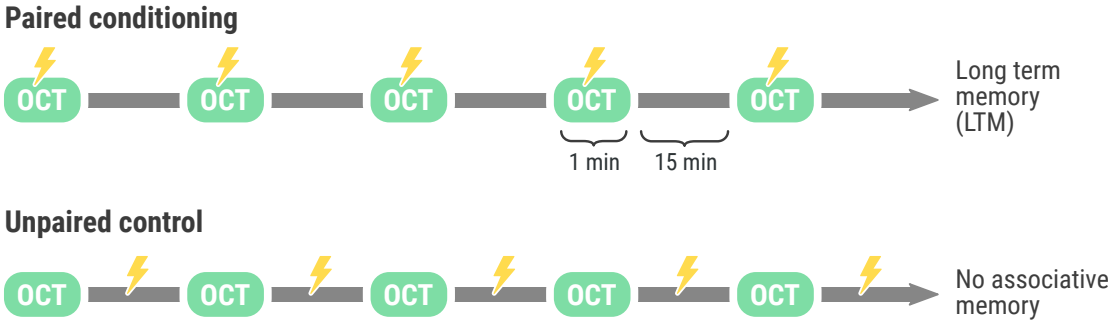

Figure 2.3: Conditioning protocol for the *Drosophila melanogaster*, allowing the formation of long term memories.

ters, such as glutamate or GABA (γ-aminobutyric acid), are identical from one species to another. The brain of Drosophila has the advantage of having simplified neural circuits corresponding nevertheless to complex functions.

2.2.1 Associative memory

Fruit flies have an ability of basic learning, as they are capable of making association between different events. Standard behavioral tests [95] show that the fruit fly is capable to associate a given odor to another stimulus, that could be appetitive or aversive. Being that the same odor can be associated with both, we represents a real learning process, and not just a naïve behavior of the fly.

Associative conditioning is based on the use of two stimuli called unconditional stimulus (CS^-) and conditional stimulus (CS^+). The unconditional stimulus induces, by itself, a reflex response. In our case, it is an aversive stimulus, produced by the sending of electric shocks, which causes the flight of the *Drosophila*. On the contrary, the conditional stimulus, which will be for our experience the presentation of an odor, does not induce an answer before learning. Learning involves associating the conditional stimulus followed by the unconditional stimulus.

The layout for a conditioning system is presented in Figure 2.3. An airflow is first broadcast for 90 seconds. The odor Octan-3-ol (OCT), is presented to the fly and soon after, the aversive stimulus is presented. Twelve shocks, lasting one second, are delivered every five seconds for one minute. OCT, a conditional stimulus, has a predictive value because it is diffused shortly before sending the unconditional stimulus. The electroshocks and odor are delivered in a custom made barrel, designed to be able to deliver at the same time the conditional stimulus (flow of OCT diffused thanks to pumps) and the unconditional stimulus (electric shock thanks to an electrifiable grid covering the walls of the barrel tubes).

2.3 Mushroom body, the center of olfactory memory

It is well known from the literature that a specific part of the fly's brain is responsible for the learning of odors: the mushroom body [96], seen in Figure 2.4.

It extends in a volume of approximately $150 \times 100 \times 80$ μm^3 on each of the hemispheres of the brain. The olfactory stimuli passes through the olfactory neurons whose receptors are located at the antennas. These neurons then project information at the anten-

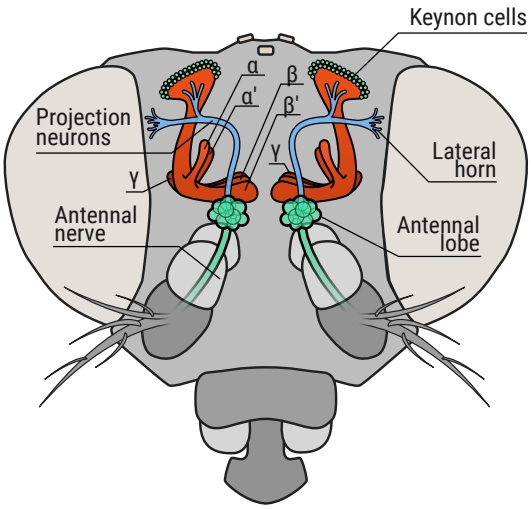

Figure 2.4: Schematic view of the olfactory system in the *Drosophila melanogaster*, showing the Mushroom body (colored in orange), the olfactory center of insects.

nal lobes composed of glomeruli. The information is then relayed in part at the level of the mushroom body by the antenno-glomerular tract. The MB is composed of a dense network of neurons called Kenyon cells, about 2000 per hemisphere [97]. Cell bodies cast their dendrites at a region called the calyx, receiving olfactory information from the antennal lobes.

2.3.1 Axonal projections

As shown in Figure 2.5, there are three categories of Kenyon cells whose axonal projections form different lobes. The α / β neurons have their axonal projections which branch off into a vertical branch called the α lobe and a horizontal branch, the β lobe. It is the same for neurons of type $\alpha\prime$ / $\beta\prime$ whose axons bifurcate in two branches forming the $\alpha\prime$ and $\beta\prime$ lobes. The γ lobe is formed by the axons of γ neurons which do not bifurcate. Each of these types of neurons plays a special role in learning processes. For example, α / β neurons are particularly involved in the formation of long-term memory [98]. The cell bodies of Drosophila neurons are about 2 µm in diameter, small size that makes it difficult to record their electrical activity by electrophysiology techniques [99, 100]. Optical imaging approaches for monitoring neuronal activity are therefore particularly relevant to the Drosophila model because they potentially allow access to information at the cellular level within a global neural network.

2.4 Memory storage and retrieval

The memory allocation is a set of processes on which information is stored in a neural circuit [101]. The majority of current studies make a in depth analysis of the anatomical structures, physiological processes, and molecular pathways necessary for the capacity of memory storage, but little is still know on how individual memories are stored in the brain [102].

The first precise insights in how neurons could store complex informations, while keeping its plasticity, where given by the Hebbian theory [103], usually summarized by the sentence “neurons wire together if they fire together” [104]. The idea behind the theory is that neurons tend to create stronger synaptic bounds if they are activated within the same temporal window. As ultimately the neuronal activation comes from external stimuli, this allows the association of events to be stored, thus allowing the formation of memories.

2.4.1 Memory engrams

Memories are physically stored in the brain, in specific populations of neurons that form “memory engrams”, also called “memory traces” [105].

The idea is not new, coming from the

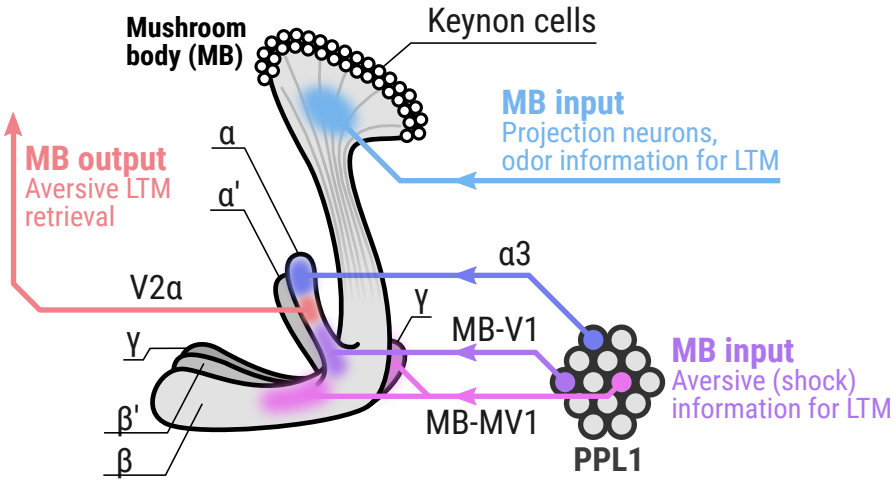

Figure 2.5: Schematic view of the Mushroom body, with the projected axons from the Kenyon cells.

beginning of the 20th century, described in two books of the German scientist *Richard Semon* [106, 107]. Semon coined the term "engram", which he defined as "the enduring though primarily latent modification in the irritable sub-stance produced by a stimulus (from an experience)" [106]. The term "Engram" is an equivalent of "Memory trace", more commonly used by contemporary neuroscientists.

Engram is the physical and/or chemical changes that takes places in the neurons during a learning event, while *Engrams cells* are defined as a population of neurons that are activated by this learning [102]. These cells are known to be spatially distributed in the brain in a sparse manner,a concept that can be clearly verified by memory manipulation experiments in mice using optogenetics [108]. By combining the activity-dependent, doxycycline-regulated c-fos-tTA system and ChR2-mediated optogenetics, the researchers were able to label with ChR2 a sparse population of DG neurons in mice that were activated by contextual fear conditioning memory. Subsequently, when these cells were reactivated by blue light in a context different from the original one used for the conditioning, these animals displayed freezing behavior as evidence of fear memory recall.

Regarding the *Drosophila melanogaster*, when a given odor was paired with an electric shock, defined neurons within the olfactory learning pathway, such as those in the antennal lobes and mushroom bodies, changed their responses selectively toward the odor used in the training [98, 108]. This suggests the formation of specific engram cells, that associate both stimuli. Although, the memory traces were not identified at the single cell level, but rather as a global response change of the lobes.

2.5 Neuronal activity

Neurons are complex cells capable of electrical and biochemical activity, and there are many functional imaging modalities for the analysis of its activity in vivo. The developments of genetically encoded reporters make it possible to follow specifically in certain neurons the activation of different molecular pathways (better described in Section 2.6).

2.5.1 Ca^{2+} probes

For neurobiology in *Drosophila*, it is common to use probes based on calcium exchange, as intracellular Ca^{2+} calcium ions are universal second messengers involved in many physiological processes including neuronal communication. The concentration of calcium ions Ca^{2+} in the cytoplasm of neurons is about 10 thousand times lower than that of the extracellular medium, and during the passage of an action potential, calcium ions enter the cytoplasm of the neurons, changing the concentration. To monitor this biochemical signaling pathway is therefore of great interest for the study of neuronal activity.

Thus, many calcium indicators have been developed, such that currently there are more than a hundred synthetic or genetically encoded calcium indicators (GECI). All these indicators are based on the same mode of operation, namely absorption or emission properties varying according to the coupling or not to calcium ions. The most commonly used calcium indicators up to a few years ago were synthetic indicators such as fura-2, fluo-4 or Oregon Green BAPTA-1 AM ester. This type of probe for in vivo studies have limitations such as they cannot be expressed in sub-populations of specific neurons or in well-defined sub-cellular compartments. It is to overcome this limitation that many families of calcium probes encoded genetically have been developed. Some of these probes consist of a single fluorescent protein such as Camgaroo, Pericam, GECO and G-CaMP and others are based on the use of two fluorescent proteins and the FRET mechanism (Förster Resonance Energy Transfer), as per for example the TN-XXL probe [109] or the Cameleon probe [110].

The G-CaMP probe is a molecule created by fusion of the cpEGFP fluorescent molecule with calmodulin (CaM) and the peptide sequence called M13. Calmodulin is a molecule that can bind to four Ca^{2+} ions. When the intracellular Ca^{2+} concentration is low, the G-CaMP molecule is weakly fluorescent because its chromophore is exposed to the intracellular medium. During the passage of an action potential, membrane channels open, allowing Ca^{2+} ions from the extracellular medium to enter the cytoplasm. The intracellular concentration of Ca^{2+} then increases, leading to a conformational change in the G-CaMP molecule. This rearrangement results in a significant variation in its fluorescence yield [111].

2.6 Genetic tools

The study of memory in the *Drosophila* is profoundly assisted by the genetic tools that allows the precise activation of genes in specific cell types. For our study, the expression of *mCherry* as a nuclei marker and *GCaMP6f* as a neuron activity probe, both expressed exclusively in the kenyon cells, allows a global *in vivo* view of the memory traces.

2.6.1 UAS/GAL4 system

A transgene is a DNA fragment corresponding to the sequence of the gene that one wants to express in a different organism, and their transfer in the Drosophila genome is mainly done using P-elements [112]. For the transgene to be transmitted to the offspring, it must be inserted into the germ cells of a young Drosophila embryo. These P-elements, also called transposons, lead to the ran-

dom insertion of the transgene into the genome. The genetic system allowing the expression of a transgene in a group of well-defined neurons, the most commonly used in Drosophila, is called UAS / GAL4 [113]. A P-element carries the gene coding for a protein called GAL4. It is inserted randomly into the genome of the Drosophila which leads to the expression of the GAL4 protein under the control of the endogenous promoter located upstream of the insertion site. The expression of this promoter is then specific for the subgroup of cells where this promoter is strongly expressed. For example, if the P-element bearing GAL4 is inserted downstream of an endogenous promoter of cytoskeletal proteins such as tubulin or actin, the GAL4 protein will be expressed in the vast majority of cells of the body. This is called a ubiquitous promoter. This is only an example; in our case, the expression drivers used will allow a precise spatial targeting of a small subgroup of neurons.

The GAL4 protein is derived from yeast and is therefore not naturally present in *Drosophila*. The endogenous regulatory sequences of Drosophila are not activated by this protein. The second essential component of the UAS / GAL4 system is the sequence UAS (for "Upstream Activation Sequence") which is a regulatory sequence activated by the GAL4 protein. The UAS / GAL4 expression system thus makes it possible to generate transgenic models by genetic crossing as shown in FIG. 1.5. A first Drosophila, for example a virgin female, carries in its genome the gene coding for the GAL4 protein downstream of a promoter (defined by the insertion site of the element-P). The gene is then transcribed into the cells where the promoter is active and the GAL4 protein synthesized. But, this protein alone has no effect. The male Drosophila carries in its genome a regulatory sequence UAS and the gene coding for the transgene of interest downstream thereof. Since the UAS sequence requires the presence of GAL4 to be activated, the transgene is not expressed in this second Drosophila. By crossing the two Drosophila presented above, the genome of the offspring will contain both the gene coding for the expression of the GAL4 protein in a cellular subtype but also the UAS regulatory sequence. The transgene will therefore be expressed in the cells where the GAL4 molecule is present. Originally developed for the Drosophila model, the UAS / GAL4 expression system also extends to zebrafish today.

2.6.2 UAS-mCherry-NLS

For the identification of the single neurons, we used a NLS marker with the red fluorescent protein *mCherry*, so that every nuclei of the Mushroom body could be imaged [114].

The *mCherry* is a red fluorescent protein (fluorophore) derived from the protein *drFP583* (also known as *DsRed*). It is a 28.8 kDa monomer of 236 amino acids with a peak fluorescent excitation at 587 nm and emission at 610 nm. It is stable and realtively resistant to photobleaching.

Nuclear Localization Sequence (NLS), is a small amino acid sequence (from 8 to 10 amino acids) targeting proteins of the nucleus of the cell.

2.6.3 UAS-G-CaMP6f

We measure the intracellular Ca^{2+} concentration of the neurons using *GCaMP6f* [115]. It is highly correlated

with the neuronal activity, as it causes rapid changes in intracellular free calcium [116, 117].

GCaMP is a calcium sensor protein in which green fluorescent protein (EGFP), calmodulin (CaM), myosin light chain fragment (M13) is genetically linked. This protein is formed by binding calmodulin to one side (N terminal side) of EGFP and myosin light chain M13 fragment to the other side (C terminal side). When calcium ion binds to calmodulin, the Ca^{2+} / CaM complex interacts with M13 to change the conformation of EGFP (the fluorophore), thereby changing the fluorescence intensity.

Several versions of the GCaMP complex have been developed in recent years, and for our flies we use the latest variety, GCaMP6f [117].

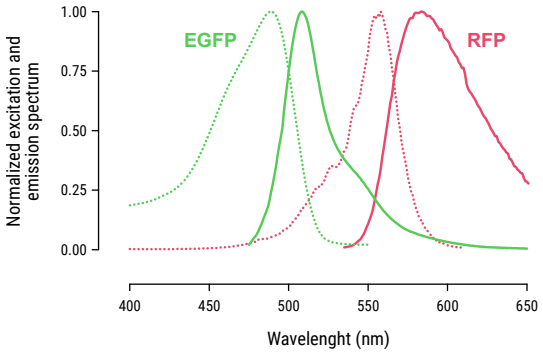

Figure 2.6: Excitation spectrum for the green (EGFP) and red (RFP) proteins used. Doted lines show the excitation spectrum, and full lines the emission. Note the gap between both profiles, which allows the simultaneous use of both proteins without cross-interference.

2.7 Conclusion

The fruit fly is a humble organism, but it is this simplicity that we can exploit to better understand how the memory works. By using the *Drosophila melanogaster* as a model, we are able to express specific markers for nuclei and neuronal activity exclusively in the desired Kenyon cells. This will allow us to verify the behavior of the neuronal network after a process of paired learning, using the protocols described in the following Chapters.

Chapter 3

Data acquisition

You can have data without information, but you cannot have information without data

Daniel Keys Moran

All the information needed to elucidate our questions about how memories are stored in the fly's brain need to be carefully acquired. Without well trained flies, or images acquired with high quality, none of the processes described in the following Chapters would be of any use. During this Chapter we present how the data were acquired, as well as the difficulties and problems encountered.

The processes of creating the experimental groups, the dissection of the flies and image acquisition were made by *Mélanie Pedrazzani*, PhD student, and *Lisa Scheunemann*, post-doc, both from the laboratory of Genes and Dynamics of Memory Systems, at ESPCI - Paris, under the supervision of *Thomas Préat* and *Paul Tchénio*.

3.1 Fly conditioning

Conditioning is fundamental to create the experimental groups we need to assess the memory traces in the brain. Two sets of experiments were made, both using odor stimulation as the conditioned stimulus and electroshocks as unconditioned.

The conditioned stimulus (**CS**) is a stimulus — odor, for our case of olfactory conditioning — that gains meaning following pairing with an unconditioned stimulus. The Unconditioned stimulus (**US**) is the stimulus that generates an unlearned behavioral response: the shock or sugar in fly olfactory conditioning.

3.1.1 Odors as **CS**

Fruit flies are extremely sensitive to odors, what suits them well for conditioning tests [42]. Here we use two odors, 3-octanol (**OCT**) and 4-methylcyclohexanol (**MCH**) as conditioned stimulus, that has proven not to trigger inherent behavioral response. Thus, they can be both associate with an appetitive or aversive response, and have been widely used for conditioning experiments in *Drosophila*.

3-octanol (**OCT**)

Octanol is an organic compound, with formula $C_8H_{18}O$ and molecular weight of 130.231 g/mol. This molecule is naturally found in spearmint oil, oatmeal, basil, allspice leaves and truffles, serving also as an alarm pheromone for some ants [118].

4-methylcyclohexanol (**MCH**)

Methylcyclohexanol is an organic compound, with formula $C_7H_{14}O$ and molecular weight of 114.188 g/mol. It is a colorless liquid that is poorly soluble in water. The substance is slightly irritating to the eyes and the skin. Exposure to high vapor concentrations may cause irritation of the eyes and upper respiratory tract.

3.1.2 Electroshocks as **US**

Electroshocks are commonly used as a unconditioned stimulus for paired learn-

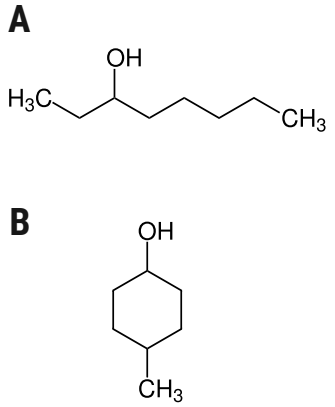

Figure 3.1: Molecular structures for (A) 3-octanol and (B) 4-methylcyclohexanol

ing, and here we use the standard protocol adapted by Preat [119].

During training, groups of 50–100 flies were first exposed for 60 seconds to a first odor (odor A) (either undiluted OCT or MCH). During this time, they received an electroshock (ES) (1.5 second pulses of DC). After a 45 seconds rest period, flies were exposed for 60 seconds to the second odor (odor B), which was not paired with ES. Flies were then kept in a vial with regular solid food.

3.1.3 Group A (OCT & MCH)

For this first group, the flies were trained using two different odors, OCT and MCH, being one of them paired with the electroshocks and the other left as a control.

3.1.4 Group B (Only OCT)

This group of flies received only OCT during the image acquisition

3.2 Dissection protocol

In order to optically follow the brain activity of the Drosophila, it is necessary to create an optical access to the brain. The cuticle of the Drosophila being highly diffusing, a micro-surgery was carried out under a binocular loupe in order to reveal the brain. The steps in the preparation of the live sample are shown in Figure 3.2.

The fly is first glued on a plastic slide, pierced in the center, without prior anesthesia. The glue used is a biocompatible dental glue (3M ESPE Protemp). An alignment wire keeps the Drosophila head in a correct position. The orientation of the head is adapted to the area of interest to be imaged so as to minimize the thickness of tissue traversed by the light.

The second step consisted of opening the Drosophila head using very thin scalpels to remove a rectangular cuticle region, 300 µm by 400 µm, which covers the brain. Underlying fat tissue was pushed to the corners of the window, and the tracheae was cut and pushed to clear the view of the brain. All actions had to be performed extremely carefully so as not to damage the glial cells that surround the brain, as well as the mushroom body itself. All stages of microsurgery were performed in the presence of a physiological fluid to preserve the brain. The composition of this aqueous solution, called Ringer's solution, was as follows: 130 mM NaCl, 5 mM KCl, 2 mM $MgCl_2$, 2 mM CaCl 2, 36 mM $C_{12}H_{22}O_{11}$ (sucrose), 5 mM HEPES-NaOH (Sigma-Aldrich). The pH of the solution is 7.3 [120].

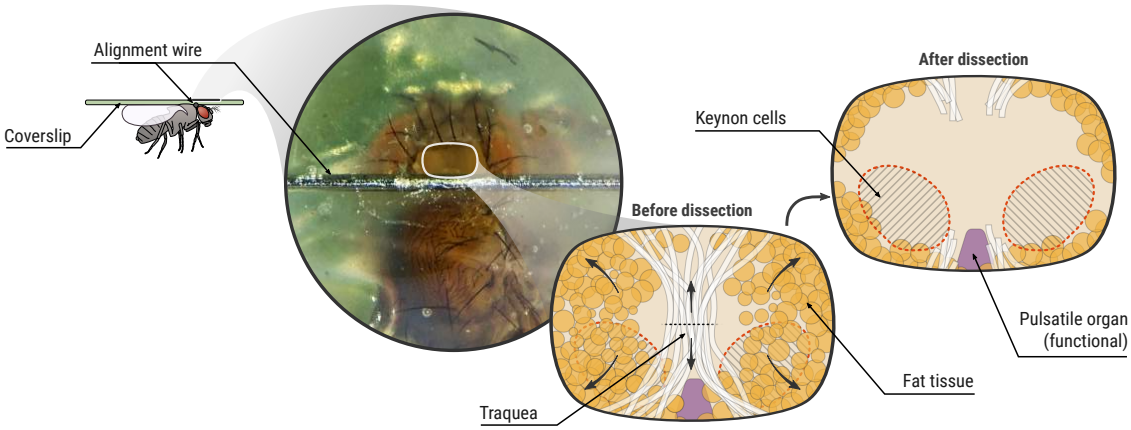

Figure 3.2: Dissection protocol for imaging the Mushroom body. Special care must be taken during this step, so that the brain is not damaged during the microsurgery.

3.3 Odor delivery system

The olfactory stimulation system is shown schematically in Figure 3.3. Upstream of the system are two pumps. One of the two pumps feeds a pipe circuit controlled by a series of solenoid valves. These solenoid valves make it possible to generate different stimulation configurations. The pipes are immersed in bottles containing neutral paraffin oil, for "air defect" and "air control" configurations, or with added chemical product: 4-methylcyclohexanol (MCH, purity equal to 99%, Fluka 66360 Sigma-Aldrich) or octan-3-ol (OCT, purity greater than 95%, Fluka 74878, Sigma-Aldrich). Since these products are hydrophobic, the solutions are prepared in odorless paraffin oil (international VWR, Sigma-Aldrich). These two chemical odors are naturally repulsive alcohols for Drosophila and traditionally used in all associative conditioning protocols involving olfaction. 3 ml of product is dissolved in 100 ml of paraffin oil. The flow coming out of this part of the assembly corresponds to one third of the total flow delivered to Drosophila. The other two thirds of the flow are generated by a second pump. This second pump is connected to a pipe immersed in a bottle filled with neutral paraffin oil which creates a constant main airflow whatever the chosen stimulation configuration.

Taking into account the dilution of the chemicals in the paraffin oil as well as the ratio between the odor flow and the main air flow, the final concentration of odor arriving at the level of the Drosophila antennas is of 1% . Continuous main flow minimizes sudden changes that could lead to brain activity in the Mushroom body without this response being related to olfactory stimulation. It is to avoid this same artifact that a configuration called "air control" has been created. It ensures that the brain responses observed were not responses due to air turbulence created by the mechanical movement of tilting solenoid valves. This system of sending odors was coupled to the environmental cell (a custom-made chamber) placed under the microscope objective, as show in Figure 3.4.

In order to prevent the odor from stagnating in the cell, another pump made possible to evacuate the odor in order to avoid desensitization of the olfactory receptors of the Drosophila. The solenoid valves were individually controlled by logic signals from a NI-USB (National Instrument) card to define the desired

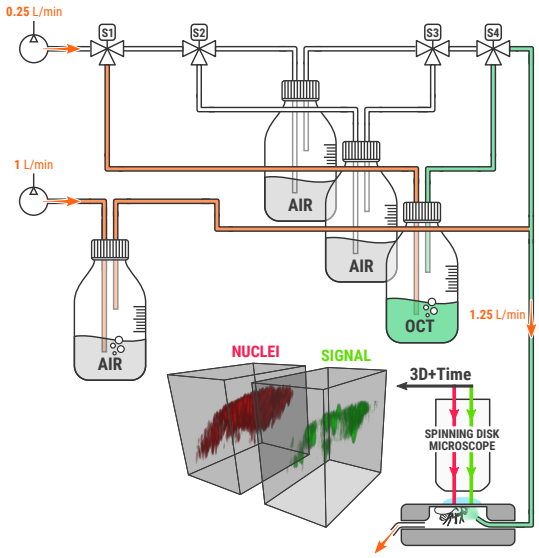

Figure 3.3: Schematization of the odor delivery system.

pacing configuration

3.4 Image acquisition

In traditional confocal microscopy, the acquisition of the image is done by laser scanning techniques, exciting the sample point by point. This imaging technique is then limited by the lateral scan speed of the excitation beam, made either with piezoelectric shims or galvanometric mirrors.

Nevertheless, even for confocal microscopy, where the dynamics of the scanning is optimized by the use of non-mechanical displacements provided for example by acousto-optical deflectors [121], the scanning speed is limited by the brightness of the sample. Indeed, to perform fast confocal microscopy, the time spent per pixel must be very low, imposing a large excitation power in order to collect sufficient fluorescence photons. This characteristic is a limitation for in vivo imaging where the sample must be preserved to the maximum of the deleterious effects of an excess of light excitation, as well as decrease of response signal caused by photobleaching.

3.4.1 Confocal spinning disk

In confocal microscopy, the acquisition time of an image depends directly on its size. To follow the neuronal activity, the duration of a point scanning laser technique is not adapted to the fast three-dimensional imaging of a living system that our project requires. The use of a multiconfocal spinning disk microscope allows the excitation beam to be parallelized, thus increasing the temporal dynamics of imaging.

The microscope used for our data acquisition is a Zeiss Examiner Z1 Axio, equipped with an EMCCD (Electron Multiplying Charge Coupled Device, Photometrics Delta Evolve). The light excitation is performed by two diode-pumped lasers emitting at wavelengths of 491 nm and 561 nm (maximum power of 50 mW, Roper Scientific). The sample is scanned using a CSUX1-M1N-E confocal head. This Nipkow disc, consisting of a spiral arrangement of 20000 50 µm diameter filtering holes spaced from each other by 250 µm, rotates at a maximum speed of 5000 rpm synchronously with a second disc made of same number of micro lenses of diameter 250 µm. When the discs rotate, about 1000 laser beams simultaneously scan the sample.

This parallelization of the scanning laser beams increases drastically the imaging speed. The imaging frequency per plane is limited to 60 Hz, the limit imposed by the speed of rotation of the disk. A set of interference optical filters (model 59022 ET - EGFP / mCherry, Chroma) define the different spectral paths of the microscope, being that each of the filters

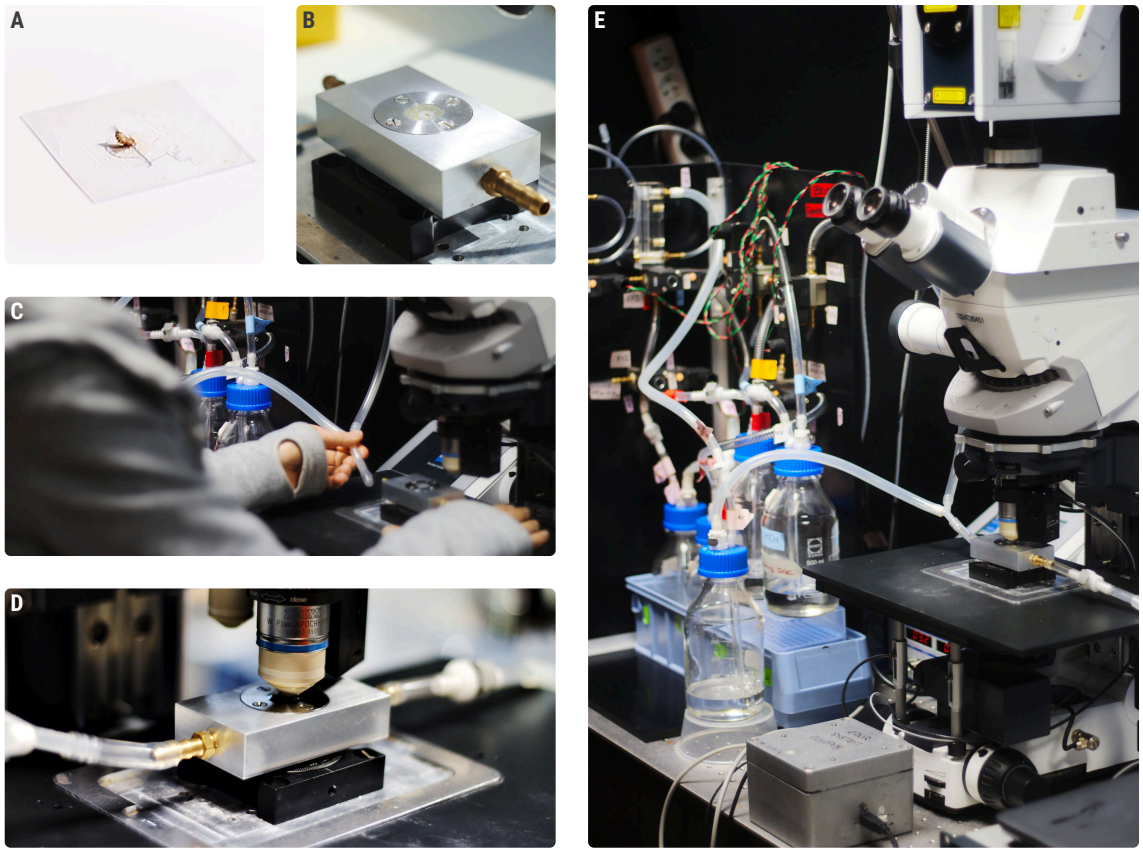

Figure 3.4: Photos from data the acquisition process. (A) Fly glued on the coverslip, ready for dissection. (B) Fly after dissection, with coverslip attached to the custom-made chamber. (C) chamber being attached to the microcope for image acquisition. (D) Close view of the chamber, with air ducts for odor delivery. (E) Global view of the acquisition system, with the odor delivery mechanism on the background.

consists of two transmission bands. The dichroic plate is used to reflect the excitatory light to the sample and transmit the fluorescence emitted to the camera.

Two water immersion microscope objectives are available on this device: Zeiss 40x ON 1.0 Vis-IR W apochromat 421462-9900 (working distance: 2.5 mm) and Zeiss 63x ON 1.0 Vis-IR W apochromat 421480- 9900 (working distance: 2.1 mm). Although initial tests were made with the 63x objective, all the data acquired for this project uses the 40x. The higher magnification could give us a better resolution for the detection of nuclei, but it was not possible to accommodate the whole MB within the field of view of the microscope.

These objectives have a transmission of the order of 80%, from 400 nm to 900 nm. They were mounted on a piezoelectric shim of 100 µm stroke (Pifoc P-721.SL2, PI) allowing a fine axial translation of the lens, of 5 nm resolution, and the rapid acquisition of stacks of images in depth. in the sample. The resonance frequency of the Pifoc loaded at 200 g is 180 Hz. The maximum acquisition rate of 60 Hz does not resonate with that of the piezoelectric shim. The sample holder was mounted on a translation plate in order to adjust its position laterally.

A set of mirrors and filters (Dualview Photometrics DV2) was mounted on the transmission path of the microscope, upstream of the camera, to allow simultaneous acquisition at the camera of two wavelengths (in our case, the RFP as nuclei marker and EGFP for neuronal activity).

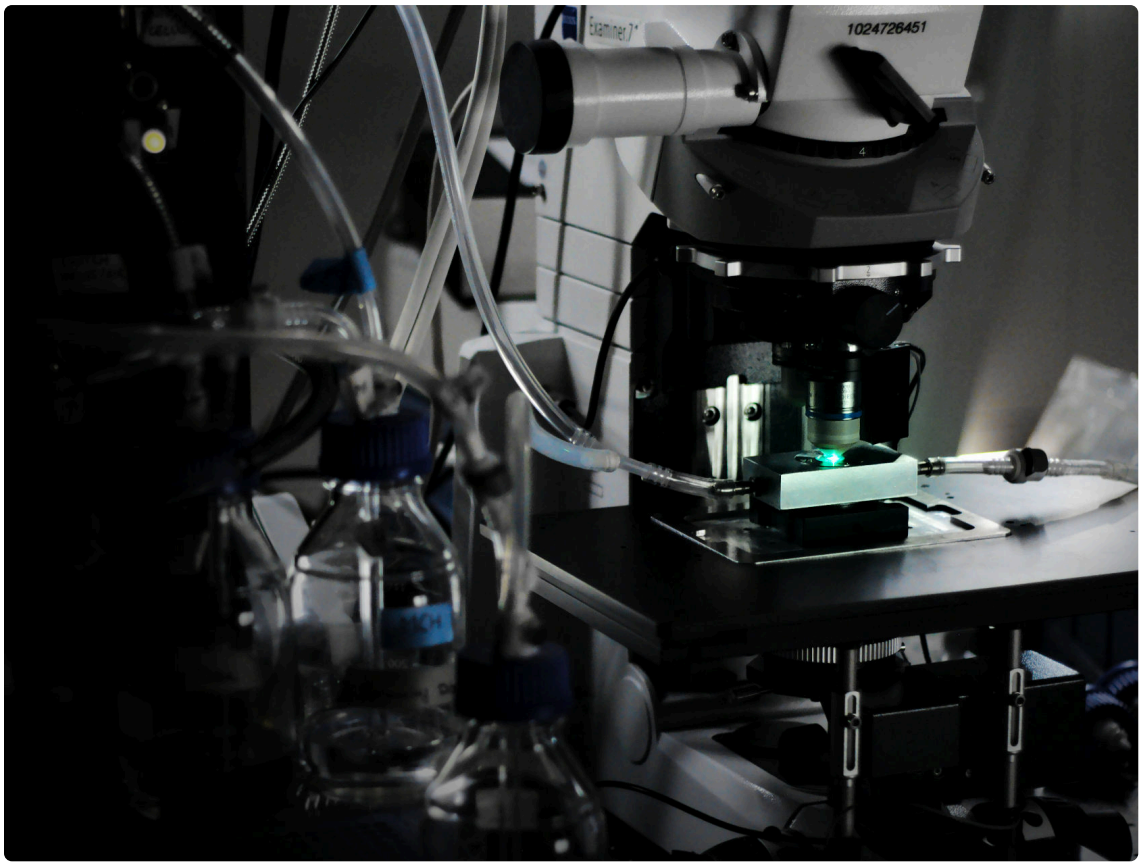

Figure 3.5: Microscope during image acquisition. While odor stimulation is being given to the fly through the custom chamber, the spinning disk microscope records the 3D+Time images of neuronal activity in the Mushroom body of the *Drosophila melanogaster*.

The entire system was controlled by the VisiView 2.1.3 software (Visitron Systems GmbH) allowing the easy control of the exposure time or the gain of the camera, the multidimensional acquisition of the images (multispectral and depending on the time) as well as the writing of macros for the control of materials attached to the microscope by logic signals.

3.4.2 Dual-view system

To speed-up the imaging process, we used a DualView Photometrics DV2 system. It made possible to image, in two distinct spectral bands, the same fluorescent object. Its operating principle is based on the spatial separation, using mirrors and a diagonal slide, of the two emission bands.

The dichroic plate reflects the component of the lower wavelength emission, around 520 nm, while the component of the highest wavelength emission, around 610 nm, is transmitted. Each spectral component is then imaged simultaneously on one half of the EMCCD sensor.

3.4.3 3D+ Time images

Acquiring the images results in a 5 dimensional *.tiff* file, with axis XYZTC and data recorded at 16-bit format. Each plane has a size of 256 by 512 pixels, as we use half of the sensor for each channel (the full resolution of the camera is of 512x512 pixels). Each pixel has a size of 0.161 25 µm x 0.161 25 µm, resulting that each slice of the acquired image has a size of 41.28 µm by 82.56 µm.

The step size of the acquisition was defined at 1.5 µm, with 45 slices being sufficient to cover the whole Mushroom body. Thus, each stack covers 67.5 µm in depth.

Every slice had a exposure time of 20 ms, so that each stack needs 0.9 seconds to be acquired. Faster acquisitions would be desired, for a higher temporal resolution, but a lower number of slices would compromise the full recording of the Mushroom body in depth. Although, this temporal resolution proved to be enough to capture the GCaMP6f response, recorded in about 2 to 3 frames.

3.5 Data artifacts

While acquiring our images, we pushed the confocal spinning disk system to the operational limits regarding the speed of acquisition. Unfortunately, this led to some artifacts that were sometimes not completely understood, but needed to be handled during post-processing.

3.5.1 Axial motion blur

Fast and deep image acquisition is fundamental to resolve the signals from the whole mushroom body. In total, we acquire 67.5 µm in 0.9 seconds, leaving only 20 ms per slice. This leads to an axial motion blur artifact, shown in Figure 3.8. The Figure shows that when acquiring images with an exposition of 20 ms, while the camera registered the data for the first slice, the axial position of the microscope was still on the bottom of the stack (from the previous time frame). As consequence, between Slice 1 and 2, the axial position needed to travel the whole stack from bottom to the top, leaving a motion blur effect. We can see, also in Figure 3.8 that having a higher exposition time of 200 ms solves the problem, so that we have on the first slice the data that actually comes from the good position (with a close look, it is still possible to notice a subtle motion blur on the first slice).

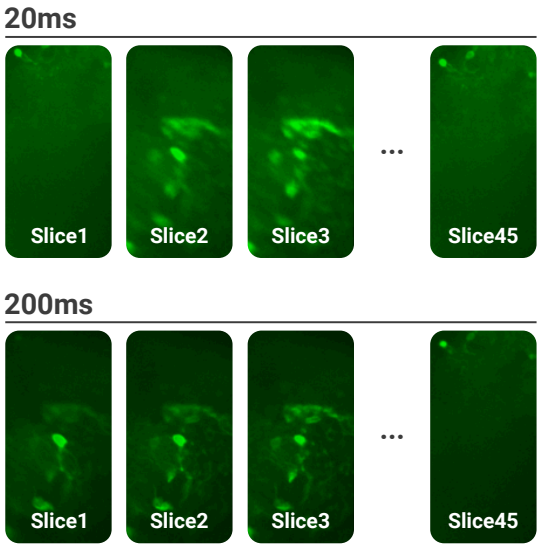

Figure 3.6: Axial motion blur during image acquisition.

This artifact can be quite common in 3D microscopy, but it remains often unnoticed if the data is only checked and/or analyzed using axial max projections as, for this case, the actual position of the slice on the stack is irrelevant. Nevertheless, for a true 3D analysis of the data, this problem must be taken into account.

Although, in our case, the 200 ms image acquisition was far too slow, such that we would miss the neuronal response. We circumvented the problem by acquiring at 20 ms per slice, but making sure that the first and last slices of the stack contained background only, so no data would be affected by this issue.

3.5.2 Anchored Z position

This problem is exemplified in Figure 3.7. For the best of our comprehension, while the microscope scans from

Figure 3.7: Axial motion blur during image acquisition. The image shows the 3D volumetric reconstruction of the *mCherry* channel for three consecutive frames, with the anchored z position being noticeable in the middle frame. Note that the axial motion blur, described on Subsection 3.5.1, is also present on the top of the image.

the top to the bottom of the stack, the focal plane gets locked in the same position for a few frames. Thus, the controller software receives different images and saves them to consecutive frames, but they are in fact being acquired at the same position. This gives the elongated effect that we can see in the middle panel of Figure 3.7.

One initial hypothesis was that the problematic slices were just duplicates of the same acquired image, as result of a mistake from the software (as a memory cache problem). However, since the noise pattern of the "duplicated" slices was different, we concluded that they were consecutive acquisitions of the same plane, and not a simple data duplication.

This artifact was hard to reproduce, happening randomly on about half of the acquisitions, usually after the 100^{th} frame and with variable intensity (sometimes just two or three slices, being hardly noticeable). Also, the technical assistance of the microscope could not identify the source of problem, or fix the issue.

We hypothesize that the problem might be related to the piezoeletric motor that controls the focal plane in depth. A mechanical problem, or a defective change in current, might keep the focal plane at the same position, while the software acts as if the focal plane was changing.

Not being able to fix the problem directly on the microscope, we've chosen to detect and ignore the problematic frames in a post-processing stage, as described in Section 6.2.

3.5.3 Laser intensity drop

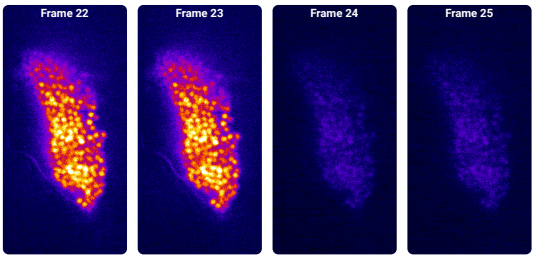

Figure 3.8: Axial max projection, showing the sudden decrease of laser intensity for the red channel.

Another issue, less frequent, happening in just a small fraction of the acquisitions, was the sudden intensity drop of the laser used for the *mCherry* channel. Probably due to some bad contact in the laser input, the problem was fixed after a revision of the microscope. Interestingly, the proposed algorithm for nuclei detection, explained in Chapter 4 was robust enough to keep a good detection accuracy even for the frames with low signal.

3.5.4 Noise flash

One last problem, found in just a few examples from the dataset, is that full random frames could be just filled with random noise. This would drastically affect the detection and signal measurement, so the problematic frame was completely removed from the sequence, and replaced by a copy of the previous frame. An example of this artifact is shown in Figure 3.9.

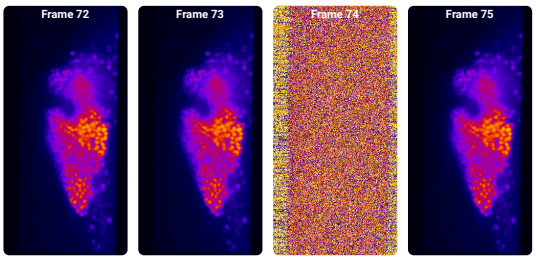

Figure 3.9: Sudden noise frame during a image acquisition.

3.6 Conclusion

The process of acquiring consistent and high quality 5-dimensional (XYZCT) data is a great challenge, but of fundamental importance to understand the mechanisms leading to long-term memory formation in the *Drosophila melanogaster* brain. By using a confocal spinning disk for a fast 3D acquisition of two channels (one for nuclei and another one for neuronal activity), we were able to record activity from the whole Mushroom body while the fly experienced a given odor.

The dissection process, necessary to expose the brain to the image acquisition, demanded extreme caution and the protocol took two and a half years to be fine-tuned. Also, the odor delivery system, that was capable of presenting the odor during the image acquisition, had to be precisely adjusted to make sure the air pressure changes wouldn't cause an over-stimulation of the fly.

Thus, the presented protocol for data acquisition was capable to produce a precise recording of the mushroom body while the fly experienced a memory event, that could be automatically processed with the following the protocol presented in the next Chapters.

Chapter 4

Neuron detection

It has long been an axiom of mine that the little things are infinitely the most important.

Arthur Conan Doyle,
The Memoirs of Sherlock Holmes

If we aim to analyze the memory formation event at the single cell level, the very first step needed is to detect the involved neurons as precisely as possible. This is an important challenge, as we face relevant constrains: the high density of neurons in the Mushroom body; the low spatial resolution of the images and the axial distortions that are inherent to the 3D image acquisition [122]. On this chapter we'll explore the results of the current state-of-the-art methods for 3D detection, how they poorly performed on our dataset and the resulting method that we developed to solve this issue.

4.1 Cell localization

The olfactory activity of the brain happens in the Mushroom body, a structure that is relatively isolated and constituted of about 2000 neurons. Ideally, each neuron would have a membrane marker, and a 3D segmentation would be performed for every cell, that would allow to precisely measure the Ca^{2+} activity inside the volume via a GCaMP marker on another channel. However, this became impracticable for two main reasons: first, the non regular shape of neurons drastically increases the complexity of a segmentation task. Second, for the resolution that we are constrained to, neurons would hardly be distinguishable from each other by a membrane marker.

The solution came from the detection of nuclei, via an *mCherry* marker. Having the position of the nuclei allowed us to estimate a central reference point for the neuron body, which can be further used to delimitate a volume for signal measurement.

Here it is important to endorse that the goal was to detect its central position, and not to perform a segmentation of the nuclei. Besides not bringing additional information for our needs, a segmentation of nuclei (that is, the delimitation of its boundaries) would hardly be precise, as for our resolution the nuclei approached the Point spread function (PSF).

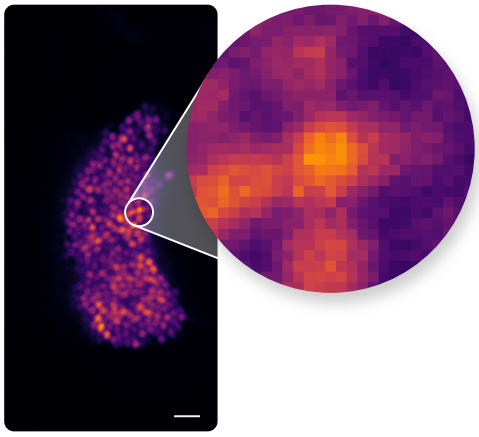

Figure 4.1: Middle slice of a typical Mushroom body, containing the nuclei marked with fluorescent *mCherry*. Scalebar of 5 µm

On Figure 4.1 we can see that one nuclei is about 1 µm wide, and it is made of around 10 pixels. Sizes vary slightly from nuclei to nuclei, but the average size remains the same between different flies.

4.2 Ground truth

The only way to asses with precision the quality of the detections was to have a ground truth. This is not obvious for the Mushroom body, for which the literature shows that about its made of about 2000

neurons, but their exact location cannot be obtained in another way.

4.2.1 Manual annotation

One first possible approach is the manual annotation of the 3D stacks. This operation can be highly biased, especially for 3D images, on which the annotation consists of a visual assessment of the individual slices, truing to determine which one contains the central position for every nuclei. The manual annotation was made in one example brain, independently by two evaluators (myself and *Mélanie Pedrazzani*, responsible for the biological assays during the first half of the project).

The process used the ImageJ/Fiji plugin *Cell Counter* [123]. To increase reprodutibility, the following protocol was used:

1. Load the 3D stack with Fiji
2. Set the colormap to Grays (Image → Lookup Tables → Grays)
3. Reset the intensity range of the colormap. Scroll to a slice where you can see the objects. Then, click on Image → Adjust → Brightness/Contrast → Reset (on the window that opens)
4. Open the Cell Counter Plugin (Plugins → Analyze → Cell Counter → Cell Counter)
5. Click the "Remove" button until there is only one type of counter ("Type 1")
6. Click on the image window to select it
7. Click on "Initialize", on the Cell Counter window
8. Zoom the image up to 400% (Ctrl + Scroll Up)
9. Select the Counter Type 1
10. Add the annotations by clicking on the center of the objects.
11. When finished, click "Save Markers" to save the results.

One initial unanticipated result is that it wasn't possible to find the expected 2000 neurons on the image, being that the two manual annotations found 1078 and 827 nuclei. This fact can be explained by the lack of axial resolution for the images, being that it was common to find "merged" nuclei, which could be the union of two or more individual nuclei (also making the annotation less precise and more subjective). This creates an important constrain on the idea of having the single cell information, that will be handled on the way we capture the signal (see Chapter 6)

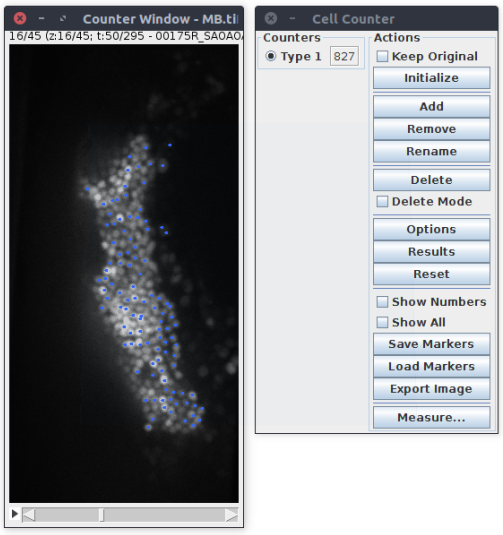

Figure 4.2: Graphical User Interface of Cell Counter, ImageJ plugin used for annotation

4.2.2 Synthetic images

Another approach to quantify the accuracy of the detection methods consisted

of generating a synthetic image that resembles the real acquisition. On this computer generated image, we could easily verify the precision of the detections, since the true position of the nuclei was known.

The main difficulty of this approach is to generate an image that's close enough to the original, regarding the noise level, resolution, density of objects, light diffusion and PSF effects.

Overall idea

Initially, a real image was used as a base for the generation of an corresponding synthetic image. From this, a 3D volume corresponding to the foreground (Mushroom body) was extracted, and a desired number of spheres were generated inside this volume. These spheres were convolved by a PSF, noise was added and the axial resolution simulated. The coordinates of the spheres was saved as ground truth in a separated file.

Volume extraction

Firstly, we specified a desired volume for the synthetic Mushroom body (MB). Usually 1000 µm^3 corresponded roughly to the structure . The volume can be defined as a set of foreground pixels, but the intensity threshold that can generate this foreground, for a given volume, was initially unknown. To extract the foreground, an threshold level was iteratively increased while the foreground volume is being checked (basically, the amount of voxels that pass the threshold multiplied by the individual voxel volume). The iteration stops when the desired volume was reached.

Nuclei positioning

On the real MB, the nuclei are approximately distributed in a homogeneous form. To simulate this, we partitioned the foreground volume into the number of desired synthetic nuclei using a k-means clustering algorithm, k being the number of desired points. To speed up the process, a random sub-sampling of the volume was used, usually taking 1% of the points was enough to obtain the synthetic nuclei homogeneously distributed throughout the volume. The first steps are shown on Figure 4.3.

Synthetic nuclei

The resulting centroids of the k-means algorithm were used as the central position of the synthetic nuclei, marked as a single voxel on the 3D image (also, they were saved as the ground truth of the images, to verify the detection methods). To simulate the actual nuclei, with the obtained centroids we used morphological operations, dilating initial voxels using an 3D spherical kernel with the desired nuclei size. At this step we allowed small random variations of the kernel diameter, up to $\pm$ 3 pixels.

At this stage, the nuclei were solid spheres with homogeneous intensity, that is every voxel had intensity 1. To simulate the uneven distribution of fluorophores inside a nucleus, every voxel was given a random value between 0 and 1.

Scattering light

The original image was acquired using a confocal spinning disk microscope, so by definition its resolution was limited to the diffraction limit of the light. To

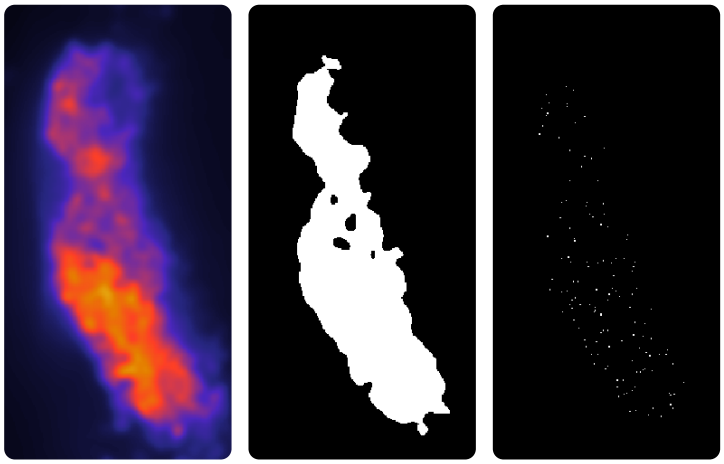

Figure 4.3: First steps for the generation for synthetic images. From the left to the right: Original image, extracted foreground and subsampled image.

simulate this constrain, the image containing the synthetic nuclei was then convolved by a Point spread function (PSF) [124] extracted from real microscope images (using fluorescent beads smaller than the microscope resolution). The extracted PSF is shown at Fig 4.4, on which we can clearly see the distortion caused by the lower axial resolution.

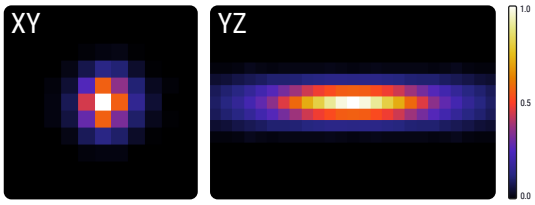

Figure 4.4: Point spread function used for the convolution during the creation of synthetic images. The PSF was extracted by using beads smaller than the microscope resolution.

Additionally, a whole scattering of light through the MB generates an overall glow around the foreground. This is also simulated by adding to the image an highly blurred version of itself.

Simulated noise

The presence of noise from the camera sensor is inherent to the image acquisition, and this also was taken into account when generating the synthetic images. Poisson noise was applied to reach a chosen level of signal to noise ratio (SNR, defined by the average signal intensity divided by the standard deviation of intensities within the synthetic nuclei only) that corresponds to the original image.

Axial resolution

Typically, the axial (Z) resolution of a 3D image stack is lower relatively to the camera sensor (XY) resolution. Until this step the synthetic image contained isometric voxels, an "ideal" image. To simulate the real microscopy condition, the synthetic image was rescaled to the same size that had the original image it was based on. Also, the intensity range of the synthetic image was scaled to the same levels as the original one. A comparison between the synthetic and real images is shown on Figure 4.5.

4.2.3 Synthetic videos

The synthetic images described so far were still frames.*Minhui Wu*, intern in the lab from June to August of 2016, adapted the algorithm to produce a sim-

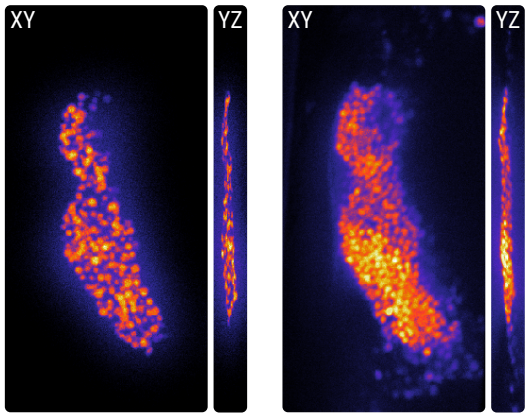

Figure 4.5: Comparison between the synthetic image (left) and the real acquisition (right). It is possible to preserve the general shape of the Mushroom body, while having an image where the true position of the nuclei is known.

ulation over time.

The changes on individual frames were captured by the foreground extraction, following the border of the MB for each frame. In case k-means was performed independently, the obtained labels of the centroids wouldn't match, meaning we wouldn't be able to obtain ground truth tracks of the nuclei. This problem was solved by using the resulting centroids of a frame as seed points for the next, and consecutively. This way, a smooth adjustment of the centroid positions between each frame could be produced from the new extracted volume.

Figure 4.6 shows consecutive frames of a generated video. From the original file we could see a natural pulsation of the brain, that is well reflected on the synthetic video.

4.2.4 Jaccard Index

Once the ground truth both from manual annotations and synthetic images was obtained, it was possible to assess the accuracy of any detection algorithm (as for the state of the art methods that will be described on section 4.3).

We consider a given detection to be a *True positive* if its distance from the ground truth is smaller than the average diameter of the nuclei. If no nuclei was within range, or more than one detection was close to the same ground truth points, they were considered *False positives*.

As measure of accuracy we used the Jaccard index [125] J, defined as:

$$J(D,G) = \frac{|D \cap G|}{|D \cup G|} \tag{4.1}$$

where D is the set of resulting detections of the method, G is the set of ground truth positions (from manual annotations or synthetic images).

$$J = \frac{Tp}{Fp + Tp + Fn} \tag{4.2}$$

Tp is the true positive count (elements both in D and G), Fp is the False positive count (elements in D but not in G) and Fn is the False negative count (elements in G but not in D). In case of a high amount of false positives (Fp) or missed detections (M), the Jaccard index approaches zero. Oppositely, in case of perfect match, the Jaccard index value is one.

4.3 Spot detectors

As nuclei resembles single spots, the use of methods developed specifically for spot detection was rational.

We checked the current state of the art for 3D spot detection [126], to identify methods that could identify precisely the location of spots.

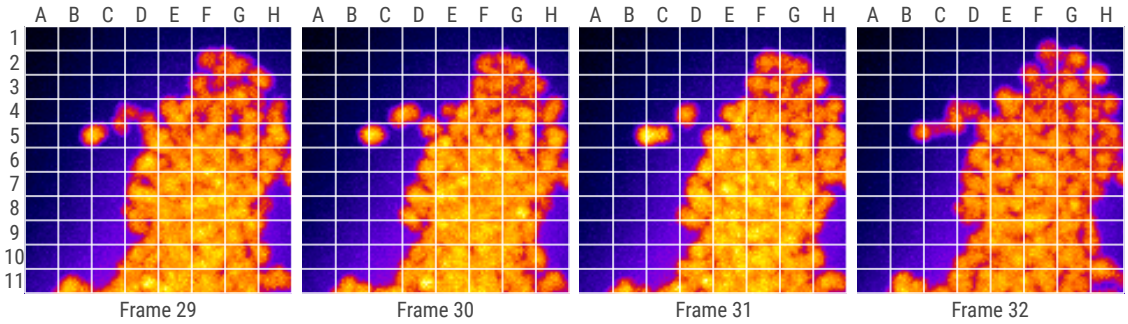

Figure 4.6: Consecutive time frames from a synthetic video. Note the movement of the brain within the quadrant D4, on which nuclei move in and out of focus. On the quadrant E3 is possible to notice a movement where an compression of the MB displaces a big part of the structure to the bottom-right

The need for estimating the position of nuclei and spot of various size in general is not new and has been the subject of many studies. In 2D, methods range from local background subtraction and linear or morphological image filtering to wavelet-based multiscale detectors (see [127] for an overview). While the need is more recent in 3D, the methods used are in fact much the same. A recent comparison the about efficiency of methods was made in 2015 by Štěpka *et al.* [126]. The 3D morphological maxima (EMAX) presented by Matula *et al.* was then suggested as a method that combines both a high accuracy and a low number of parameters [128]. Another method, the Undecimated Wavelet transform (UDWT) [129] is by far the most cited and therefore probably the most used by the scientific community for quantification. Both methods are briefly described here.

4.3.1 Undecimated Wavelet (UDWT)

In [129], Olivo-Marin introduced a method based on the undecimated wavelet transform. A 3D undecimated wavelet transform of the image is computed, then non-significant wavelet coefficients of selected scales are discarded by a weighted automated thresholding. Spots are enhanced by computing the product of the denoised wavelet coefficients. This method requires two parameters: a "wavelet scales" matching the sizes of the objects we aim at detecting and a "sensitivity" parameter which corresponds to the thresholding weight (available here: http://icy.bioimageanalysis.org/plugin/Spot_Detector).

4.3.2 3D morphological maxima (EMAX)

In [128], Matula *et al.* described a method based on the 3D morphological maxima transform. First, noise is suppressed with a 3D Gaussian filter with σ corresponding to the expected size of the spots. Then, a morphological maxima transform is computed. This transform identifies those local intensity maxima whose height exceeds a specified threshold h. This method requires two parameters: a "smoothing" σ and a "height" h (available here: http://cbia.fi.muni.cz/acquiarium.html).

4.3.3 Parameter scanning and results

As described on subsections 4.3.2 for EMAX and 4.3.1 for UDWT, both methods depend on user tuned parameters to properly realize the detection. To avoid any sort of bias when check-

ing the accuracy of the methods, a range of parameters that would maximize the Jaccard index were scanned, and only the best parameter set was used for the index calculation.

Results for UDWT

The detection was performed using the ICY implementation of the algorithm [56].

The scale of the wavelet is a free parameter, but it was fixed according to the size of the object being detected, as described by their authors. However, another parameter called *sensitivity* had to be adjusted, and it was scanned to maximize the Jaccard Index.

The detection results were compared with the two manual annotations of the Mushroom body (section 4.2.1), and the algorithm with optimal parameter set obtained an average of 335 False positives, 50 True positives and 902.5 False negatives, resulting in a Jaccard index of 4%.

For the synthetic image containing 2000 objects, 146 False positives, 103 True positives and 1897 False negatives were obtained, resulting in a Jaccard index of 5%

Results for EMAX

We used an implementation of the algorithm given by the software package *Acquiarium*[130]. Two parameters were used, an intensity value for thresholding and a sigma value for Gaussian blurring for noise removal.

When comparing to the manual annotations, on the average we obtained 483 False positives, 122 True positives and 830.5 False negatives, resulting in a Jaccard index of 8%. For the synthetic image, the results were 586 False positives, 226 True positives and 1774 False negatives, resulting in a Jaccard index o 9%.

4.4 SMAX 3D spot detection

Regarding the low Jaccard indices obtained by both UDWT and HMAX, we considered the state of the art methods for spot detection inappropriate for our data-set. Thus, we proposed a new spot detection method *Smax*, able to handle the peculiarities of our system.

4.4.1 Method description

As we mentioned earlier, 3D stacks in confocal microscopy are made of series of 2D image acquisitions, as the camera is composed of a 2D array of sensors. This usually results in a 3D image with a lower resolution in the z direction (axial to the acquisition). This lower resolution is partly due to the fact that the distance between the acquired 2D images is always higher than the pixel size in the x and y directions. It is also due to the Point Spread Function (PSF) of such an optical system that is typically wider in the z direction than in the x or y directions.

A simple but crucial solution to this anisotropy issue consists in using the acquisition metadata and a cubic spline interpolation [131] in the z direction to generate intermediary plans to obtain voxels with equal size on x, y and z directions. This difference in scale can be better understood on Figure 4.8, on wich the left voxel spans a whole 1.5 µm step of the microscope. Filling the missing data with synthetic interpolated plans does not bring additional information

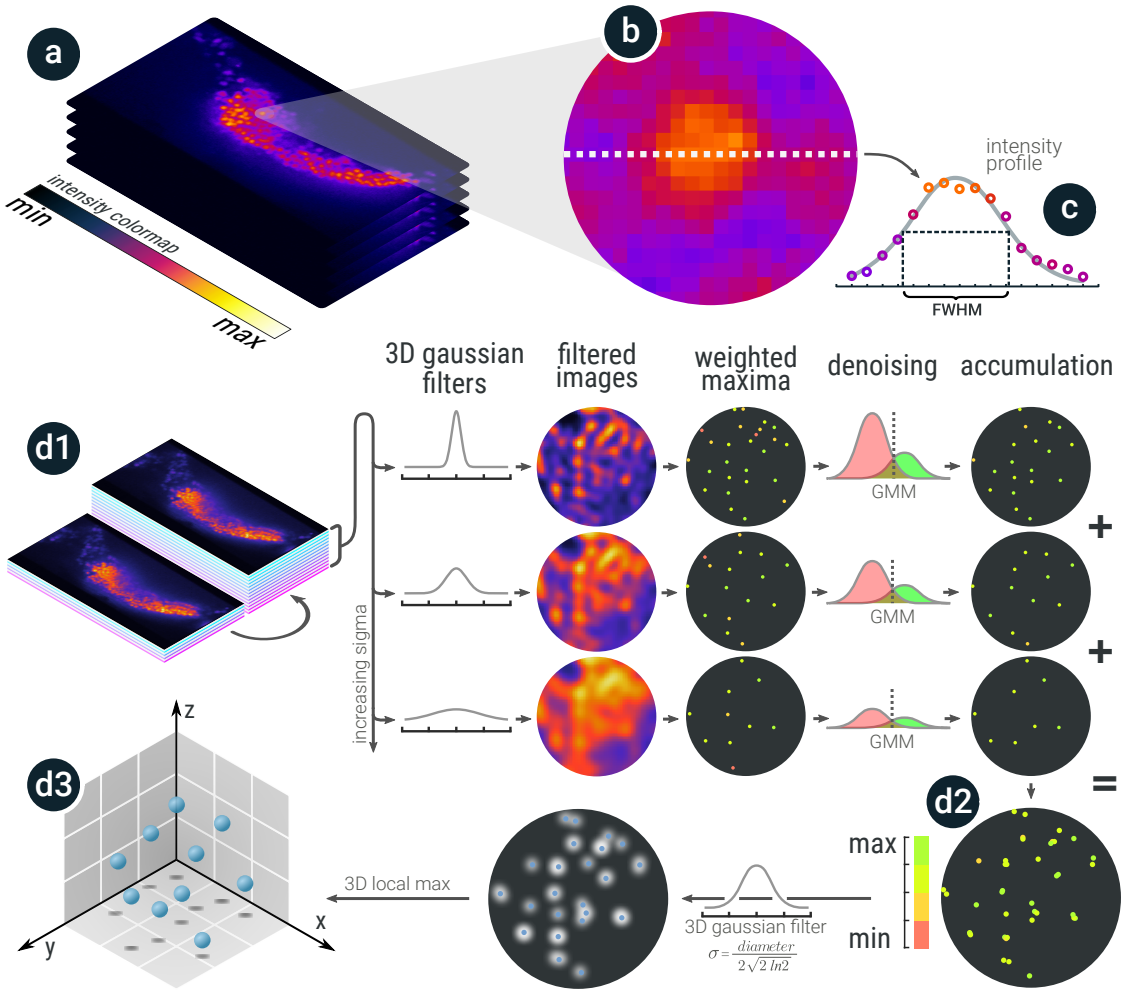

Figure 4.7: Summary of SMAX, the proposed method for spot detection. (a) An image stack of the Mushroom body of Drosophila acquired with a spinning disk microscope (b) Detail of a nucleus (c) A good approximation of the nucleus diameter (the single input parameter of the method) can be obtained by the Full Width at Half Maximum (FWHM) of a Gaussian fit on an intensity profile. (d1-3) Stages of the Smax algorithm. (d1) Image interpolation (d2) Weighted maxima denoising using Gaussian Mixture Model (GMM) followed by maxima accumulation. (d3) Maxima accumulation image is then convolved with a kernel corresponding to the targeted nucleus size, final local maximas are extracted. All processes are performed in 3D.

but makes possible a proper use of isometric 3D kernel and neighborhood in the following image analysis steps, while allowing a sub-resolution precision for the axial direction.

Following this anisotropy correction, a standard deviation σ is computed from a diameter value provided by the user. For that purpose, it is considered that this diameter is ideally obtained from the Full Width Half Maximum (FWHM) [132] of a Gaussian that would be fit on an average spot intensity profile (see Figure 4.7c). This fit measured is done on a subsample of isolated nuclei, and measured on the xy plane (minimizing the PSF effects). Therefore, σ is reversely obtained using:

$$\sigma = \frac{diameter}{2\sqrt{2\ln 2}} \tag{4.3}$$

This value can be divided by the pixel size (extracted from the file metadata) in case the diameter is provided in μm.

A bank of 10 Gaussian filters that span $[\sigma - \frac{\sigma}{2}; \sigma + \frac{\sigma}{2}]$ was created to detect slight variations of size around the average nucleus diameter provided. The number of

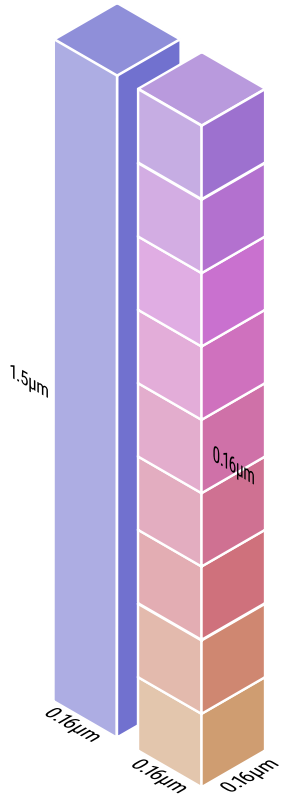

Figure 4.8: Comparison of scale between the voxel on the original image (left) and an isometric voxel (right)

filters was set to 10 because we observed that for most combination of spot sizes and noise levels related to real applications, Jaccard indices were not improved above 3 to 5 filters in the bank, depending on datasets, as shown by Figure 4.9 for simulations using synthetic images containing 1000 objects. Therefore, a higher number would in most cases increases the computational cost without improving the precision. Figure 4.9 also illustrates that Smax is less accurate on a dataset with a higher variability of object sizes. For each filter, local maxima were detected and collected using a $3 \times 3 \times 3$ spherical neighborhood.

At this stage, for each filter, the local collected maxima were produced by actual bright objects or by background noise. Therefore the distribution of intensities associated to maxima is most often bimodal (considering that every object have a similar intensity distribution, that is greater than the background). The two components of this distribution were then identified for each scale using a Gaussian Mixture Model (GMM) with a two components fit using the Expectation-Maximization algorithm. A threshold automatically defined as the value where both components are intersecting such as the maxima associated with intensities above this threshold are kept while the maxima associated with intensities below this threshold are discarded. This process offers a stringent denoising process, independent for each filter scale (see Figure 4.7d2).

Following this step, all remaining maxima collected for each filter were accumulated into a single 3D array. As objects were supposed to be further apart than resolution (that is, above the Nyquist sampling rate of the microscope [133]), this array should contain local accumulations of maxima mostly in volumes that are about the size of a nucleus. Therefore, an ultimate 3D Gaussian filtering using σ was applied. This filtering was supposed to merge accumulated detections that belong to the same object into a single Gaussian blob. Finally, 3D local maxima from this filtered array were identified, representing the final detections, and saved to disk in a .csv file (see Figure 4.7d3).

The described protocol for Smax can be summarized in Algorithm 1.

4.4.2 High 3D density

The high density of nuclei on the Mushroom body makes the detection task more complex, as the PSF merges nuclei that are too close together, specially if they are stacked on the axial direction.

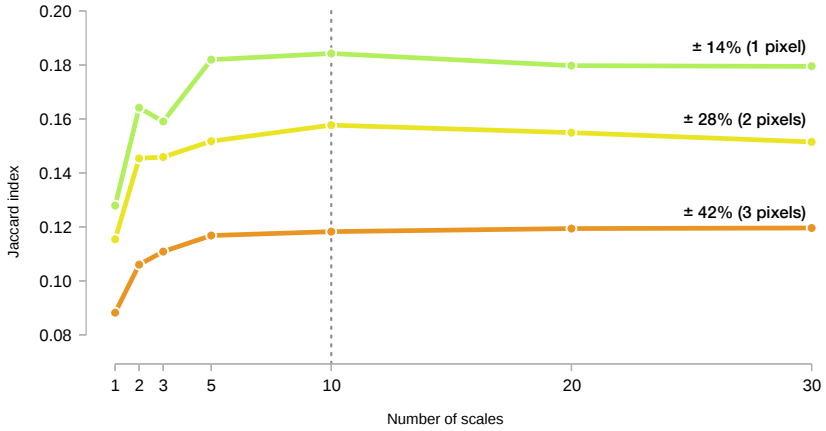

Figure 4.9: Evolution of *Smax* results with the number of scales used in the filter bank for three level of object sizes variability within a given dataset. The plot shows the Jaccard indices obtained on a synthetic images containing 1000 objects of 7 pixels in diameter, with sizes randomly varying from one to three pixels (curves from top to bottom) around that diameter. The dashed line indicates the chosen number of scales used as a default for the filter bank of *Smax*.

Algorithm 1: SMax

input : 3D Image I, Full Width at Half Maximum s
output: array of (x,y,z) spot positions I_{final}
$I_{\text{iso}} \leftarrow \texttt{CubicSplineInterpolationInZ}(I)$;
$\sigma \leftarrow 0$;
$I_{\text{acc}} \leftarrow 0$;
repeat
  $I_{\sigma} \leftarrow \texttt{GaussianConvolution}(I_{\text{iso}},\sigma)$;
  $I_{\text{detections}} \leftarrow \texttt{MaxDetection}(I_{\sigma},\ s)$;
  $I_{\text{acc}} \leftarrow I_{\text{acc}} + \texttt{Denoising}(I_{\text{detections}})$;
  $\sigma \leftarrow \sigma + \Delta\sigma$
until $\sigma < \sigma_{\text{max}}$;
$I_{\text{final}} \leftarrow \texttt{MaxDetection}(I_{\text{acc}},\ s)$

4.4.3 Single measurable parameter

An advantage of the proposed method is that it requires only a single parameter from the user. Furthermore, this parameter is a physical quantity: the average diameter of the object we aim to detect. This value can be easily estimated from the data by computing the Full Width at Half Maximum (FWHM) of a Gaussian fit on the average profile of a set of randomly chosen objects (see Figure 4.7c). This is typically the way empirical Point Spread Functions (PSF) are constructed albeit with under resolution beads while our approach is typically suited to packed objects that can be distinguished.

4.4.4 Slight variations in size

The method we propose is meant to be used to detect a large set of packed objects of similar size. By similar size we mean that there may be a slight variation in the population of object size around the expected value but its variance is assumed small. This is the case for 3D nuclei: they don't have all the exact same size, but for an adult population, and without the possibility of cell division, the difference in size should me minimal. This slight variation is cap-

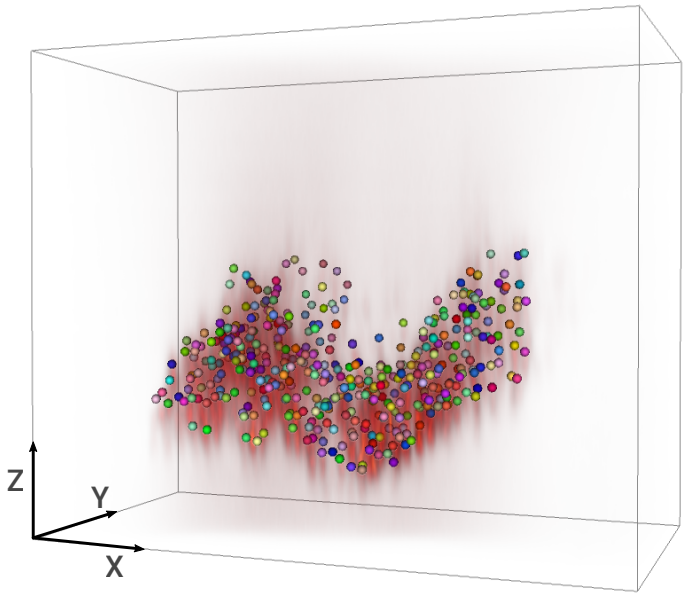

Figure 4.10: Volumetric reconstruction of the nuclei signal together with the resulting detections.

tured by scanning a tight range of values around the specified diameter. Filters that approximately match a nucleus size will produce maxima in a close vicinity of each other, thus producing a signal accumulation that can be clustered in an ultimate aggregation step.

4.4.5 Supplemental datasets

Smax was developed with the detection of nuclei on the Mushroom body in mind, but the method should be generic and applicable to other sort of 3D images, once regarding the fact that the desired objects reassemble spots above the microscope resolution and no other kind of objects (filaments or cell borders, for example) are present in the image. We tested the method (together with the two other methods presented in section 4.3) with three other datasets, presented bellow. The real images were manually annotated using the same procedure as explained in Section 4.2.For the synthetic image, the ground truth was used for the Jaccard index calculation. This allowed a more extensive comprehension on the weakness and strengths of the methods, as analyzed in Section 4.5.

Early embryo

A 3D image of an early *C. elegans* embryo was used to test the efficacy of the method for objects that were bigger than the ones observed in the Mushroom body (max projection on Figure 4.11). Altough being a realtively simple case, images of this kind are still being manually annotated today, and new methodologies are still being developed to increase eficiency and accuracy [134]. For this particular case, all the methods we compared performed relatively well.

Synthetic image with large objects

To better understand the detection of large objects, another synthetic image

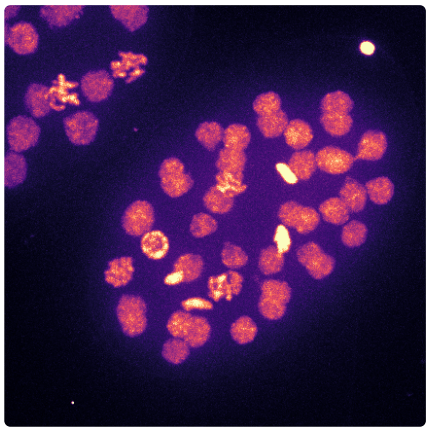

Figure 4.11: Axial max projection of the *C.elegans* embryo.

was generated. This image had 50 objects and was based on the *C. elegans* embryo image, following the size measured from the embryo nuclei. The max projection of the image can be seen on Figure 4.12.

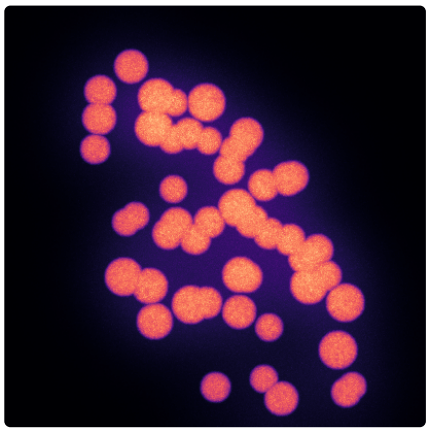

Figure 4.12: Axial max projection of the synthetic image containing large objects, based on the *C.elegans* embryo.

Centrioles

For this image, a 3D stack from centrioles, the algorithm was tested for the detection of points in different densities, as well in a condition with a high level of noise. The objects had a more similar size than in the images of the Mushroom body, but they tend to form clusters (as seen on Figure 4.13). Also, as the image is a sectional crop of an much larger image, about $\frac{1}{3}$ of the stack is composed of only background, which stresses the ability of the algorithms to ignore background noise.

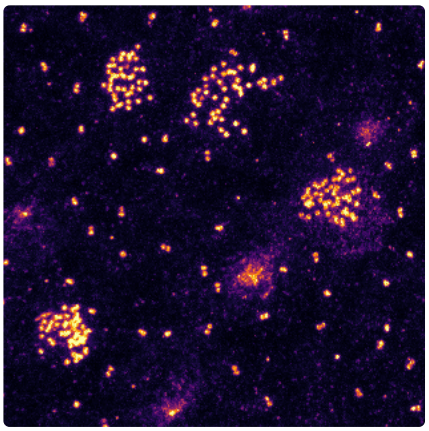

Figure 4.13: Axial max projection of image containing centrioles, especially interesting to test the detection of clustered objects and resilience to noise.

4.5 Methods comparison

Smax was compared to the state of the art methods using the 4 datasets presented. The results can be found in Figure 4.15. Using the Jaccard index to assess the accuracy of the detections, we were able to conclude that for every dataset *Smax* performs equably or with a higher accuracy, especially for densely packed objects on a uniform background.

For the datasets with relatively larger objects (*C. elegans* embryo and Synthetic image with 50 objects) the performance is close to 100%, regardless of the method. These cases present spots that are composed of several voxels in diameter, with a relatively high distance between them, thus being relatively easier to detect.

For the other datasets (Mushroom body, synthetic image with 2000 objects and Centrioles), the accuracy of *Smax* was significantly higher than the compared

methods. The smaller size of the objects, their relative high proximity and their stacked position in z made the detection less trivial.

None of the methods from the state of the art takes into account the lack of isometry of the image, and we realized that this feature had an important impact on the accuracy. When correcting for the isometry of the images before applying the methods, by using the same interpolation as for *Smax*, we obtained a significant increase in accuracy for the other methods, sometimes with a Jaccard index 15× higher, as seen in Figure 4.16, almost reaching the accuracy levels of *Smax*. This shows that the isometry correction is neglected by the state of the art methods, despite playing an important role for the accuracy of the detection.

A mushroom body of an adult *D. melanogaster* should contain about 2000 neurons, according to the literature [135], and for this reason we used a synthetic image containing 2000 objects. However, our detection found only 319 True positives points for the MB (from a total of 604 detections), with a Jaccard index of 23%. Although a low value, it is an improvement of 280% when compared to the state of the art methods. The missing and inaccurate points were mainly the result of the low axial resolution of the image, limited both by the diffraction limit of the light and by the low number of slices that we were constrained to acquire because of the temporal resolution.

4.6 Conclusion

The current state of the art methods couldn't perform accurately enough for the detection of nuclei on the Mushroom body of the *Drosophila melanogaster*. Our proposed method, *Smax*, although not perfect, but dedicated to our context, increased the accuracy considerably. This allowed us to proceed with the next step of the process, the neuron tracking.

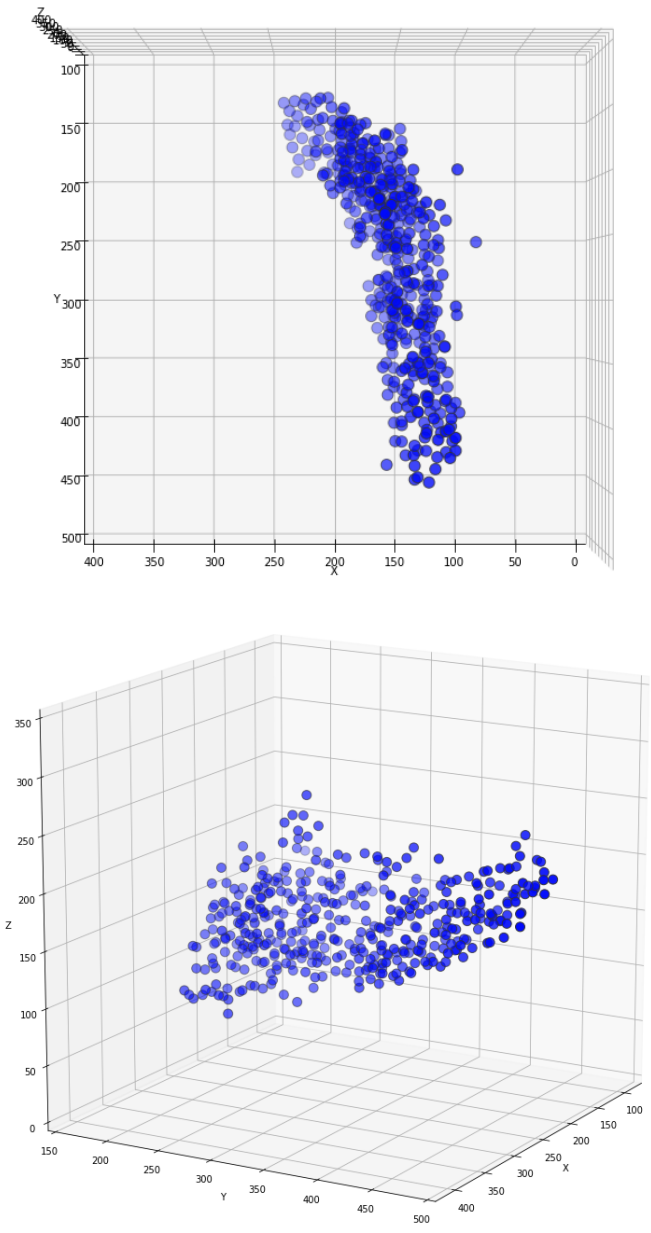

Figure 4.14: Resulting detections of the *Smax* algorithm for one Mushroom body. From this Figure we can clearly see how the common aproach of having a axial max projection of the data can cause a huge loss of data. As the MB is a 3D structure, and a considerable number of neurons are stacked on top of each other, a truly 3D analysis is fundamental if we seek a comprehensive understanding of the memory patterns inside the brain.

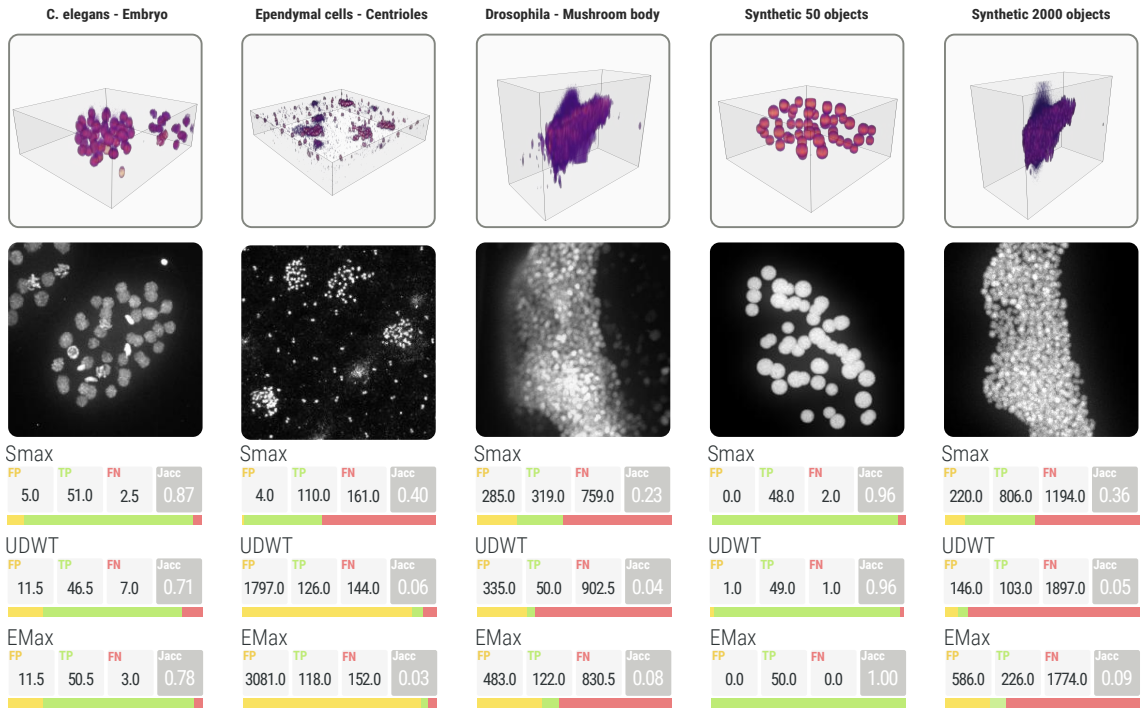

Figure 4.15: Quantitative comparison of Smax with two state of the art approaches. *Smax* is compared to UDWT and eMax approaches using 5 3D stack datasets. From left to right: image of distinguishable nuclei in *Caenorhabditis elegans* manually annotated, image of centrioles in mice ependymal cells manually annotated, image of a large amount of packed nuclei in Drosophila's mushroom body manually annotated and synthetic images containing 50 objects and 2000 objects for which ground truths are known. From top to bottom a 3D rendering view of the dataset, a maximum intensity projection on the z axis and the quantitative comparison of spot detection algorithms. Each box of result indicates from left to right the values of false positives, true positives, false negatives (colored bars indicating the proportion for each case) and the Jaccard index. A detection is considered as positive when it fall in a sphere of nucleus size around any of the original objects positions. *Smax* sole parameter was set to an average nucleus diameter. Parameters for the two other methods were systematically scanned in order to choose the best Jaccard Index which in principle unfavors our method (see Figure 4.16).

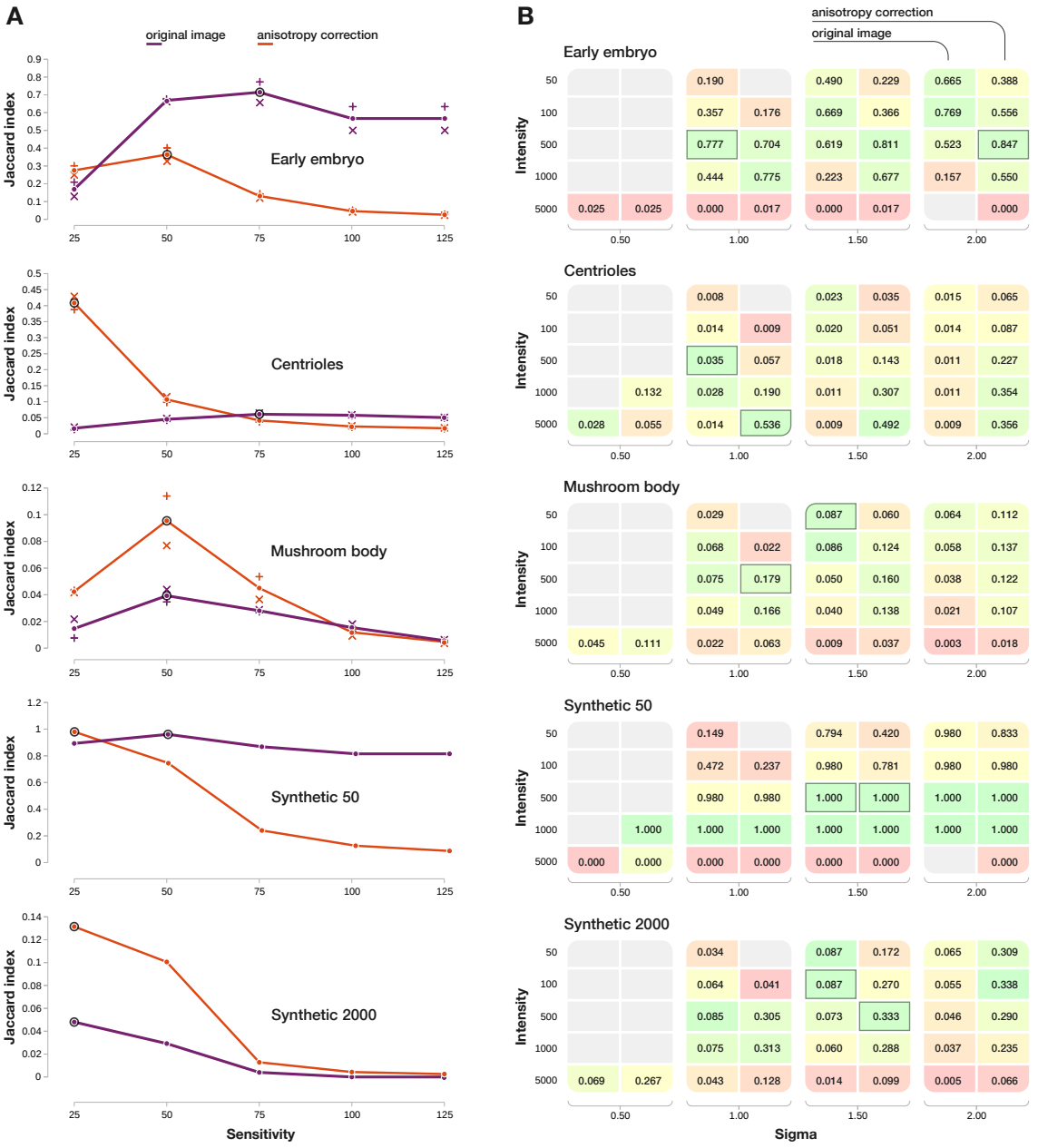

Figure 4.16: UDWT and Emax parameter scanning for comparison with Smax. (A) Jaccard indices obtained by scanning the "sensitivity" parameter of the Icy spot detector (UDWT) for original and image with corrected anisotropy. Full line shows the average Jaccar index obtained by the the two manual annotations (+ and × symbols). Note that the synthetic images use the computer generated ground truth, not an manual annotation. The scale for the parameter scan was chosen as matching the objects size (as specified by the authors). The values obtained demonstrate that the quality of the Icy spot detection can be improved for every case, except the embryo image, by interpolating the image in the z direction prior detection (although, without reaching the accuracy obtained by *Smax*). However, the same interpolation step decreases the accuracy of the same detector in the case of the real *C. elegans* embryo image, as the False positive rate increases drastically, lowering down the Jaccard index. (B) Jaccard indices (mean for the two ground truths for manual annotations) obtained by scanning the two parameters of eMax, applied directly on original images (left side of group) or after anisotropy correction (right side of group). Gray squares indicate cases where the provided implementation of the algorithm couldn't perform the detection. Color ranges from red to green, rescaled using all Jaccard index values obtained on each dataset. For both methods, the parameters corresponding to the best Jaccard index for raw and anisotropy corrected images are emphasized.

Chapter 5

Neuron tracking

I'm on the right track baby
I was born this way.

Stefani Joanne Angelina Germanotta (Lady Gaga)

The previous chapter shows how we were able to detect nuclei from the neurons in the Mushroom body, with a relatively high precision. However, these detections were independent through time, and if we were willing to measure the signal from the individual neurons, detected nuclei from the different time frames needed to be linked accordingly.

If the brain was perfectly still through time, and every nuclei correctly detected at all the time frames, the tracking task would be consisted of finding the closest detection in the next time frame. Unfortunately, none of these assumptions was true. As the flies were imaged *in vivo*, there was a natural movement of the brain, and the nuclei detection were not consistent for most nuclei during the whole acquisition. In this Chapter we present how we minimized the movements of the brain using registration, in order to correctly track neurons through time.

5.1 Brain movement

The fact that we acquired *in vivo* images was one of the fundamental aspects of this research project. This allowed us to observe the brain as close as possible to its natural behavior, giving us the unique change to look deep into how the memory is organized. But making an *in vivo* study came with a price, as we also needed to deal with the natural movements of the brain. Two strategies could take place here: first, trying to minimize the movement of the brain before the acquisition. Second, perform a numerical post-processing stage. Although being the first option the common choice for the majority of current studies regarding the Mushroom body, we discovered that it may lead to artifacts and behavioral changes, as they will be describes throughout this chapter.

5.1.1 Origins of movement

During the dissection process, the fly was properly glued to the coverslip, avoiding global head movements. However, this process alone wasn't able to cancel all the movements of the brain. Two main factors may induce movements on the brain: first, the expansion and contraction of the proboscis can considerably push the whole brain structure. Second, the pulsatile organ, that allows the air diffusion through the linfa of the fly, can generate contractions that were noticable during the image acquisiton.

Another category of movement that was encountered in about 10% of the flies was a relatively huge axial drift, unrelated to the movement described above. In this case, the whole structure drifted downwards, especially during the first third of the acquisition. A reason might be the settling of the fly with an unfinished fixation process, as the fly was held only by the glue during the acquisition. This drift needed to be corrected in post processing, as described in the Section 5.2.

5.1.2 Techniques for limiting the movement

As the origin of the movement is known, it is common to apply several different techniques during the experiment preparation to minimize its effects.

For the first cause, the proboscis expansion, the most common approach is the fixation using biocompatible glue during the fly preparation on the coverslip. This step is done for all of our flies, and it is common through the bibliography [136].

The second source of movement is more complex, and several techniques can be found to try to minimize it.

Rupture of the muscle

One approach, rather drastic, is to cut through a cirurgical process the muscle responsible for the movement of the pulsatile organ. This technique, although used by several works [135–137], is extremely difficult to be performed (increasing the rate of flies that present artifacts) and might induce unknown features to the behavior of the brain. Thus, we decided to not perform this process on our work.

Temperature cooling

Reducing the temperature of the fly, by the use of dry ice, is a common method [137–139]. It is used specially when performing the dissection, as the movement of the fly greatly increases the difficulty of the process. Although, in our case, we decided not to perform the ice cooling, as its effects on how the memory traces are expressed on the brain are unknown.

Neuromuscular blockers

The chemical use of neuromuscular blockers, as Philanthotoxin [140], a blocker of muscular glutamate receptors was also proposed [139], but its use promotes changes in behavior for neuronal activity [141, 142], so it wasn't indicated for our case.

Agarose fixation

One promising approach was the fixation of the brain using agarose. After solidification, it drastically minimized the movement of the brain, making the acquisition much more stable. However, after several experimentations, we realized that it possibly caused artifacts on the brain activity, as increased sporadic activity of the brain. This might be caused by the fact that the agarose needs to be applied at high temperature, causing unspecified damage to the neurons.

At the end, only the physical fixation of the proboscis was used during our specimen preparation. All the remaining movement of the brain was fixed via computational means, as explained in the following sections

5.2 Brain registration

By registration we mean the process of matching two different sets of points. In our case, this means to match the nuclei detection from two different time frames, regardless of the spacial deformation that occurred between them. It is worth to remind that not only the movements of the brain were a issue here, but also the inherent imprecision of the detection process. Not every nuclei was detected at every single time frame, which created the necessity for the registration process to handle noise and missing points.

It is important to state that the registration process is done by mathematical transformations of the point-cloud con-

stituted by the detected nuclei. Two kinds of transformations exists, *rigid* and *non-rigid*. For the rigid transformation only translation, scaling and rotation are allowed, thus being that the general aspect of the point cloud is not changed. Non-rigid transformations allow operations that do change the shape of the point cloud, as shearing for example. The deformations observed on the brain required a non-rigid transformation, as usually the deformation was not similar on every part of the Mushroom body. Our registration process is composed of two steps, first an affine registration to handle the coarse movements, and then a Coherent-Point-drift [143] to make the fine adjustments.

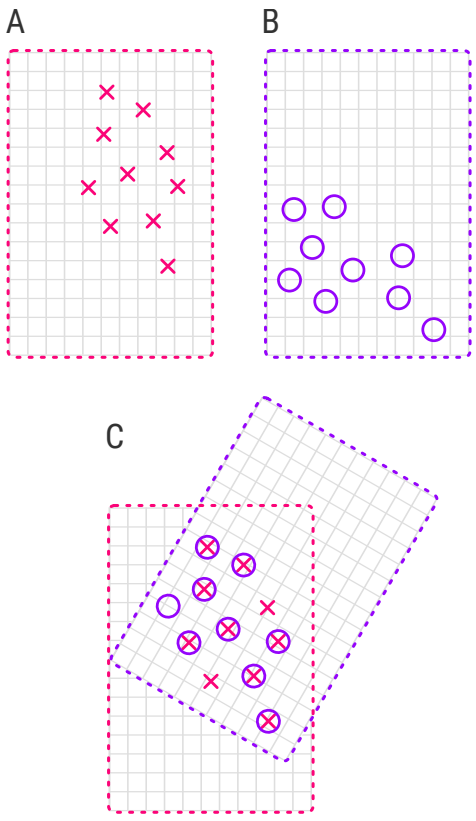

Figure 5.1: Schematic representation of an registration process. (A) is the base image, used as reference, and (B) is the image to be registered. (C) shows the result of a rigid transformation on (B), using rotation and translation to match the two set of points. Note that outliers are possible within the registration process, as it is driven by the global cost minimization of the points match.

5.2.1 Affine registration

The affine transformation preserves the collinearity of the points, so that if a set of points belongs to a line before the transformation, they will still belong to a line (a different one, tough) after the process [144]. This doesn't mean that the affine transformation is rigid, as deformations as translation, scaling, reflection, rotation, shear mapping or any combination of those are possible.

The operation for the affine transformation can be defined in a single matrix, that once multiplied by the point cloud, returns the transformed set of points.

Initially, our first attempt was to set the middle frame of the acquisition as reference, and register all the other frames to it. For the majority of cases this approached worked well, but for the flies on which the axial drift was too important, the cost minimization usually would fall into a local minima, as the two point clouds are initially too far apart.

The solution arose by means of a *chained registration*. We still kept the middle frame as final reference point, but the registration was done sequentially between frames until the reference frame was reached. As the process involved redundant calculations for when registering different time frames, the speed of calculation was significantly increased by saving the intermediary transformation matrices that were common between intervals that intersect, as seen in Figure 5.2.

The final result mostly minimizes the axial drift of the image. Although being an improvement, the contractions caused by the pulsatile organ of the fly are still present, as they were highly non-rigid deformations that could not be solved by the affine transformation.

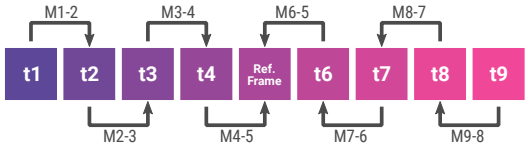

Figure 5.2: Schematic representation of the chained registration process, where each box represents one time frame t. For the registration of $t4$, the matrix $M4$-5 is computed. But for the registration of $t3$, only the matrix $M3$-4 needs to be computed, as the second needed matrix, $M4$-5, was already calculated and stored.

5.2.2 Coherent point drift

The registration through affine transformation was able to correct the coarse part of the movement, as the axial drift, but it wasn't capable of fixing the small local deformations of the brain, as they were highly non-rigid.

As the registration isn't done on the raster image itself, but rather on the point cloud that results from the nuclei detection, the problem was in fact a point-set registration. Several algorithms proposed ways to register a set of points, but the Coherent Point Drift (CPD) [143], proposed by A. Myronenko and X. Song, was well indicated in our case, as it is capable of handling 3D information, perform local deformations and is robust to noise, outliers or missing data.

The method considers the alignment of the two point-sets as a probability estimation problem, where the set to be registered represents the centroids of a Gaussian Mixture Model (GMM), which are fitted to the reference point-set by maximizing the likelihood. The strength of the method is that the GMM are constrained to move coherently as a group, preserving the overall topological structure, while allowing for local deformations.

The process isn't parameter free tough. Three free parameters exists: ω, λ and β. The parameter ω varies between 0 and 1, representing an assumption on the amount of noise present in the data. λ represents the trade-off between the regularization and the overall goodness of fit. β is the width of the Gaussian used for the GMM model, and the higher the value, the more the transformation approaches a rigid registration.

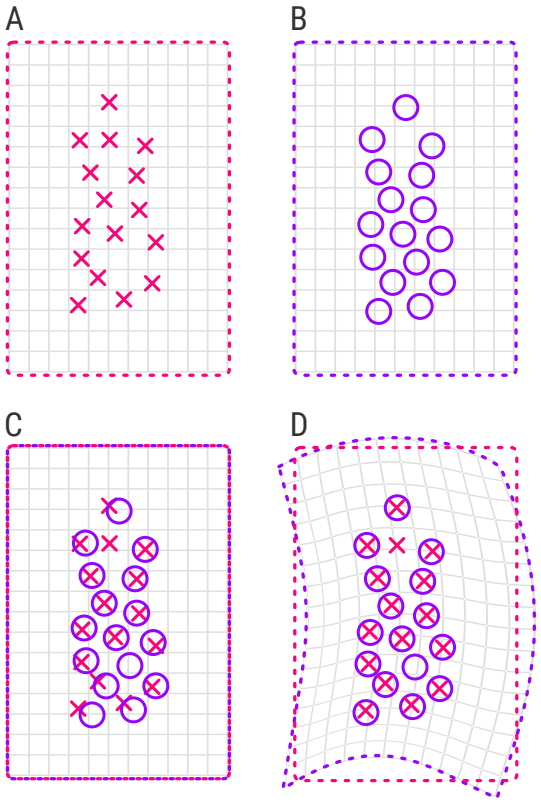

Figure 5.3: Schematic representation of a non-rigid, with local deformation, registration process. (A) is the base image, used as reference, and (B) is the image to be registered. (C) Is the superimposition of (A) and (B), without registration. (D) shows the result of a coherent point drift. Note that here also, outliers are allowed.

The parameters ω and λ where left to the default settings of the algorithm, while β was manually adjusted based on the visual match between different time frames to reference point. The lack of ground truth for linking detections made an automated parameter scanning unfeasible. The parameter was scanned to allow small corrections on the point cloud, as the coarse part of the movement was already corrected by the previous affine transformation. However, in

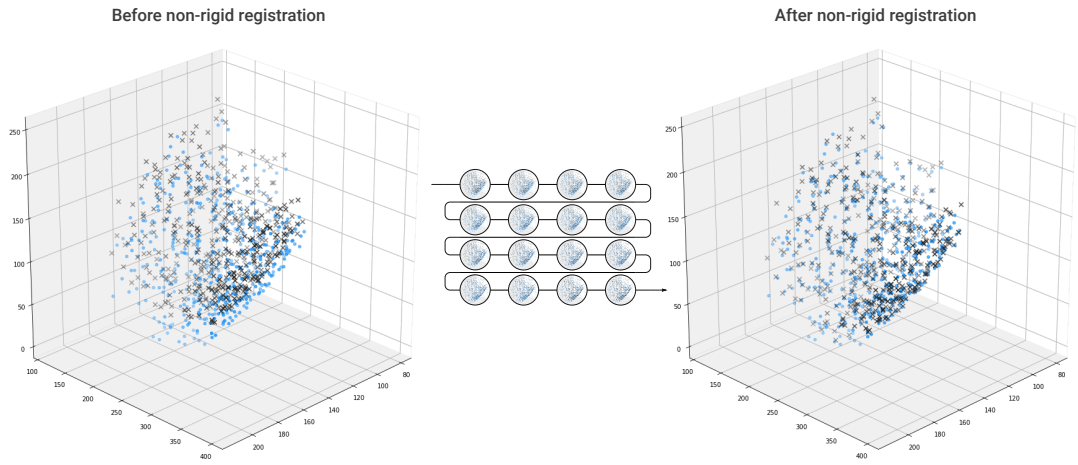

Figure 5.4: Cost minimization process of the CPD algorithm. In blue we see the point cloud used as reference, and black crosses are the points submitted to registration. On the left the two point-sets on the same 3D space, after the affine registration, where we can see some mismatch, specially on the bottom right corner. On the right side, after the CPD registration, the point-set is morphed, better matching the reference frame but without losing the overall structure of the Mushroom body.

case future work (based on the synthetic videos described on Section 4.2.3) would be able to generate realistic movement of 3D stacks, we predict that the automatic scanning of the three parameters needed for CPD could make the affine registration not needed.

On Figure 5.4 we can see the result of the minimization process from CPD, for two frames once the affine registration was applied. As the two point clouds were already globally registered, the process converged rather quickly, using just a few seconds per frame.

5.3 Nuclei tracking

Once achieved, the registration process made that for a given nucleus, the detected points overt time were closer in the 3D space between different frames. However, these points were not yet linked, as the detections were independent for each time frame. A naïve strategy of linking the closest points between frames would give better results than before the registration process, but still would fail because of noise and missing detections (as there is not guaranteed that every nuclei produce a detection at every time frame).

After the registration, the point cloud made of detections of an individual nucleus over time was much more dense than before, and the distance between clouds of distinct nuclei displayed a higher distance between themselves. Also, "real" nuclei presented a point cloud more dense than random noise. These features allowed us to use a density based clustering method to identify the individual nuclei.

The tracking process is summarized in Algorithm 2

5.3.1 Clustering

To use a clustering method for tracking the detections may not be the most common approach from the literature, as seen in Section 1.5.3, but taking in consideration certain aspects of our data model, it becomes clear how it was an interesting approach for the tracking of nuclei.

Algorithm 2: ClusterTracks

input : Detections from Smax, D
output: Labeled data frame, D_{labeled}
repeat
  $D_{\text{registered}} \leftarrow$ `AffineRegistration(`D, t, t_{ref}`)`;
  $D_{\text{registered}} \leftarrow$ `CPDregistration(`$D_{\text{registered}}$, t, t_{ref}`)` ;
  $t \leftarrow t + 1$;
until $t < t_{\text{final}}$;
$D_{\text{labeled}} \leftarrow$ `DBSCAN(`$D_{\text{registered}}$`)` ;
$D_{\text{labeled}} \leftarrow$ `ClusterFix(`D_{labeled}`)` ;
$D_{\text{labeled}} \leftarrow$ `TrackSmoothing(`D_{labeled}`)` ;

Usually, tracking algorithms make the assumption that a given point needs to be linked to another in a different time frame. Then, hypothesis are built on how the point position might evolve though space, taking in consideration parameters that are know from the data (as maximum movement speed, possibility of duplication, maximum displacement etc) [145].

In our case, the clustering approach allows to limit the number of hypothesis that would need to be set on a usual tracking scheme. We know that division of the tracks are not expected, as the short time of acquisition don't allow cell division. Also, because of the non-rigid registration of the Mushroom body, we can assume that detections from a given nucleus over time are co-localized, within the precision of the spot detection method (Chapter 4).

Thus, our approach consisted in performing a clustering on the 3D space that contains the points from every time frame, a time projection of all points into a singe space, from 4D (3D+time) to 3D. On this time projection, the detected points should form dense clusters, if the nuclei were detected for the majority of the time frames, and noise should appear as sparse points.

DBSCAN

Density-based algorithm for discovering clusters in large spatial databases with noise (DBSCAN) [146] is a clustering method that uses the notion of density from the dataset to form clusters, largely used by recent works as one of the usual clustering methods [147–149]. It is by design able to handle noise, meaning that not every point on the data-set is forced to be part of a given cluster. These characteristics made the method highly adapted to our problematic. After the registration process, detections that corresponded to a true nucleus over time were likely to co-localize, forming dense clouds of points (thus, easily detected by DBSCAN). Points corresponding to noise were not expected to be part of any cluster, so the fact that the method is able to label point as noise, was in our favor.

The method consists in an iterative scheme that uses two parameter for the definition of density, ϵ (distance measurement) and $minPts$ (amount of points). Firstly, the algorithm defines a point set classified as *core points*, called p, that must have at least $minPts$ neighbors closer than the ϵ distance. A set of connected core points defines a cluster. Any other point within ϵ distance to a cluster (directly reachable by a core

point) is grouped to the same cluster. Points further than ϵ to any core point are labeled as noise.

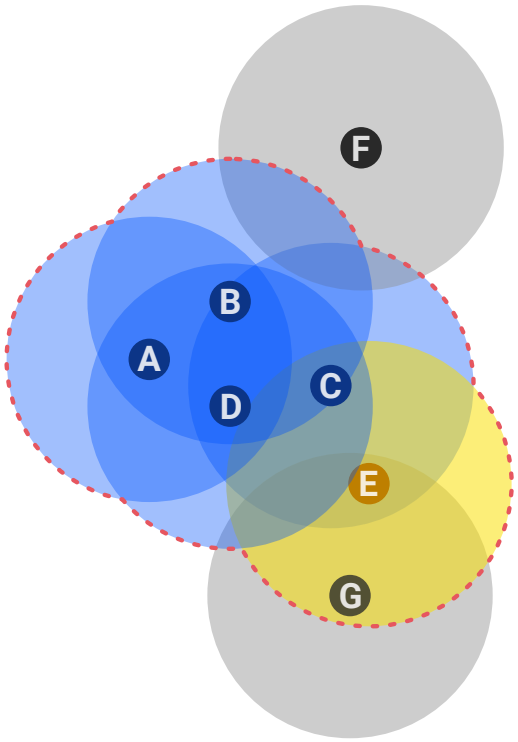

Figure 5.5: Illustration of the DSCAN definition of clusters. The ϵ distance value is defined by the radius of the circles, and for this schematic, the $mimPts$ value is 2. The points A, B, C and D form the core points, as each one have at least $minPts$ closer than ϵ. The point E is part of the cluster, because is reachable from C, but it is not a core point. F and G are labeled as noise, as they cannot be reached by any core point (G is reachable by E, but E is not a core point of the cluster). Thus, the final cluster is shown by the dotted red line.

5.3.2 Parameter estimation

As stated, DBSCAN isn't a parameter free method. However, as we posses some prior information on the data behavior, it is possible to estimate the best parameters for the clustering.

Core point distance

The ϵ value is directly correlated with the size of the nuclei, as the distance between detections over time from the same nucleus derivates mainly from the detection imprecision. Thus, we apply the FWHM value used during the nuclei detection as ϵ (see Chapter 4).

Minimum number of points

The minimum number of points cannot be directly estimated as the ϵ value, mainly because it depends on some uncontrolled factors as the movement of the brain and proportion of missing detections on certain frames.

We approached the problem through an iterative process. First, we assumed that the final number of detected clusters should be close to the median number of detections through all the frames. This supposition is possible because the real number of neurons does not change through time, making the process of independent detections for every time frame an estimation of the "detectable" neurons.

Then, the DBSCAN algorithm is applied for a range of $minPts$ values, starting with one. The value is iteratively increased, and the final number of clusters measured. The $minPts$ value that reaches a number of clusters closer to the median amount of detections is chosen as parameter for the DBSCAN.

5.3.3 Fixing clusters

The clustering process, as described so far, ignores completely the information that each point had about the time frame it was acquired. For example, it is possible that a given cluster have two detections for the same time frame. However, we know that this should not be the case, as each cluster should correspond to an unique nucleus, thus having only one detection per time frame.

Two process may lead to this: First, by chance a noise can be detected close to a real nucleus, thus being part of the cluster after the DBSCAN. This process should be rather sporadic, and not happen often. Second, it is possible that two groups of points were too close together, and the two clouds were merged in a single cluster.

The whole process was computed independently for each cluster, but the identification of the condition begins with the same query: for every cluster, a distribution of the number of points for the same time frame, and the median value of this distribution is taken.

Median 0

A median value of zero means that the cluster has, for the majority of the frames, missing detection. For this case, the cluster is excluded from the rest of the process (all the points are marked as noise)

Median 1

A median value of one means that for the majority of time frames the cluster have only one detection. It is still possible that some frames have more than one detection, and on this case the point closer tho the centroid of the cluster is chosen, and the other is labeled as noise.

Median 2 or higher

If the median is higher than one, this means that we have a case of merged clusters, being that the number of merged clusters is equal to the measured median. For this case, the cluster was divided using a k-means algorithm [150], with k as the median value.

The whole process repeats iteratively, until no cluster contains a median value higher than one. Figure 5.6 illustrates the process.

5.3.4 Missing data

Because of the natural movement of the brain, photo-bleaching of neurons and noise of the acquisition, it is most often the case that a given neuron will not have a detection for every time frame. It is rather common that for a given track few points are missing.

As the tracks are going to be used for the signal measurement (Chapter 6), they need to be retrieved at every time point. The missing points are solved by means of a linear interpolation [151] between the neighbors in time.

This interpolation approach is possible for two main reasons: first, the missing detections are rather sporadic, because the clusters that weren't dense enough were already removed during the DBSCAN step, making that if a track still persists until this stage, it has at least more than half of the time frames represented. Second, because of the registration that was performed prior to the clustering, we don't expect big movements from the detected nuclei.

Note that the actual signal that needs to be measured isn't registered, it follows the "real" coordinates of the points. The interpolation is made both on the registered and non-registered spaces (as a given point have the same label for both). But, for the measurement of the signal, the tracks on the "real" space are used.

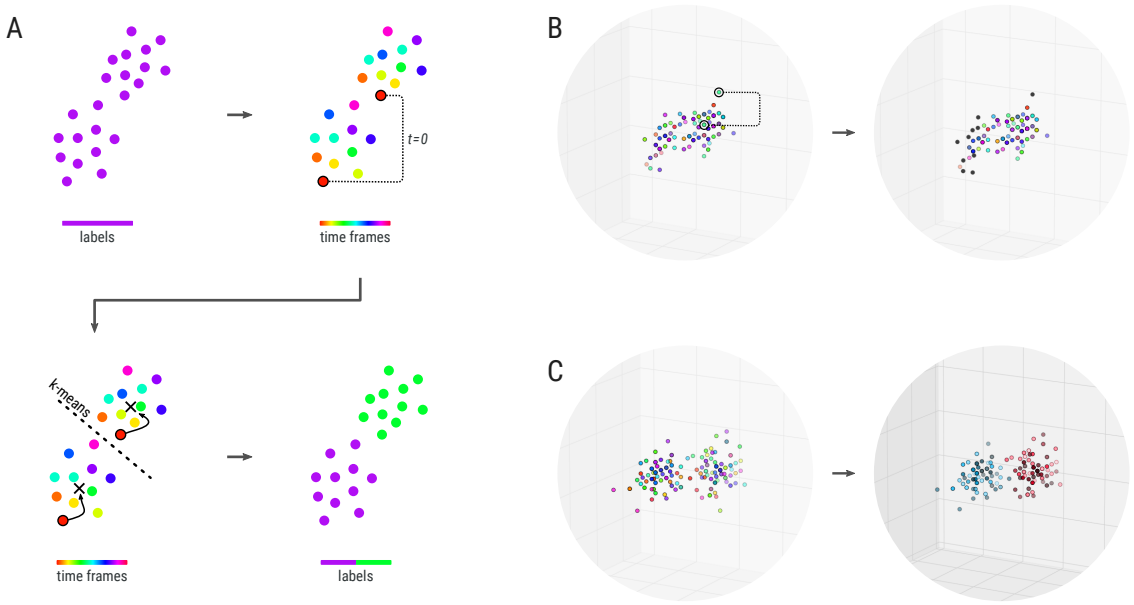

Figure 5.6: Using time information to increase the quality of clusters. (A) Schematic representation of a case where the median value is 2, and thus the cluster is divided. (B) Real data from a case with median 1, so that duplicates (one example shown being conected by a dashed line) are marked as noise (black dots on the right image) and the point closer to the centroid is kept. (C) Real data for a case where the median is 2, and the resulting split cluster.

5.3.5 Track smoothing

The inherent imprecision of the detection, together with smaller movements that could not be corrected by the registration process, end up by resulting on tracks that may sometimes have a considerable noise level. Tracks with low consistency with the real path of the neurons is likely to cause artifacts when we measure the neuron GCaMP signal (see Chapter 6).

We approach this problem by a simple, dimension independent, smoothing of the spatial coordinates vector for every neuron. Every track is smoothed by a convolution with a gaussian kernel, using the same σ value of 1. This process is able to correct the noise of the tracks, while keeping the normal movement of the brain

5.3.6 Track validation

As for the detection of nuclei, the tracking must be validated. For this, we performed a similar approach, were both manual annotations were made and a synthetic sequence of images was constructed.

Fro comparison, the tracking was operated independently by 3 software program 1) ours: memotrack, 2) ICY [152] and 3) TrackMate [153]. ICY and TrackMate were chosen both because they were available online and because they received good evaluations from a recent spot tracking performance review [152]. After tracking, trajectories that were interrupted (that is their duration were shorter than the total sequence) were discarded as the complete sequence was needed to read the GFP signal. Distances between the remaining trajectories and annotated ground truth (manual or synthetic) were computed and a trajectories with an average distance over time from its closest ground truth larger than 3 times the nucleus size was

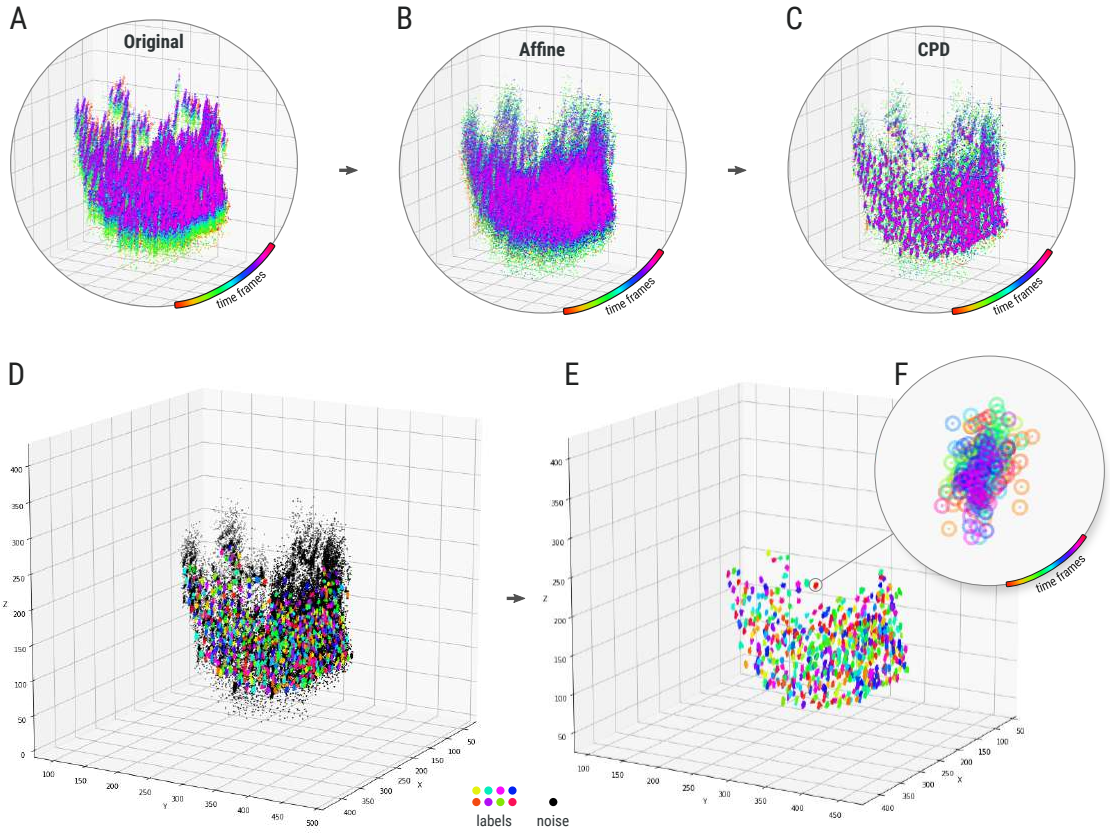

Figure 5.7: Summary of the neuron tracking process. (A) Shows the original set of detected points, color coded by time. (B) Result of the Affine registration, which mainly corrects the larger drifts of the data. (C) After the Coherent-Point-Drift (CPD) non-rigid registration, detections are well aligned and can be clustered. (D) Result of the DBSCAN clustering, with clusters in color and noise in black. (E) Noise is ignored and missing points are interpolated, making the final tracks. (F) Detail for one of the clusters, showing that the cluster is a collection of points from every time frame, thus making a track of the nucleus through time.

considered wrong (mostly to allow for the imprecision in the axial direction).

Correct trajectories defined this way represented the true positives (TP) in supplementary figures 5.8 and 5.9. False Negative (FN) were defined as ground truth nuclei that did not match any trajectories. False Positive (FP) were software defined trajectories that did not match any ground truth. Note that this last category is unavailable for manually annotated data as it would necessitate to annotate all nuclei of a 3D sequence over time (about 250,000 data points!), which is virtually impossible for a human being. Finally, note that there was not such a thing as True Negative (TN) as software program do not generally output trajectories corresponding to spurious objects that we anyway wouldn't have annotated.

The validation leads to the conclusion that our suggested method has a high accuracy for detecting the tracks of neurons in the Mushroom body. This is mainly possible because our method includes prior knowledge of the data, as the natural deformations of the brain and the fact that tracks should not split or disappear through the whole sequence.

5.4 Conclusion

The strategy of registration followed by clustering, rather than a conventional tracking approach, allowed us to make

MANUAL ANNOTATION | **SYNTHETIC IMAGES**

A Only complete tracks

Result	TP	FP	FN	Ground	Jacc		Jacc
482	18	n/a	1	19	0.95	Memotrack	0.53
96	8	n/a	11	19	0.42	ICY	0.02
0	0	n/a	19	19	0.00	TrackMate	0.00

C Only complete tracks

Result	TP	FP	FN	Ground
1064	1060	4	936	2000
38	37	1	1962	2000
0	0	0	2000	2000

B With incomplete tracks

Result	TP	FP	FN	Ground			
482	18	n/a	1	19	0.95	Memotrack	0.53
192	14	n/a	5	19	0.74	ICY	0.13
52	4	n/a	15	19	0.21	TrackMate	0.06

D With incomplete tracks

Result	TP	FP	FN	Ground
1064	1060	4	936	2000
306	253	53	1694	2000
304	119	185	1696	2000

Figure 5.8: Validation of our tracking approach Memotrack against two other methods, ICY and TrackMate, using manual annotated and synthetic 3D+time sequences. A. Results obtained using manual annotations and considering only complete trajectories along the whole sequence. That is, if the duration of a trajectory provided by a software program was less than the length of the sequence, it was discarded. This is because the signal needs to be captured along the whole sequence, not during a subpart of it. TP is True Positive, FP is False Positive, FN is False Negative, Result is the output of a software and Ground is the ground truth. Note that False Positive are not available for manual annotation because it was impossible to annotate exhaustively all trajectories of a 3D+time sequence. Memotrack, our method, outperforms other methods with 18 out of the 19 annotated trajectory correctly retrieved. B. Results obtained using manual annotations and considering trajectories with length at least as long as half of the whole sequence. This relax in stringency increases the number of successfully tracked nuclei by other software. Those results would not be acceptable or even useful as such to monitor the signal all along the sequence but they enable to understand partly the weakness of the other approaches. Other approaches cannot track nuclei over a long time period without failing because of the low accuracy of spot detection. Our approach, that rely on the non rigid registration of the whole sequence is very robust to detection errors and actually tracks all nuclei that were successfully detected enough time to form a cluster. For the same reason, the length threshold cannot improve the result obtained by our approach as all trajectories retrieved is the length of the full sequence. C. Results obtained using synthetic annotations and considering only complete trajectories along the whole sequence. Memotrack, our method, outperforms other methods. D. Results obtained using synthetic annotations and considering trajectories with length at least as long as half of the whole sequence. Interestingly, while unusable, we see here that this relax in stringency increases the number of tracked nuclei by other methods but also increases the number of false positive, indicating that even small trajectories provided by those software program are not necessarily correct.

use of the prior knowledge we have on how the data behaves, minimizing the amount of assumptions and parameters we would need to scan for a more classical tracking technique.

The proposed approach should work accordingly for other datasets with similar characteristics, such as *in vivo* tissues with non-rigid deformations, on which point clouds are detected. The algorithm has a few inherent restrictions, as the inability to handle tracks that divide through time (as cells in division) or points that move freely through the space (as free particles in solution) However, for a considerable number of biological applications (almost every spot detection for tissues *in vivo* or in cell culture), these constrains are just the nature of the data.

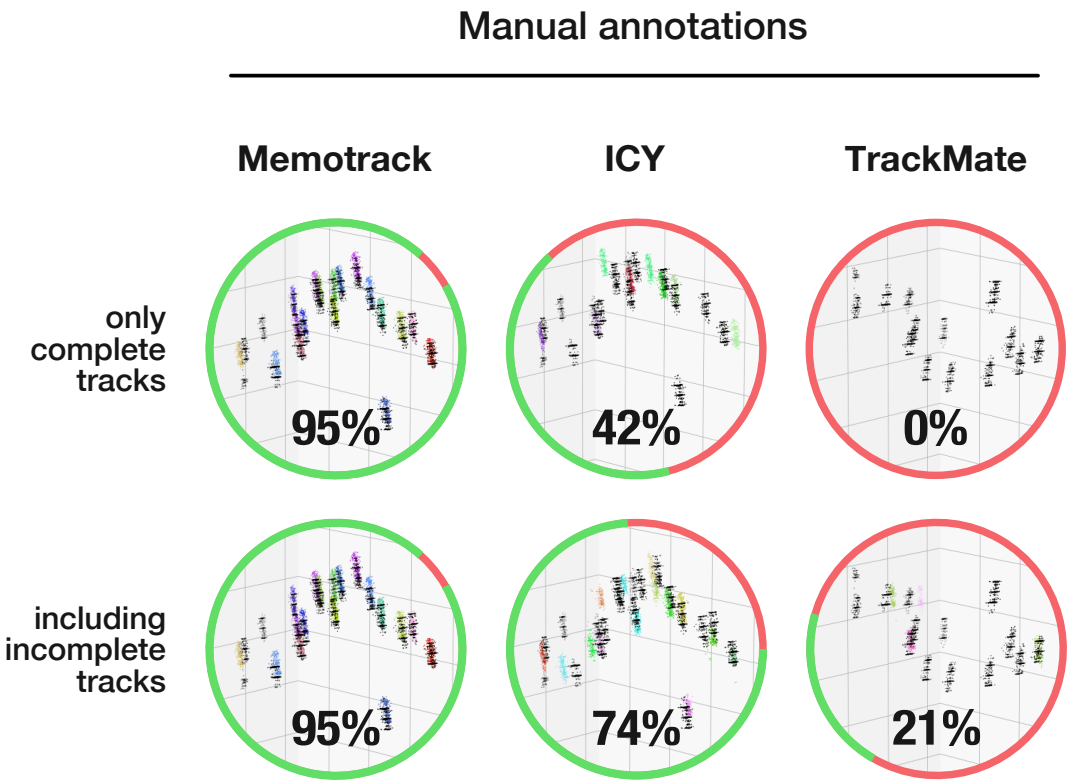

Figure 5.9: Visualization of manually annotated nuclei trajectories (in black, see online methods) and their corresponding trajectories obtained by the tracking software (in color). Top row: only complete trajectories that last the whole sequence were kept, it is the case we were interested in to monitor the single cell signal all along the sequence. We can see that, beyond the fact our method tracks correctly most manually annotated nuclei, the closest trajectories provided by ICY may in fact match other nuclei and be False Positives, an hypothesis that cannot be validated or unvalidated because it was impossible to manually annotate all trajectories in the sequence of 3D stacks. Bottom row: result when we allowed the length of the trajectories to be shorter but at least as long as half of the sequence. Again, those trajectories could not be used for the analysis as they are too short but underline the main limitation of other approaches: other approaches cannot track object stably over a long period of time due to the unreliability of the spot detection step.

Chapter 6

Measuring neuronal activity

And of course, the brain is not responsible for any of the sensations at all.

Aristotle

The processes described in Chapters 4 and 5 serve as necessary base for measuring the brain activity at the single cell level. Once having the tracks of individual neurons, it is possible to measure the actual GCaMP activity, thus bringing a direct measurement on how the brain operates conditioned to a given stimulus.

6.1 Signal localization

Our dataset is acquired in two channels, the first (*mCherry*) acts as nuclei marker, and was used so far for the detection of neurons. The second (*GCaMP*) is the actual activity of the neurons, and should be measured and linked to the corresponding nuclei.

On Figure 6.1 we show how the neuronal activity is not exactly colocalized with the nuclei signal. The top panel shows the correlation between the base level for both channels. Bottom panel shows how during an Octan-3-ol (OCT) stimulus, the increase of GCaMP intensity doesn't happens where we had the highest intensity of *mCherry* which corresponds to the center of the nuclei. The middle range of the GCaMP signal, when compared to the *mCherry*, show that the response is localized around the nuclei, and not on the center of it.

This means that even tough we tracked the nuclei, the position of the tracks is not where we should measure the signal from the neurons.

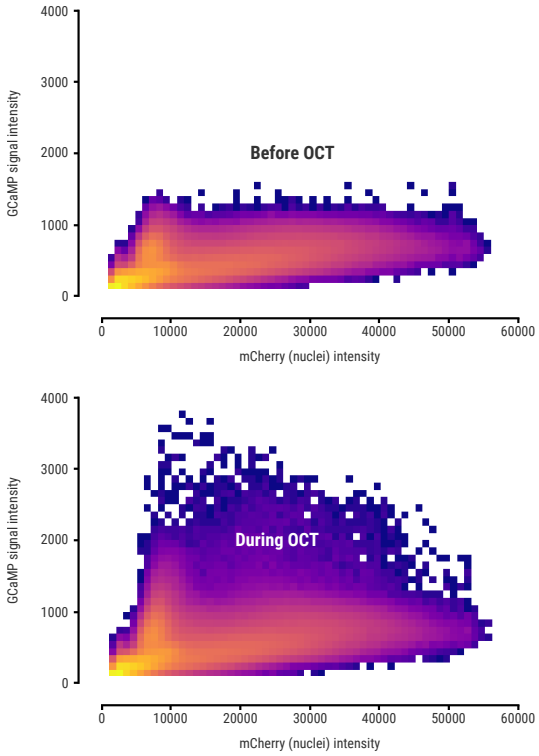

Figure 6.1: Intensity co-localization between *mCherry* (nuclei) and *GCaMP* (neuronal activity), shown as 2D histograms.

6.1.1 Space tessellation

Although not perfectly co-localized, the response signal of a given neuron should be within its vicinity. Hence, we proceed with a Voronoi tessellation [154] of the space, using as seed points the detected nuclei.

This allowed a discrete repartition of the 3D space. However, a standard tessellation divides the whole space, which causes a problem on the borders of the Mushroom body, as the nuclei on the extremities would have a much higher volume, that extends until the edges of the image. To counter this problem, we limit the tessellation around each nucleus to a maximum distance of two times the average nuclei diameter. This allows to have an fairly tessellated MB, without causing artifacts on the borders.

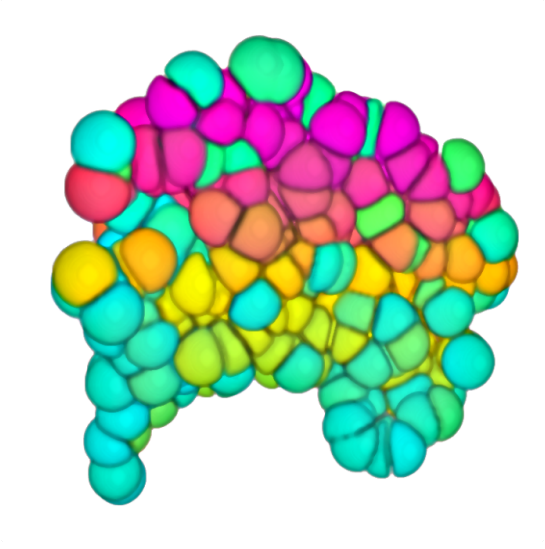

Figure 6.2: Volumetric visualization of the 3D tessellation. Each neuron is defined by a unique volume in the 3D space, without intersections.

6.2 Track quality

Because of the artifacts that randomly degraded the image during the acquisition (as described on Section 3.5.2) not every time frame could be used for signal measurement. Thus, we developed a methodology that could identify the problematic frames, and interpolate the dubious data from the neighboring time frames that don't present the artifact.

6.2.1 Center of mass stability

The process consists on the following assumption: during a normal acquisition, the center of mass of the Mushroom body (based on the detected nuclei) should move only slightly through space. During the artifact, as a considerable part of the MB is missing, the center of mass should shift rather drastically for one time frame. Thus, we measured the derivative of the centroid position through time, value then normalized between 0 and 1.

6.2.2 Ignoring artifacts

The quality measurement works then as an indirect way to asses the frames on which we had the microscope artifact. We still need to set a threshold as the minimum quality level that can still be used for the analysis, and by visual comparison of the quality measurement and the behavior of the 3D stacks the value was set at 80%. Thus, frames with lower values were removed, and the values interpolated from the closest neighbors in time.

6.3 Signal measurement

Once we have a certain volume assigned to each one of the detected neurons, it is possible to measure the activity of individual cells through time. For each time frame, and for each volume, we measure the intensity level on the 99 percentile and keep it as the neuron activity for the given time frame.

The measurement of the 99 percentile instead of an average or the maximum intensity value is able to avoid certain artifacts.

In case of the average (or even the median) the measured value would be sensitive to the size of the volume, especially on the borders of the Mushroom body, where a considerable part of the volume may not have the base background level that is present on the central region of the MB. Thus, the average (or median) would be abnormally lower on the borders.

The measurement of the maximum value within the volume would be highly sensitive to noise. Avoiding the absolute maximum value also minimizes the crosstalk signal between neighbor-

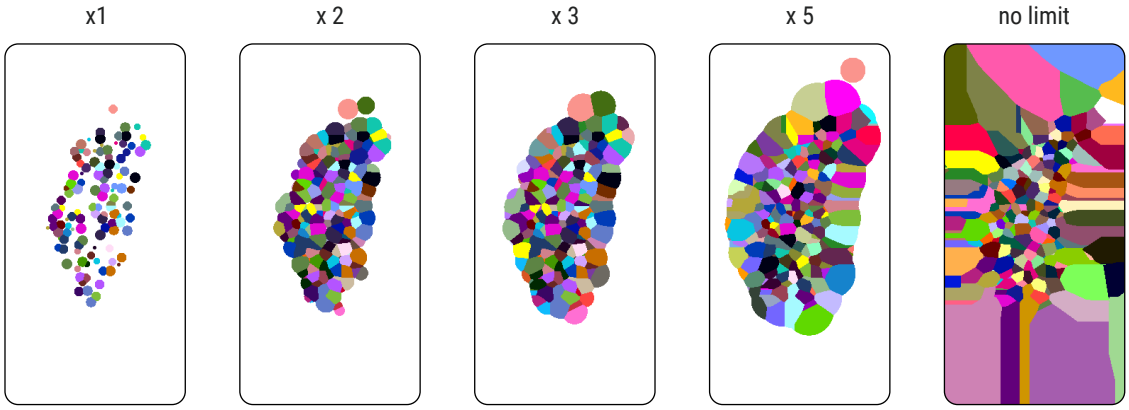

Figure 6.3: Tessellation limits. Increasing the maximum distance for the tessellation allows the inclusion of the space between nuclei, but values too high might cause problems on the borders. For the final tessellation we use the value of 2 times the nuclei diameter (second panel). All images show the middle slice of the tessellated volume.

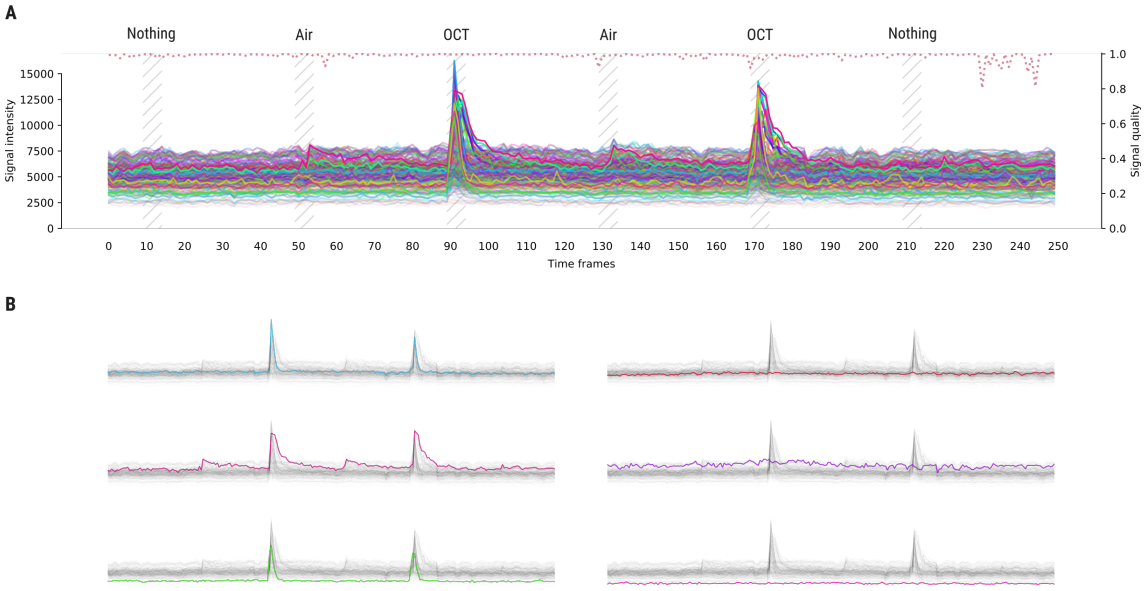

Figure 6.4: Raw signals from a naïve fly. (A) shows the measured signals for a group of 432detected neurons. Each line has its opacity proportional to the standard deviation of the signal. The two groups of peaks correspond to the response to the OCT stimulus. (B) Isolated tracks of 6 different neurons. On the left we can see that the two peaks are usually formed by the same group of neurons that respond twice. On the right, three examples of neurons that don't respond to the stimulus, forming the baseline of the response.

ing neurons, because the edges of the voronoi tessellation are probably close, but not a perfect match, of the cell borders.

6.3.1 Noise filtering

The noise level of the measured signal is more complex than just the Poisson noise [155] derived from the camera sensor. Small incongruences between the detected track and the real path of the cells may also increase the noise level, because of the mismatch between the measured region and the real signal.

We minimize the noise level, while keeping the peaks relatively sharp by using a low-pass Butterworth filter [156].

6.3.2 Signal normalization

Normalization of the signal is fundamental for the correct interpretation of the

neuronal responses, and to enable the comparison of activity between different flies.

We use the standard normalization methodology for GCaMP activity in neurons [157], shown in Equation 6.1:

$$F(t) = \frac{\Delta F}{F_0} \tag{6.1}$$

The fluorescence intensity F for a given time frame t is defined as the variation of intensity ΔF divided by the baseline of the signal, F_0.

We use as baseline the median of a moving window of 10 frames before and 10 frames after the time t. This value was chosen so that the neuron response wouldn't interfere with the baseline, as usually the responses are no longer than 3 time frames. Having a moving baseline, instead of a fixed baseline on the beginning of the acquisition, also compensates for the natural photo-bleaching of the fluorescent marker.

6.4 Odor stimulation regions

Figures 6.4 and 6.5 also show hashed regions, for which the fly was exposed to a certain stimulus, and thus a response from the brain might be expected. For every case, the stimulation window took 5 seconds, and the following order was used:

1. **Nothing (S)**
   During this window, nothing is presented to the fly, it is a control for the base level of the brain.

2. **Air (A)**
   Here the fly is exposed to a neutral air flow, without any odor being diluted. Although the fly is constantly receiving an air flow, during this time window the flux is switched to another air bottle. This window can be used as control for the effects of pressure change, that are unrelated to the actual odor stimulation

3. **Octanol (O)**
   This stimulation window is the only one where we expect peak responses from the detected neurons. However, not all neurons should respond during this window, just a subset of the whole mushroom body.

4. **Air (A)**
   A second air stimulation allows to verify if the brain returns to a resting state after the octanol stimulation.

5. **Octanol (O)**
   A second Octanol stimulation window is important to check the consistency of the brain, as the same neurons (at a similar intensity level) should respond to both stimulus.

6. **Nothing (S)**
   The sequence ends with another control window without any sort of stimulation, so that the resting state of the brain after the stimulations can be verified.

6.5 Conclusion

By having the neurons of the Mushroom body to express a GCaMP marker together with a *mCherry* NLS, we were able to measure the neuronal activity at the single cell level.

Because the data was subject to acquisition artifacts that made some frames unreliable, we developed an automated

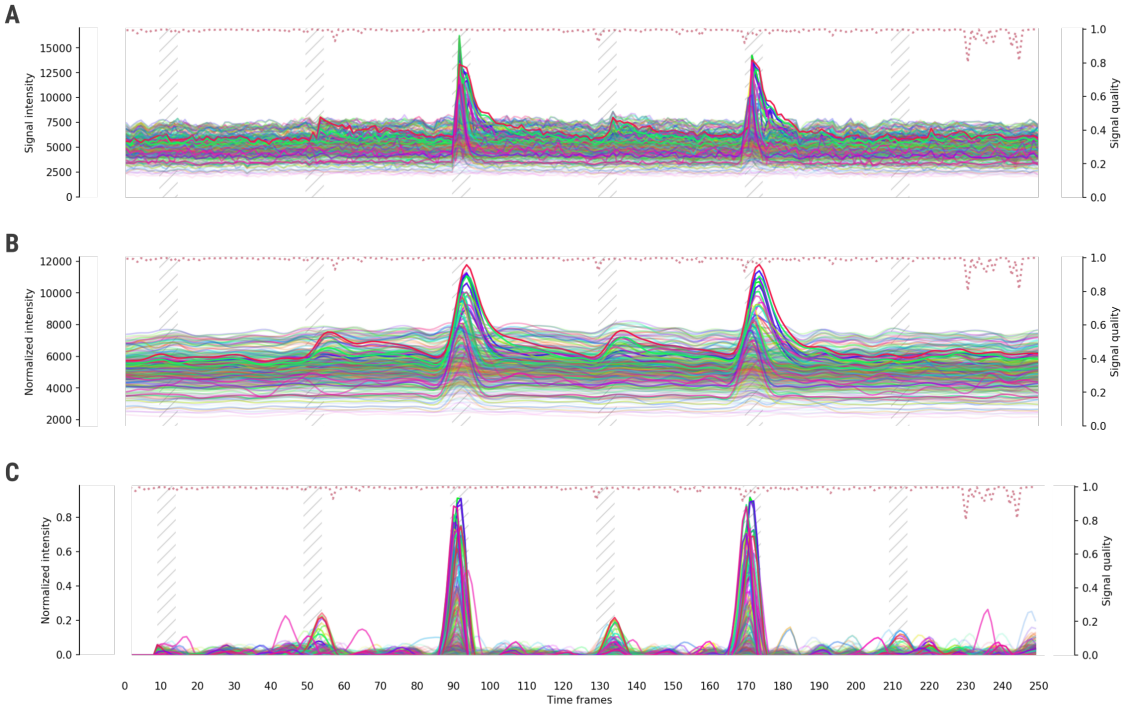

Figure 6.5: Normalization process for a naïve fly. Each line is the signal of an individual neuron, and the opacity is proportional to the standard deviation of the signal. (A) The raw signal, measured for 432 neurons. (B) Frequency filtered signal. (C) Signals after moving baseline normalization.

system to detect the problematic frames and interpolate the missing data from the neighborhood frames. We were then able to tessellate the 3D space using the detected nuclei as seeds, thus creating a volume in which we could measure the Ca^{2+} ions change of the individual neurons.

The raw data needed to be normalized, and this was done by a frequency filter followed by a base-line normalization. This allowed comparison of peaks between different flies, opening the way for a series of possible analysis, explored in the following Chapters.

Chapter 7

Memory traces

To observe attentively is to remember distinctly

Edgar Allan Poe

The methodology explored in the previous Chapters allowed us to observe in an automated way the whole Mushroom Body, at the single neuron level, while the fly experiences an stimulus. For the best of our knowledge, this has never been accomplished before. This opens several opportunities to better understand how the brain process information, and how long term memory is stored. The ability to measure the actual memory traces directly from the individual neurons grants us the ability to solve in a quantitative way open questions of the neuroscience community: does learning involves an increased response from the Kenyon cells ? Does it involve the recruitment of new neurons ? How is the memory trace distributed spatially in the brain ?

7.1 Responsive neurons

State of the art work regarding the memory in the *Drosophila's* Mushroom Body make use of manually selected neurons that are responding to the stimulus, identified by a region of interest defined by the user [135]. This creates an important margin for biased results, as the users could be cherry-picking the signals they want to analyze.

Here, we made an automated detection of every neuron in the Mushroom body (strictly speaking, every resolvable neuron. For details check Chapter 4). This rules out the human interference from the data analysis, but brings a small issue: as expected, the majority of the neurons were not responding to the stimulus, remaining at the level of the background noise. Any sort of comparison between the test and control groups would be affected by this as, in fact, the interesting neurons (the ones that respond to the stimulus) are the outliers of the distribution. The distribution of all neurons can be seen on Figure 7.3A.

To tackle this issue, we needed an automated way to identify the responsive neurons from the ones that remained at the level of background signal. A threshold could be set as a filter, so that only neurons with a peak higher than the defined threshold within the octanol stimulation window would be kept for the future steps of analysis.

Figure 7.3A displays no obvious bimodal distribution, making a precise assumption of the threshold value not evident from the data. Thus, we kept the threshold at an arbitrary value of 10%, based on the expected increased response of GCaMP6f [117] and the noise baseline observed from the data.

The usage of this threshold gave us the distribution observed at Figure 7.3B. Note that now there is a more clear separation between the peaks from the two AIR and OCT windows, indicating that we are selecting a sub-set of the ensemble that is responding to the stimulus.

7.1.1 Spacial distribution

Following the literature, responsive neurons from the mushroom body should be organized in a stochastic way [158, 159]. A general characteristic of sensory systems is that dense representations by neurons tuned by the sensory periphery are transformed into sparse representations by neurons tightly fitting into deeper layers. More specifically, in the olfactory system, olfactory

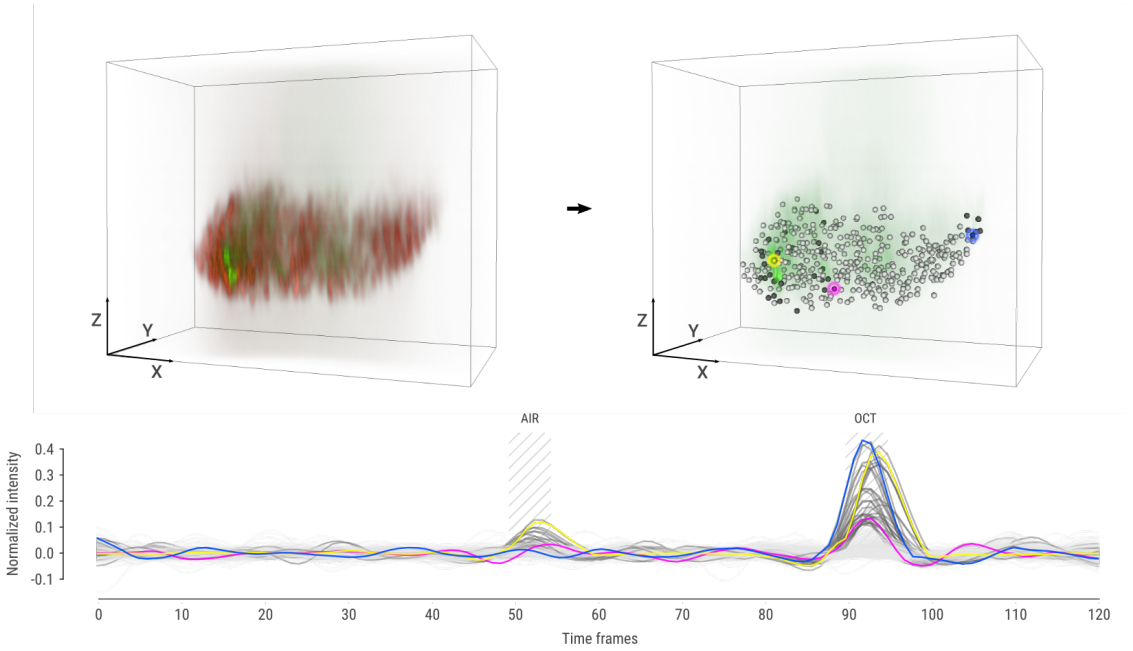

Figure 7.1: Tracks of responsive neurons for **unpaired control**. The volumetric reconstruction on the left shows the nuclei marker together with the GCaMP activity during the OCT response, while the volume on the right shows the detected neurons. Light gray spheres and lines show neurons that were not responsive, and dark gray indicates responsive neurons (for a 10% intensity gain threshold). Three neurons were highlighted in blue, pink and yellow to exemplify the signal in different parts of the Mushroom body. The plot shows the normalized signal from the individual neurons, indicating also the stimulation windows.

receptive neurons (ORNs) respond to a wide range of different odors [160] and synapse on projection neurons (PNs) of the antennal lobe within structures called glomeruli . At this layer, synaptic and circuit mechanisms produced even larger tuning curves in PNs [161] while making the responses of different glomerular channels more independent from each other [162]. Thus, in the antennal lobe, the identity of the odor is represented by a dense code consisting of only about 51 different PN types.

Hence, the detected responsive neurons were likely to be uniformly distributed through the Mushroom body. This can be verified in two examples shown in Figures 7.1 & 7.2, in which the responsive neurons are shown in dark gray, and the non-responsive in white. Tracks corresponding to each neuron are also shown.

7.2 Consistency of response

It is well known from the literature that if the same stimulus is presented different times to the fly, the same set of neurons should respond [135]. The idea behind this fact is that the group of neurons that respond to the stimulus is the spatial representation of that particular set of inputs to the mushroom body. So, when receiving the same stimulus for the second time, the same pattern of activation should emerge in the Mushroom body.

As our system allows the tracking of signal from all the individual neurons, this assumption can be verified. We expect the same (or, at least, a very similar) set of neurons to respond when the OCT stimulation is presented twice.

Experimentally, the fly received a stimulation sequence in the following order:

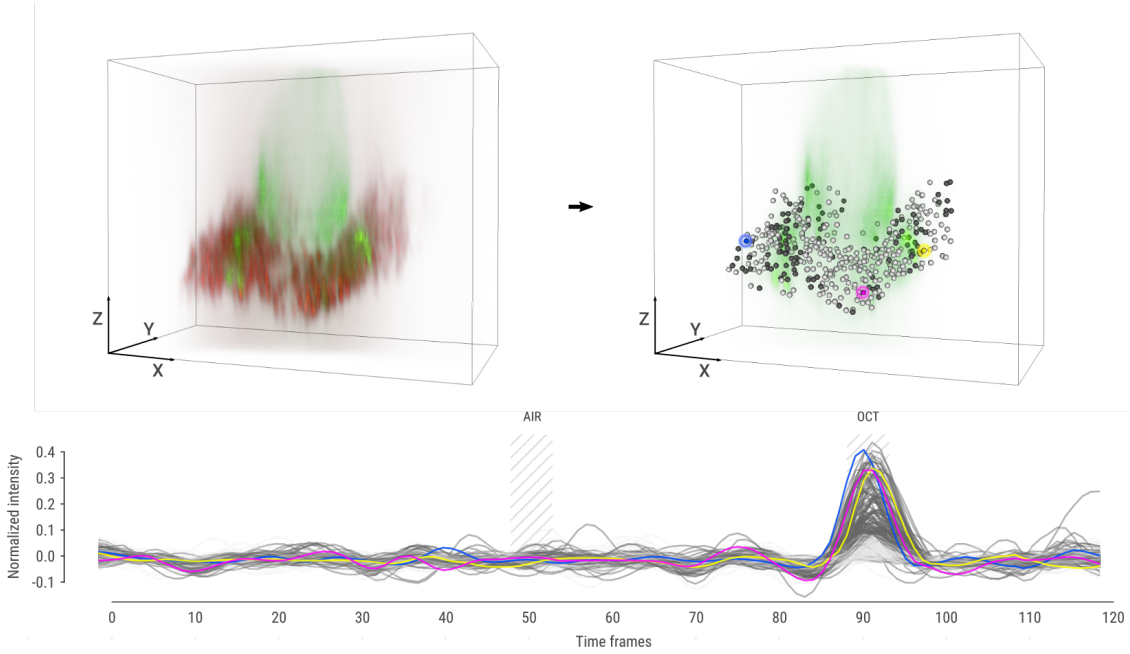

Figure 7.2: Tracks of responsive neurons for **paired conditioning**. The volumetric reconstruction on the left shows the nuclei marker together with the GCaMP activity during the OCT response, while the volume on the right shows the detected neurons. Light gray spheres and lines show neurons that were not responsive, and dark gray indicates responsive neurons (for a 10% intensity gain threshold). Three neurons were highlighted in blue, pink and yellow to exemplify the signal in different parts of the Mushroom body. The plot shows the normalized signal from the individual neurons, indicating also the stimulation windows.

1. No stimulation (S)
2. Only air (A)
3. Octanol stimulation (O)
4. Only air (A)
5. Octanol stimulation (O)
6. No stimulation (S)

This sequence, SAOAOS, allow us to verify if the response is really caused by the odor, as we have the air stimulus intercalated with the octanol. To compare the responses from the different octanol stimulations, first we identify the set of responsive neurons, the ones that have a peak response higher than 10% for the normalized signal.

Afterwards, the set of signals is treated as a n dimensional dataset, where each dimension is one responsive neuron and each feature the peak value of the given neuron within the window of stimulation.

This creates, for each stimulation window from SAOAOS, a n dimensional vector that represents the current state of activity of the brain. Thus, on this space, the proximity means similar activity pattern of the brain.

A distance matrix between the vectors of each stimulation window can be done, by calculating the distance between each pair of vectors u and v. As measurement, we use a *cosine distance*, defined as:

$$1 - \frac{u \cdot v}{\|u\|_2 \|v\|_2} \tag{7.1}$$

Where $u \cdot v$ is the dot product of the two vectors, u and v. By using the cosine distance, we limit the effects of the high dimensionality on the space [163]. More common measurements, as an Euclidean

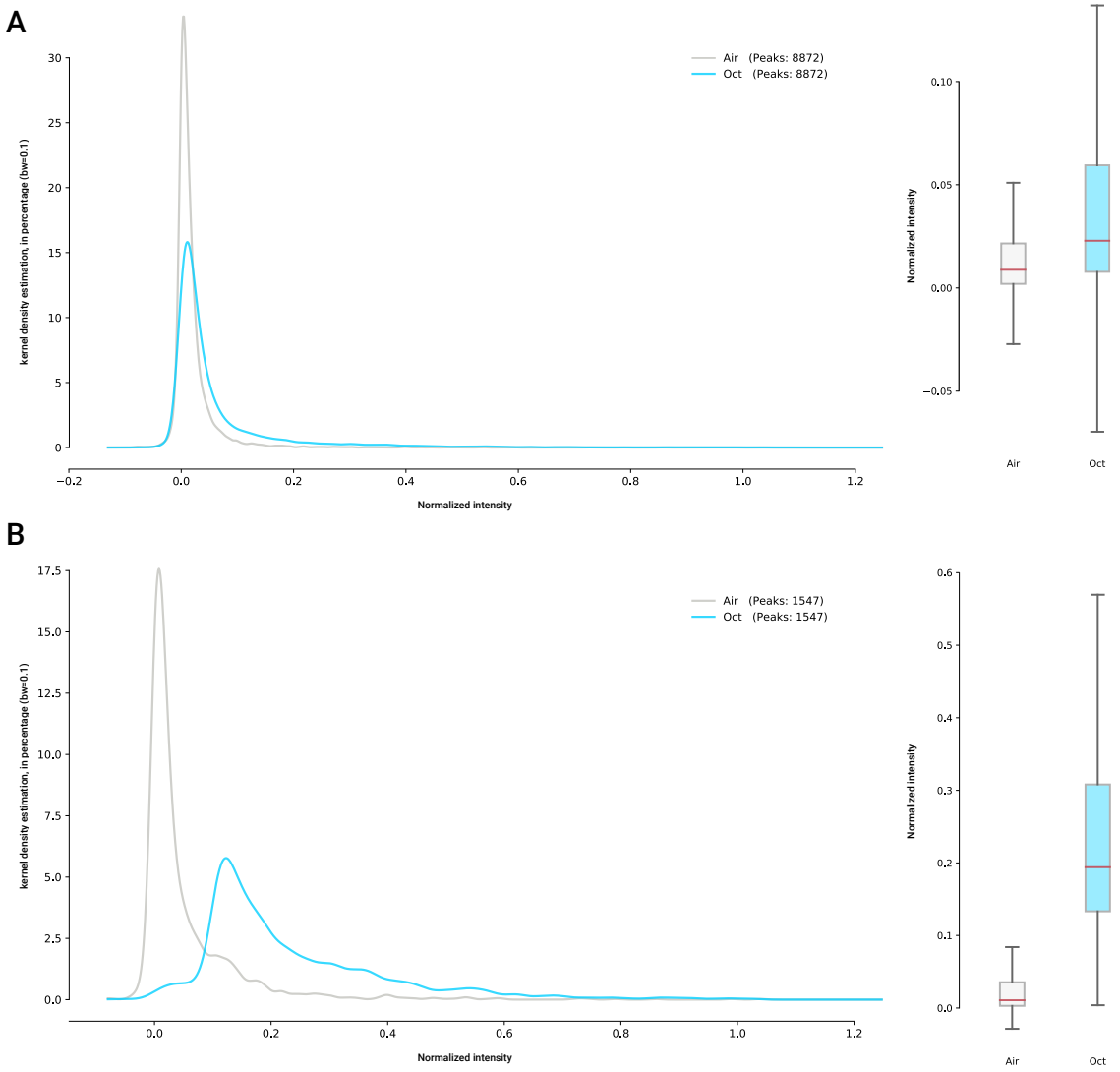

Figure 7.3: Distribution of peaks for air and octanol windows, for all flies with paired conditioning of the dataset (A) Without any threshold, the distribution of intensities is similar in both windows, being just sightly slanted for the octanol (blue) because of the few responsive neurons. (B) Distribution showing only the neurons with normalized peak higher than 0.1, making a clear separation between both distributions.

distance for example, loose meaning on higher dimensions becauseof the *curse of dimensionality* [164]. The resulting signals and matrices for two examples of flies (control and test groups) can be seen in Figure 7.4.

It is possible to conclude that similar patterns of activation of the brain are seen when the fly experiences the same stimulus, as the distance between the two OCT is relatively small when compared to the rest of the acquisition.

7.3 Responsive neuron count

The single neuron tracking allows us to measure, in a robust and non-biased way, the amount of neurons that respond to a given stimulus. By counting the number of neurons that respond above the 10% threshold, we can make the distribution shown in Figure 7.5, that shows a significant difference between the Paired conditioning and Unpaired control groups (p-value: 0.001421, Mann-Whitney two-sided test).

This rather simple test is only possible because of the developed methodology, and brings, in a quantitative way, the answer to a fundamental question: The formation of Long-term memories within the Mushroom body **is** dependent on the recruitment of new neurons. Further implications of this discovery will be discussed within Chapter 8.

7.4 Neuron intensity

Interestingly, intensities of responding neurons were not different between the paired and unpaired groups, which could be one of the mechanisms for storing the memory traces within the Mushroom body. The results of this analysis can be seen on Figure 7.6

This conclusion can only be brought by the single cell analysis. In case this same experiment were to be verified by a measurement of global intensity change in the whole MB, the conclusion would be that, for the paired conditioning, there was an increase in intensity. But what truly happens is that more neurons are being recruited, with the same level of intensity. Further aspects will also be discussed within Chapter 8.

7.5 Signal cross-talk

It is also important to verify whether the additional neuron count of the octanol paired group could result from a cross-talk of signal.

If the intensity of responsive neurons increased after conditioning, the increased GCaMP signal could scatter to the neighborhood, causing a signal crosstalk. This would mean that additional signal could be detected in an area in which it would be accounted for a different neuron. Thus, if this neighbor neuron also surpass the threshold level, the neuron count would artificially increase.

To test for this possibility, we identified the signals of neighboring neurons closer than 2 times the diameter of the soma and only the neuron with the highest response was kept for neuron count. With this filter applied, neuron count for the octanol paired group was still significantly higher compared to the unpaired group, while MCH paired and unpaired group did not differ in neuron count (Figure 7.7).

7.6 Conclusion

The comprehensive 3D tracking of single neuron activity allowed us to explore the memory traces in the mushroom body in ways that weren't possible before.

By measuring the signal of every neuron through time, we could verify that the same activity pattern of the brain emerges when a stimulus is presented twice to the same fly, which confirms the current understanding of how the Kenyon cells receive their inputs.

Regarding the intensity level of response from the single neurons, we can conclude that the long-term memory formation has no impact on it. For the two groups analyzed, unpaired control and paired conditioning, no statistical significance was observed for the intensities.

However, flies from the paired group showed a significantly higher number of responsive neurons, leading to the conclusion that the long-term memory formation implies neuron recruitment.

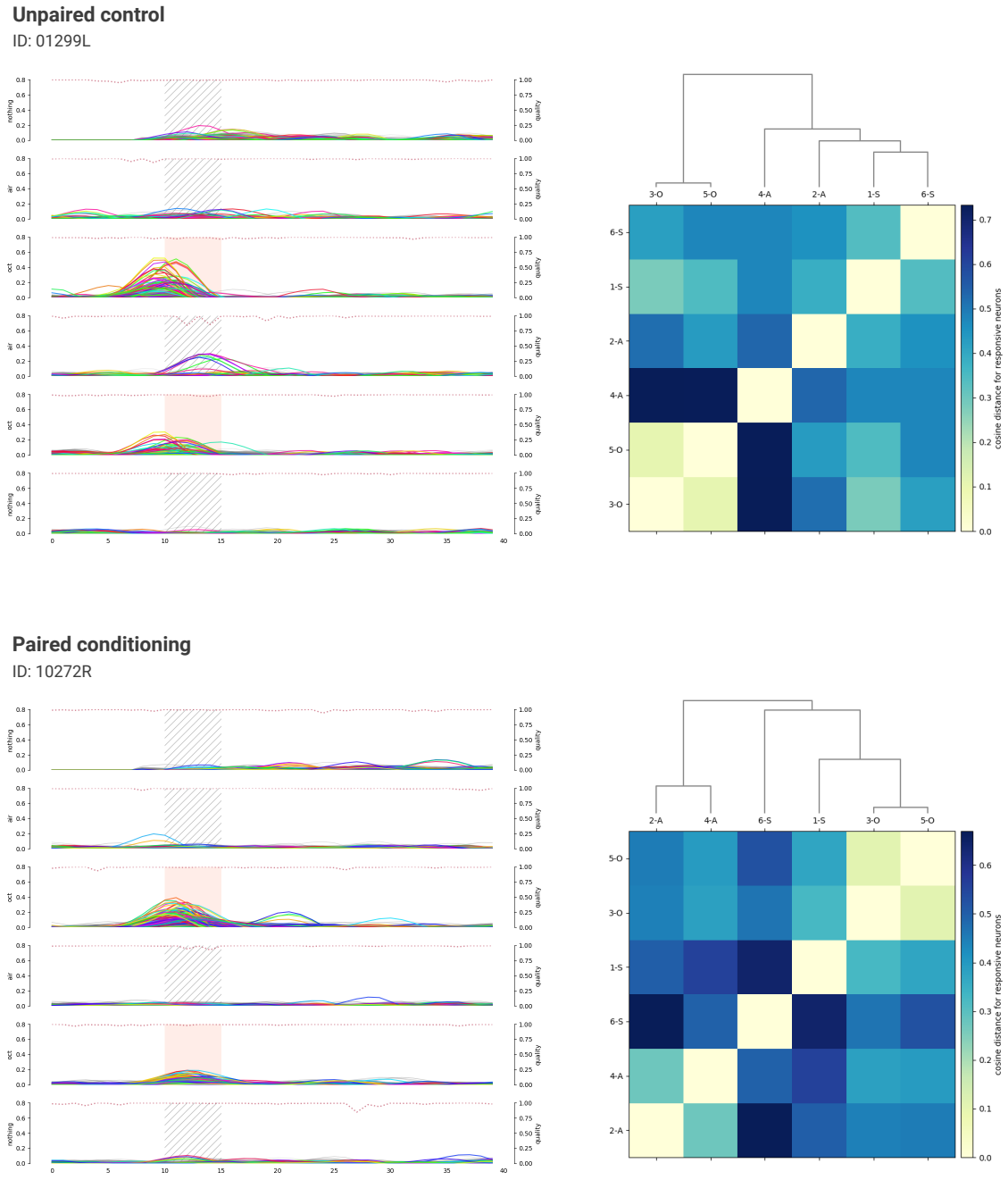

Figure 7.4: Consistency of response to OCT, shown for two examples of flies. On the left we see the tracks of individual neurons from a single experiment with sequence SAOAOS, where for visualization the tracks are split so that the alignment of the stimulation windows is noticeable. On the right we see the distance matrix for each case, having as labels a number representing the order of the stimulation (1 to 6) and a letter for the category. On the matrices is observable the proximity of both OCT stimulations, showing that a similar pattern of brain activation was measured.

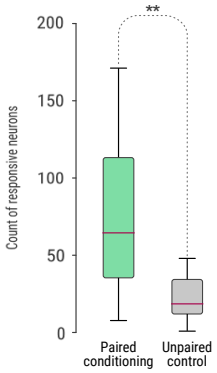

Figure 7.5: Count of responsive neurons, showing a significant difference between the Paired conditioning and Unpaired control groups (p-value: 001421, Mann-Whitney two-sided test).

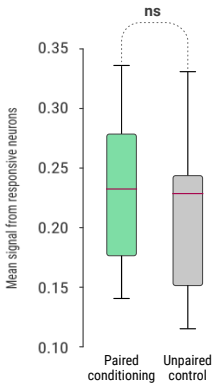

Figure 7.6: Distribution of mean signal for responsive neurons from the two groups, showing no statistical difference (t-test with p-value: 0.24848).

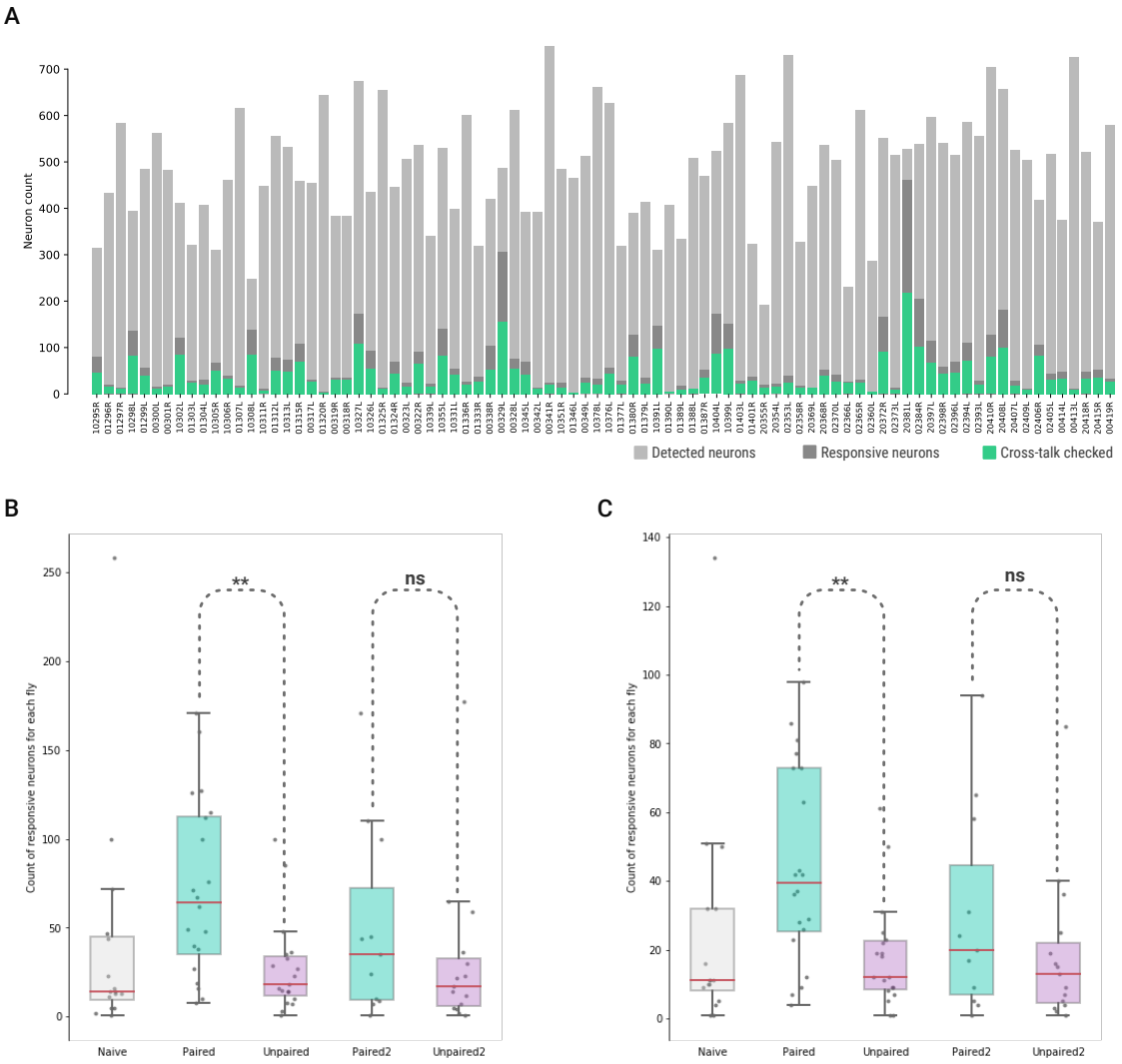

Figure 7.7: Verification of signal crosstalk for all the flies of the dataset. To verify the effects of crosstalk on our signal measurement, for every responsive neuron we checked the signal of the neighbours closer than 2 times the diameter of the soma, and only the highest of them was kept. (A) summary of the dataset, where light gray shows the number of detected neurons, dark gray the amount of responsive neurons (in average, 13.5% of total detections) and green only the neurons that passed the crosstalk check (in average, 62.9% of the responsive neurons). (B) Distribution of dataset for responsive neurons (dark gray in A) showing significant difference between the test group (p-value: 001421) and no significant different for the control group (p-value: 0.323919). (C) Distribution after the crosstalk check, on which the significance in test group is kept (p-value: 0.001890) and no difference for control group (p-value: 0.323753). For all cases, a Mann-Whitney two-sided test was performed.

Chapter 8

Conclusion

> *I am turned into a sort of machine for observing facts and grinding out conclusions.*
>
> **Charles Darwin**

Understanding the formation of long-term memories is a great challenge, and a large active field of research in neuroscience. The work presented on this thesis brings to the scientific community a new quantitative insight on how the brain is capable of storing long-term memories as, for the best of our knowledge, for the first time we were able to quantitatively measure, *in vivo* and through time, the total ensemble of neurons that forms the Mushroom body of the *Drosophila melanogaster*, while the fly experiences a memory recall.

From this quantitative analysis, we were able to achieve two important conclusions: Firstly, the paired conditioning of the flies results in the recruitment of new neurons for the representation of long-term memories. Secondly, this same process doesn't change the level of activity on the individual neronal level.

Those are straightforward conclusions, that wouldn't have be possibly drawn without the extensive methodology that was developed, both on the computational and experimental sides.

8.1 Main aspects

A few points distinguish our protocol from the current methodologies, giving us an unique setting on which new insights can be achieved.

8.1.1 Single cell analysis

One of the main contributions of the presented methodology when compared to the state-of-the-art approaches, is the fact that we are able to detect the signals at the single cell level. While the usual approach within the field is to measure the signal from a limited number of cells,

8.1.2 Automated detection

Another point that is a strong advantage of the methodology here proposed is the fact that the process is fully automated. Other state of the art methodologies uses manual or semi-automated procedures for detecting the neurons [135], which might cause biases and strongly decreases the throughput of the analysis.

8.1.3 Parallelization

The whole process can run independently for each fly, making a parallelization possible. This is important, as it allows us to process the complete database (more than a hundred flies) in a relative small time, usually of one to two days for a complete analysis.

8.1.4 Open Source

No great achievement can be done by one person alone, and this is not different for the work presented here on this thesis. The methodology we present was only made possible because it is based on free & open-source tools that compose the elemental bricks needed to construct the software. Thus, we also make available to the community all that was here de-

Figure 8.1: All the code needed for the analysis presented on this thesis can be found on GitHub, on the address https://github.com/biocompibens/memotrack or by scanning the QRcode above.

veloped, on the GitHub online repository at the address https://github.com/biocompibens/memotrack. Besides the analysis itself, the presented code also generates as report the majority of visualizations seen throughout this thesis.

8.2 Data acquisition

One of the biggest challenges encountered throughout this Thesis was the proper acquisition of data that could sustain our inquiries.

The majority of current research done in long-term memory of the Mushroom body make use of a single 2D plane, usually acquired via 2-photon microscopy. This provides an image with high spatial resolution, but lacks the temporal precision needed for the analysis when capturing the whole 3D structure. Thus, we make use of a confocal spinning disk for the acquisition of 5 dimensional (XYZCT) image stacks.

Also, the preparation of the flies for image acquisition differs in some points from the previously used protocols. To keep the physiological responses as close as possible from the real operational conditions of the brain, two main factors were important, and made our method different from the others.

Firstly, we avoided the use of anesthetics procedures, as CO_2, before the dissection. This increases the difficulty of the micro-surgery, but minimizes the possibility of having alterations on the normal behavior o the brain.

Another important aspect is that we don't make use of the rupture of muscles to diminish the brain movement. This also minimizes the possibility of having artifacts on the acquired signal, but the increased movement makes so that the tracking of neurons is more challenging.

Since the beginning of the project, counting the stages of standardization of the method, 292 flies were imaged, resulting in about 2.5 TB of raw data. About half of the initial data was used for the standardization of the dissection and odor stimulation protocols, and could not be used for the final analysis.

8.3 Detection & tracking

The relative low spatial resolution of our data, and the fact that we aim to handle the whole 3D structure of the MB, while still having the resulting movements of the *in vivo* acquisition, made the detection and tracking of every neuron particularly demanding.

When testing current state of the art methods for nuclei detection, we couldn't obtain a suitable precision. The high density of objects, together with the large anisotropy of the data, made necessary the development of a methodology designed specifically for the characteristics of our data.

For the final dataset, composed of 122 flies and used for the final analysis, our method detected an average of 408 neurons per Mushroom body (as seen

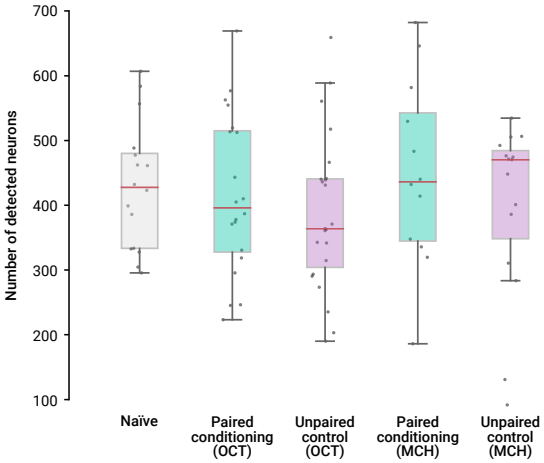

Figure 8.2: Distribution of detected number of neurons for each fly, between the different test groups, showing no significant difference between datasets. This allow us to verify that the difference in the count of responsive neurons is not related to the total number of detected neurons.

in Figure 8.2). Despite being well known from the literature that the MB should have about 2000 Kenyon cells, we proved, by means of synthetic images and manual annotations, that our method is close to the actual limit of objects that can be identified, regarding the resolution of our data. The details can be found in Chapter 4.

We made sure that, besides the incomplete set of detected neurons, all the signal response was measured by means of a 3D tessellation of the space surrounding each detection. Furthermore, because the number of responsive neurons is usually much inferior than the total set of 2000 cells, associated with the fact that the response is known to be sparse, limited impact can be expected by this shortage of detections.

The tracking stage can be also understood as the process of giving a label to each one of the neurons, which is fundamental if we aim to analyze their individual signals.

Most of the current tracking methodologies are adapted for tracking spots that have an important displacement through space, with a relatively low dense set of objects. The common tracking algorithms are also usually set to deal with splitting tracks or objects crossing each other paths. None of these assumptions were true in our dataset, where the density of objects is relatively high, and the movement is the result of a more global deformations of the brain, and not the individual displacement of the neurons. This created the need for specific tracking methodology, that we developed to handle these peculiarities, as explained during Chapter 5.

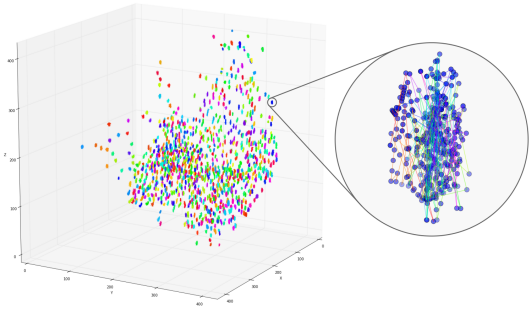

Figure 8.3: Result of the tracking for one Mushroom body. On the left, each color shows one track (labeled neuron) and each cloud is the ensemble of positions of that given neuron through time. On the right we see the detail of one of the detected neurons, with the tracks linking the positions through time.

8.4 Memory traces

By getting the correct detection and tracking of the neurons from the Mushroom body, we were able to measure the response of the flies to the odor stimulation.

We used two groups of flies to identify the memory traces: for the first group, that received a paired conditioning, flies were trained to associate the odor to an electroshock, by receiving the two stimulus together. The second group was the unpaired control, which also receives both stimulus, but with a time delay between them, in a way that the association was not made possible.

These groups allowed us to investigate which are the changes in neuronal activity that encode the memory traces representing the association between odor and electroshock. A direct comparison between brains of flies from the two groups was not directly possible, as the axonal inputs of the MB are spatially arbitrary. Thus, spatial correlations of response wouldn't reflect the actual differences between groups.

However, global comparisons are possible. For example, the memory trace can be encoded in newly recruited neurons, or in a increased response of the same set of neurons. Our methodology, allowing the measurement and identification of the subset of neurons that are are activated by the odor stimulation, could identify that, in fact, the long-term memory stored within the mushroom body is the result of the recruitment of a new set of neurons exclusively. Regarding the intensity of response, we could verify that the activity level of individual neurons remained unchanged between the two groups. This discovery, beyond the method itself, is a major contribution of this thesis as, for the best of our knowledge, no other research group so far was able to achieve this sort of response quantification from the total ensemble of neurons from the Mushroom body.

8.5 Overview

Technically challenging, the *in vivo* single neuron analysis of the whole Mushroom body of the *Drosophila melanogaster* was made possible by the methodology developed through this Thesis. Besides revealing that long-term memories are encoded by the recruitment of new neurons, we make the computational tools needed for this analysis available to the scientific community, opening the possibility for new findings on how memories are organized within the brain.

Chapter 9

Perspectives

Carry on my wayward son,
For there'll be peace when
you're done.

Kerry Livgren
(Kansas)

The work developed in this thesis open the way for several improvements in the current state of the art for the study of memory. In this Chapter we'll discuss some principles of improvement for the method, as well as some future applications that could bring other insights on the memory formation.

9.1 Back projection

The precision of the detected nuclei position is of great importance for the final accuracy of the measured signal from the Kenyon cells in the Mushroom body. It is from these positions that we create the individual volumes for the measurement of neuronal activity, so imprecise positions would lead to wrong signal measurement.

However, the precision of the detection is limited by the actual resolution of the data. Because of the PSF and close distance between the nuclei, we can only assume that the detected position had a probability of being the true position of the nuclei.

During the nuclei tracking stage, described on Chapter 5, we made use of a registration procedure to minimize the movements of the brain. Ideally, after the registration step, every detection of a given nuclei should match perfectly in space, forming a single spot. In reality, we observe that the detections form a cloud with characteristics of a normal distribution. This cloud of points is in fact a multiple sampling of the same nuclei through time, it is possible to assume that the center of the cloud corresponds to a more precise estimation of the nuclei position in this registered space.

The registration procedure purpose is only to label the neurons. Once each point is tracked, the labels are passed to the coordinates of the original detections. This way we completely lose the estimation of the real position that could be done via the centroid of the 3D cloud in the registered space. We hypothesize that it is possible to use this information in a proccess we call **back projection**:

Since we can assume that the brain is an rather elastic and stable tissue, not allowing the free movement of the neurons (but only local deformations), the process would be constituted of the steps presented in Algorithm 3.

This process might be able to increase the precision of the detections. Initial trials were partially successful, only showing artifacts in regions where the obtained tetrahedron is almost coplanar, what interferes with the calculation of the barycentric coordinates.

9.2 Graph features

Although the process to obtain the brain responses with single neuron precision is rather complex, as described throughout this thesis, the final conclusions we obtain from it are based on two simple measurements: the count of responsive neurons and the intensity of the responses.

We predict that a more in depth analysis of the data can bring new insights on the way memory is spatially organized in

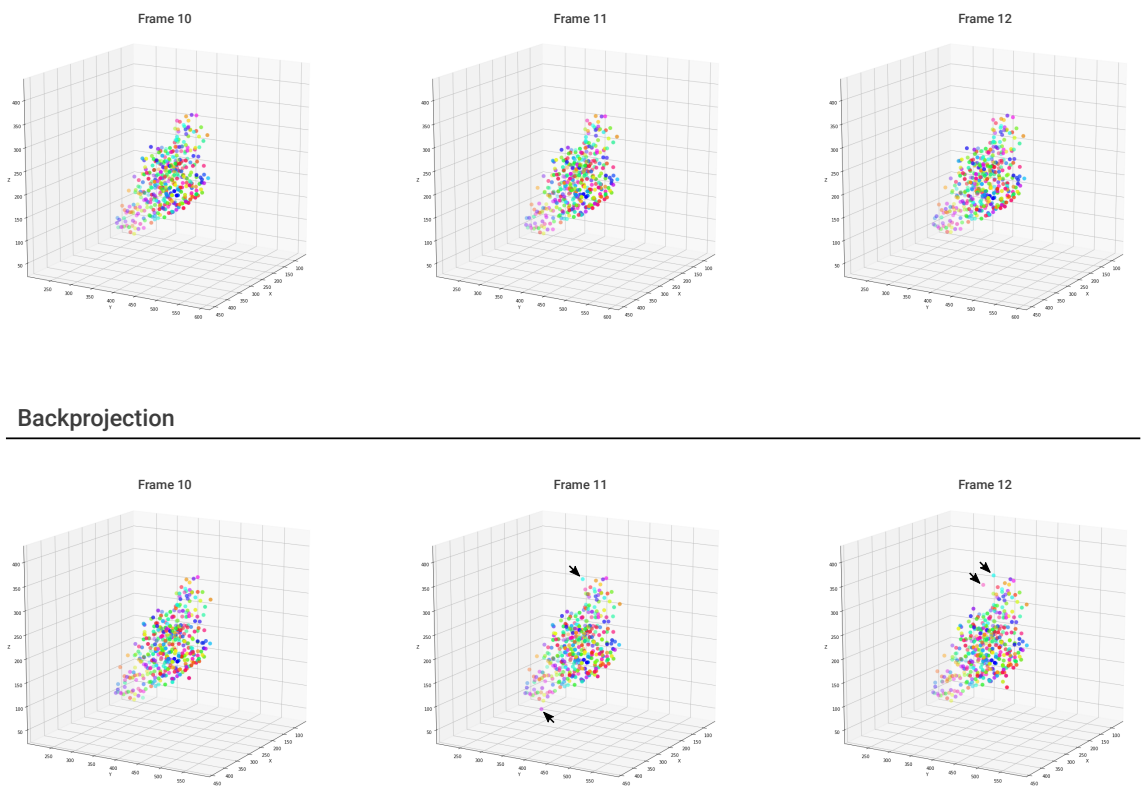

Figure 9.1: Initial trials for the backprojection algorithm. Black arrows indicate examples of cases on which the barycentric coordinates couldn't be precisely calculated, resulting in artifacts.

the brain. One of the ways we can begin to search for patterns is through the creation of spatial graphs from the detected neurons. From the graphs, having the response intensity stored on the edges or nodes, we could measure a set of features, that could lead to new insights on how the responsive neurons are organized. One example of how this graph can be build can be seen in Figure 9.2. Examples of three features extracted directly from the graphs can be found in Figure 9.3.

Especially interesting would be the possibility to compare the obtained features between different flies. A direct relationship of the patter of response between different individuals is not expected, but since the features obtained from the graph can be spatially independent, a direct comparison between two brains would be made possible.

9.3 Training under the microscope

All the work and data described within this thesis is based on the long term memory obtained from the flies. This means that initially the fly is trained and is able to construct the associative memory and, only afterwards a consolidation period it is submitted to the dissection and imaged for analysis.

One interesting alternative would be to actually see the activity of the neurons **during** the memory formation. This could lead to exciting discoveries on temporal patterns of activation between the Keynon cells that receive the projections from the antennal lobe and the ones that receive the aversive (shock) information.

To accomplish this, little would need to

Algorithm 3: Backprojection

input : Labeled dataframe, D_{initial}
output: Backprojected dataframe, D_{back}
$DistTree \leftarrow$ `BuildDistanceTree(`D_{initial}`)` ;
$t \leftarrow 0$;
repeat
  $Cluster \leftarrow 0$;
  repeat
    $Points_{closest} \leftarrow$ `GetClosestPoints(`$DistTree$, t, $Cluster$`)` ;
    $BarycentricWeights \leftarrow$ `GetBarycentricWeights(`$Points_{closest}$`)` ;
    $D_{\text{back}} \leftarrow$ `UpdateCluster(`$BarycentricWeights$, $Cluster$`)` ;
    $Cluster \leftarrow Cluster + 1$;
  until $Cluster < Cluster_{final}$;
  $t \leftarrow t + 1$;
until $t < t_{\text{final}}$;

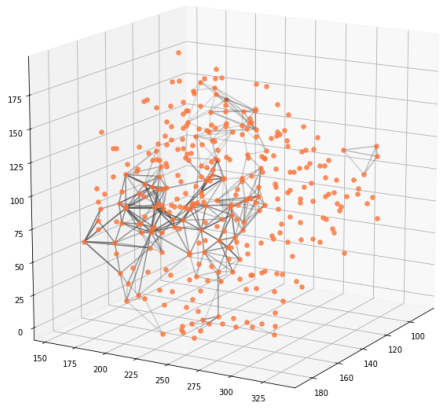

Figure 9.2: Example of graph built from the detected neurons. The edges are constructed using a Delaunay triangulation, and store as information the intensity of the responses (width of the edges). Edges with values lower than a threshold are pruned, resulting in a graph that represents the response from the brain to the stimulus.

be adapted on the detection & tracking methods. However, the process of image acquisition needs to be highly customized to support the delivery of electroshocks to the fly during the acquisition itself.

This is a great technical challenge, that the laboratory of Thomas Préat started to tackle together with Mélanie Pedrazzani, during her thesis work. A custom made chamber, as shown in Figure 9.4 was schematized. It would allow the delivery of electroshocks for conditional pairing with the odor stimulation. This way, it would be possible to see the fly's brain response while the association is being formed.

9.4 Genes knockout

From a genetic point of view, humans and the fruit fly have significant similarities, as about 60% of genes are conserved between the two species. According to a recent analysis, 77% of the genes associated with identified human diseases have a homologue in the Drosophila genome [165]. Thus, the *Drosophila melanogaster* is used as a genetic model for various human diseases including Parkinson's disease and Huntington's disease.

The system developed during this thesis allows the precise measurement of the neuronal activity during memory recall. Being so, it would be also possible to knockout or modify genes related to human diseases and better study how their actions change the activity patterns of

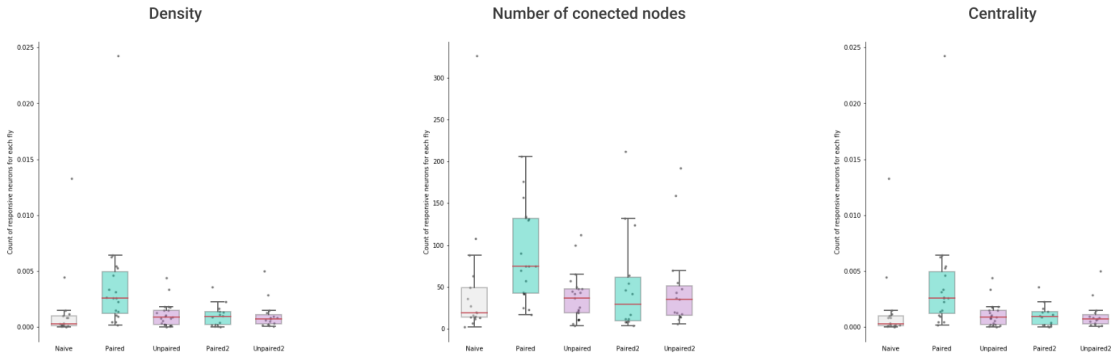

Figure 9.3: Example of three features extracted from graphs. Initial tests showed that features extracted directly from the graphs can lead to similar conclusions as the neuron count.

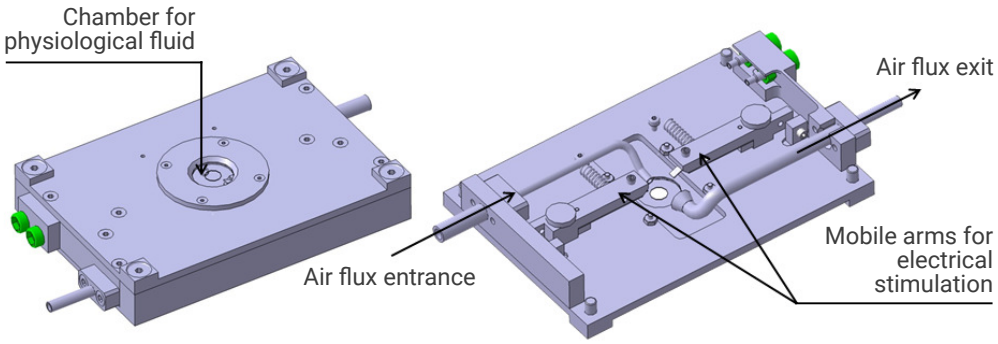

Figure 9.4: Custom made chamber for electroshock stimulation during odor delivery. This device would allow the paired conditioning of flies while the activity of the Mushroom body is being recorded. Image courtesy of *Mélanie Pedrazzani*.

neuronal activity within the brain.

Chapter 10

Annexes

SOFTWARE

Smax: accurate detection of packed resolvable objects in 3D fluorescence microscopy

Felipe Delestro[1], Mélanie Pedrazzani[2], Paul Tchenio[2†], Thomas Preat[2] and Auguste Genovesio[1*]

Abstract

Background: 3D spot detection tools are heavily used to collect positions of biological objects and extract quantitative information from 3D microscopy images. The fluorescently labeled objects of interest can range from tiny biological objects as individual proteins, viral particles or endosoms to much larger such as cell nuclei or parasites depending on the microscope resolution. While general approaches to spot detection showed some success, especially with diffraction limited objects, anisotropy of 3D microscopy image stacks and object specificity are almost systematically overlooked while non-obvious parameters tuning is often required. We show on some examples that those aspects can have dramatic and silent effects on the localization accuracy of resolvable, albeit densely packed, objects of similar size such as nuclei in a 3D tissue.

Results: in this work, we propose a tool that couple a straightforward anisotropy correction with an iterated maxima accumulation to detect position of similar objects in 3D image stacks. While a simple approach, we demonstrate quantitatively, using real and synthetic data, that it significantly outperforms state of the art methods to the task of detecting the position of a large number of densely packed objects in a 3D image.

Conclusions: while universal methods in spot detection achieved some success, we show evidences that a dedicated approach to the detection of the positions of densely packed objects is required to reach a satisfactory level of accuracy. Importantly, the proposed approach implemented in an open source package doesn't require parameter tunning but a single accessible physical input value: the approximated object diameter.

Keywords: 3D imaging; high density; nuclei; spot detection

Introduction

In 3D fluorescence microscopy, spot detection is widely used as one of the fundamental steps to extract quantitative information from biological scenes. Several methods and software programs have been proposed, and regularly compared, to achieve this task in a generic fashion [1–3]. Methods range from local background subtraction and linear or morphological image filtering to wavelet-based multiscale detectors (see [4] for an overview). To our knowledge, the most recent and complete comparison of methods for 3D spot detection was made in 2015 by Štěpka *et al.* [3]. In this review, two methods, the 3D morphological maxima (EMax) [5] and the Undecimated Wavelet transform product (UDWT) [6] were shown to combine a good accuracy with a low number of parameters. On one hand, the straightforward EMax introduced by Matula *et al.* simply consists in a denoising step using a 3D Gaussian smoothing followed by a morphological maxima transform. Local intensity maxima exceeding a given height are then retained. This approach requires two parameters: a "smoothing" σ and a "threshold" h (implementation available from `http://cbia.fi.muni.cz/acquiarium.html`). On the other hand, UDWT introduced by Olivo-Marin is a more sophisticated approach implemented in Icy. It is by far the most cited and therefore probably the most used by the scientific community for quantification. Briefly, a 3D undecimated wavelet transform of the image is computed, then non-significant wavelet coefficients of selected scales are discarded by a weighted automated thresholding. Spots are enhanced by computing the product of the denoised wavelet coefficients. This method requires two parameters: a set of "wavelet scales" matching the sizes of the objects we aim at detecting and a "sensitivity" parameter which cor-

*Correspondence: auguste.genovesio@ens.fr
[1]Computational Bioimaging and Bioinformatics, IBENS, ENS INSERM CNRS, PSL, 46 rue d'Ulm, 75005 Paris, France
Full list of author information is available at the end of the article
†PT deceased in July 2015

responds to the thresholding weight (implementation available from `http://icy.bioimageanalysis.org/plugin/Spot_Detector`). As assessed by their performance in recent comparison [3], both methods can be considered as state of the art in biological spot detection.

Note that considered objects to be detected can be of very different nature and their size can range from under-resolution scales such as in the cases of proteins, viral particles or endosoms to much larger resolvable scales such as in the cases of nuclei or parasites whose size are often higher than the microscope resolution. However in practice, the same algorithms are blindly used by end users whatever the objects, because there is necessarily a scale for which any of those objects can appear as a fluorescent blob. Despite of the variability of objects types and properties, the aforementioned approaches showed some success and provides a good solution especially for applications where inter objects distance is close to the resolution of the microscope [7, 8] or when the objects are large and distinguishable while their number is relatively low [9]. They are also useful when the precision of the objects' position is not crucial to reach the final aim. This is the case for instance when those positions are used for initializing further cell segmentation algorithm such as the seeded watershed [10] to detect nuclei or cell contours. Then, in this case, the final result is robust to slight variation in the seed location and possible inaccuracy in the determination of the last has little consequence on the final aim.

However, many applications still require the spot detection to provide precise location. This is the case when spot positions are further used to construct tracks of objects over time in order to compute dynamic quantities such as speed or diffusion coefficient [11]. It is also the case when the aim is to extract precise and individual fluorescence emission over time of another marker from a densely packed set of nuclei, as when quantifying individual neuron activity for instance. In practice, while testing the two best available tools previously described on 3D image stacks containing a high number of packed objects, we observed large positional inaccuracies. Those inaccuracies were mainly introduced by two factors. First, in most dataset, z resolution is lower than the x,y resolution. While obvious, this aspect is in practice loosely taken into account by most tools. One of the reason may be that the consequence on spot detection become apparent only when the density of spots is high. This is also an effect that was not properly estimated in recent reviews because, in these works, 3D spots in synthetic images were generated along x-y rather than on top of each other in the z direction [3, 12]. Second, in available tools, parameter settings is often overlooked and left to the user choice while their values can drastically change the final results. However, the aim of object detection is to obtain the positions of every object in the image rather than letting the user fine tune parameters to select a subjective set of objects.

Here, we propose a method that addresses those two aforementioned issues in the context of a large set of densely packed resolvable objects (see Figure 1 for an overview and Methods for details). "Densely packed" means that objects are close to each other, including in the z direction. "Resolvable" means that distance between objects is supposed to be above the resolution of the microscope in x/y directions as we do not claim to solve the case where those objects would not be resolvable. However, some objects, resolvable in x/y directions, may not be resolvable in the z direction. Those hypothesis are typically met when imaging a very large number of nuclei in a 3D living tissue over time with a fluorescent microscope. Indeed, in this case, technical constraints as the use of a spinning disk microscope, impose detection of thousands of 3D nuclei of similar size in a 3D volume at a low resolution.

Results

Smax improves object detection accuracy

The proposed method was compared to state of the art using both annotated ground truth and synthetic datasets. Figure 2 reports that all methods performed similarly well when objects were spread and clearly distinguishable. In contrast, the proposed approach enabled to obtain significantly better results on both real and synthetic data sets when a large number of nuclei or centrioles were packed together in a full 3D tissue. In particular, a large amount of objects were missed by the UDWT and eMax methods.

Smax requires a single physical measurable parameter

An advantage of the proposed method is that it requires only a single parameter from the user. Furthermore, this parameter is a physical quantity: the average diameter of the object we aim to detect. This value can be easily estimated from the data by computing the Full Width at Half Maximum (FWHM) of a Gaussian fit on the average profile of a set of randomly chosen objects (see Figure 1c). This is typically the way empirical Point Spread Functions (PSF) are constructed albeit with under resolution beads while our approach is typically suited to packed objects that can be distinguished.

Smax can capture slight variations in size

The method we propose is meant to be used to detect a large set of packed objects of similar size. By similar size we mean that there may be a slight variation in the population of object size around the expected value but its variance is assumed small. This is the case for instance for 3D nuclei: they don't have all the exact same size. This slight variation is captured by scanning a tight range of values around the specified diameter. Filters that approximately match a nucleus size will produce maxima in a close vicinity of each other, thus producing a signal accumulation that can be clustered in an ultimate aggregation step (see the Methods section for more details).

Discussion

Unbiased comparison using parameter scanning

The sole parameter input in our method, the nucleus diameter, is unambiguous and can be easily estimated. In contrast, in alternative methods, the choice of parameters is not systematically obvious or related to a physical entity. For instance, there is a"sensitivity" parameter in the Icy spot detector plugin that is non straightforwardly related to a quantity that could be estimated, and therefore this parameter requires tuning by the user. In order to ensure that an arbitrary choice of parameters could not unfavor the other methods in our systematic comparison, we scanned all combinations of parameters and selected the one that maximized the Jaccard index. The results are summarized in Figue 3. Note that knowing the ground truth is required to compute the Jaccard Index. Therefore, in turn, this approach disfavored our own method as in real case scenario ground truth would obviously not be available and parameters would have to be manually set in a non optimal way. Figure 3 shows that Emax and UDWT with an optimal parameter settings were as accurate as our approach for unambiguous images with large nuclei. However, it also shows that whatever the parameter settings both methods performed poorly compared to the proposed approach in the case of images with a densely pack set of objects.

Impact of anisotropy correction

Further analysis showed that a significant fraction of errors produced by the two other methods came from inaccuracies in the Z direction and that correcting anisotropy prior using those methods could increase the accuracy (see Figure 3). However, correcting anisotropy alone is not sufficient to reach the level of accuracy of Smax. In order to check what was the part of improvement brought by the anisotropy correction alone we applied it prior using the other methods. Note that, as we recalled earlier, these approaches do not propose such an option. So we simply computed an interpolated image of all datasets prior running another complete parameter scan for both existing methods. The results compiled in Figure 3 shows that in the case of eMax it systematically improves the results for the five datasets while the improvement is less obvious in the case of UDWT for which results get worse for the *C. elegans* embryo image. Indeed, in this case, interpolating seems to produce additional false positive. In any case the results never reach the accuracy obtained by the proposed approach.

Restrictions of the proposed approach

Smax is not applicable to any type of object. Specifically, it has two limitations: it can not be applied in cases where other type of structures, as filaments for instance, would be present and it cannot either be applied in case objects are of obviously various size. Smax assumes that the image is made of a foreground that mainly consists of a packed set of quasispherical objects of similar size lying on a possibly noisy but rather uniform background. However, this case should encompass a large set of applications as fluorescent stain are in principle specific to a given protein or organel.

Conclusions

Precise estimation of objects positions in cell tissues is of great importance to the field of bioimage analysis. In this paper, we demonstrated that some generic methods, by overlooking the anisotropy of image stack, ignoring the object specificity, and allowing for ad-hoc parameter tuning, could produce poor results. We propose a method with a single meaningful parameter that can be easily estimated and we show using manually annotated and synthetic datasets that it significantly outperforms existing methods to detect a large set of packed nuclei or centrioles. We demonstrated quantitatively that this approach is more relevant than generic methods for a set of applications of interest to the bioimaging community.

Methods

Spot detection algorithm

3D stacks in confocal microscopy are made of series of 2D image acquisitions. This usually results in a 3D image with a lower resolution in the z direction (axial to the acquisition). This lower resolution is partly due to the fact that the distance between the acquired 2D images is always higher than the pixel size in the x and y directions. It is also due to the Point Spread Function (PSF) of such an optical system that is typically wider in the z direction than in the x or y directions.

A simple but crucial solution to this anisotropy issue consists in using the acquisition metadata and a

cubic spline interpolation in the z direction to generate intermediary plans to obtain voxels with equal size on x, y and z directions. Filling the missing data with synthetic interpolated plans does not bring additional information but makes possible a proper use of isometric 3D kernel and neighborhood in the following image analysis steps.

Following this anisotropy correction, a standard deviation σ is computed from a diameter value provided by the user. For that purpose, it is considered that this diameter is ideally obtained from the Full Width Half Maximum (FWHM) of a Gaussian that would be fit on an average spot intensity profile (see Figure 1c). Therefore, σ is reversely obtained using:

$$\sigma = \frac{diameter}{2\sqrt{2\ln 2}} \quad (1)$$

This value can be divided by the pixel size in case the diameter is provided in μm.

A bank of 10 Gaussian filters that span $[\sigma - \frac{\sigma}{2}; \sigma + \frac{\sigma}{2}]$ is created to detect slight variations of size around the average nucleus diameter provided. The number of filters is set at 10 because we observed that for most combination of spot sizes and noise levels related to real applications, Jaccard indices were not improved above 3 to 5 filters in the bank, depending on datasets, as shown by Figure 4 for one of our synthetic 3D stack. Therefore, a higher number would in most cases increases the processing time without improving the precision. Figure 4 also illustrates that Smax is less accurate on a dataset with a higher variability of object sizes. For each filter, local maxima are detected and collected using a $3 \times 3 \times 3$ spherical neighborhood.

At this stage, for each filter, the local collected maxima are produced by actual bright objects or by background noise. Therefore the distribution of intensities associated to maxima is most often bimodal. The two components of this distribution are then identified for each scale using a Gaussian Mixture Model (GMM) with a two components fit using the Expectation-Maximization algorithm. A threshold is defined as the value where both components are intersecting such as the maxima associated with intensities above this threshold are kept while the maxima associated with intensities below this threshold are discarded. This process offers a stringent denoising process independent for each filter (see Figure 1d2). Following this, all remaining maxima collected for each filter are accumulated into a single 3D array. As objects are supposed to be further apart than resolution, this array should contain local accumulations of maxima mostly in volumes that are about the size of a nucleus. Therefore, an ultimate 3D gaussian filtering using σ is applied. 3D local maxima from this filtred array are the final detections (see Figure 1d3).

Synthetic datasets

The synthetic images were generated using the foreground mask of an actual image stack. First, the isometry is corrected via interpolation on the axial direction. Then, a chosen amount of nuclei positions is uniformly sampled onto the foreground and relocated evenly using the k-means algorithm to ensure they are spread as nuclei and above resolution. After convergence, the center of each partition is dilated to the desired nucleus size (allowing slight variation). At this point the image is binary, so the heterogeneity of fluorescence is simulated by an additive Gaussian noise centered on zero on foreground voxels. The 3D stack is then convolved with the point spread function measured from the microscope on isolated micro beads. An additional glow is produced to better simulate the light scattering through the tissue, and subsequently a Poisson noise is applied to reach a chosen signal to noise ratio of 4 corresponding to the camera sensor (SNR is defined by the average signal intensity divided by the standard deviation of intensities within the synthetic nuclei only). Finally, to simulate the low resolution in the z axis, the stack size is downsampled back to the number of slices of the original image. Two synthetic images were used for evaluation, one with 50 large objects, based on a image of *C. elegans* embryo and another one with 2000 small and packed objects, based on *D. melanogaster*'s mushroom body.

Manually annotated images

The detection algorithms were also compared using manually annotated ground truth performed by two different people. The annotations were made in 3D, with the help of the Cell Counter ImageJ plugin (https://imagej.nih.gov/ij/plugins/cell-counter.html). It consisted in scanning the image visually and marking the center of each nucleus. In the case of the embryo image, where the nuclei are large and well separated, the annotation was straightforward as the distances between nuclei were larger than the nuclei themselves. On the other hand, the manual annotation of the mushroom body (MB) nuclei could contain a few mistakes as the nuclei were smaller and packed at a higher density, making the distinction between different nuclei in 3D visually challenging, especially on the axial direction (according to the literature, the MB can have up to 2000 nuclei[13]).

Accuracy evaluation

To evaluate and compare the accuracy of all the methods, a detection is considered a true positive when it falls within a sphere of the object size around each object position referred in the ground truth (note that if two objects are detected in the same sphere only one

is accounted as correct, the other is accounted as incorrect). As measure of accuracy we used the Jaccard index J, defined as:

$$J(D,G) = \frac{|D \cap G|}{|D \cup G|} = \frac{Tp}{Fp + Tp + M} \quad (2)$$

where D is the set of resulting detections of the method, G is the set of ground truth positions (from manual annotations or synthetic images), Tp is the true positive count (elements both in D and G), Fp is the False positive count (elements in D but not in G) and M is the missed detections count (elements in G but not in D). In case of a high amount of false positives (Fp) or missed detections (M), the Jaccard index will approach zero. Oppositely, in case of perfect match, the Jaccard index value is one.

Competing interests
The authors declare that they have no competing interests.

Author's contributions
FD and AG designed the method. MP, PT and TP designed the experiments and acquired the images. FD and AG wrote the manuscript. All authors revised the manuscript.

Acknowledgements
We thank Nathalie Spassky for the image of centrioles and Sara Alrawi for the images of *C. elegans* embryos.

Funding
ANR-10-LABX-54 MEMOLIFE, ANR-11-IDEX-0001-02 PSL*, ANR-15-CE32-0008-01 MemoMap and Fondation PGDG.

Availability of data and materials
Source code of Smax, example images and annotated ground truth to reproduce the results are available at https://github.com/biocompibens/smax

Author details
[1]Computational Bioimaging and Bioinformatics, IBENS, ENS INSERM CNRS, PSL, 46 rue d'Ulm, 75005 Paris, France. [2]Genes and Dynamics of Memory Systems, CNRS, ESPCI, PSL, 10 Rue Vauquelin, 75005 Paris, France.

References

1. Smal, I., Loog, M., Niessen, W., Meijering, E.: Quantitative comparison of spot detection methods in fluorescence microscopy. IEEE Trans. Med. Imaging **29**(2), 282–301 (2010)
2. Sage, D., Kirshner, H., Pengo, T., Stuurman, N., Min, J., Manley, S., Unser, M.: Quantitative evaluation of software packages for single-molecule localization microscopy. Nature methods **12**(8), 717–724 (2015)
3. Štěpka, K., Matula, P., Matula, P., Wörz, S., Rohr, K., Kozubek, M.: Performance and sensitivity evaluation of 3d spot detection methods in confocal microscopy. Cytometry Part A (2015)
4. Smal, I., Loog, M., Niessen, W., Meijering, E.: Quantitative comparison of spot detection methods in fluorescence microscopy. Medical Imaging, IEEE Transactions on **29**(2), 282–301 (2010)
5. Matula, P., Verissimo, F., Wörz, S., Eils, R., Pepperkok, R., Rohr, K.: Quantification of fluorescent spots in time series of 3d confocal microscopy images of endoplasmic reticulum exit sites based on the hmax transform. In: SPIE Medical Imaging, pp. 76261–76261 (2010). International Society for Optics and Photonics
6. Olivo-Marin, J.C.: Extraction of spots in biological images using multiscale products. Pattern Recognition **35**(9), 1989–1996 (2002). doi:10.1016/S0031-3203(01)00127-3
7. Genovesio, A., Zhang, B., Olivo-Marin, J.-C.: Tracking of multiple fluorescent biological objects in three dimensional video microscopy. In: Image Processing, 2003. ICIP 2003. Proceedings. 2003 International Conference On, vol. 1, p. 1105 (2003). IEEE
8. Arhel, N., Genovesio, A., Kim, K.-A., Miko, S., Perret, E., Olivo-Marin, J.-C., Shorte, S., Charneau, P.: Quantitative four-dimensional tracking of cytoplasmic and nuclear hiv-1 complexes. Nature methods **3**(10), 817–824 (2006)
9. Toyoshima, Y., Tokunaga, T., Hirose, O., Kanamori, M., Teramoto, T., Jang, M.S., Kuge, S., Ishihara, T., Yoshida, R., Iino, Y.: Accurate Automatic Detection of Densely Distributed Cell Nuclei in 3D Space. PLoS Computational Biology **12**(6), 1–20 (2016). doi:10.1371/journal.pcbi.1004970
10. Wählby, C., SINTORN, I.-M., Erlandsson, F., Borgefors, G., Bengtsson, E.: Combining intensity, edge and shape information for 2d and 3d segmentation of cell nuclei in tissue sections. Journal of Microscopy **215**(1), 67–76 (2004)
11. Genovesio, A., Liedl, T., Emiliani, V., Parak, W.J., Coppey-Moisan, M., Olivo-Marin, J.-C.: Multiple particle tracking in 3-d+t microscopy: method and application to the tracking of endocytosed quantum dots. IEEE Trans. Image Process. **15**(5), 1062–1070 (2006)
12. Chenouard, N., Smal, I., de Chaumont, F., Maška, M., Sbalzarini, I.F., Gong, Y., Cardinale, J., Carthel, C., Coraluppi, S., Winter, M., Cohen, A.R., Godinez, W.J., Rohr, K., Kalaidzidis, Y., Liang, L., Duncan, J., Shen, H., Xu, Y., Magnusson, K.E.G., Jaldén, J., Blau, H.M., Paul-Gilloteaux, P., Roudot, P., Kervrann, C., Waharte, F., Tinevez, J.-Y., Shorte, S.L., Willemse, J., Celler, K., van Wezel, G.P., Dan, H.-W., Tsai, Y.-S., Ortiz de Solórzano, C., Olivo-Marin, J.-C., Meijering, E.: Objective comparison of particle tracking methods. Nature methods **11**(3), 281–289 (2014). doi:10.1038/nmeth.2808. arXiv:1504.05462v1
13. Campbell, R.a.a., Honegger, K.S., Qin, H., Li, W., Demir, E., Turner, G.C.: Imaging a population code for odor identity in the Drosophila mushroom body. The Journal of neuroscience : the official journal of the Society for Neuroscience **33**(25), 10568–81 (2013). doi:10.1523/JNEUROSCI.0682-12.2013

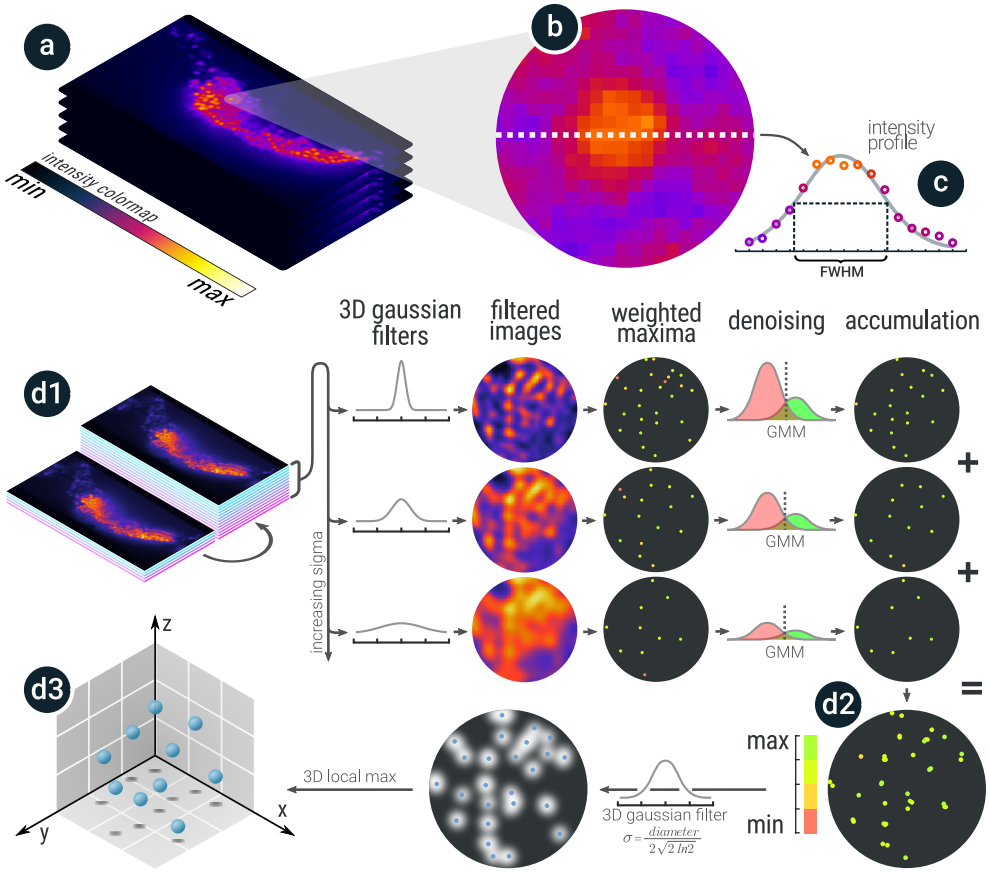

Figure 1 Summary of the method. (a) An image stack of the Mushroom body of Drosophila acquired with a spinning disk microscope (b) Detail of a nucleus (c) A good approximation of the nucleus diameter (the single input parameter of the method) can be obtained by the Full Width at Half Maximum (FWHM) of a Gaussian fit on an intensity profile. (d1-3) Stages of the Smax algorithm. (d1) Image interpolation (d2) Weighted maxima denoising using Gaussian Mixture Model (GMM) followed by maxima accumulation. (d3) Maxima accumulation image is then convolved with a kernel corresponding to the targeted nucleus size, final local maximas are extracted. All processes are performed in 3D.

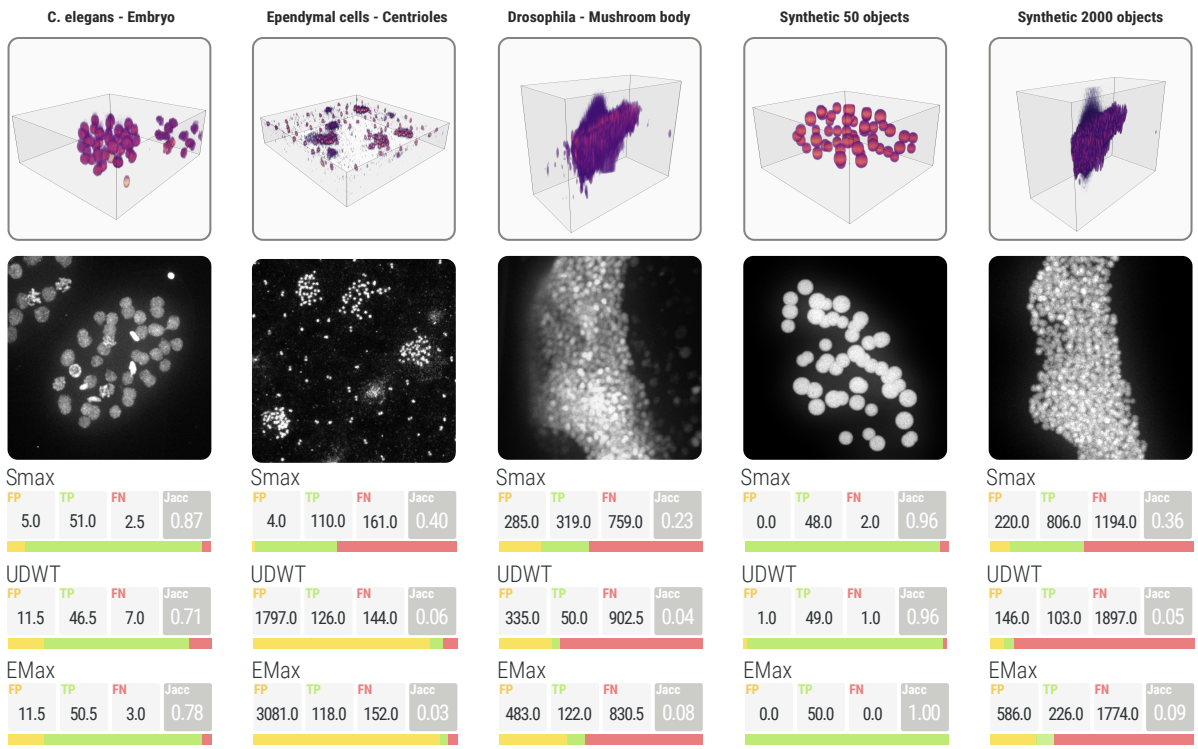

Figure 2 Quantitative comparison with two state of the art approaches. *Smax* is compared to UDWT and eMax approaches using 5 3D stack datasets. From left to right: image of distinguishable nuclei in *Caenorhabditis elegans* manually annotated, image of centrioles in mice ependymal cells manually annotated, image of a large amount of packed nuclei in Drosophila's mushroom body manually annotated and synthetic images containing 50 objects and 2000 objects for which ground truths are known. From top to bottom a 3D rendering view of the dataset, a maximum intensity projection on the z axis and the quantitative comparison of spot detection algorithms. Each box of result indicates from left to right the values of false positives, true positives, false negatives (colored bars indicating the proportion for each case) and the Jaccard index. A detection is considered as positive when it fall in a sphere of nucleus size around any of the original objects positions. *Smax* sole parameter was set to an average nucleus diameter. Parameters for the two other methods were systematically scanned in order to choose the best Jaccard Index which in principle unfavors our method (see Figure 3).

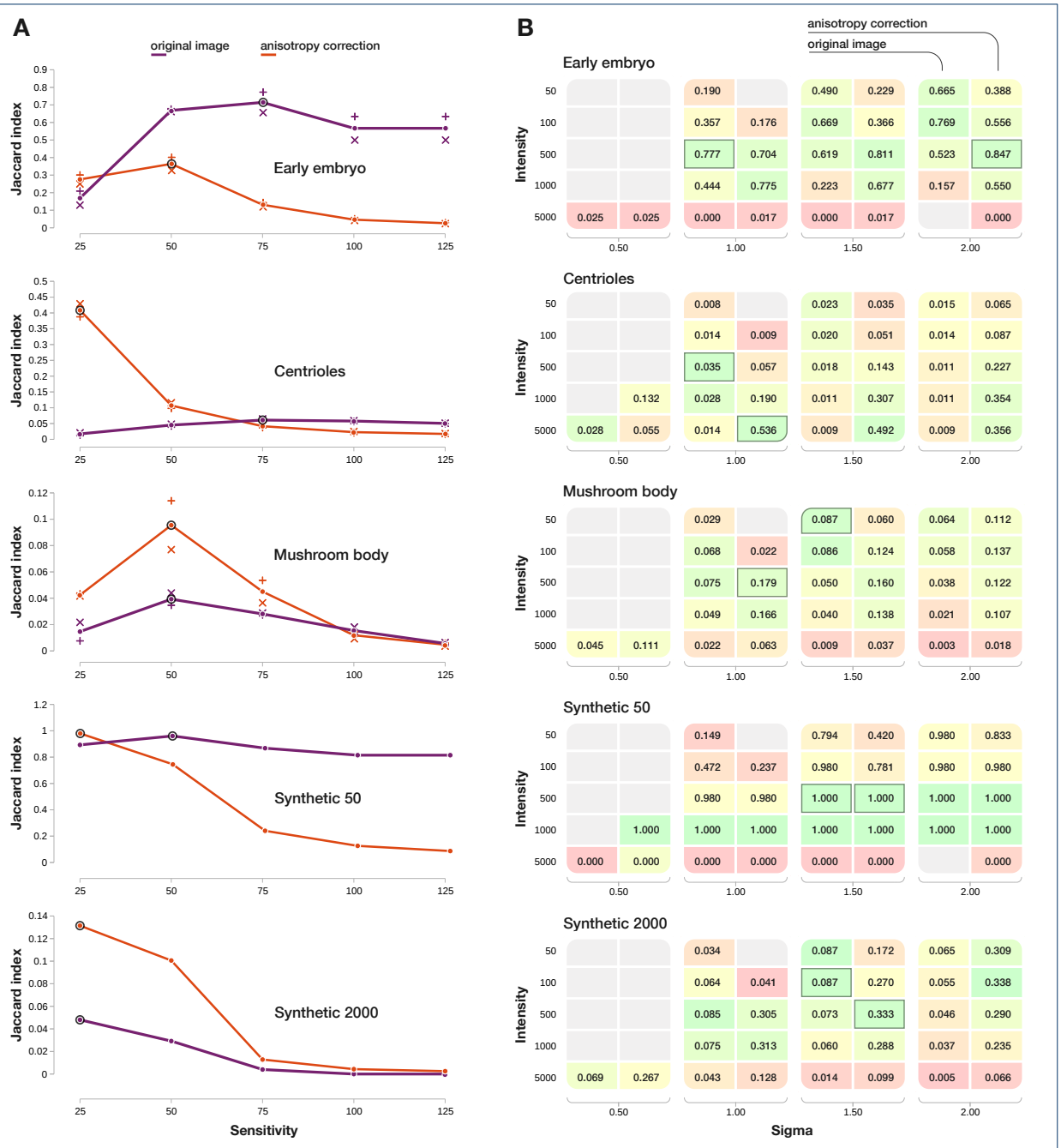

Figure 3 UDWT and Emax parameter scanning for comparison with Smax. (A) Jaccard indices obtained by scanning the "sensitivity" parameter of the Icy spot detector (UDWT) for original and image with corrected anisotropy. Full line shows the average Jaccar index obtained by the the two manual annotations (+ and × symbols). Note that the synthetic images use the computer generated ground truth, not an manual annotation. The scale for the parameter scan was chosen as matching the objects size (as specified by the authors). The values obtained demonstrate that the quality of the Icy spot detection can be improved for every case, except the embryo image, by interpolating the image in the z direction prior detection (although, without reaching the accuracy obtained by *Smax*). However, the same interpolation step decreases the accuracy of the same detector in the case of the real *C. elegans* embryo image, as the False positive rate increases drastically, lowering down the Jaccard index. (B) Jaccard indices (mean for the two ground truths for manual annotations) obtained by scanning the two parameters of eMax, applied directly on original images (left side of group) or after anisotropy correction (right side of group). Gray squares indicate cases where the provided implementation of the algorithm couldn't perform the detection. Color ranges from red to green, rescaled using all Jaccard index values obtained on each dataset. For both methods, the parameters corresponding to the best Jaccard index for raw and anisotropy corrected images are emphasized. Parameters corresponding to the best Jaccard index for raw images were used for the comparison with *Smax* provided in Figure 2.

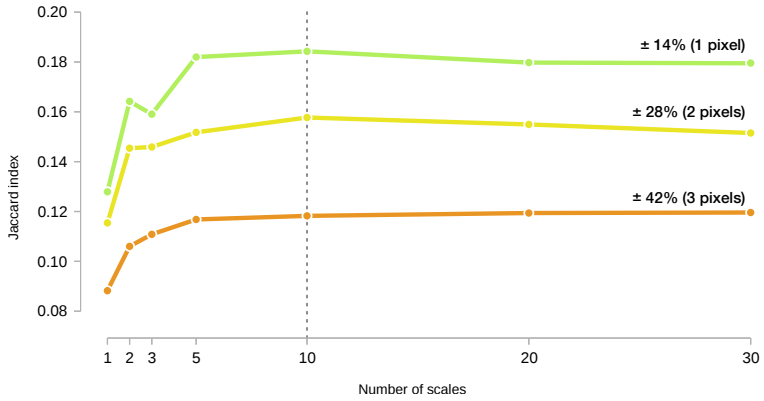

Figure 4 Evolution of *Smax* results with the number of scales used in the filter bank for three level of object sizes variability within a given dataset. The plot shows the Jaccard indices obtained on a synthetic images containing 1000 objects of 7 pixels in diameter, with sizes randomly varying from one to three pixels (curves from top to bottom) around that diameter. The dashed line indicates the chosen number of scales used as a default for the filter bank of *Smax*.

In vivo memory trace analysis by large-scale automated tracking of single neuron activity

Felipe Delestro[1☆], Lisa Scheunemann[2☆], Mélanie Pedrazzani[2], Paul Tchenio[2], Thomas Preat[2*] and Auguste Genovesio[1*]

1 Computational Bioimaging and Bioinformatics, IBENS, ENS, INSERM, CNRS, PSL, 46 rue d'Ulm, 75005 Paris, France.
2 Genes and Dynamics of Memory Systems, Brain Plasticity Unit, CNRS, ESPCI Paris, PSL, 10 Rue Vauquelin, 75005 Paris, France.

☆ equal contribution
***** co-correspondence: auguste.genovesio@ens.fr, thomas.preat@espci.fr

Abstract

Long-term memory (LTM) formation is a fundamental function of the brain. However, much of this complex process remains to be understood, thus constituting an active research area. Impediments to progress are primarily due to critical experimental barriers. Indeed, the LTM research community has not yet succeeded in devising an *in vivo* approach that can combine the advantages of exhaustively observing all neurons dedicated to a given type of stimulus, and simultaneously achieve a resolution that is precise enough to capture individual neuron activity. Current experimental data from *in vivo* observations are either restricted to a few dozen single neurons, or are based on larger brain volumes but at a low spatial resolution. Consequently, fundamental questions such as whether LTM formation increases the response level of responsive neurons or if it recruits new neurons remain to be answered. In *Drosophila melanogaster*, the mushroom body (MB) represents the olfactory memory center of the brain. In this work we present an experimental setup coupled with a computational method that provides *in vivo* measurements of the activity of hundreds of single neurons, by exploiting confocal 3D imaging over time of the whole MB cell body layer *in vivo* while it is exposed to olfactory stimulation. Our fully automated procedure enabled the high-throughput analysis of approximately 500 single neurons from the whole MB cell body layer of each of the 216 flies in various conditions. Using this approach, we identified for the first time an increase in responsive neurons count after LTM formation and a stable single neuron signal, suggesting neuronal recruitment. We predict that this method, which should further enable studying the population pattern of neuronal activity, has the potential to uncover fine details of memory formation and plasticity.

Introduction

The uniqueness of each human being is largely defined by what is learned and remembered during a lifetime. However, we are still far from deriving an integrated view of the dynamic actions that occur during a single memorization event. In particular, the specific plasticity

changes that take place during the consolidation and remodeling of long-term memories are poorly understood [1]. LTM is thought to be stored in neuronal populations showing physical or chemical changes as a result of a learning event, and whose activation by the original stimuli results in memory recall [1,2]. The existence of these so-called memory engrams was first proposed a century ago[3]. Since then, neuropsychologists and neurobiologists have made great efforts in identifying and characterizing memory engram cells in the brain [1]. Deciphering how stable neuronal information is coded remains one of the greatest challenges in neuroscience due to the hundreds of thousands of highly interconnected neurons that compose a memory network in humans and mammalian model systems.

In the context of detecting memory traces, genetic approaches including immediate early gene-based strategies have clearly advanced our understanding of how neural activity underlies behavior, *i.e.* how the functional dissociation of short-term memory and long-term memory (LTM) may be realized within different brain structures [1,3]. For example, it is widely accepted that activation of the transcription factor CREB represents an indispensable step in commencing the structural synaptic changes necessary for LTM formation [4]. Additionally, recent developments in the field of *in vivo* imaging tools have allowed neuroscientists to characterize cellular and molecular processes underlying memory formation with unprecedented precision [5]. But since memory encoding generally takes place in a subset of sparsely distributed neurons within a larger assembly, the network dynamics during memory consolidation remains difficult to tackle. A principle bottleneck comes from the lack of a suitable methodology to study memory-specific biochemical processes in heterogeneous neuron assemblies. Despite immense improvements regarding *in vivo* imaging techniques, recording neuronal activity that combines high temporal and spatial resolution with a large-scale population analysis remains unrealized to date. In addition to these technical limitations, addressing plasticity changes that occur within a whole memory network at a single-cell resolution is difficult in rodent models due to the size of brain structures such as the hippocampus or neocortex.

To overcome these limitations, we used the spinning disk imaging technology and developed a dedicated 3D tracking algorithm to detect single cells from a neuronal network and monitor activity changes from the cell body of individual neurons, which allowed to characterize a memory engram *in vivo*. To demonstrate the power of this novel approach, we proposed to answer a fundamental question in the field: during memory recall of a trained stimulus, is the LTM engram characterized by an increased intensity of responding neurons or an increased number of responsive neurons [6] (Figure 1A)? We applied this method using the Drosophila model, which is compelling in respect of size, behavioral complexity and tractability of cellular processes [7–9] (Figure 1B).

The mushroom body (MB), the olfactory memory center of the fruit fly *Drosophila melanogaster*, is comparatively small but highly organized. Each MB hemisphere consists of approximately 2,000 Kenyon cells (KCs), whose cell bodies are densely packed at the MB calyx and whose axons first bundle within the peduncle and then form 5 discrete lobular structures (from the α/β, α'/β' and γ neurons) [7]. The KCs receive input from cholinergic projection neurons (PN) that transmit odor information coming initially from olfactory receptors neurons (ORNs) in the antennae and the maxillary palps, which then relay their

information to PNs in the antennal lobe (AL) [10] (Figure 1B). The ease of genetic manipulation in Drosophila has contributed to its development as a successful model organism, especially in the field of neuroimaging. Using *in vivo* imaging techniques with genetically encoded activity reporters, *i.e.* the calcium probe GCaMP [8], odor responses have been demonstrated at the level of the KC cell bodies that can be detected with single-cell resolution [11]. Several studies have shown that odor responses at the level of the MB are sparse [11,12]. Because projections neurons are randomly connected to KC in each fly, the activity that a given odor elicits in the MB is not stereotypic, revealing global differences between individuals [13]. The MB lobes are innervated by a complex but highly structured modular network of dopaminergic neurons that transmit information about positive or negative stimuli [14]. These dopaminergic neurons modulate MB intrinsic activity and tightly regulate behavioral outputs. Thus, the MB displays important features of a memory network: its sparse and non-hardwired coding is thought to be essential for accurate learning, since it minimizes the overlap between input stimuli and allows for plastic changes [15]. Notably, the MB displays functional homologies to the hippocampus [16], and its consolidation processes are very similar to those of humans and mammals [4,9].

Using a well-established conditioning paradigm, Drosophila can robustly learn to avoid an odor that was previously paired with electric shocks [7]. Stable protein synthesis-dependent LTM is exclusively formed when fruit flies are exposed to 5x spaced training cycles, which is a specific conditioning pattern during which the training cycle is repeatedly experienced with intervening resting intervals [9]. The MB is innervated by a well characterized pattern of anatomically discrete dopaminergic neurons (DANs) that provide the shock information during associative learning [17,18]. Dopamine release modulates cAMP-dependent signals of odor-evoked activity in MB intrinsic Kenyon cells (KCs), which shapes plasticity of specific output synapses from the MB network that drive the behavioral avoidance response [19–21] (Figure 1C). This unique situation permits researchers working in the field of Drosophila memory research to control the basic network that builds LTM and the plasticity changes at the level of odor-activated KC cell bodies directly reflect memory-dependent traces. However, although recent work has described MB anatomy in very fine detail [14], a qualitative and quantitative analysis of individual MB neurons remains difficult, since its defined sub-classes are functionally heterogeneous and odor responses are sparse. Several studies have found activity signatures that are specific to LTM [22,23]. In detail, these studies identified increased calcium responses to the trained odor in the axons of specific subpopulations of KC, representing an early LTM-specific activity signature in α/β neurons and a late-phase signature in γ neurons. Nevertheless, these studies analyzed large sets of neurons at the MB lobes level, and measured a global increase in odor response intensity after LTM training. Consequently, the underlying mechanism remains inconclusive and it is still unknown if this results from an increase in odor responsive neurons or if additional neurons are recruited into the LTM engram. MB neurons at the axonal level are beyond individual resolution of current 3D in vivo imaging approaches. Therefore, we focused on the cell body layer of the MB to analyse memory traces on a single cell level. Since cellular calcium signals should reflect back-propagating neuronal activity from the axons, response patterns of MB cell bodies to a learned odor are thought to represent the plasticity changes that have occured during LTM formation.

To summarize, the fact that KCs are organized in a very dense structure together with the functional heterogeneity and sparse responses of the MB memory network has hindered any detailed investigation of the significance, as well as the formation dynamics, of identified LTM traces. Technically, these constraints originate, on one hand, from the use of two-photon microscopy, which offers a good resolution but is too slow to image a complete set of MB neurons during a single odorant presentation in 3D and over time. On the other hand, population analysis of the entire MB can only be achieved by an automated algorithm that tracks the approximately 2,000 MB cell bodies in 3D and over time, a challenge that has remained unsurpassed to date [24].

In order to detect and record activity changes of the KCs in this work, we simultaneously expressed a nuclear marker (mcherryNLS) and an activity reporter (the genetically encoded calcium reporter GCamp6f) and acquired their two spectral channels in 3D over time. By using a spinning disk microscope [25], we were able to overcome the temporal limitations and record the total assembly of MB cell bodies. To analyze the responses from a maximum number of MB cell bodies, we then developed a 3D tracking algorithm that simultaneously addressed three main challenges: the high number of densely packed somata, the 3D confocal anisotropy, and the presence of erratic and non rigid movements in living flies. Single nuclei detections and tracking could then be used to monitor activity and record odor responses from individual neurons of whole MB cell bodies in several conditions. To demonstrate the potential of this system, we have quantitatively assessed that after LTM formation, more neurons respond to the trained odor, while response intensities remain unchanged, suggesting that LTM is supported by a recruitment of neurons.

Results

Conditioning and 3D+time multiconfocal imaging of mushroom bodies *in vivo*

In order to image a large cellular population with a spatial and temporal resolution that allows detection of activity from single cells, we needed to overcome the speed limitations imposed by point scanning and two-photon microscopes. For this, we used a spinning disk microscope that offered a faster acquisition at the cost of a slightly lower resolution [26]. Indeed, such a short stimulus response duration for odorants in the MB imposed a high frequency of 3D stack acquisition, thus defining the maximum number of 2D images that could be obtained in a 3D stack at a given time point. Conversely, in order to obtain the most information given the resolution limit imposed by the point spread function (PSF) in the axial direction, a maximum z-step size between 2D images was imposed (see online methods for details). After optimization, acquisition of the entire population of the Drosophila memory center (*i.e.* the KCs of the MB) at the cell body level was made possible. To analyze and compare memory-dependent activity in these cells, we trained two groups in parallel. One group was exposed to an associative conditioning that paired the odor octanol with electric shocks, following a well-established spaced paradigm for inducing LTM in Drosophila [9] (Figure 1D). The second group received the odorant and electric shock stimuli with a time

delay that does not allow the formation of associative memory, which served as the unpaired control (Figure 1D). After a 24-h consolidation phase following LTM conditioning, flies were dissected to allow direct access to their brains, which were then imaged under the microscope, while simultaneously presenting octanol odor pulses. In this manner, we could record KC activity during memory recall (Figure 1D). For dissection, flies were affixed ventral side up on a coverslip and the head position was stabilized using an alignment wire (Figure 1E). We then turned the coverslip over to open a small window in the coverslip, which allowed us to open the cuticle at the back of the head while leaving the rest of the fly intact [8]. Underneath the cuticle, the brain is surrounded by fat tissue and a thin layer of trachea that hinder direct observation of the KC cell bodies. In order to maintain a high degree of normal brain function, we gently cut the trachea and pushed both the fat and trachea aside, without removing either tissue (Figure 1E). Another important issue is the pulsatile organ (*i.e.* the heart tube), which terminates at the posterior edge of the brain. The rhythmic activity of the pulsatile organ can strongly move the brain, which is deleterious for *in vivo* brain imaging. Contrary to our procedure, imaging studies that aim single cell resolution disrupt the physiological function of the pulsatile organ by disconnecting its innervating muscles, which may affect brain physiology [11]. Interestingly, our dissection technique prevents strong activity in this organ, and the remaining fat tissue serves as a physiological buffer that minimizes shifting of the brain. Using this procedure, we obtained a level of brain movement that could be corrected using image processing, allowing us to record brain activity in the presence of a functional pulsatile organ (Figure 1E).

This fly preparation provides direct optical access to the MB neurons. Taking advantage of the precise genetic targeting techniques available in Drosophila, we co-expressed the nucleus marker NLSmcherry (red) and the calcium sensor GCaMP6f (green) in all KCs for subsequent cell detection and response analysis, respectively. This step ensures that only a small part of the brain is labeled, minimizing the out-of-focus background. We then confirmed that expressing these fluorescent reporters in the MB did not interfere with LTM formation (Supplementary Figure 1). Next, the fly preparation was positioned within a custom-built odor delivery system under the microscope (Figure 1F). This system uses serial air dilutions to maintain a constant airflow of 1.25 L/min at the level of the fly's antennae. Switching between clean and odorized air streaming using synchronous two-way valves creates odor or air pulses; the odor concentration was thus set to 1/500. The open head capsule, covered in Drosophila Ringer's solution and fully isolated from the odor delivery system, was positioned under the objective of the microscope (Figure 1F). All flies were exposed to the same sequence of stimuli, alternating between 5s of odor stimuli or air control pulses and 35s of no stimuli (see online methods). We acquired both spectral channels in parallel, with red NLS mcherry labeling for KC nuclei and green GCaMP6f for calcium activity. By using an acquisition speed of 20 ms per 2D image, we could obtained 3D stack of 45 2D images every 900ms. This ensured that the 3D stack covered the whole 3D zone of the KC somata continuously, with z-step size of 1.5 µm between two 2D images. This also ensured that any event lasting longer than 900ms could be captured. The volume rendering of a raw 3D stack as well as some maximum intensity projections are displayed in Figure 1F and Supplementary Video 1. This demonstrates that imaging the entire Drosophila memory center, *i.e.* the MB cell body network, at a single-cell resolution is feasible, and

opens the door to an unmatched analysis of full population activity dynamics underlying memory-dependent plasticity.

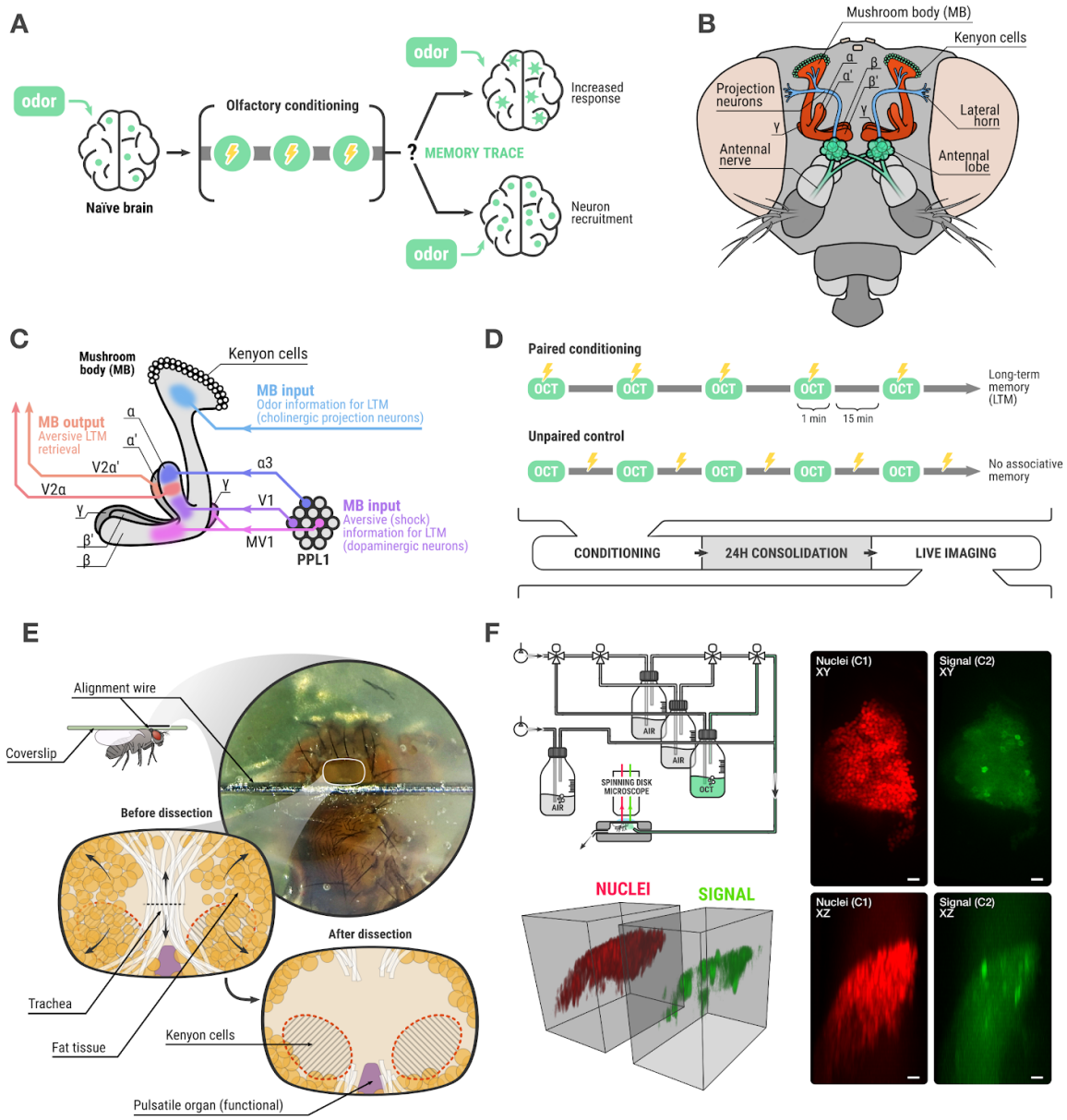

Figure 1. Biological model and data acquisition. (**A**) In naïve flies, a small population of neurons are activated upon odor stimulation (represented by green dots). LTM conditioning consists in a repeated presentation of an odor paired with electric shock. After LTM formation, the overall signal was shown to increase. Therefore, to illustrate the capability of our method, we seek to measure if LTM traces was either made from an increased population of responding neurons, or from the increased intensity of the originally responding neuron. (**B**) Frontal view of the *Drosophila melanogaster* olfactory system. Olfactory receptor neurons of the antennal nerve project to individual glomeruli of the antennal lobes, where they synapse with projection neurons and with local interneurons. From the antennal lobes, the olfactory information is conveyed by projection neurons to the mushroom body (MB), the olfactory learning and memory center, and to the lateral horn. Upon

odor stimulation, a stereotypic pattern of glomeruli activity is observed in the antennal lobe, while the pattern of responses of Kenyon cells is not stereotypic because projections neurons are randomly connected to Kenyon cells in each fly. (**C**) Details of the MB innervation, where the Kenyon cells receive odor inputs from projection neurons as well as aversive shock information via dopaminergic inputs. Briefly, a specific population of dopaminergic cells from the PPL1 cluster, namely MV1, V1 and α3, is thought to convey the shock information to axons comprising the horizontal lobes of the MB (α, α' and γ heel). The co-activation of KCs then leads to plastic changes at the level of the KC and KC output synapses, and LTM is retrieved by the specific MB output neurons (MBONs), V2. (**D**) The spaced conditioning protocol, which allows flies to pair the odor information to the electric shocks and forms a long-term Memory (LTM). (**E**) Details of the dissection process, in which the MB is exposed for imaging. (**F**) Top-left : odor delivery system which simultaneously allows image acquisition and odor delivery to the fly. Bottom-left: 3D volume rendering of a 3D stack after acquisition. Right: maximum intensity projections of nuclei and signal channels along Z axis (top) and Y axis (bottom) of a 3D stack. Scale bar is 10µm

Fully automated monitoring of densely packed single neuron activity

After image acquisition, a single 3D movie consisted of 120 consecutive 3D stacks of 45 2D images each. The tracking algorithm consisted in four steps: 1) anisotropy correction, 2) spots detection, 3) rigid and non rigid registrations of those detections and 4) reconstruction of trajectories through density based clustering of those registered detections. First, the uneven shape of the 3D Point Spread Function (PSF) and the distance between two 2D images (1.5µm) being 10 times larger than between two pixels within a 2D image (0.16µm), made that the resolution was much lower in the z axis than in the x/y axes. Anisotropy of 3D stacks in fluorescence microscopy is common. However, it is often overlooked in subsequent image analysis leading to suboptimal precision of 3D spot detection algorithms, especially in the axial direction. The first step of our approach lowers down the aforementioned effect: void between consecutive 2D images in a 3D stack was artificially filled with 9 interpolated 2D images using cubic splines (see the left panel of Figure 2A). This could not correct for the anisotropy of the PSF but produced cubic voxels more relevant to the 3D convolutions performed at the second step. For the second step (spot detection), in order to capture small variations in nucleus volume, the interpolated 3D stacks were convolved with a bank of 10 isotropic 3D Gaussian filters ranging in size around the average nucleus diameter. This process produced, for each input 3D stack, 10 output 3D stacks (one per filter), each emphasizing a slightly different spot size (see Figure 2A). The average nucleus size, the sole parameter of the spot detection step, could easily be estimated from isolated nuclei. 3D local maxima were then identified from each of those output 3D stacks and partitioned into background noise or actual nuclei signal thanks to a two component Gaussian mixture model fit based on their intensity level. Indeed, local maxima in theory should follow a bimodal intensity distribution since those located on nuclei are expected to be significantly brighter than those found in the background noise. Remaining maxima corresponding to nuclei on each filtered 3D stack were drawn with their original intensity into a single empty 3D stack. This aggregated signal was then merged by convolution with a Gaussian filter matching the average nucleus size. These processes, at end, enabled reconstruction of a 3D stack with denoised spots. 3D maxima locations (x,y,z) extracted from these artificial 3D

stacks were found to be much closer to the ground truth than the one obtained with any other existing methods, as assessed by comparison made on synthetic simulations and on manually annotated data (see Figure 2A describing the spot detection method and Supplementary Figure 2 describing the evaluation against other methods). However, even with this efficient approach, the nuclei were so densely packed that many of them were frequently undetected over time leading to blinking detections and available multi-target tracking software to fail dramatically. We observed that those poor performances were mainly due to the inability of current tracking methods to reconstruct a correct linkage in the presence of a large amount of missing detections. Indeed the flickering of detections through time made it difficult to recover trajectories without further assumption on the content of the scene, a typical lack in broadspectrum application software. In order to overcome these issues and obtain reliable trajectories from this large set of scattered detections, we took advantage of the fact that the MB cell body layer is a tissue; thus even if the fly can move with erratic movements and the tissue can bend locally, the distance between any two closeby nuclei should remain almost still in average during sequence acquisition. For instance, we do not expect nuclei to move in a way that they could cross each others or exchange position. Therefore, as a third step, a rigid registration between all detected 3D points at all time steps was first performed to remove the global shift due to the large movements of the fly (Figure 2A-B). Then this first coarse alignment was followed by a more precise elastic registration (see online methods and Figure 2C). After this procedure, all detections over time for each single neuron resulted in a clearly identifiable cluster, even if they would not contain detection for all time steps. Each of these clusters in this 3D+time registered dataset corresponded to a single trajectory in the unregistered images. Identification of each cluster was subsequently obtained in a fourth and last step by applying a 3D density-based clustering (DBSCAN) in the 3D+time registered dataset (Figure 2D). DBSCAN is a clustering method that offers several advantages. It automatically identifies the number of clusters, takes into account the local density and disregards isolated points considered as spurious detection or background noise without associating them to a group. Interestingly, we were able to estimate the optimal DBSCAN parameters from the data (Supplementary Figure 3). Once each detection was either associated to a cluster and therefore to a trajectory or dismissed as isolated background noise, missing detections in each trajectory could easily be reconstructed by interpolation in the original coordinates (Figure 2E). In addition, merged trajectories of N objects could also easily be identified as those clusters containing about N times the right amount of detections, be split and individually recovered (Supplementary Figure 4). A careful evaluation of the tracking algorithm using both manually annotated and synthetic datasets demonstrated that it outperforms currently available software for this task (see online methods and supplementary figure 12, 13 and 14). Complete extraction of the raw signal intensity in the GCaMP channel was subsequently obtained by gathering the average intensity in non-intersecting volumes around all successive positions along each trajectory. Figure 2 shows the raw (Figure 2F) and normalized (Figure 2G) signals for all neurons tracked in a single fly (see online methods for signal normalization). Since the process was fully automated, it was possible to run the same analysis in parallel on many fly acquisitions using a computing cluster. As a validation step, 23 naïve flies that had never been exposed to octanol were each exposed to 45 seconds of no events, then 5s of air, then 35s of no event then 5s of octanol then air again as described in Figure 2F-G (see online methods for full

details). The full sequence was simultaneously imaged and automatically analyzed. The results indicate that an average of 500 neurons per fly were tracked (Figure 2H). From our evaluation on manually annotated and synthetic datasets, we could assess that almost all of them were true positives matching real neurons (see supplementary figure 13). Furthermore, comparing the neuron count responding in the air window versus the neuron count responding in the octanol window revealed a significant difference, demonstrating that the odor signal could be captured by monitoring the single-cell signal of KC soma (Figure 2I).

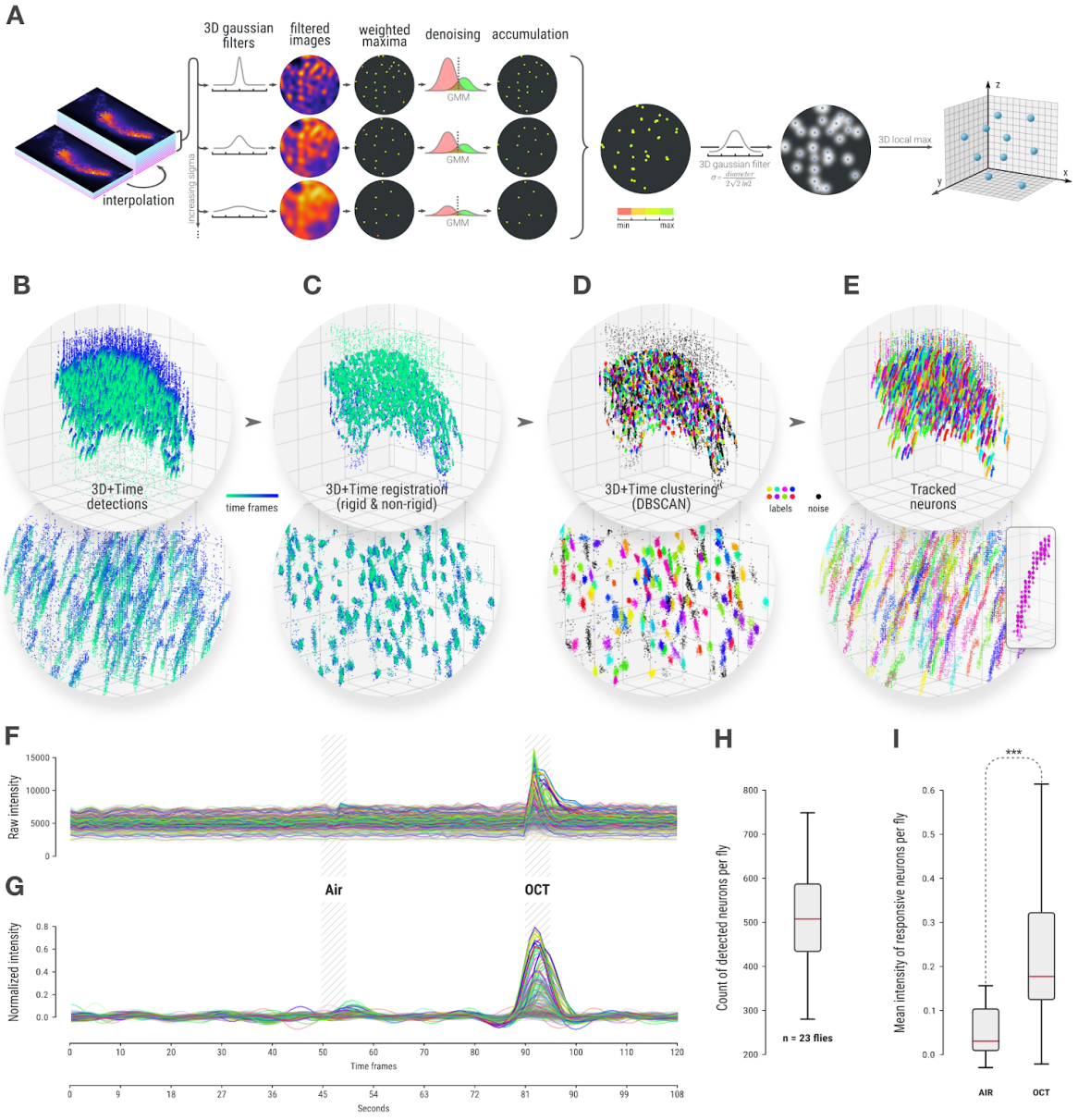

Figure 2. Detection, tracking and signal measurement for densely packed single-neuron analysis. (**A**) 3D nuclei detection method with anisotropy correction, multiscale detection and filtering that produces 3D spots locations. While we show that results are more accurate than the one obtained with available spot detection methods for this task, they still contain spurious detection or regularly miss detecting nuclei along the whole sequence leading tracking software to fail in this context. (**B**) Detected positions of nuclei in 3D for every time frame of a 3D+time sequence grouped together. Colormap represents time and the bottom image is a zoom in the center of the cloud. (**C**)

The same 3D+time point cloud after rigid and non-rigid registrations forms visible clusters. (**D**) Clustering of dense region by DBSCAN enables to identify those clusters and remove noise. (**E**) Final nuclei trajectories in the original spatial coordinates are identified by successive individual detections over time with the same cluster id (here the same color). Merged trajectories and missing detection can easily be reconstructed at this point (see Supplementary Figure 4) (**F**) For each detected nucleus, the raw GCaMP signal is measured over time in a volume around the nuclei. 500 individual neurons signal from the same MB cell bodies are displayed here. (**G**) Normalized signal displayed only for responsive neurons selected has having a peak above 0.1 (see online methods). (**H**) Count of responsive neurons per fly for a group of 23 naïve flies. (**I**) Mean intensity of responsive neurons per fly during air and OCT stimulation windows showing a highly significant difference (Wilcoxon signed-rank test, p-value: 7.3089e-68).

Long-term memory formation is supported by an increase of responsive neurons

Next, we asked whether this method would allow analyzing whole population memory traces in the Drosophila MB. For this, flies were exposed to the 5x spaced training cycles of octanol and electric shock pairings that are classically used to induce LTM (Figure 1D). As an unpaired control, a second group of flies received non-overlapping odor and shock presentations, which does not allow for the formation of associative memory (Figure 1D). After the 24-h consolidation phase, flies were dissected and the entire KC cell body population was imaged as previously described for the naïve group. Here, presenting octanol during image acquisition resembles the situation during memory retrieval. Data analysis was performed automatically, identically and in parallel for the two groups.

A minority of flies displayed either no clear increase of neuronal activity in response to the odorant presentation, or non-specific KC activity. We therefore developed an automated quality control for odor responses that we used as a filter to identify responsive flies, and we excluded non-responsive flies from our analysis. The number of excluded flies was close between the different conditions: out of 36 fly acquisitions in the paired condition and 40 in the unpaired condition, a total of 29 paired flies and 27 unpaired flies passed our automated quality control (Supplementary Figure 5). The results from the automated analyses are presented for two examples from the unpaired control group (Figure 3A) and the paired group (Figure 3B). The volumetric reconstruction of the KC cell bodies shows the GCaMP activity during the octanol (OCT) response window, with time traces showing the normalized signal from the individual neurons over the whole acquisition time (Figure 3A-B). At any time point, the response level of an individual neuron can be assessed and located within the KC population (Figure 3A-B, additional examples can be seen in Supplementary Figure 6 and Supplementary Video 2). When comparing responsive neurons from the paired and unpaired groups, more neurons seem to respond to octanol in the paired group. Indeed, plotting the count for responsive neurons from both groups demonstrates that the number of neurons responding to octanol in the paired group is significantly higher (and almost doubled) as compared to the unpaired control (Figure 3C). In addition, the mean intensity of responding neurons was not significantly different between the paired and unpaired groups (Figure 3D).

We wondered whether this effect could possibly result from the fluorescent glow produced by an increased GCaMP signal in neighboring cells. If this were the case, an increased neuron response intensity would create an artificial increase in the responsive neuron count. To test this hypothesis, we temporarily excluded from the analysis the signal of several responsive neurons, such that none of the remaining neurons could be closer to one another than a distance equivalent to twice the size of an individual soma. When iteratively removing neurons that were too close to one another, the dimmest was always selected first in order to remain consistent with our hypothesis. Once the responding neurons were filtered in this way, the neuron count for the octanol-paired group remained significantly higher than for the unpaired group (Supplementary Figure 8). This demonstrates that the increase in neuron count cannot be explained by a glowing effect due to a hypothetical increase in the intensity of the GCaMP signal.

To control if this increased neuron count from the wild-type octanol-paired group could be specific to the trained odor and not due to the LTM conditioning in general, we trained flies to pair an electric shock with a second odor, methylcyclohexanol (MCH). Again, we trained one group by pairing MCH with shocks, and a second unpaired control group received MCH and electric shocks at separate time points. During image acquisition, OCT was presented to the flies 24h later and the responsive cell count was not found to be significantly different (Supplementary Figure 7). Thus, the increase in responsive neurons observed in Figure 3C was specific to an LTM association between OCT and electric shock.

A hallmark of LTM across phyla is the requirement of repeated training cycles with resting intervals, while the presentation without resting intervals, i.e. massed training, will not lead to protein-synthesis-dependent LTM [27]. In flies, 5x massed training leads to a memory called long-term anesthesia-resistant memory (LT-ARM) that is not sensitive to the inhibition of translation [9]. We therefore tested the neuron count of odorant-responsive cells after 5x massed training and again compared the paired with the unpaired group as it was done for 5x spaced training (Figure 3C). Importantly, no increase in the number of responsive neurons was observed for the paired 5x massed group demonstrating the specificity of additional responding neurons to LTM formation (Figure 3C).

To further prove the specific role of neuronal recruitment for LTM, we targeted the knockdown of the protease crammer (Cer) in the MB by RNA interference (RNAi). Cer belongs to the cathepsin family, an important regulator of gene expression and specifically involved in LTM formation leaving short-term as well as LT-ARM performances unperturbed [28]. If the recruitment of neurons is specific to LTM formation, we expected to observe no increase in responsive neurons in these flies after LTM training. Indeed, when we imaged Cer knockdown flies after 5x spaced training, no increase in the count of odor-responsive neurons was detected between paired and unpaired trained flies (Supplementary Figure 11). However, we suggest that response pattern to the naive odor stimuli after Cer knockdown was altered because, while there was no difference between groups, we found a high level of overall odorant responding neurons. Importantly, in all of these tests, the number of KC detected using the mCherry reporter did not differ between the different conditions (Supplementary Figure 9).

Altogether, we described a 3D imaging and automated response tracking method for an entire memory center that allows quantitatively and qualitatively capturing odor responses. By using this system to compare odor traces from individual neurons, we suggest that neurons are recruited during LTM consolidation to participate within the memory engram that encodes the behavioral response.

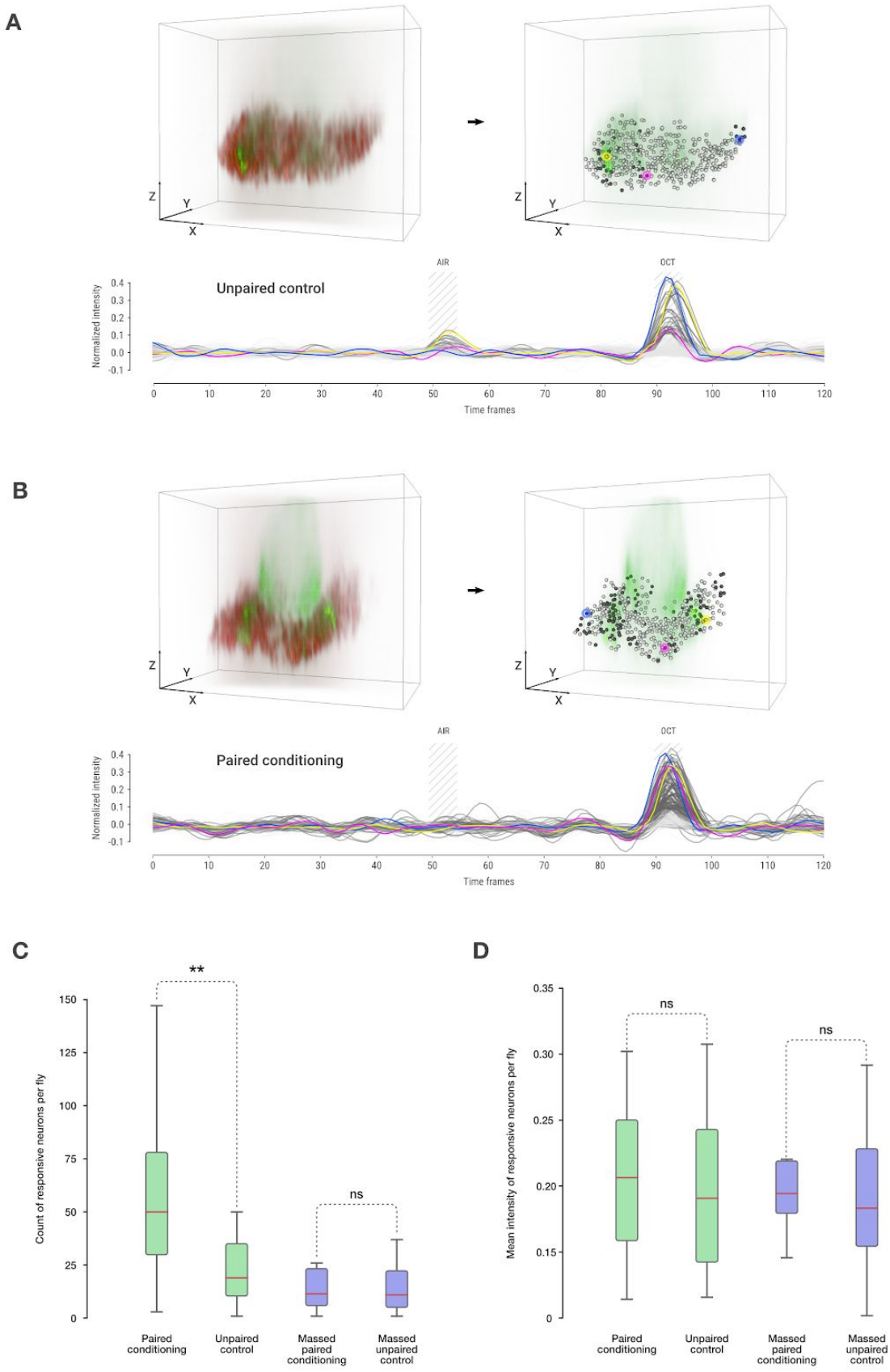

Figure 3. Detection of responsive neurons from spaced and massed trained flies. (**A**) An illustrative sample from the unpaired control group after 5x spaced training. The volumetric reconstruction on the left shows the mCherry nuclei signal together with GCaMP activity during the

OCT response. On the right, the GCaMP signal is shown together with the detected nuclei. The plot shows the normalized signal from the individual neurons. Light gray spheres and lines represent neurons that did not respond, and the dark gray color indicates neurons that responded. Three neurons are highlighted in pink, yellow and blue (with the corresponding signal of the same color) to show that the signal of individual neurons can be monitored in different parts of the mushroom body. (**B**) An illustrative sample from the paired 5x spaced conditioning group using the same visualization as in panel A. (**C**) Comparison of the numbers of responsive neurons per fly between the paired 5x spaced conditioning to form LTM (n=29) and the unpaired control (n=27) groups (Mann-Whitney two-sided test p-value: 0.001098) as well as between the paired 5x massed conditioning to form LT-ARM (n=14) and the unpaired control (n=16) groups (Mann-Whitney two-sided test p-value: 0.97894). Results show that the number of responsive neurons increases after paired conditioning but not after massed paired conditioning. (**D**) Comparison of the mean intensity of responsive neurons per fly at stimulus time in the same flies and conditions as in panel C. Statistical tests could not reject the null hypothesis of an equal mean distribution of intensity (t-test p-value 5x spaced paired vs unpaired p-value: 0.882074 and t-test p-value 5x massed paired vs unpaired p-value: 0.5291736).

Discussion

The search for the memory engram remains one of the most challenging goals in modern neuroscience [1,2]. Experimental attempts to identify specific memory engram-bearing cells have proven largely inconclusive due to methodological limitations [1]. Recent “memory engram technology” developed in mammals allows the labeling and subsequent manipulation of specific memory engrams in particular brain regions [3]. Nevertheless, most of these technologies require better temporal and spatial resolutions. Interestingly, “three-dimensional imaging of intact brains to study the functional properties of engram circuits *in vivo* by calcium imaging of engram cell activity in multiple brain regions” has been proposed as a future research direction in the field by a recent review on memory engrams [1].

Here, we implemented 3D live imaging of the whole *Drosophila melanogaster* MB cell bodies and subsequently developed a fully automated neuron tracking and monitoring system to quantitatively compare memory traces on a large scale. The sparsity of the neuron response dictated that a 3D volume containing the whole mushroom body cell bodies should be acquired at single-cell resolution, and at a time frequency fast enough to image the odor responses. These strong constraints pushed the spinning disk confocal imaging to its limits and produced 3D stacks containing many densely packed fluorescent spots. For this reason, available generic spot detection methods produced highly inaccurate results, which did not permit obtaining reliable 3D positions of soma[29–31]. As a consequence, none of the current state of the art algorithms used to track multiple spots through time could produce satisfactory results. To address these issues, we developed dedicated methods for densely packed spot detection and tracking that took advantage of our specific context. We first proposed a dedicated spot detection approach that could perform a maxima accumulation across multiple scales of anisotropy-corrected 3D stacks. This method, particularly efficient on densely packed spots laying on a uniform background, made it possible to retrieve many more spot locations than current state of the art methods as assessed quantitatively on both synthetic and real manually annotated 3D stacks (see supplementary figure 2). However, the

ability of spot detection to constantly and accurately detect all nuclei along the whole sequence remained unreached. Indeed, blinking detections made long time tracking of individual nuclei difficult with classical linkage methods. Based on this initial set of noisy detections, we then developed a robust multi-tracking approach that takes advantage of the fact that nuclei are not freely moving but belong all to the same tissue, and therefore remain in average at a relatively still distance from their direct neighbors even when the tissue is bending or shift altogether. We then made the reasonable assumption that nuclei cannot cross each other and that registering in a non rigid way all 3D detection overtime should form local clusters corresponding each to most positions of a trajectory. Indeed, after rigid and non rigid registrations, so as to cancel the effect of large global spatial shifts and non-rigid deformations of the tissue, all detections of the same nucleus over time were closer together, while detections from different nuclei were spread apart from each other. A density-based clustering performed on this registered dataset enabled us to group and label all detections of individual soma over time. In this setup, it was possible to recover many individual trajectories, to split artificially merged spots into individual soma, and to reconstruct all missing detections. Furthermore, thanks to these identified trajectories, it was possible to retrieve the intensity signal of individual neurons through time from the GCamp channel. Importantly, we demonstrated using manually annotated and synthetic 3D+time datasets that our approach outperformed any other existing methods to the purpose of tracking densely packed nuclei (see supplementary figure 13 and 14).

Our approach made it possible to robustly recover the signal of approximately 500 single neurons from the whole MB cell body layer for each one of the 216 flies *in vivo*. This level of throughput, which has never been attained before, offers new perspectives as it is large-scale (encompassing the whole MB cell bodies) and can operate with single-neuron precision. Although the MB contains approximately 2,000 neurons per hemisphere, our imaging conditions could only successfully resolve about a 1,000 neurons by manually counting NLS-mCherry-positive neurons (Supplementary Figure 2C: TP+FN in Smax represent the manual count of all nuclei in one 3D stack at a fixed time point). Furthermore, synthetic simulations demonstrated that when processing artificial MB populated with 2,000 labeled neurons, our system was able to track robustly about a 1,000 neurons, almost all of them being true positive (see Supplementary Figure 13C). Therefore, we estimate that our approach, limited by the resolution constraint, is capable of tracking correctly about half of the 1,000 manually identified MB neurons within our acquisitions and do not generate false positive. In total, this suggests that we can locally detect about one in four neurons. Nevertheless, this subsampling is uniformly distributed over the whole mushroom body, and provides access to a broad view with unprecedented precision. Moreover, given that we were able to capture the GCaMP signal from our entire acquisition, we are confident that our method can be used to describe a comprehensive response pattern of MB neurons to a given odor.

By comparing flies that had either undergone an LTM-specific associative training or an unpaired protocol (in which training stimuli were presented with a time lapse that did not allow any association), we discovered for the first time that during LTM retrieval (in contrast to other memory components tested by massed training) more neurons respond to the trained odor. We therefore hypothesize that new neurons are recruited within the MB

network to build an LTM engram. This effect was specific to the trained odor, since presentation of the control odor that was given without electric shock during conditioning did not differ between the paired and unpaired groups. Moreover, we could show that interfering specifically with LTM formation using an RNAi-mediated knockdown of Cer, we lost the effect of an increased number in odorant-responding neurons during LTM retrieval. Taken together, our approach made it possible to robustly follow odor responses over time on a single-cell level, as well as answer a fundamental question about the temporal evolution of the memory engram network.

Contrary to short-term memory, it is well established that LTM is dependent on CREB-dependent signaling and *de novo* protein synthesis across phyla [4]. However, questions about the ongoing reorganization and recruitment of neurons into the LTM engram continue to be highly debated [6,32]. In recent years, the combination of transgenics and optogenetics has allowed neuroscientists to identify memory engram cells by detecting and tagging specific populations of cells that are active during different learning phases [3]. In agreement with our results, one recent study found an activation of neurons in the prelimbic cortex during the retrieval of fear memory in mice in addition to those neurons active during stimulus presentation or early memory recalls [33]. However, this study, like most studies on genetic tagging and whole population engram analyses in rodents, was performed in fixed samples, which lack temporal resolution and do not permit a qualitative analysis of the signals.

In contrast to these findings, other studies have demonstrated that a consolidated memory trace, representing memory-dependent structural or molecular changes, can be restricted to neurons that were previously activated by the stimuli presented during associative learning [6,34]. Our own results demonstrate that during LTM retrieval, the intensity of responding neurons does not differ in paired flies as compared to the unpaired control. Thus, it is unlikely that LTM-dependent plasticity changes solely result from an increased excitability in stimulus-responding neurons.

How can new odorant-responsive neurons be recruited into the memory engram? In mammals, it has been proposed that GABAergic interneuron dendrite dynamics play a potential role in cortical function and long-term circuit plasticity in mammals[35]. Release of inhibition by GABAergic interneurons in the hippocampus could also be used to define the sparse representation of learning stimuli in the hippocampus, and to determine which neurons participate in a given engram [36]. Likewise, the sparse representation of odor responses in MB neurons is thought to be brought about by a GABAergic feedback loop [37]. This GABAergic input to the MB is executed by the anterior paired lateral neuron (APL), and disruption of the APL-MB feedback averts sparse odor representations in the MB [37]. Interestingly, mild interference with APL inhibition, which causes a moderate increase in the number of odor responding neurons in the MB, leads to memory enhancement [38]. Additionally, a recent study provides evidence for a direct inhibitory connection from dopaminergic neurons involved in aversive memory formation to the APL that likewise leads to memory enhancement. [39]. Even though the involvement in LTM retrieval remains to be shown, neuronal recruitment as a result of LTM consolidation could be mediated by APL inhibition of MB activity.

A principal component of LTM across phyla is the spacing effect, training sessions need to be spaced by resting intervals in order to initiate LTM-dependent plastic changes [27]. Thus, the spacing effect could act specifically on GABAergic feedback and release inhibition of MB neurons after LTM training. Another possible mechanism is the accumulation of subthreshold traces that could lead to a decrease in input resistance, thereby pulling neurons above the response threshold after spaced training. Indeed, it has been demonstrated that brief subthreshold events can act as Hebbian signals for long-term plasticity [40]. Interestingly, several studies have demonstrated that neurons with high CREB activity are preferentially recruited into LTM engrams [41]. Possibly, these neurons do not respond to naïve stimuli, but are more likely activated by an accumulation of subthreshold events during the repeated presentations of spaced training. Along these lines, one interesting direction for future studies would be to determine the dynamic evolution of the recruitment of MB neurons during memory consolidation.

Altogether, we used the Drosophila MB as a unique memory network model and developed an imaging and activity tracking method that allows addressing whole population plasticity changes by following individual neurons in 3D and over time. Importantly, this method will also make automated 3D detection and activity tracking possible for many additional samples. Our approach offers the potential to acquire a precise count of responsive neurons, as well as to capture the spatial organization of responsive and non-responsive neurons. Although future studies will focus on performing acquisition during conditioning, the application of this approach should also open the door for dedicated rich euclidean graph-based spatial analyses of the memory engram.

Online methods

Fly conditioning

For the training protocols, we used the odors 3-octanol (OCT) and 4-methylcyclohexanol (MCH) as the conditioned stimuli. The two odors, which have been widely used for conditioning experiments in *Drosophila*, can both be associated with an appetitive or aversive response.

During training, groups of 50–100 flies were initially exposed for 60 seconds to the first odor (odor A: either 0.36 mM OCT or 0.325 mM MCH diluted in paraffin oil), during which time they received 12 consecutive electric shocks (ES) corresponding to 1.5-second pulses of DC. After a 45-second rest period, flies were exposed for 60 seconds to the second odor (odor B), which was not paired with ES. This training cycle was repeated 5 times, with a 15-min resting interval. Flies were then kept in a vial with regular solid food.

Dissection protocol

Flies were glued on a plastic slide using a biocompatible dental glue (3M ESPE Protemp) and pierced in the center, without any prior anesthesia. An alignment wire was used to maintain the Drosophila head in a correct position. The orientation of the head was adapted to the area of interest to be imaged so as to minimize the thickness of tissue the light must travel through.

Next, Drosophila heads were opened using very fine scalpels to remove a rectangular cuticle region (300 µm x 400 µm) covering the brain. The underlying fat tissue was pushed to the corners of this window, and the tracheae were cut and pushed aside to obtain a clear view of the brain. In general, all actions must be performed extremely carefully so as not to damage the glial cells that surround the brain, as well as the MB itself. All microsurgery was performed in the presence of a physiological fluid (Ringer's solution) to preserve the brain. The composition of this aqueous solution is as follows: 130 mM NaCl, 5 mM KCl, 2 mM $MgCl_2$, 2 mM $CaCl_2$, 36 mM $C_{12}H_{22}O_{11}$ (sucrose), and 5 mM HEPES-NaOH (Sigma-Aldrich). The pH of the solution is 7.3[8].

Odor delivery system

Two pumps were positioned upstream of the odor delivery system, one of which feeds a pipe circuit controlled by a series of solenoid valves. These valves made it possible to generate different stimulation configurations. The pipes were either immersed in bottles containing neutral paraffin oil for “air defect” and “air control” configurations, or bottles with added chemical product: 4-methylcyclohexanol (MCH, purity equal to 99%, Fluka 66360, Sigma-Aldrich) or octan-3-ol (OCT, purity greater than 95%, Fluka 74878, Sigma-Aldrich). Since these products are hydrophobic, the solutions were prepared in odorless paraffin oil (International VWR, Sigma-Aldrich); we used 1 mL of product dissolved in 100 mL of paraffin oil. The flow exiting this part of the assembly corresponds to one-third of the total flow delivered to the fly. The other two-thirds of the flow were generated by a second pump. This second pump is connected to a pipe immersed in a bottle filled with neutral paraffin oil, which creates a constant main airflow regardless of the chosen stimulation configuration. The final odor concentration arriving at the Drosophila antennae was 1/500.

In order to prevent the odor from stagnating in the delivery chamber, another pump was used to evacuate the odor and avoid desensitization of the Drosophila olfactory receptors. The solenoid valves were individually controlled by logic signals from a NI-USB (National Instruments) card to define the desired pacing configuration.

Image acquisition and odor presentation

In our experiments, a Zeiss Examiner Z1 Axio microscope was used for data acquisition, equipped with an EMCCD (Electron Multiplying Charge Coupled Device, Photometrics Delta Evolve). The light excitation was performed by two diode-pumped lasers that emit at 491 nm and 561 nm (maximum power: 50 mW, Roper Scientific). The sample was scanned using a

CSUX1-M1N-E confocal head. This Nipkow disc, consisting of a spiral arrangement of 20,000 50-µm diameter filtering holes each spaced at an interval of 250 µm, rotates at a maximum speed of 5,000 rpm synchronously with a second disc made of the same number of micro lenses (diameter: 250 µm). When the discs rotate, approximately 1,000 laser beams simultaneously scan the sample. A set of interference optical filters (model 59022 ET - EGFP / mCherry, Chroma) were used to define the different spectral paths of the microscope, with each of the filters consisting of two transmission bands. The dichroic plate was used to reflect the excitatory light to the sample and transmit the emitted fluorescence to the camera.

A set of mirrors and filters (Dualview Photometrics DV2) were mounted on the transmission path of the microscope upstream of the camera to allow simultaneous acquisition at the camera of two wavelengths (here, mCherryRFP as a nuclei marker and GCamPEGFP to monitor neuronal activity). Two water immersion microscope objectives are available on this device: Zeiss 40x ON 1.0 Vis-IR W apochromat 421462-9900 (working distance: 2.5 mm) and Zeiss 63x ON 1.0 Vis-IR W apochromat 421480-9900 (working distance: 2.1 mm). Although the initial tests were made with the 63x objective, all of the acquired data used the 40x. Finally, the entire system was controlled by the VisiView 2.1.3 software (Visitron Systems GmbH).

Sequences of 3D stacks were saved in a 5-dimensional *.tiff* file, with axis XYZTC and data recorded in a 16-bit format. Each plane was 256 x 512 pixels, as we only used half of the sensor for each channel (the full resolution of the camera is 512 x 512 pixels). The pixel size was 0.16125 µm x 0.16125 µm, and the total size of each 2D image was 41.28 µm x 82.56 µm. The acquisition step size was defined as 1.5 µm, with 45 2D images being sufficient to cover the depth of the whole MB. Therefore, each 3D stack can cover a depth of 67.5 µm. Every 2D image had an exposure time of 20 ms, meaning that each 3D stack required 0.9 seconds to be acquired. Due to the high frequency of acquisition, we did observe an artifact that corrupted the 3D stack acquisition at random times (Supplementary Figure 10). As this issue arose in a sporadic manner, it was easy to deal with its detection, and the affected time frames were automatically excluded from the analysis and replaced by interpolated data.

In parallel to the image acquisition, flies where exposed to the octanol and air control stimuli as follows: 45 s of airflow - 5 s of air control pulse - 40 s of airflow - 5 s of octanol pulse - 40 s of airflow - 5 s of air control pulse - 40 s of airflow - 5 s of octanol pulse - 40 s of airflow. The whole acquisition time was 225 s (250 frames). To capture odor responses for LTM retrieval, we used only the first air control pulse and octanol pulse for analysis (108 s / 120 frames).

Rigid and non-rigid registration

After spot detection is applied independently on each 3D stack of a sequence. The 3D point sets obtained are aligned over time using rigid, then non rigid registration algorithms. The purpose of the rigid registration is to cancel large shifts due to erratic movements of the fly caused for instance by the pulsatile organ. The purpose of the non-rigid registration is to

correct for the movement caused by the elastic property of the tissue. Overall, the aim to align all 3D detections overtime is to form clusters in order to detect them and use them to further identify, correct, split and complete trajectories. The rigid registration find a rotation and a translation that minimizes the sum of distance between couples of points from two consecutive time frames. Those couples of point are previously identified using the Hungarian algorithm. The non rigid registration uses the Coherent Point Drift algorithm [42] that considers the two data point set to register being realisations of closeby Gaussian Mixture Models (GMM). The algorithm forces the GMM to move from one set to the other coherently as a group to preserve the topological structure of the point sets.

Manual annotation

Manual annotation of 3D stacks were performed using the ImageJ “Cell counter” plugin [43]. Two separate annotations were performed. One for the validation of the spot detection on static 3D stacks, and another one for the 3D tracking over time. For the spot detection, all nuclei in one 3D stacks were annotated independently by two experts. It consisted in marking the central position in 3D of every nuclei present in the Mushroom body (mCherryRFP signal). The XY position was relatively easier to be assessed with accuracy, while the lower axial (Z) resolution of the 3D stacks makes the process more difficult. For this last reason, annotated ground truth in 3D cannot be considered as a perfect. For tracking, manual annotations are typically time consuming and don’t guarantee a high accuracy [44]]. In our case, it was impossible to annotate every individual object, even in one dataset in an exhaustive manner. Instead, 10 random nuclei were annotated by two experts along a sequence of 250 3D stacks for a total of 5000 data points. One nucleus happened to be chosen by both annotators leading to 19 single nuclei annotated in total. In both cases (detection and tracking) the ground truth was exported in a XML file, so that a straightforward comparison could be done similarly against the results provided by ours and others methods (see supplementary Figures 12, 13, 14).

Synthetic data

Static and dynamic 3D stack were artificially designed to validate the spot detection and tracking algorithms. For static 3D stack, a real interpolated 3D stack was used to delineate a foreground using an otsu thresholding. A specified number of spheres were drawn into a similar sized volume and evenly spaced using the k-mean algorithm. These spheres were then convolved with a PSF measured from isolated spots in the original 3D stack to render a fluorescent microscopy 3D stack. Anisotropy was obtained by subsampling the obtained 3D stack in the axial direction. Gaussian noise was finally added and the known coordinates of the spheres were saved as ground truth in a separated file. To generate sequences of 3D stacks to validate the tracking, we used the same approach than with static 3D stacks except that seed points used to generate the 3D stack at time t were the positions obtained at time t-1. In this way the evolution of the outer bounds surrounding the foreground (that is the shape of the MB) would govern the movements of all somata in a smooth way resembling the natural movements and deformations of the MB during acquisition (see supplementary figure 12 and supplementary video 3). The known coordinates of all the spheres overtime were saved as ground truth in a separated file. A straightforward evaluation of our methods

and two other methods could then be performed by comparison of all results with this ground truth (see supplementary Figures 13 and 14).

Quantitative evaluation for spot detection

To evaluate and compare the accuracy of the spot detection methods, a detection is considered a true positive (TP) when it falls within a sphere of 1.5x nucleus radius around each annotated ground truth position. A detection is considered false positive (FP) when it falls outside all spheres. Note that if two detections fall in the same sphere, only one is accounted as TP, the other one is accounted as FP. A sphere that enclose no detection is accounted a False Negative (FN). There is no True Negative (TN) as no other object than nuclei are annotated and no tracking software result contains anything else than nuclei trajectories. As measure of accuracy we used the Jaccard index, a similarity index defined as the ratio between the intersection and the union of two sets. In our case the two sets are defined by the detection results and the ground truth and the Jaccard index value is then TP/(FP+TP+FN). When the intersection of the detection results and the ground truth translates in a high amount of FP or FN relative to the TP, the Jaccard index approaches zero and the detection results is considered bad quality. Oppositely, if perfect match between the detection results and the ground truth, FP=FN=0 and the Jaccard index value is one. The results for this validation can be seen in Supplementary Figure 2, for both synthetic and manually annotated images.

Quantitative evaluation for tracking

Tracking was operated by 3 software program 1) ours: memotrack, 2) ICY [45] and 3) TrackMate [46]. ICY and TrackMate were chosen both because they were available online and because they received good evaluations from a recent spot tracking performance review [44]. After tracking, trajectories that were interrupted (that is their duration were shorter than the total sequence) were discarded as the complete sequence was needed to read the GFP signal. Distances between the remaining trajectories and annotated ground truth (manual or synthetic) were computed and a trajectories with an average distance over time from its closest ground truth larger than 3 times the nucleus size was considered wrong (mostly to allow for the imprecision in the axial direction). Correct trajectories defined this way represented the true positives (TP) in supplementary figures 13 and 14. False Negative (FN) were defined as ground truth nuclei that did not match any trajectories. False Positive (FP) were software defined trajectories that did not match any ground truth. Note that this last category is unavailable for manually annotated data as it would necessitate to annotate all nuclei of a 3D sequence over time (about 250,000 data points!), which is virtually impossible for a human being. Finally, note that there was not such a thing as True Negative (TN) as software program do not generally output trajectories corresponding to spurious objects that we anyway wouldn't have annotated.

Signal normalization

Raw single neuron signal was normalized prior selecting responsive neuron in order to align the background signal for all flies of a batch. Raw signal was smoothed (using a Butterworth frequency filter at 20% of the Nyquist frequency) and normalized the standard way with (F-F0)/F0 where F is the raw signal and F0 is the value of a moving average of radius 10 around the point being normalized (windows of 20 time frames). Neurons with normalized signal containing a peak in an OCT stimulation window with a value higher than 0.1 were considered responsive neurons.

Batch alignment

All samples in this study were acquired in three different batches separated by periods of time, modifications and moving of the spinning disk microscope. Therefore we performed a correction to minimize batch to batch variations also known as batch effect. Correcting for batch effect after acquisition by reference alignment is common in high throughput experiments as microarray gene expression [47] or high content screening [48]. Each of the three batches contained different conditions. However, batches could be adjusted two by two using alignment of common references. The first batch contained naïve, spaced paired (OCT-OCT), spaced unpaired (OCT-OCT), spaced paired (MCH-OCT) and spaced unpaired (MCH-OCT) flies. The second batch performed after the manuscript review contained only the massed control, for both unpaired and paired flies. The third batch operated two months later contained spaced paired (OCT-OCT), spaced unpaired (OCT-OCT), massed control and the Crammer knockdown control flies. Alignment of batch 2 and 3 was possible using the massed control group as common reference. Alignment of these two batches to batch 1 was possible using the spaced unpaired group (OCT-OCT) as common reference. As the scale of intensities of the peak of responding neurons for the same reference group had a tendency to vary per batch, the correction itself consisted in simply aligning the 99 percentiles of those distributions and applying the correcting ratio similarly to all neuron signal of the remaining condition of the batch. We performed the alignment using the 99 percentiles and not the max of the distribution to avoid outliers.

Statistical tests

When the statistic to be tested could be considered approximately Gaussian (as the mean intensity) we performed t-tests except when the data points were paired, then we performed a Wilcoxon signed-rank test. When distribution could not be considered approximately Gaussian (as cell count), we used the Mann-Whitney U test when comparing two conditions and the Kruskal-Wallis H tests when comparing more than two conditions together. All tests were two sided. N are mentioned either on the plot or the figure captions.

Code availability

The entire code that enables using this method, reproducing these results and the tracking evaluation on annotated and synthetic data is available on Github at the following address: https://github.com/biocompibens/memotrack.

Acknowledgments

We thank Pierre-Yves Plaçais for critical reading of the manuscript. This work was funded by the Agence Nationale pour la Recherche (ANR MemoMap ANR-15-CE32-0008-01) (to A.G. and T.P.), the Labex MemoLife (to A.G. and T.P.), and the European Research Council (ERC Advanced Grant EnergyMemo, n° 741550) (to T.P.). L.S. was funded by a postdoctoral fellowship from the Deutsche Forschungs Gemeinschaft DFG (SCHE 1884/1-1). F.D. was funded by a doctoral contract from Memolife (ANR-10-LABX-54 MEMOLIFE) and Paris Sciences et Lettres (ANR-11-IDEX-0001-02 PSL).

Contributions

A.G., T.P. and P.T. conceived the project. F.D., L.S. and M.P. performed experiments. FD and AG conceived the image and data analysis methods. F.D. wrote the code for 3D+time image and data analysis, L.S. and M.P. performed imaging experiments on the Drosophila brain. F.D. A.G., T.P. and L.S. analyzed the data. A.G., F.D. and L.S. wrote the manuscript.

Competing interests

The authors declare no competing interests.

Supplementary material

Supplementary Figures

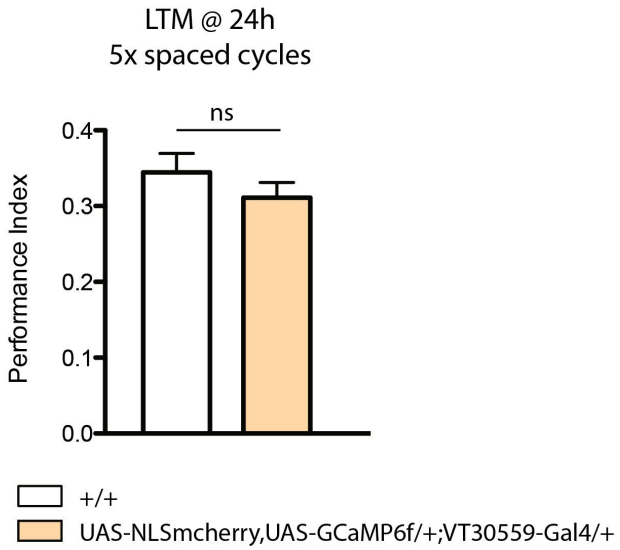

Supplementary Figure 1. Long-term memory scores for wild-type and transgenic flies used during conditioning and image acquisition. A value of zero indicates a random decision of the fly between the paired and control odors. Transgenic flies displayed normal LTM performances.

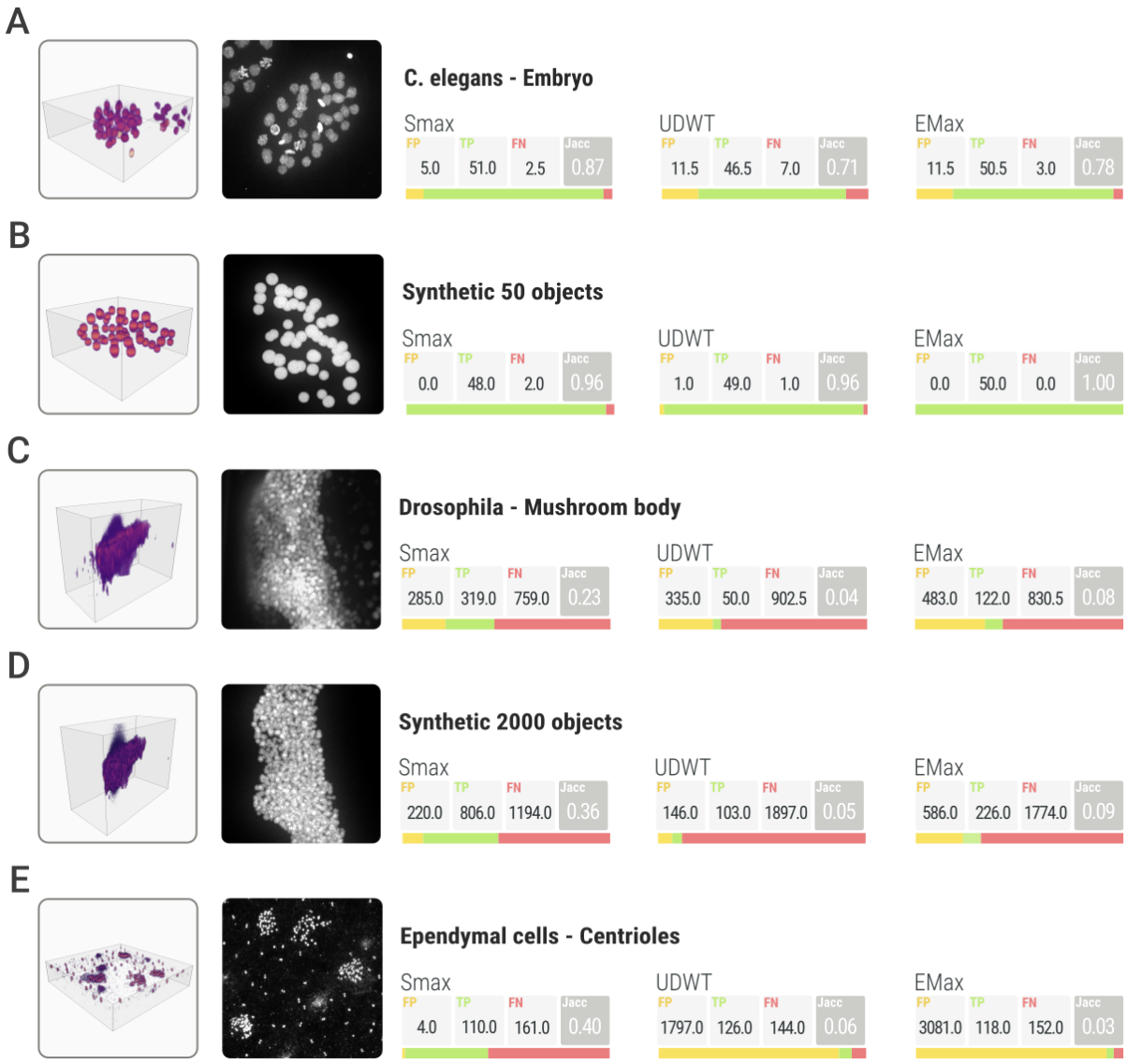

Supplementary Figure 2. Quantitative comparison of our spot detection method alone (without tracking) against two other state of the art spot detection methods on a range of examples. Our approach, called *Smax* here, is compared to the UDWT [31] and eMax [49] using 5 datasets to demonstrate that it is particularly efficient at adressing the case where nuclei are densely packed. The two other methods were promoted in a recent review on spot detection [29]. They are considered efficient and only require a few parameters. Importantly, they are widely used. **(A)** A 3D stack of *C. elegans* with manual annotation of distinguishable nuclei. **(B)** A synthetic reproduction where ground truth is known. **(C)** A 3D stack of a Drosophila mushroom body with a large quantity of manually annotated packed nuclei. **(D)** A synthetic reproduction where ground truth is known. **(E)** A set of manually annotated centrioles from ependymal cells. A volumetric reconstruction and an axial maximum intensity projection are shown for each 3D stack. In each row, the results box indicates (from left to right) the values of false positives (FP), true positives (TP), false negatives (FN; colored bars indicating the proportion for each case) and the Jaccard index (Jacc). TP+FN is either the ground truth count for synthetic data or is assessed manually for real 3D stack. FP+TP corresponds to the detected objects count. A detection is considered positive when it falls in a sphere the size of a nucleus, around any of the original nuclei positions. The sole parameter of Smax was set to the average nucleus diameter which can be easily estimated from the data. Parameters for the two other methods were chosen to be the best possible: a large range of parameters were tried automatically in

order to choose the combination that produces the detections that best match the ground truth (best Jaccard index). Importantly, the ground truth must then be known to systematically scan for parameters and choose the best set, so in principle choosing the parameters of the two others method this way disadvantaged our own approach that does not require any parameter settings. We chose to scan parameter ranges such that the difference of results which looks large could not be blamed on missettings the other methods' parameters: we objectively selected the best ones for the two other approaches.

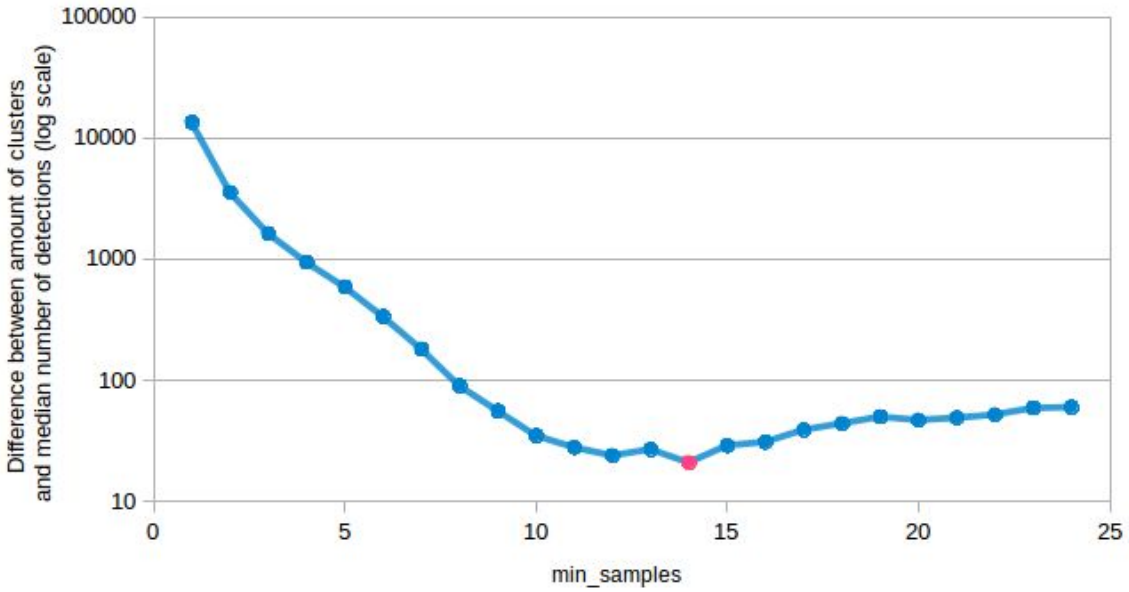

Supplementary Figure 3. Parameters estimation for the density-based algorithm DBSCAN. DBSCAN is a clustering algorithm that computes local density to identify clusters. This method is also able to handle noise by design, meaning that not every point in the dataset will necessarily be part of a given cluster in opposition to widely used algorithms such as k-means or Gaussian mixture models. These characteristics make this approach highly relevant to our problematic. The algorithm consists in an iterative process that uses two parameters to define density: ε (a distance measurement) and *min_samples* (a minimum amount of points). From our data, it was possible to estimate the best parameters for clustering. ε is directly related to the size of the nuclei, so we set it to the FWHM obtained from the average nucleus size at the detection step. On the other hand, the minimum number of points could not be directly estimated as the ε value, mainly because it depends on several uncontrolled factors such as the movement of the brain and the proportion of missing detections in a given time frames. We solved this problem through an iterative process. First, we assumed that the final number of detected clusters should be close to the median number of detections over time. This is a reasonable hypothesis since the number of neurons does not change through time. Then, the DBSCAN algorithm is iteratively applied for increasing values of *min_samples*. The min_samples value that best match the median number of detections over time is chosen as parameter for DBSCAN (indicated by the pink dot in the figure example).

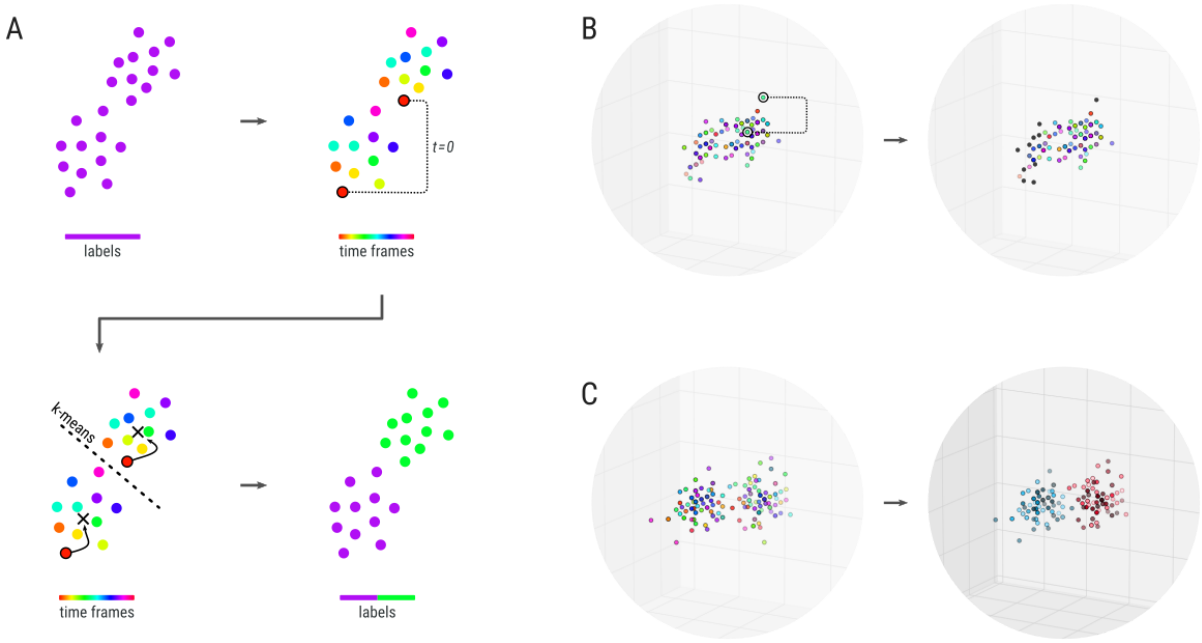

Supplementary Figure 4. Time information improves the quality of clusters. (**A**) A schematic representation of a case where the median number of time frames in a cluster is 2, meaning it contains 2 trajectories. The cluster is then automatically split. (**B**) Real cluster where the median number of time frames is 1, meaning it contains only one trajectory. Then duplicates (the points connected by a dash line) are marked as noise (black dots on the right image) and the point closest to the centroid cluster is kept while the other is discarded from the trajectory. (**C**) Real cluster where the median number of time frames is 2, with the resulting split cluster (in blue and red).

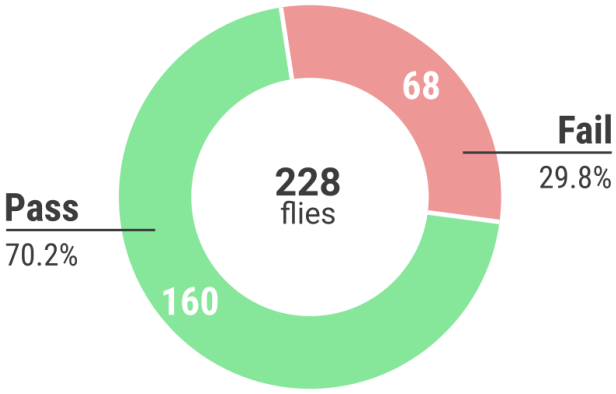

Supplementary Figure 5. Automated fly filter. In some acquisitions, the KCs did not show any response to the odor, while other acquisitions displayed a continuously erratic response. These are invalid acquisitions that were presumably caused by errors during the fly preparation. To avoid the bias of a manual selection of the datasets, we developed an automated procedure to sort the flies. It consisted in comparing the distribution of responsive neurons within the window of octanol stimulation and the initial control window at the beginning of the sequence, using a Mann-Whitney rank test. Flies with a p-value higher than 0.01 were excluded (“Fail”), the remaining flies were used for the analyses (“Pass”). This process guaranteed that the analysis was performed using flies that showed a biological response.

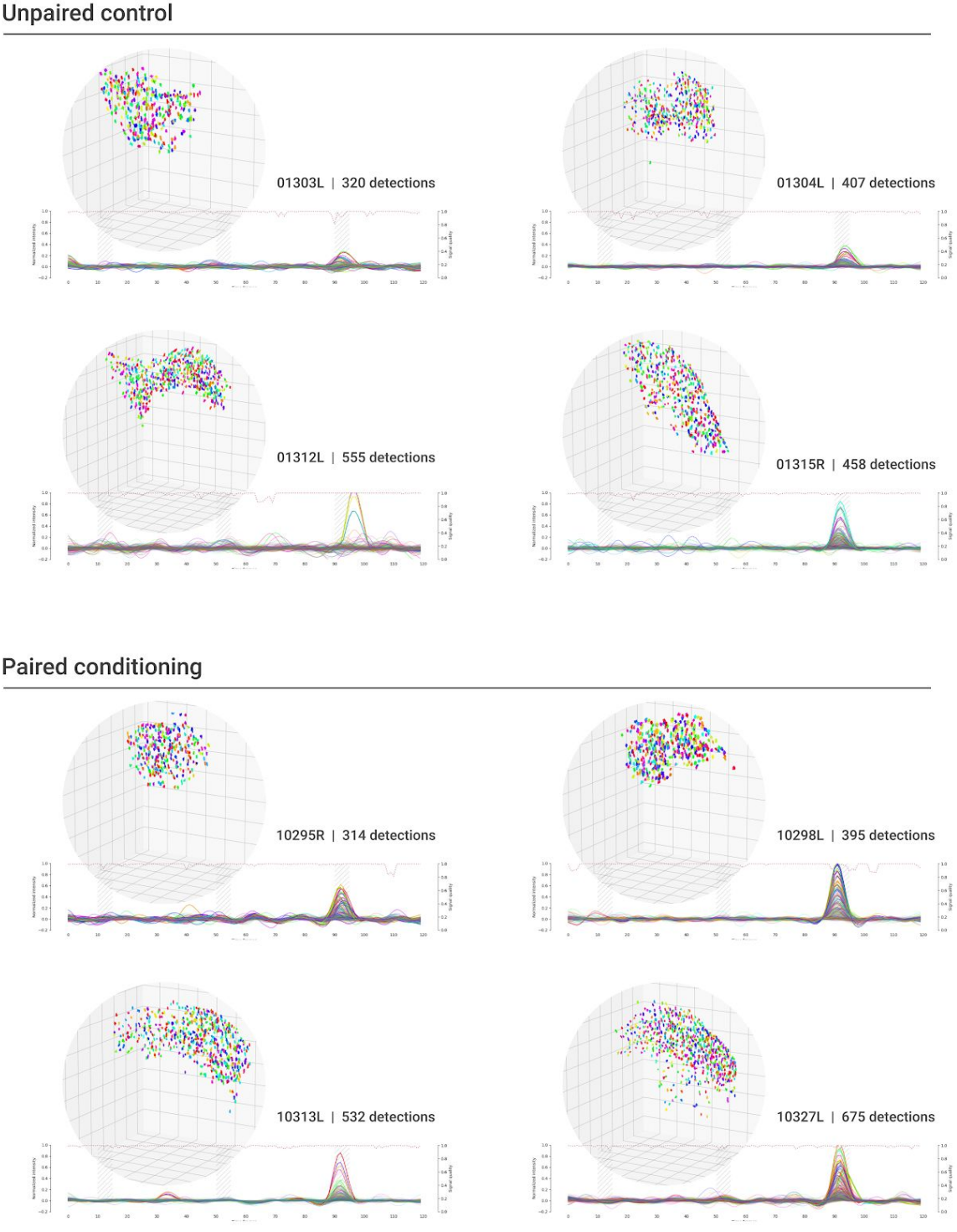

Supplementary Figure 6. Visualization of a few examples of analyzed flies. The top group shows examples from the unpaired control, whereas the bottom group shows flies subjected to paired conditioning. The 3D scatterplot illustrates the tracked detections for each fly (comprising a projection of all time frames to the 3D space); each track is individually colored. The line plot directly under each scatterplot shows the normalized signal measured for each neuron. The three hashed bars indicate the control regions: the first is no stimulus, the second is air and the third is octanol.

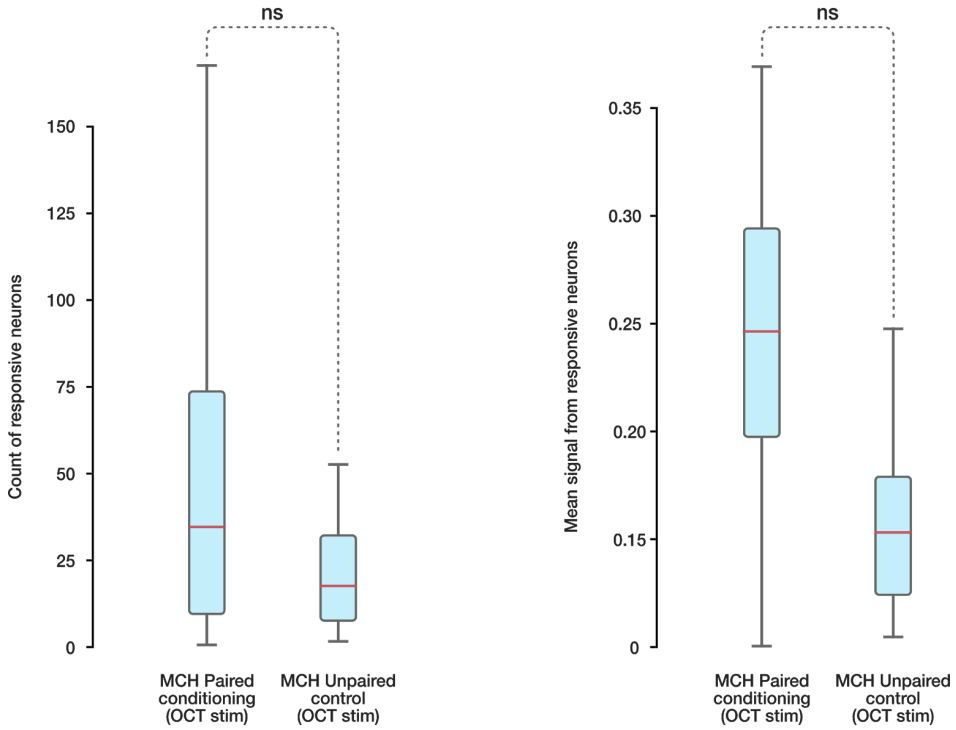

Supplementary Figure 7. Responsive neurons of flies trained with MCH and tested with OCT. Left: There is no significant difference in the count of OCT-responding neurons between the group trained with MCH and its unpaired control (Mann-Whitney test two-sided, p-value: 0.363336). During the conditioning, flies that received MCH also received OCT (albeit without the presentation of shocks). Right: Response intensities do not differ significantly between the MCH-trained paired and unpaired group (Mean signal comparison t-test p-value: 0.067987). The sample sizes is 11 for the paired and 15 for the unpaired group.

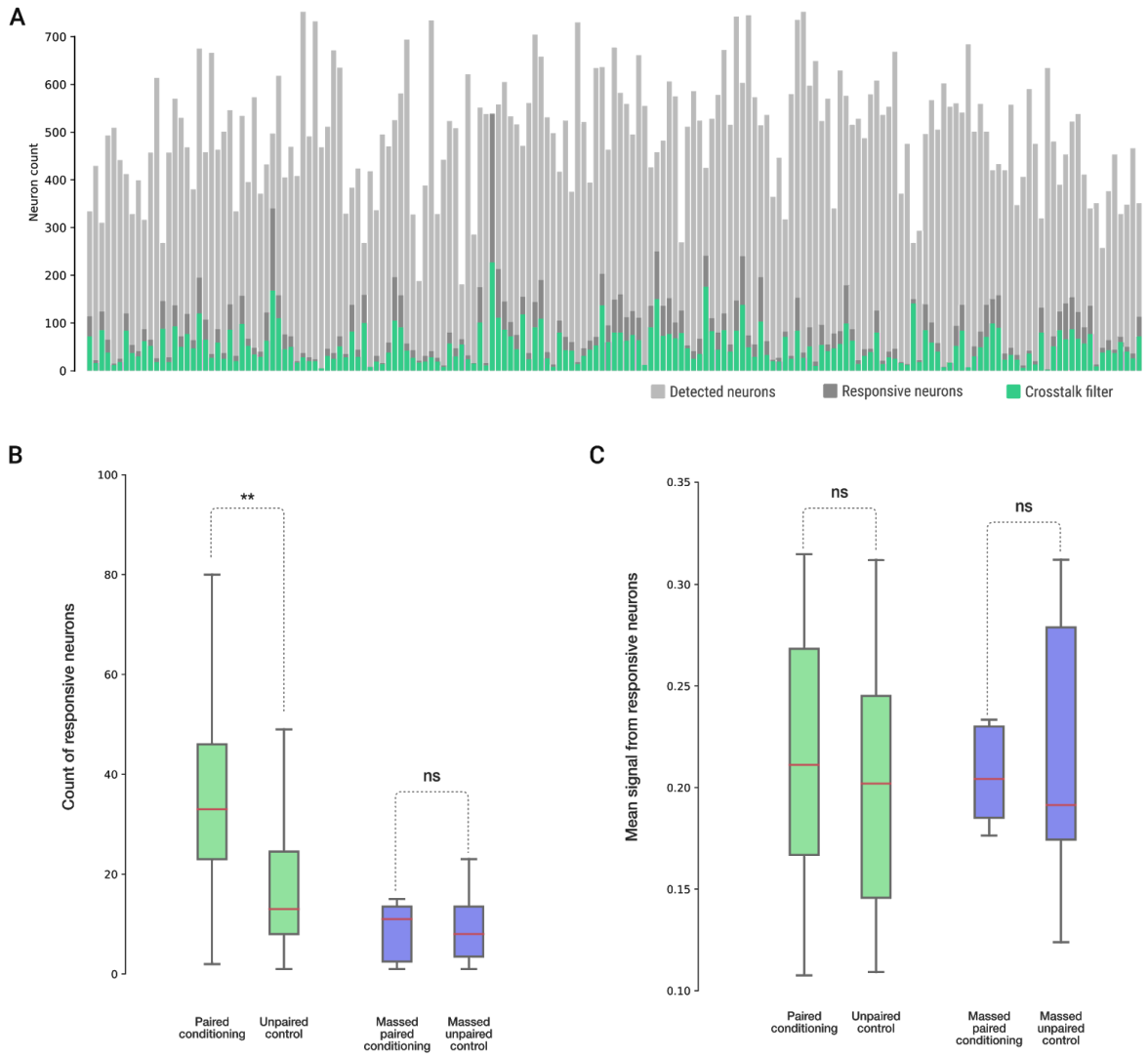

Supplementary Figure 8. In this control, we rule out the possibility for the observed increase in neuron count to be an artefact due to an increase in neighboring neuron intensity by applying a "crosstalk filter". From each group of closeby responsive neurons (defined as neurons closer than twice the diameter of the soma), only the neuron with the highest signal was kept. Thus the crosstalk filter discarded possibly suspectful neuron from the analysis, artificially ensuring that no neuron counted as responsive could be located close to one another. (**A**) Summary of the dataset, where each column corresponds to one fly. The light gray color shows the number of detected neurons, dark gray is the amount of responsive neurons (17.1% of total detections in average), and green represents only those neurons that passed the so called crosstalk filter, or in other words were kept (63% of the responsive neurons in average). (**B**) The same distributions as in Figure 3, after applying the crosstalk filter (and thus removing with high stringency nuclei that might be erroneously selected as responsive), show that the difference in count between the group trained with OCT and its control is conserved (p-value: 0.0014992), and that the difference in count remains non-significant for the control group with massed training (p-value: 0.881899). A Mann-Whitney two-sided test was performed in both cases. (**C**) Similar conclusion can also be drawn for the mean signal intensities from responsive neurons that shows no statistically significant differences. The sample sizes from the 4 groups (from left to right) are 29, 27, 14 and 16.

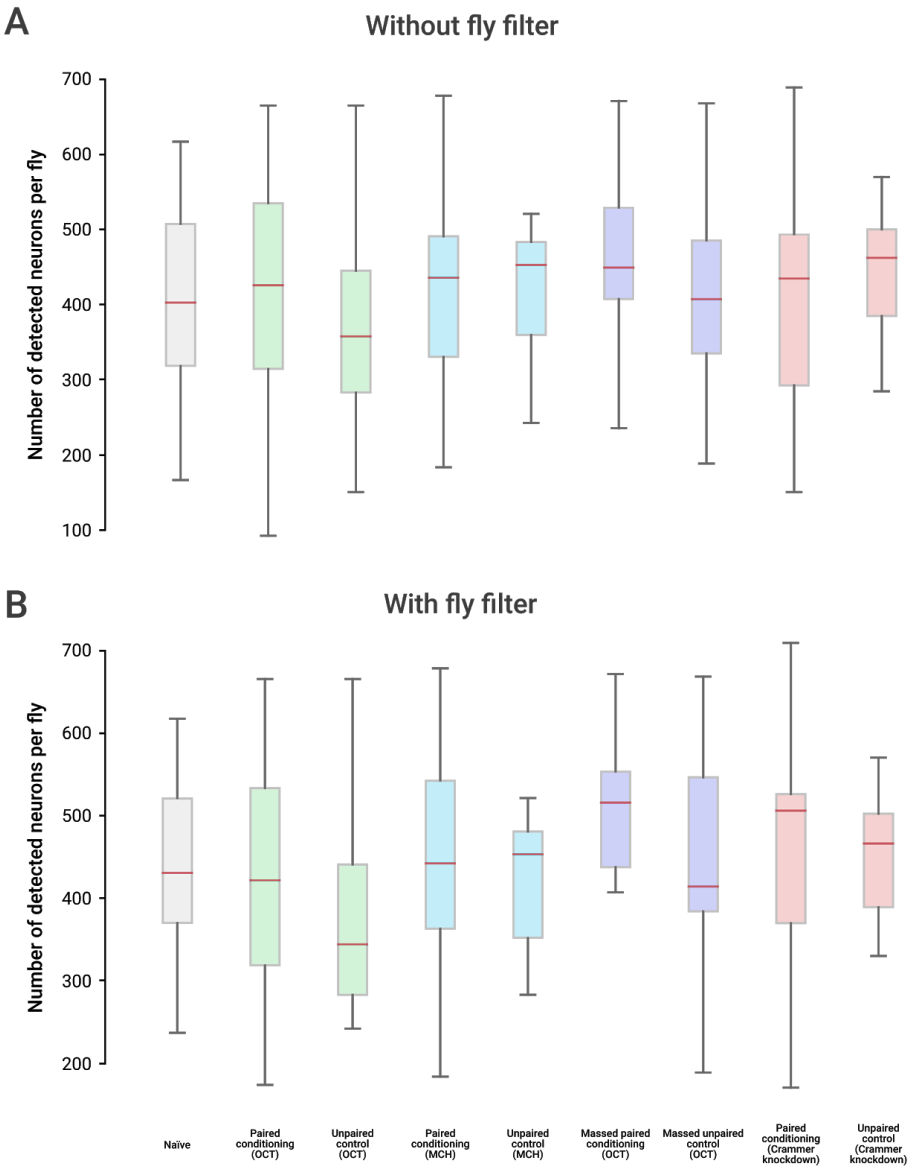

Supplementary Figure 9. The total number of detected neurons is stable before and after applying our quality control filter. (**A**) The total amount of soma detected using the Gal4-driver channel for all tested groups does not show any significant difference between the datasets (Kruskal-Wallis H-test p-value: 0.303595). The sample sizes from the 9 groups (from left to right) are 23, 37, 44, 22, 23, 24, 22, 16 and 18. (**B**) The same distributions as in (A), but restricted to the flies that passed the automated quality control filter (Kruskal-Wallis H-test p-value: 0.1549522). The sample sizes from the 9 groups (from left to right) are 14, 30, 31, 12, 15, 16, 17, 12 and 17.

Supplementary Figure 10. Detection of 3D stack artifacts. A 3D volumetric reconstruction of the *mCherry* channel is shown for three consecutive time frames; the artifact of an anchored z position is noticeable in the middle time frame. To automatically detect the artifact, we made the following assumptions: 1) during a normal acquisition, the mushroom body center of mass (based on the set of detected nuclei) should only move slightly. 2) Since a considerable part of the MB was missing when this artifact arose, there should be drastic shift in the center of mass at this time frame. Thus, we measured the derivative of the centroid position through time, normalized to a range between 0 and 1. This quality measurement can then work as an indirect way to identify the time frames in which there was a microscope artifact. A threshold must still be set as the minimum quality level that can be used for the analysis; by visually comparing the quality measurement and the 3D stacks, the value was set at 80%. Time frames with lower values were thus removed, and the missing neuron positions interpolated in time.

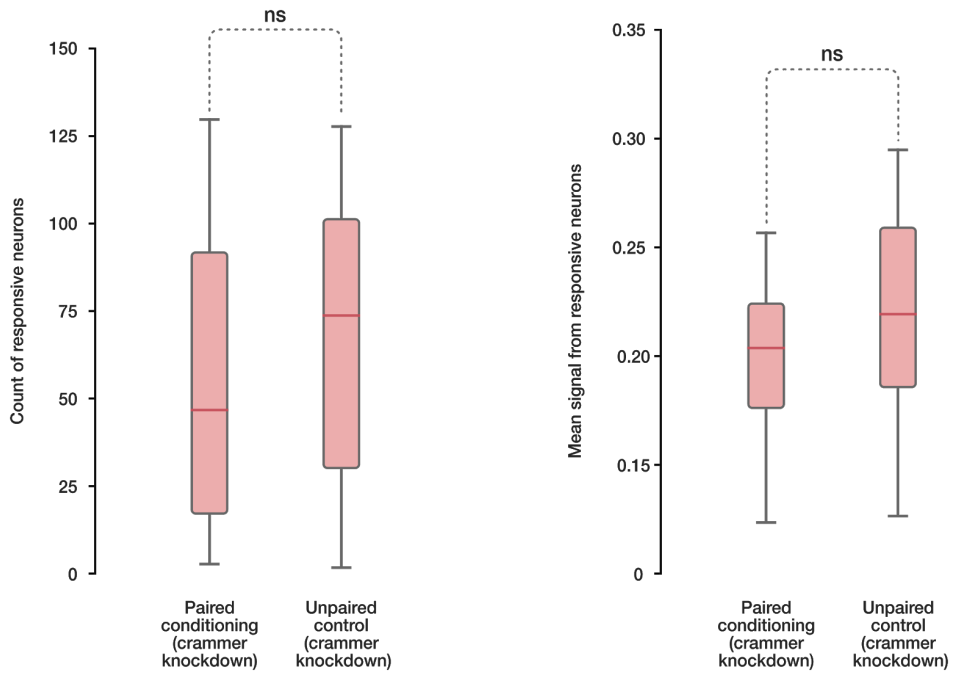

Supplementary Figure 11. Detection of responsive neurons from 5x spaced trained flies after Cer knockdown. The UAS-Cer-RNAi was targeted by VT30559-Gal4 simultaneously with the two reporter UAS-GCaMP6f and UAS-NLS-mCherry. Left: Comparison of distribution for the count of responsive

neurons between the paired conditioning (n=11) and unpaired control (n=15) groups (Mann-Whitney two-sided test p-value: 0.56800). Right: Distribution of mean signal for responsive neurons from the two groups, showing no statistical difference (t-test p-value: 0.388411).

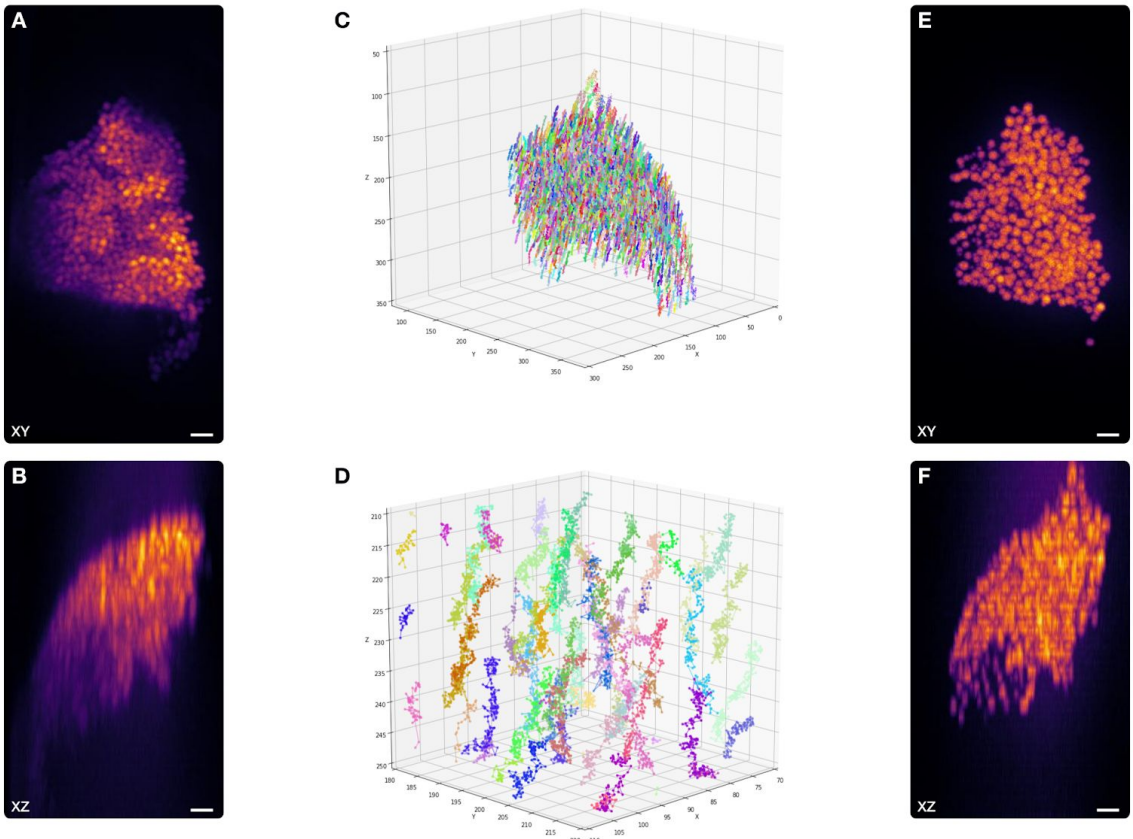

Supplementary Figure 12. Synthetic 3D+time stacks of densely packed nuclei to evaluate the tracking performance against other methods. (**A**) Maximum intensity projection of a real 3D stack that provides a foreground region to generate synthetic somata, along the Z axis. (**B**) Maximum intensity projection of the same 3D stack along the Y axis. (**C**) 2000 generated trajectories in successive volumes over time (see online methods). (**D**) Detail of a central region of the generated trajectories. (**E**) Maximum intensity projection of a synthetic 3D+time sequence generated by convolution and noise addition from the generated trajectories, along the Z axis. (**F**) Maximum intensity projection of the same synthetic 3D stack along the Y axis. Scale bars are 10µm. Although synthetic 3D + time sequences are close to the real 3D + time sequences, they are of course not similar, but a great advantage over manual annotation is that the ground truth is known and all (2000) nuclei are then annotated. Therefore they enable to provide satisfactory quantitative comparisons between algorithms for detection and tracking. Importantly, they enable to quantify False Positive (see supplementary figure 13).

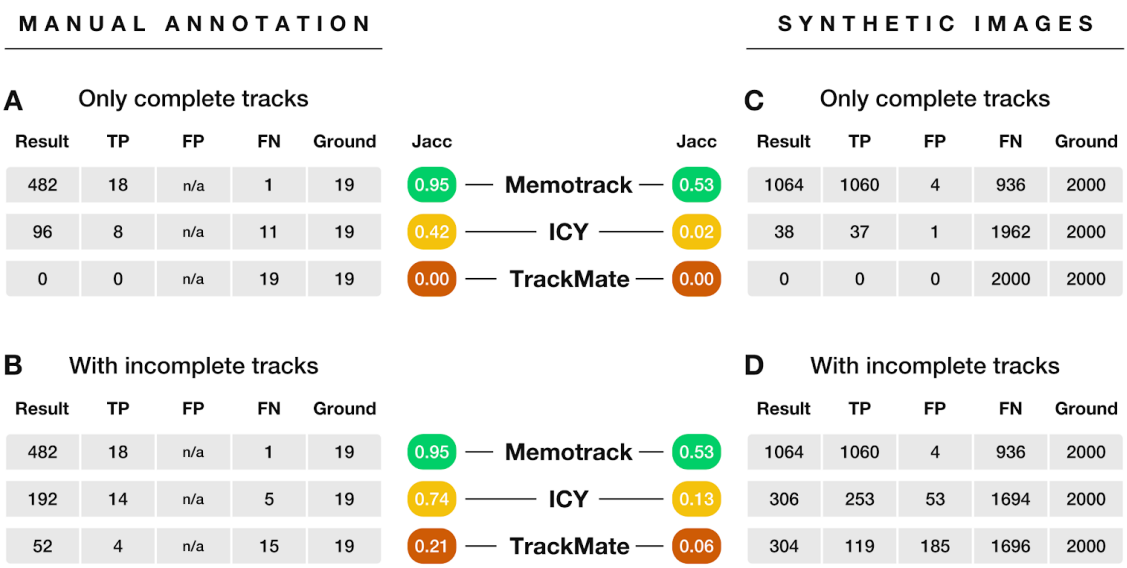

Supplementary Figure 13. Validation of our tracking approach Memotrack against two other methods, ICY and TrackMate, using manual annotated and synthetic 3D+time sequences. **A.** Results obtained using manual annotations and considering only complete trajectories along the whole sequence. That is, if the duration of a trajectory provided by a software program was less than the length of the sequence, it was discarded. This is because the signal needs to be captured along the whole sequence, not during a subpart of it. TP is True Positive, FP is False Positive, FN is False Negative, Result is the output of a software and Ground is the ground truth. Note that False Positive are not available for manual annotation because it was impossible to annotate exhaustively all trajectories of a 3D+time sequence. Memotrack, our method, outperforms other methods with 18 out of the 19 annotated trajectory correctly retrieved. **B.** Results obtained using manual annotations and considering trajectories with length at least as long as half of the whole sequence. This relax in stringency increases the number of successfully tracked nuclei by other software. Those results would not be acceptable or even useful as such to monitor the signal all along the sequence but they enable to understand partly the weakness of the other approaches. Other approaches cannot track nuclei over a long time period without failing because of the low accuracy of spot detection. Our approach, that rely on the non rigid registration of the whole sequence is very robust to detection errors and actually tracks all nuclei that were successfully detected enough time to form a cluster. For the same reason, the length threshold cannot improve the result obtained by our approach as all trajectories retrieved is the length of the full sequence. **C.** Results obtained using synthetic annotations and considering only complete trajectories along the whole sequence. Memotrack, our method, outperforms other methods. **D.** Results obtained using synthetic annotations and considering trajectories with length at least as long as half of the whole sequence. Interestingly, while unusable, we see here that this relax in stringency increases the number of tracked nuclei by other methods but also increases the number of false positive, indicating that even small trajectories provided by those software program are not necessarily correct.

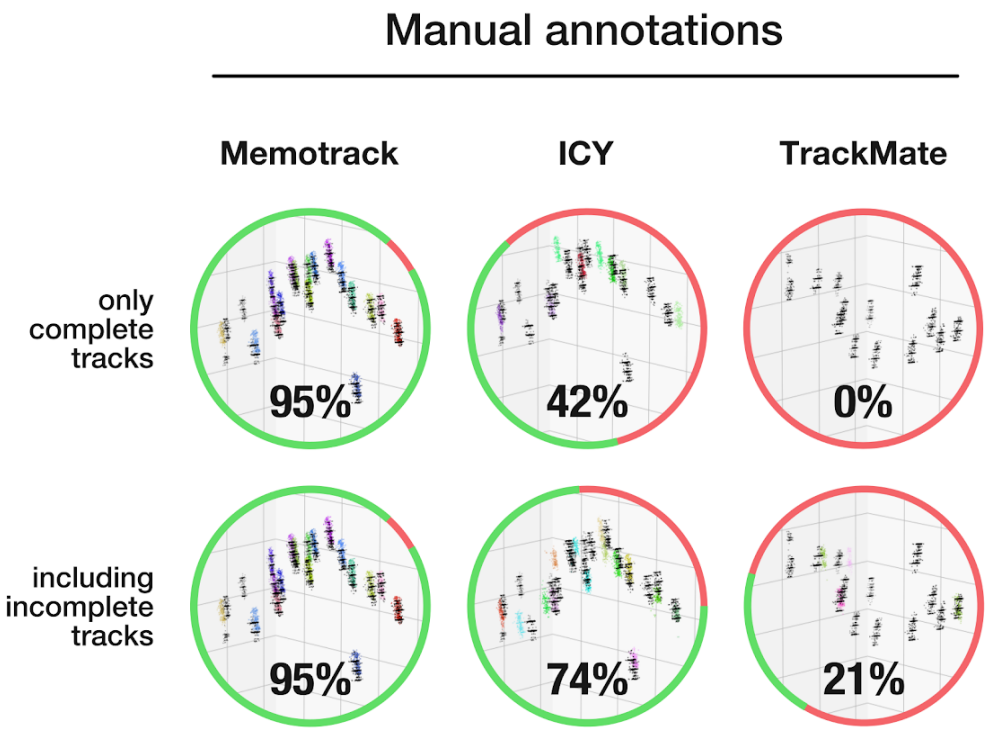

Supplementary Figure 14. Visualization of manually annotated nuclei trajectories (in black, see online methods) and their corresponding trajectories obtained by the tracking software (in color). Top row: only complete trajectories that last the whole sequence were kept, it is the case we were interested in to monitor the single cell signal all along the sequence. We can see that, beyond the fact our method tracks correctly most manually annotated nuclei, the closest trajectories provided by ICY may in fact match other nuclei and be False Positives, an hypothesis that cannot be validated or unvalidated because it was impossible to manually annotate all trajectories in the sequence of 3D stacks. Bottom row: result when we allowed the length of the trajectories to be shorter but at least as long as half of the sequence. Again, those trajectories could not be used for the analysis as they are too short but underline the main limitation of other approaches: other approaches cannot track object stably over a long period of time due to the unreliability of the spot detection step.

Supplementary Videos

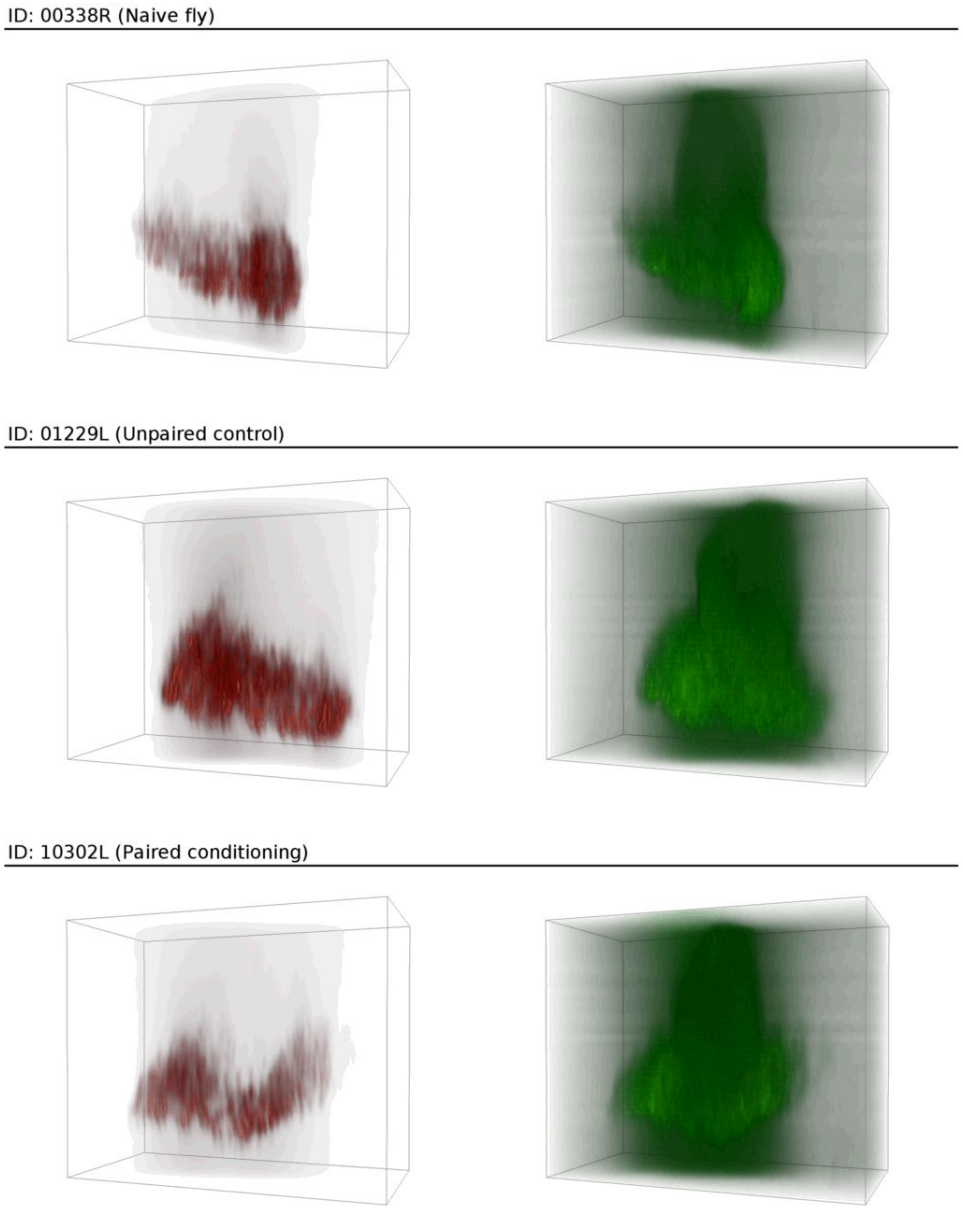

Supplementary Video 1. Volumetric rendering of the raw acquired data. The videos on the left represent the nuclei of the mushroom body neurons, while the videos on the right portray the GCaMP activity of those neurons. The appearance of ‘OCT’ at the top right of each row corresponds to the time when flies received an octanol stimulation.

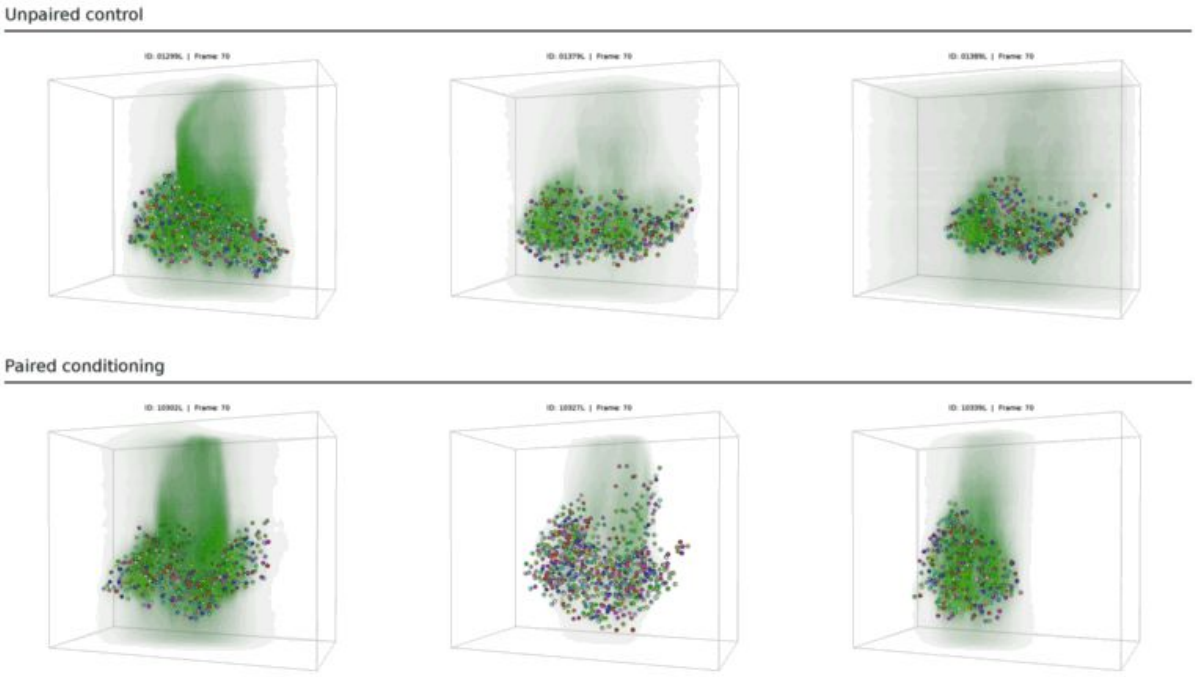

Supplementary Video 2. Volumetric rendering of GCaMP activity together with tracked neurons. The top row shows the signal for three flies from the unpaired control group, while the bottom row shows three flies from the group that received the paired conditioning. Flies received the octanol stimulation starting at frame 90 (corresponding to the appearance of ‘OCT’ at the top right of each row).

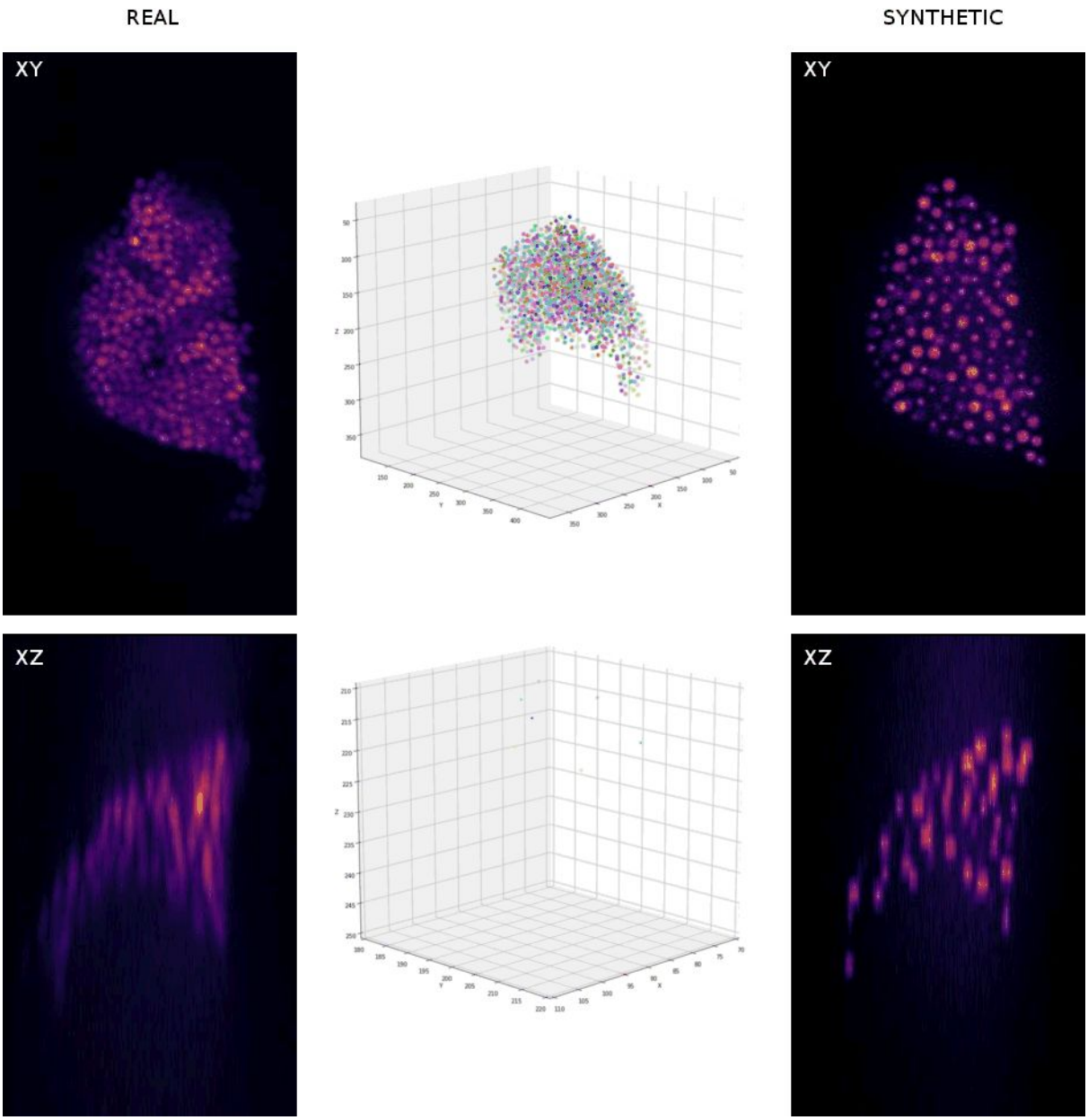

Supplementary Video 3. Generation of synthetic sequence of 3D stacks. Left column shows the middle 2D image (not a maximum intensity projection) from a real 3D stack, in XY (top) and XZ (bottom) views over time. Panels in the middle column shows the generated synthetic coordinates (see online methods) based on the real 3D stack on the left. The top panel shows an overview of all generated 3D positions overtime corresponding to the MB cell bodies on the left. The bottom panel shows a zoomed version inside the synthetic cloud and synthetic trajectories are drawn over time. Right column shows the middle image of the resulting synthetic sequence obtained by convolving the synthetic positions with the PSF of the microscope, adding noise and a similar subsampling to reproduce the anisotropy of the real sequence of 3D stacks, in XY (top) and XZ (bottom) views over time.

References

1. Tonegawa, S., Pignatelli, M., Roy, D. S. & Ryan, T. J. Memory engram storage and retrieval. *Curr. Opin. Neurobiol.* **35**, 101–109 (2015).
2. Poo, M.-M. *et al.* What is memory? The present state of the engram. *BMC Biol.* **14**, 40 (2016).
3. DeNardo, L. & Luo, L. Genetic strategies to access activated neurons. *Curr. Opin. Neurobiol.* **45**, 121–129 (2017).
4. Kandel, E. R. The molecular biology of memory: cAMP, PKA, CRE, CREB-1, CREB-2, and CPEB. *Mol. Brain* **5**, 14 (2012).
5. Yang, W. & Yuste, R. In vivo imaging of neural activity. *Nat. Methods* **14**, 349–359 (2017).
6. Kitamura, T. *et al.* Engrams and circuits crucial for systems consolidation of a memory. *Science* **356**, 73–78 (2017).
7. Keene, A. C. & Waddell, S. Drosophila olfactory memory: single genes to complex neural circuits. *Nat. Rev. Neurosci.* **8**, 341–354 (2007).
8. Riemensperger, T., Pech, U., Dipt, S. & Fiala, A. Optical calcium imaging in the nervous system of Drosophila melanogaster. *Biochim. Biophys. Acta* **1820**, 1169–1178 (2012).
9. Tully, T., Preat, T., Boynton, S. C. & Del Vecchio, M. Genetic dissection of consolidated memory in Drosophila. *Cell* **79**, 35–47 (1994).
10. Keller, A. & Vosshall, L. B. Decoding olfaction in Drosophila. *Curr. Opin. Neurobiol.* **13**, 103–110 (2003).
11. Honegger, K. S., Campbell, R. A. A. & Turner, G. C. Cellular-resolution population imaging reveals robust sparse coding in the Drosophila mushroom body. *J. Neurosci.* **31**, 11772–11785 (2011).
12. Campbell, R. A. A. *et al.* Imaging a population code for odor identity in the Drosophila

mushroom body. *J. Neurosci.* **33**, 10568–10581 (2013).

13. Caron, S. J. C., Ruta, V., Abbott, L. F. & Axel, R. Random convergence of olfactory inputs in the Drosophila mushroom body. *Nature* **497**, 113–117 (2013).
14. Aso, Y. *et al.* The neuronal architecture of the mushroom body provides a logic for associative learning. *Elife* **3**, e04577 (2014).
15. Laurent, G. Olfactory network dynamics and the coding of multidimensional signals. *Nat. Rev. Neurosci.* **3**, 884–895 (2002).
16. Wolff, G. H. & Strausfeld, N. J. Genealogical correspondence of mushroom bodies across invertebrate phyla. *Curr. Biol.* **25**, 38–44 (2015).
17. Aso, Y. *et al.* Specific dopaminergic neurons for the formation of labile aversive memory. *Curr. Biol.* **20**, 1445–1451 (2010).
18. Aso, Y. & Rubin, G. M. Dopaminergic neurons write and update memories with cell-type-specific rules. *Elife* **5**, (2016).
19. Gervasi, N., Tchénio, P. & Preat, T. PKA dynamics in a Drosophila learning center: coincidence detection by rutabaga adenylyl cyclase and spatial regulation by dunce phosphodiesterase. *Neuron* **65**, 516–529 (2010).
20. Owald, D. & Waddell, S. Olfactory learning skews mushroom body output pathways to steer behavioral choice in Drosophila. *Curr. Opin. Neurobiol.* **35**, 178–184 (2015).
21. Séjourné, J. *et al.* Mushroom body efferent neurons responsible for aversive olfactory memory retrieval in Drosophila. *Nat. Neurosci.* **14**, 903–910 (2011).
22. Akalal, D.-B. G., Yu, D. & Davis, R. L. A late-phase, long-term memory trace forms in the γ neurons of Drosophila mushroom bodies after olfactory classical conditioning. *J. Neurosci.* **30**, 16699–16708 (2010).
23. Yu, D., Akalal, D.-B. G. & Davis, R. L. Drosophila alpha/beta mushroom body neurons form a branch-specific, long-term cellular memory trace after spaced olfactory conditioning. *Neuron* **52**, 845–855 (2006).

24. Chen, L., Chan, L. L. H., Zhao, Z. & Yan, H. A novel cell nuclei segmentation method for 3D C. elegans embryonic time-lapse images. *BMC Bioinformatics* **14**, 328 (2013).
25. Nakano, A. Spinning-disk confocal microscopy—a cutting-edge tool for imaging of membrane traffic. *Cell Struct. Funct.* **27**, 349–355 (2002).
26. Nakano, A. Spinning-disk confocal microscopy -- a cutting-edge tool for imaging of membrane traffic. *Cell Struct. Funct.* **27**, 349–355 (2002).
27. Philips, G. T. & Carew, T. J. It's all about timing. *Cell* **139**, 23–25 (2009).
28. Comas, D., Petit, F. & Preat, T. Drosophila long-term memory formation involves regulation of cathepsin activity. *Nature* **430**, 460–463 (2004).
29. Štěpka, K. *et al.* Performance and sensitivity evaluation of 3D spot detection methods in confocal microscopy. *Cytometry A* **87**, 759–772 (2015).
30. Matula, P. *et al.* Quantification of fluorescent spots in time series of 3D confocal microscopy images of endoplasmic reticulum exit sites based on the HMAX transform. in *SPIE Medical Imaging* 76261H–76261H–7 (International Society for Optics and Photonics, 2010).
31. Olivo-Marin, J.-C. Extraction of spots in biological images using multiscale products. *Pattern Recognit.* **35**, 1989–1996 (2002).
32. Maviel, T., Durkin, T. P., Menzaghi, F. & Bontempi, B. Sites of neocortical reorganization critical for remote spatial memory. *Science* **305**, 96–99 (2004).
33. Luo, L., Callaway, E. M. & Svoboda, K. Genetic Dissection of Neural Circuits: A Decade of Progress. *Neuron* **98**, 865 (2018).
34. Choi, J.-H. *et al.* Interregional synaptic maps among engram cells underlie memory formation. *Science* **360**, 430–435 (2018).
35. Lee, W.-C. A. *et al.* A dynamic zone defines interneuron remodeling in the adult neocortex. *Proc. Natl. Acad. Sci. U. S. A.* **105**, 19968–19973 (2008).
36. Rozov, A. V., Valiullina, F. F. & Bolshakov, A. P. Mechanisms of Long-Term Plasticity of

Hippocampal GABAergic Synapses. *Biochemistry* **82**, 257–263 (2017).

37. Lin, A. C., Bygrave, A. M., de Calignon, A., Lee, T. & Miesenböck, G. Sparse, decorrelated odor coding in the mushroom body enhances learned odor discrimination. *Nat. Neurosci.* **17**, 559–568 (2014).
38. Liu, X. & Davis, R. L. The GABAergic anterior paired lateral neuron suppresses and is suppressed by olfactory learning. *Nat. Neurosci.* **12**, 53–59 (2009).
39. Zhou, M. *et al.* Suppression of GABAergic neurons through D2-like receptor secures efficient conditioning in Drosophila aversive olfactory learning. *Proc. Natl. Acad. Sci. U. S. A.* (2019). doi:10.1073/pnas.1812342116
40. Fino, E., Deniau, J.-M. & Venance, L. Brief subthreshold events can act as Hebbian signals for long-term plasticity. *PLoS One* **4**, e6557 (2009).
41. Han, J.-H. *et al.* Neuronal competition and selection during memory formation. *Science* **316**, 457–460 (2007).
42. Myronenko, A. & Song, X. Point set registration: coherent point drift. *IEEE Trans. Pattern Anal. Mach. Intell.* **32**, 2262–2275 (2010).
43. Schindelin, J. *et al.* Fiji: an open-source platform for biological-image analysis. *Nat. Methods* **9**, 676–682 (2012).
44. Chenouard, N. *et al.* Objective comparison of particle tracking methods. *Nat. Methods* **11**, 281–289 (2014).
45. Chenouard, N., Bloch, I. & Olivo-Marin, J.-C. Multiple hypothesis tracking for cluttered biological image sequences. *IEEE Trans. Pattern Anal. Mach. Intell.* **35**, 2736–3750 (2013).
46. Tinevez, J.-Y. *et al.* TrackMate: An open and extensible platform for single-particle tracking. *Methods* **115**, 80–90 (2017).
47. Luo, J. *et al.* A comparison of batch effect removal methods for enhancement of prediction performance using MAQC-II microarray gene expression data.

Pharmacogenomics J. **10**, 278–291 (2010).

48. Birmingham, A. *et al.* Statistical methods for analysis of high-throughput RNA interference screens. *Nat. Methods* **6**, 569–575 (2009).
49. Matula, P. *et al.* Quantification of fluorescent spots in time series of 3D confocal microscopy images of endoplasmic reticulum exit sites based on the HMAX transform. in *Medical Imaging 2010: Biomedical Applications in Molecular, Structural, and Functional Imaging* **7626**, 76261H (International Society for Optics and Photonics, 2010).

List of Figures

Bibliography

1. Hawkins, J. & Blakeslee, S. *On Intelligence: How a New Understanding of the Brain Will Lead to the Creation of Truly Intelligent Machines* ISBN: 0805078533 (St. Martin's Griffin, 2005).
2. Haykin, S. *Neural Networks: A Comprehensive Foundation (2nd Edition)* 842. ISBN: 0132733501. <http://www.amazon.com/Neural-Networks-Comprehensive-Foundation-Edition/dp/0132733501> (Prentice Hall, 1998).
3. LeCun, Y., Bengio, Y. & Hinton, G. Deep learning. *nature* **521,** 436 (2015).
4. Krizhevsky, A., Sutskever, I. & Hinton, G. E. *Imagenet classification with deep convolutional neural networks* in *Advances in neural information processing systems* (2012), 1097–1105.
5. Van den Oord, A. *et al. WaveNet: A Generative Model for Raw Audio* 2016. eprint: arXiv:1609.03499.
6. Rolls, E. T. & Treves, A. The relative advantages of sparse versus distributed encoding for associative neuronal networks in the brain. *Network: computation in neural systems* **1,** 407–421 (1990).
7. Scanziani, M. & Häusser, M. Electrophysiology in the age of light. *Nature* **461,** 930–939 (Oct. 2009).
8. Heeger, D. J. & Ress, D. What does fMRI tell us about neuronal activity? *Nature Reviews Neuroscience* **3,** 142 (2002).
9. Squire, L. R. Memory and brain (1987).
10. Binder, J. R. & Desai, R. H. The neurobiology of semantic memory. *Trends in cognitive sciences* **15,** 527–536 (2011).
11. Ferbinteanu, J., Kennedy, P. J. & Shapiro, M. L. Episodic memory—from brain to mind. *Hippocampus* **16,** 691–703 (2006).
12. Gasbarri, A., Pompili, A., Packard, M. G. & Tomaz, C. Habit learning and memory in mammals: behavioral and neural characteristics. *Neurobiology of learning and memory* **114,** 198–208 (2014).
13. Herry, C. & Johansen, J. P. Encoding of fear learning and memory in distributed neuronal circuits. *Nature neuroscience* **17,** 1644 (2014).
14. Baddeley, A. Working memory: looking back and looking forward. *Nature reviews neuroscience* **4,** 829 (2003).
15. Goldman-Rakic, P. S. Working memory and the mind. *Scientific American* **267,** 110–117 (1992).

16. Matthes, H. *et al.* Mouse 5-hydroxytryptamine5A and 5-hydroxytryptamine5B receptors define a new family of serotonin receptors: cloning, functional expression, and chromosomal localization. *Molecular pharmacology* **43,** 313–319 (1993).

17. Livnat, S., Felten, S. Y., Carlson, S. L., Bellinger, D. L. & Felten, D. L. Involvement of peripheral and central catecholamine systems in neural-immune interactions. *Journal of neuroimmunology* **10,** 5–30 (1985).

18. Callier, S. *et al.* Evolution and cell biology of dopamine receptors in vertebrates. *Biology of the Cell* **95,** 489–502 (2003).

19. Smidt, M. P. & Burbach, J. P. H. A passport to neurotransmitter identity. *Genome biology* **10,** 229 (2009).

20. Wildemann, B. & Bicker, G. Developmental expression of nitric oxide/cyclic GMP synthesizing cells in the nervous system ofDrosophila melanogaster. *Journal of neurobiology* **38,** 1–15 (1999).

21. Chiang, A.-S. *et al.* Three-dimensional reconstruction of brain-wide wiring networks in Drosophila at single-cell resolution. *Current Biology* **21,** 1–11 (2011).

22. Freeman, M. R. & Doherty, J. Glial cell biology in Drosophila and vertebrates. *Trends in neurosciences* **29,** 82–90 (2006).

23. Lemon, W. C. *et al.* Whole-central nervous system functional imaging in larval Drosophila. *Nature communications* **6,** 7924 (2015).

24. Freeman, M. R. Drosophila central nervous system glia. *Cold Spring Harbor perspectives in biology* **7,** a020552 (2015).

25. Stork, T., Sheehan, A., Tasdemir-Yilmaz, O. E. & Freeman, M. R. Neuron-glia interactions through the Heartless FGF receptor signaling pathway mediate morphogenesis of Drosophila astrocytes. *Neuron* **83,** 388–403 (2014).

26. Dupuis, J., Louis, T., Gauthier, M. & Raymond, V. Insights from honeybee (Apis mellifera) and fly (Drosophila melanogaster) nicotinic acetylcholine receptors: from genes to behavioral functions. *Neuroscience & Biobehavioral Reviews* **36,** 1553–1564 (2012).

27. Hannan, F. & Hall, L. M. in *Comparative Molecular Neurobiology* 98–145 (Springer, 1993).

28. De Belle, J. S. & Heisenberg, M. Associative odor learning in Drosophila abolished by chemical ablation of mushroom bodies. *Science* **263,** 692–695 (1994).

29. Tong, M. T., Peace, S. T. & Cleland, T. A. Properties and mechanisms of olfactory learning and memory. *Frontiers in behavioral neuroscience* **8,** 238 (2014).

30. Pavlov, I. P. *Conditioned reflexes* 1927.

31. Hawkins, R. D., Abrams, T. W., Carew, T. J. & Kandel, E. R. A cellular mechanism of classical conditioning in Aplysia: activity-dependent amplification of presynaptic facilitation. *Science* **219,** 400–405 (1983).

32. Kandel, E. & Tauc, L. Heterosynaptic facilitation in neurones of the abdominal ganglion of Aplysia depilans. *The Journal of Physiology* **181,** 1–27 (1965).

33. Castellucci, V., Pinsker, H., Kupfermann, I. & Kandel, E. R. Neuronal mechanisms of habituation and dishabituation of the gill-withdrawal reflex in Aplysia. *Science* **167,** 1745–1748 (1970).

34. Byrne, J. H. & Kandel, E. R. Presynaptic facilitation revisited: state and time dependence. *Journal of Neuroscience* **16,** 425–435 (1996).

35. Kandel, E. R. & Schwartz, J. H. Molecular biology of learning: modulation of transmitter release. *Science* **218,** 433–443 (1982).

36. Cedar, H. & Schwartz, J. H. Cyclic Adenosine Monophosphate in the Nervous System of Aplysia californica: II. Effect of serotonin and dopamine. *The Journal of general physiology* **60,** 570–587 (1972).

37. Castellucci, V. F. *et al.* Intracellular injection of t he catalytic subunit of cyclic AMP-dependent protein kinase simulates facilitation of transmitter release underlying behavioral sensitization in Aplysia. *Proceedings of the National Academy of Sciences* **77,** 7492–7496 (1980).

38. Dash, P. K., Hochner, B. & Kandel, E. R. Injection of the cAMP-responsive element into the nucleus of Aplysia sensory neurons blocks long-term facilitation. *Nature* **345,** 718 (1990).

39. Benzer, S. Fine structure of a genetic region in bacteriophage. *Proceedings of the National Academy of Sciences* **41,** 344–354 (1955).

40. Chapeville, F. *et al.* On the role of soluble ribonucleic acid in coding for amino acids. *Proceedings of the National Academy of Sciences* **48,** 1086–1092 (1962).

41. Benzer, S. Behavioral mutants of Drosophila isolated by countercurrent distribution. *Proceedings of the National Academy of Sciences* **58,** 1112–1119 (1967).

42. Quinn, W. G., Harris, W. A. & Benzer, S. Conditioned behavior in Drosophila melanogaster. *Proceedings of the National Academy of Sciences* **71,** 708–712 (1974).

43. Konopka, R. J. & Benzer, S. Clock mutants of Drosophila melanogaster. *Proceedings of the National Academy of Sciences* **68,** 2112–2116 (1971).

44. Tully, T. & Quinn, W. G. Classical conditioning and retention in normal and mutantDrosophila melanogaster. *Journal of Comparative Physiology A* **157,** 263–277 (1985).

45. Dudai, Y., Jan, Y.-N., Byers, D., Quinn, W. G. & Benzer, S. dunce, a mutant of Drosophila deficient in learning. *Proceedings of the National Academy of Sciences* **73,** 1684–1688 (1976).

46. Rogers, M., Graham, J. & Tonge, R. P. Using statistical image models for objective evaluation of spot detection in two-dimensional gels. *Proteomics* **3,** 879–886 (2003).

47. Guan, H., Kubota, T., Huang, X., Zhou, X. S. & Turk, M. *Automatic hot spot detection and segmentation in whole body FDG-PET images* in *Image Processing, 2006 IEEE International Conference on* (2006), 85–88.

48. Thomann, D., Rines, D. R., Sorger, P. K. & Danuser, G. Automatic fluorescent tag detection in 3D with super-resolution: application to the analysis of chromosome movement. *Journal of microscopy* **208,** 49–64 (2002).

49. Meijering, E. Cell segmentation: 50 years down the road [life sciences]. *IEEE Signal Processing Magazine* **29,** 140–145 (2012).

50. Anoraganingrum, D. *Cell segmentation with median filter and mathematical morphology operation* in *Image Analysis and Processing, 1999. Proceedings. International Conference on* (1999), 1043–1046.

51. Liao, Q. & Deng, Y. *An accurate segmentation method for white blood cell images* in *Biomedical Imaging, 2002. Proceedings. 2002 IEEE International Symposium on* (2002), 245–248.

52. Genovesio, A. *et al.* Multiple particle tracking in 3-D+ t microscopy: method and application to the tracking of endocytosed quantum dots. *IEEE Transactions on Image Processing* **15,** 1062–1070 (2006).

53. Saxton, M. J. & Jacobson, K. Single-particle tracking: applications to membrane dynamics. *Annual review of biophysics and biomolecular structure* **26,** 373–399 (1997).

54. Jaqaman, K. *et al.* Robust single-particle tracking in live-cell time-lapse sequences. *Nature methods* **5,** 695 (2008).

55. Schindelin, J. *et al.* Fiji: an open-source platform for biological-image analysis. *Nature methods* **9,** 676 (2012).

56. De Chaumont, F. *et al.* Icy: an open bioimage informatics platform for extended reproducible research. *Nature methods* **9,** 690 (2012).

57. Carpenter, A. E. *et al.* CellProfiler: image analysis software for identifying and quantifying cell phenotypes. *Genome biology* **7,** R100 (2006).

58. Zelle, J. M. *Python programming: an introduction to computer science* (Franklin, Beedle & Associates, Inc., 2004).

59. Robinson, D. *The Incredible Growth of Python* Accessed: 2018-06-26. <https://stackoverflow.blog/2017/09/06/incredible-growth-python/>.

60. Van der Walt, S. *et al.* scikit-image: image processing in Python. *PeerJ* **2,** e453 (2014).

61. Pedregosa, F. *et al.* Scikit-learn: Machine learning in Python. *Journal of machine learning research* **12,** 2825–2830 (2011).

62. Prechelt, L. An empirical comparison of seven programming languages. *Computer* **33,** 23–29 (2000).

63. Shihavuddin, A. *et al.* Smooth 2D manifold extraction from 3D image stack. *Nature Communications* **8,** 15554 (2017).

64. Irshad, H., Veillard, A., Roux, L. & Racoceanu, D. Methods for nuclei detection, segmentation, and classification in digital histopathology: a review—current status and future potential. *IEEE reviews in biomedical engineering* **7,** 97–114 (2014).

65. Rujuta, O. & Vyavahare, A. Review of Nuclei Detection, Segmentation in Microscopic Images. *J Bioengineer & Biomedical Sci* **7,** 2 (2017).

66. Smal, I., Loog, M., Niessen, W. & Meijering, E. *Quantitative comparison of spot detection methods in live-cell fluorescence microscopy imaging* in *Biomedical Imaging: From Nano to Macro, 2009. ISBI'09. IEEE International Symposium on* (2009), 1178–1181.

67. Štěpka, K. *et al.* Performance and sensitivity evaluation of 3D spot detection methods in confocal microscopy. *Cytometry Part A* **87,** 759–772 (2015).

68. Genovesio, A. *Une méthode de poursuite de tâches multiples : application à l'étude de la dynamique d'objets biologiques en microscopie 3D+T* PhD thesis (université Paris Descartes, 2005).

69. Saxton, M. J. Single-particle tracking: connecting the dots. *Nature methods* **5,** 671 (2008).

70. Meijering, E., Dzyubachyk, O. & Smal, I. in *Methods in enzymology* 183–200 (Elsevier, 2012).

71. Meijering, E., Smal, I. & Danuser, G. Tracking in molecular bioimaging. *IEEE signal processing magazine* **23,** 46–53 (2006).

72. Kalaidzidis, Y. Intracellular objects tracking. *European journal of cell biology* **86,** 569–578 (2007).

73. Dorn, J. F., Danuser, G. & Yang, G. Computational processing and analysis of dynamic fluorescence image data. *Methods in cell biology* **85,** 497–538 (2008).

74. Meijering, E., Dzyubachyk, O., Smal, I. & van Cappellen, W. A. *Tracking in cell and developmental biology* in *Seminars in cell & developmental biology* **20** (2009), 894–902.

75. Jaqaman, K. & Danuser, G. Computational image analysis of cellular dynamics: a case study based on particle tracking. *Cold Spring Harbor Protocols* **2009,** pdb–top65 (2009).

76. Rohr, K. *et al.* Tracking and quantitative analysis of dynamic movements of cells and particles. *Cold Spring Harbor Protocols* **2010,** pdb–top80 (2010).

77. Blackman, S. & Popoli, R. Design and Analysis of Modern Tracking Systems (Artech House Radar Library). *Artech house* (1999).

78. Sonka, M., Hlavac, V. & Boyle, R. *Image processing, analysis, and machine vision* (Cengage Learning, 2014).

79. Chenouard, N. *et al.* Objective comparison of particle tracking methods. *Nature methods* **11,** 281 (2014).

80. Klar, T. A., Jakobs, S., Dyba, M., Egner, A. & Hell, S. W. Fluorescence microscopy with diffraction resolution barrier broken by stimulated emission. *Proceedings of the National Academy of Sciences* **97,** 8206–8210 (2000).

81. Betzig, E. *et al.* Imaging intracellular fluorescent proteins at nanometer resolution. *Science* **313,** 1642–1645 (2006).

82. Nägerl, U. V., Willig, K. I., Hein, B., Hell, S. W. & Bonhoeffer, T. Live-cell imaging of dendritic spines by STED microscopy. *Proceedings of the National Academy of Sciences* **105,** 18982–18987 (2008).

83. Born, M. & Wolf, E. Principles of Optics, Cambridge University Press. *New York,* 704 (1999).

84. Denk, W., Strickler, J. H. & Webb, W. W. Two-photon laser scanning fluorescence microscopy. *Science* **248,** 73–76 (1990).

85. Kawano, H., Kogure, T., Abe, Y., Mizuno, H. & Miyawaki, A. Two-photon dual-color imaging using fluorescent proteins. *Nature Methods* **5,** 373 (2008).

86. Fortini, M. E., Skupski, M. P., Boguski, M. S. & Hariharan, I. K. A survey of human disease gene counterparts in the Drosophila genome. *The Journal of cell biology* **150,** F23–F30 (2000).

87. Moro, M. L. *et al.* Pyroglutamate and Isoaspartate modified Amyloid-Beta in ageing and Alzheimer's disease. *Acta Neuropathologica Communications* **6.** doi:10.1186/s40478-017-0505-x. <https://doi.org/10.1186/s40478-017-0505-x> (Jan. 2018).

88. Devitt, G., Howard, K., Mudher, A. & Mahajan, S. Raman Spectroscopy: An Emerging Tool in Neurodegenerative Disease Research and Diagnosis. *ACS Chemical Neuroscience* **9,** 404–420 (Jan. 2018).

89. Quraishe, S., Sealey, M., Cranfield, L. & Mudher, A. Microtubule stabilising peptides rescue tau phenotypes in-vivo. *Scientific Reports* **6.** doi:10.1038/srep38224. <https://doi.org/10.1038/srep38224> (Dec. 2016).

90. Castle, W. E., Carpenter, F. W., Clark, A. H., Mast, S. O. & Barrows, W. M. *The effects of inbreeding, cross-breeding, and selection upon the fertility and variability of Drosophila* in *Proceedings of the American Academy of Arts and Sciences* **41** (1906), 731–786.

91. Lawrence, P. A. *The Making of a Fly: The Genetics of Animal Design* ISBN: 0632030488 (Wiley-Blackwell, 1992).

92. Pitnick, S. Investment in Testes and the Cost of Making Long Sperm in Drosophila. *The American Naturalist* **148,** 57–80 (July 1996).

93. Adams, M. D. The Genome Sequence of Drosophila melanogaster. *Science* **287,** 2185–2195 (Mar. 2000).

94. Bier, E. Drosophila, the golden bug, emerges as a tool for human genetics. *Nature Reviews Genetics* **6,** 9–23. ISSN: 14710056 (2005).

95. Pascual, A. Localization of Long-Term Memory Within the Drosophila Mushroom Body. *Science* **294,** 1115–1117 (Nov. 2001).

96. Keene, A. C. & Waddell, S. Drosophila olfactory memory: single genes to complex neural circuits. *Nature reviews. Neuroscience* **8,** 341–54. ISSN: 1471-003X (May 2007).

97. Aso, Y. *et al.* The mushroom body of adult Drosophila characterized by GAL4 drivers. *Journal of neurogenetics* **23,** 156–172. ISSN: 1563-5260 (2009).

98. Yu, D., Akalal, D.-B. G. & Davis, R. L. Drosophila α/β mushroom body neurons form a branch-specific, long-term cellular memory trace after spaced olfactory conditioning. *Neuron* **52,** 845–855 (2006).

99. Wilson, R. I. & Laurent, G. Role of GABAergic inhibition in shaping odor-evoked spatiotemporal patterns in the Drosophila antennal lobe. *Journal of Neuroscience* **25,** 9069–9079 (2005).

100. Turner, G. C., Bazhenov, M. & Laurent, G. Olfactory representations by Drosophila mushroom body neurons. *Journal of neurophysiology* **99,** 734–746 (2008).

101. Web, S., York, N. & Nw, A. Molecular and Cellular Approaches to Memory Allocation in Neural Circuits Alcino J. Silva, *October* **391,** 391–396 (2009).

102. Tonegawa, S., Pignatelli, M., Roy, D. S. & Ryan, T. J. Memory engram storage and retrieval. *Current Opinion in Neurobiology* **35,** 101–109. ISSN: 18736882 (2015).

103. Hebb, D. O. *et al. The organization of behavior: A neuropsychological theory* 1949.

104. Lowel, S. & Singer, W. Selection of intrinsic horizontal connections in the visual cortex by correlated neuronal activity. *Science* **255,** 209–212 (1992).

105. Tonegawa, S., Liu, X., Ramirez, S. & Redondo, R. Memory Engram Cells Have Come of Age. *Neuron* **87,** 918–931. ISSN: 10974199 (2015).

106. Semon, R. W. Die Mneme als erhaltendes Prinzip im Wechsel des organischen Lebens (dritte Auflage). *Leipzig, Wilhelm Engelmann* (1904).

107. Semon, R. Die nmemischen empfindungen.[Mnemic psychology]. *Leipzig: Wilhelm Engelmann* (1909).

108. Liu, X. *et al.* Optogenetic stimulation of a hippocampal engram activates fear memory recall. *Nature* **484,** 381 (2012).

109. Heim, N. & Griesbeck, O. Genetically encoded indicators of cellular calcium dynamics based on troponin C and green fluorescent protein. *Journal of biological chemistry* **279,** 14280–14286 (2004).

110. Miyawaki, A. *et al.* Fluorescent indicators for Ca 2+ based on green fluorescent proteins and calmodulin. *Nature* **388,** 882 (1997).

111. Akerboom, J. *et al.* Crystal structures of the GCaMP calcium sensor reveal the mechanism of fluorescence signal change and aid rational design. *Journal of biological chemistry* **284,** 6455–6464 (2009).

112. Griffiths, A. J. *et al. An introduction to genetic analysis* (Macmillan, 2005).

113. Duffy, J. B. GAL4 system in Drosophila: a fly geneticist's Swiss army knife. *genesis* **34,** 1–15 (2002).

114. Caussinus, E., Colombelli, J. & Affolter, M. Tip-cell migration controls stalk-cell intercalation during Drosophila tracheal tube elongation. *Current biology* **18,** 1727–1734 (2008).

115. Berlin, S. *et al.* Photoactivatable genetically encoded calcium indicators for targeted neuronal imaging. *Nature methods* **12,** 852 (2015).

116. Berridge, M. J., Lipp, P. & Bootman, M. D. The versatility and universality of calcium signalling. *Nature reviews Molecular cell biology* **1,** 11 (2000).

117. Chen, T.-W. *et al.* Ultrasensitive fluorescent proteins for imaging neuronal activity. *Nature* **499,** 295 (2013).

118. *Encyclopedia of Entomology (4 Volume Set)* ISBN: 1402062427. <https://www.amazon.com/Encyclopedia-Entomology-Set-John-Capinera/dp/1402062427?SubscriptionId=0JYN1NVW651KCA56C102&tag=techkie-20&linkCode=xm2&camp=2025&creative=165953&creativeASIN=1402062427> (Springer, 2008).

119. Préat, T. Decreased Odor Avoidance after Electric Shock inDrosophila Mutants Biases Learning and Memory Tests. *Journal of Neuroscience* **18,** 8534–8538 (1998).

120. Fiala, A. & Spall, T. In vivo calcium imaging of brain activity in Drosophila by transgenic cameleon expression. *Science Signaling* **2003,** pl6–pl6 (2003).

121. Bansal, V., Patel, S. & Saggau, P. High-speed addressable confocal microscopy for functional imaging of cellular activity. *Journal of biomedical optics* **11,** 034003 (2006).

122. Nwaneshiudu, A. *et al.* Introduction to confocal microscopy. *Journal of Investigative Dermatology* **132,** 1–5. ISSN: 0022202X (2012).

123. Vos, K. D. *Cell Counter* <https://imagej.nih.gov/ij/plugins/cell-counter.html> (2010).

124. Yoo, H., Song, I. & GWEON, D.-G. Measurement and restoration of the point spread function of fluorescence confocal microscopy. *Journal of microscopy* **221,** 172–176 (2006).

125. Tan. *Introduction to data mining* ISBN: 0-321-32136-7 (Pearson Addison Wesley, Boston, 2005).

126. Štěpka, K. *et al.* Performance and sensitivity evaluation of 3d spot detection methods in confocal microscopy. *Cytometry Part A,* n/a–n/a. ISSN: 15524922 (2015).

127. Smal, I., Loog, M., Niessen, W. & Meijering, E. Quantitative comparison of spot detection methods in fluorescence microscopy. *Medical Imaging, IEEE Transactions on* **29,** 282–301 (2010).

128. Matula, P. *et al. Quantification of fluorescent spots in time series of 3D confocal microscopy images of endoplasmic reticulum exit sites based on the HMAX transform* in *SPIE Medical Imaging* (2010), 76261H–76261H.

129. Olivo-Marin, J. C. Extraction of spots in biological images using multiscale products. *Pattern Recognition* **35,** 1989–1996. ISSN: 00313203 (2002).

130. Matula, P., Maska, M., Danek, O., Matula, P. & Kozubek, M. *Acquiarium: free software for the acquisition and analysis of 3D images of cells in fluorescence microscopy* in *Biomedical Imaging: From Nano to Macro, 2009. ISBI'09. IEEE International Symposium on* (2009), 1138–1141.

131. McKinley, S. & Levine, M. Cubic spline interpolation. *College of the Redwoods* **45,** 1049–1060 (1998).

132. Schmidt, T., Schütz, G., Baumgartner, W., Gruber, H. & Schindler, H. Imaging of single molecule diffusion. *Proceedings of the National Academy of Sciences* **93,** 2926–2929 (1996).

133. Young, I. T. Sampling density and quantitative microscopy. *Analytical and quantitative cytology and histology* **10,** 269–275 (1988).

134. Toyoshima, Y. *et al.* Accurate Automatic Detection of Densely Distributed Cell Nuclei in 3D Space. *PLoS Computational Biology* **12,** 1–20. ISSN: 15537358 (2016).

135. Campbell, R. a. a. *et al.* Imaging a population code for odor identity in the Drosophila mushroom body. *The Journal of neuroscience : the official journal of the Society for Neuroscience* **33,** 10568–81. ISSN: 1529-2401 (June 2013).

136. Hiroi, M. *et al.* Principal component analysis of odor coding at the level of third-order olfactory neurons in Drosophila. *Genes to cells : devoted to molecular & cellular mechanisms* **18,** 1070–81. ISSN: 1365-2443 (Dec. 2013).

137. Murthy, M., Fiete, I. & Laurent, G. Testing odor response stereotypy in the Drosophila mushroom body. *Neuron* **59,** 1009–23. ISSN: 1097-4199 (Sept. 2008).

138. Barth, M. & Heisenberg, M. Vision Affects Mushroom Bodies and Central Complex in Drosophila melanogaster. *Learning & Memory* **4,** 219–229 (1997).

139. Fiala, A., Spall, T., Diegelmann, S. & Eisermann, B. Genetically Expressed Cameleon in Drosophila melanogaster Is Used to Visualize Olfactory Information in Projection Neurons. *Current biology* **12,** 1877–1884 (2002).

140. Kachel, H. S., Patel, R. N., Franzyk, H. & Mellor, I. R. Block of nicotinic acetylcholine receptors by philanthotoxins is strongly dependent on their subunit composition. *Scientific Reports* **6,** 1–13. ISSN: 20452322 (2016).

141. Karst, H., Piek, T., Van Marle, J., Lind, A. & Van Weeren-Kramer, J. Structure-activity relationship of philanthotoxins—I. Pre-and postsynaptic inhibition of the locust neuromuscular transmission. *Comparative Biochemistry and Physiology Part C: Comparative Pharmacology* **98,** 471–477 (1991).

142. Benson, J., Schürmann, F., Kaufmann, L., Gsell, L. & Piek, T. Inhibition of dipteran larval neuromuscular synaptic transmission by analogues of philanthotoxin-4.3. 3: a structure-activity study. *Comparative biochemistry and physiology. C, Comparative pharmacology and toxicology* **102,** 267–272 (1992).

143. Myronenko, A. & Song, X. Point set registration: coherent point drift. *IEEE transactions on pattern analysis and machine intelligence* **32,** 2262–75. ISSN: 1939-3539 (Dec. 2010).

144. Hazewinkel, M. *Encyclopaedia of Mathematics (set)* ISBN: 1556080107 (Springer, 1994).

145. Shen, H. *et al.* Single Particle Tracking: From Theory to Biophysical Applications. *Chemical Reviews* **117,** 7331–7376. ISSN: 15206890 (2017).

146. Ester, M., Kriegel, H.-P., Sander, J., Xu, X., *et al. A density-based algorithm for discovering clusters in large spatial databases with noise.* in *Kdd* **96** (1996), 226–231.

147. Witten, I. H., Frank, E., Hall, M. A. & Pal, C. J. *Data Mining: Practical machine learning tools and techniques* (Morgan Kaufmann, 2016).

148. Han, J., Pei, J. & Kamber, M. *Data mining: concepts and techniques* (Elsevier, 2011).

149. Agrawal, R., Gehrke, J., Gunopulos, D. & Raghavan, P. *Automatic subspace clustering of high dimensional data for data mining applications* **2** (ACM, 1998).

150. Lloyd, S. Least squares quantization in PCM. *IEEE transactions on information theory* **28,** 129–137 (1982).

151. Meijering, E. A chronology of interpolation: from ancient astronomy to modern signal and image processing. *Proceedings of the IEEE* **90,** 319–342 (Mar. 2002).

152. Chenouard, N., Bloch, I. & Olivo-Marin, J.-C. Multiple hypothesis tracking for cluttered biological image sequences. *IEEE transactions on pattern analysis and machine intelligence* **35,** 2736–3750 (2013).

153. Tinevez, J.-Y. *et al.* TrackMate: An open and extensible platform for single-particle tracking. *Methods* **115,** 80–90 (2017).

154. Aurenhammer, F. Voronoi diagrams - a survey of a fundamental geometric data structure. *ACM Computing Surveys* **23,** 345–405 (Sept. 1991).

155. Meyer, R. R. & Kirkland, A. I. Characterisation of the signal and noise transfer of CCD cameras for electron detection. *Microscopy research and technique* **49,** 269–280 (2000).

156. Butterworth, S. On the theory of filter amplifiers. *Wireless Engineer* **7,** 536–541 (1930).

157. Jia, H., Rochefort, N. L., Chen, X. & Konnerth, A. In vivo two-photon imaging of sensory-evoked dendritic calcium signals in cortical neurons. *Nature protocols* **6,** 28 (2011).

158. Lin, A. C., Bygrave, A. M., De Calignon, A., Lee, T. & Miesenböck, G. Sparse, decorrelated odor coding in the mushroom body enhances learned odor discrimination. *Nature neuroscience* **17,** 559 (2014).

159. Honegger, K. S., Campbell, R. A. & Turner, G. C. Cellular-resolution population imaging reveals robust sparse coding in the Drosophila mushroom body. *Journal of Neuroscience* **31,** 11772–11785 (2011).

160. Hallem, E. A. & Carlson, J. R. Coding of odors by a receptor repertoire. *Cell* **125,** 143–160 (2006).

161. Bhandawat, V., Olsen, S. R., Gouwens, N. W., Schlief, M. L. & Wilson, R. I. Sensory processing in the Drosophila antennal lobe increases reliability and separability of ensemble odor representations. *Nature neuroscience* **10,** 1474 (2007).

162. Olsen, S. R., Bhandawat, V. & Wilson, R. I. Divisive normalization in olfactory population codes. *Neuron* **66,** 287–299 (2010).

163. Singhal, A. *et al.* Modern information retrieval: A brief overview. *IEEE Data Eng. Bull.* **24,** 35–43 (2001).

164. Donoho, D. L. *et al.* High-dimensional data analysis: The curses and blessings of dimensionality. *AMS math challenges lecture* **1,** 32 (2000).

165. Reiter, L. T., Potocki, L., Chien, S., Gribskov, M. & Bier, E. A systematic analysis of human disease-associated gene sequences in Drosophila melanogaster. *Genome research* **11,** 1114–1125 (2001).

RÉSUMÉ

La formation et la consolidation de souvenirs est l'une des caractéristiques fondamentales du cerveau, responsable de l'apprentissage et de comportements cognitifs élevés. Malgré son importance, ce processus n'est pas entièrement compris à ce jour et fait l'objet de nombreux travaux de de recherche, allant de l'analyse de l'activité des synapses individuelles à la reconstruction de cartes de connectivité du cerveau. Dans ce travail, nous proposons une approche intégrée pour mesurer *in vivo* l'activité de chaque neurone du corps pédonculé (Mushroom body, MB) de la *Drosophila melanogaster* dans une procédure entièrement automatisée. Il s'agit d'imager en 3D et dans le temps le MB dans sa totalité par microscopie confocale et d'opérer un suivi temporel de la position de chaque neurone afin de relever leur niveau individuel d'activité. En utilisant cette approche, nous avons découvert que pendant la formation de la mémoire à long terme, de nouveaux neurones sont recrutés au sein du corps pédonculés, tandis que l'intensité de la réponse des neurones individuels reste inchangée. Au delà de l'apport méthodologique qui permet à présent de quantifier automatiquement l'activité d'un grand nombre de neurones, ce travail a contribué à une meilleure compréhension de la formation de la mémoire à long terme.

MOTS CLÉS

Drosophile, mémoire, 3D, détection, suivi

ABSTRACT

Formation and consolidation of new memories is one of the fundamental characteristics of the brain, responsible for learning and high cognitive behavior. While important, the process isn't fully understood to the present day and is the subject of various studies, spanning from the activity analysis of individual synapses to the reconstruction of brain connectivity maps. In this work, we propose a bold approach, on which we aim to measure *in vivo* the activity of every single neuron from the whole Mushroom body (MB) of the *Drosophila melanogaster*, in a fully automated procedure. After a 3D image acquisition over time of the MB by means of confocal microscopy, an automated detection and tracking of the neurons is performed. The whole process takes place while the fly is awake and subjected to different odor stimulations, so that it is possible to associate the activity patterns at the single cell level to the stimulus that is being received. By comparing the response patterns from flies that were trained and flies that were not trained to associate an odor with an electric shock we identified changes in neuronal activity, providing information on how memory is formed. Beyond the methodological innovation that brought the possibility to track the activity of a large set of single neurons, this work contributed to the current understanding of long term memory formation.

KEYWORDS

Drosophila, memory, 3D, detection, tracking